

# THESE POUR OBTENIR LE GRADE DE DOCTEUR DE L'ÉCOLE NATIONALE SUPÉRIEURE DE CHIMIE DE MONTPELLIER

En Chimie et Physico-Chimie des Matériaux

École doctorale 459 – Sciences Chimiques Balard

Unité de recherche – Institut Charles Gerhardt de Montpellier (ICGM) – UMR5253

## Evaluation of catalytic performances of mesoporous zeolites obtained by recrystallization on isomerization of fatty acid methyl esters: towards the improvement of the biodiesel properties in cold environments.

Présentée par **Jonathan Fabian Sierra Cantor**  
le 22 décembre 2020

Sous la direction de **Corine Gérardin**  
et **Nathalie Tanchoux**

Devant le jury composé de

Mme Karine DE OLIVEIRA VIGIER, Professeure, Université de Poitiers  
Mme Bénédicte LEBEAU, Directrice de Recherches, Université de Mulhouse  
Mme Valérie MEILLE, Chargée de Recherches, Université Claude Bernard Lyon I  
M. Carlos GUERRERO FAJARDO, Assistant Professor, Universidad Nacional de Colombia  
M. Didier TICHIT, Directeur de Recherches émérite, ICGM, Montpellier  
Mme Nathalie TANCHOUX, Chargée de Recherches, ICGM, Montpellier  
Mme Corine GERARDIN, Directrice de Recherches, ICGM, Montpellier

Rapportrice  
Rapportrice  
Examinatrice  
Examineur  
Examineur-Président du jury  
Co-directrice de thèse  
Directrice de thèse





*This work is dedicated to my parents,  
my brother and my girlfriend for their  
unconditional support and patience  
during this long road.*





## Acknowledgments

First of all, I would like to thank my supervisors, Dr. Corine Gérardin and Dr. Nathalie Tanchoux, for their great guidance, their advices, encouragement, and kindly support that they give me throughout my time as Ph.D. student, especially by their constant feedback during this last period of writing my thesis. They were always available to support me, answer my questions and enrich my knowledge with questions that I had not even ask me about my work. Thank you, I have learned so much about materials, catalysis, and others research topics. I have grown as professional and as a person due to their guidance. I would like to thank Dr. Carlos Guerrero, co-supervisor on this project, for his great support, as well as to share with me the enthusiasm for development of new and sustainable technologies and the so many things that he has thought me during this time in the sein of his research group *Aprovechamiento Energético de Recursos Naturales* (APRENA - Energy Utilization of Natural Resources) of the Department of Chemistry of the National University of Colombia. I thank him for his support to follow this route and guidance during my career in research. Additionally, I would like to thank Dr. Dariusz Swierczynski for the conception of this project and his support that allowed me to undertake this work.

Furthermore, I thank the people who have been part of the research group *Des Ressources Renouvelables aux Matériaux et Molécules* (R2M2), for their support, advices, and the collaboration during the development of this work. I would like to make a special mention to Prof. Francesco Di Renzo, for his innumerable and invaluable advices for the structural characterization of the materials used as catalysts, Dr. Hugo Petitjean, for his advices and his collaboration for the infrared characterization of the acidic sites of the catalyst along with the collaboration of Dr. Maxime Riviere. Moreover, I would like to thank all research staff of the research team *Matériaux Avancés pour la Catalyse et la Santé* (MACS), doing a special mention to Olinda Gimello, for her kindly help with the characterization of the different products by chromatography and mass spectroscopy, Thomas Cacciaguerra, for the guidance in XRD analysis and for carrying out the TEM and SEM-EDX analysis of the catalytic materials, and Jeremy Rodriguez, for the help in the technical support, construction and maintenance of the different equipment used during the development of this project. I would like to thank Dr. Anne Aubert for her invaluable help in the analysis of the properties of the products through differential scanning calorimetry, as well as Emmanuel Fernandez and Philippe Gaveau for their help for the NMR analyses of zeolite materials before and after the catalytic tests.

On top of that, I would like to thank the juries for their time and feedback while evaluating this thesis. I would also like to thank the *Ecole Nationale Supérieure de Chimie de Montpellier* (ENSCM), for providing the funding which allowed me to undertake this

research. I would like to thank the *Institut Charles Gerhardt de Montpellier* (ICGM) and the research team *Matériaux Avancés pour la Catalyse et la Santé* (MACS), not only for allowed me to work in the sein of their research installations, and the use the different facilities for the development of this project, but also for giving me the opportunity to collaborate with the high quality research and administrative staff who has helped me for the development of this thesis.

Infinite gratefulness to my parents and my brother for their love, unconditional support, and patience. Their guidance and support let on me to reach to be the person that I am today. To my girlfriend, Yadira Diaz, I would like to thank for being by my side during this time. Her encouragement, support, love, and patience. I have grown a lot as person and her company has made me very happy.

*Agradecimientos infinitos a mis padres y mi hermano, su amor, apoyo incondicional y paciencia me han llevado a ser la persona que soy hoy en día. A mi novia, le quiero agradecer por estar a mi lado. Su ánimo apoyo, amor, y paciencia me han llevado a crecer como persona y su compañía me ha hecho muy feliz.*

Finally, I am grateful to my friends for their support and their friendship. I thank my friends in the laboratory from Colombia, France, and other foreign countries. I loved this international experience. We had incredibly fun moments while taking the coffee, having the lunch and when we went out. I thank my best friend in the lab, Sonia Aguilera. She helped me a lot in many ways and really, she did my life easier in this foreign land. I want to thank too the other friendships gained during these three years, especially my Colombian friends, they made me feel accompanied and closer to home. At the end, I would like to thank all people that I have not mentioned here and who support me and make possible that this thesis was done.

## Abstract

The interest in the valorization of lipid biomass as replacement of fossil oil supply has been increasing in the last years. In the present work, we chose, among the different possibilities to transform lipid biomass in high added-value products, to study the catalytic isomerization reaction of fatty acid methyl esters into alkyl-branched fatty acid methyl esters. Although the use of zeolites as catalysts seems promising to promote isomerization reactions over dimerization, the fast loss of catalytic activity prevents this process from being economically competitive. As the diffusion limitations are probably the main parameter leading to this fast deactivation, the strategy proposed here is the modification of the porous network of zeolites by adding mesopores into zeolite crystals. Two zeolites with different microporous frameworks were chosen for this project: ferrierite, with a 2-D system of pores of medium size, and zeolite Y, with a 3-D pore system with larger pores. A secondary mesoporous system was created by one-step recrystallization, and the resulting materials were deeply characterized.

Samples obtained after recrystallization of ferrierite (Si/Al: 9) present a secondary system of parallelepiped-shaped mesopores along 10-MR channel direction connected to ferrierite external surface by micropores. The recrystallized materials contain fewer but more accessible acidic sites than the parent ferrierite. Zeolite Y samples led to two different micro-mesoporous materials, depending on the amount of aluminum in the framework. In the case of a high Si/Al ratio (30), the obtained mesoporous system was wormlike with pores distributed throughout the crystal and well-connected to the microporous network, creating a hierarchical porous structure which improved accessibility to the acidic sites. In the second case, recrystallization of zeolite Y with a low Si/Al ratio (6) led to a composite of microporous zeolitic domains and mesoporous domains, which were not well connected.

The catalytic performance of these materials was evaluated in methyl oleate isomerization in batch and continuous flow conditions comparing recrystallized and parent H-form zeolitic materials. The use of H-form recrystallized ferrierite materials as the catalysts in batch conditions led to getting slight improvements in yield of branched products at all temperatures tested in comparison with the parent materials. In continuous flow conditions, the new mesopore system improved the catalytic behavior by allowing coke precursors to diffuse from the micropores to mesopores, thus retarding deactivation processes. This new catalytic system used in a continuous flow process at 285°C and 2.0 MPa allowed keeping yields in branched products up to 50% and was stable for the first eight hours of time-on-stream. In the case of zeolite Y, the presence of mesopores did not improve the catalytic performances, even in the case of a low Si/Al ratio that yielded to a number of acid sites

similar to the one in ferrierite. The stability of these catalysts during continuous flow experiments was the only improvement noticed. These results show that, even if the mesoporous network modifies the selectivity of the catalyst and its stability, the performances of the catalytic system is still strongly dependent of the microporous structure of the zeolitic material used.

The freezing points of the products of these reactions were measured by DSC, since methyl oleate isomerization products are expected to improve the cold flow properties of biodiesel synthesized from palm oil. The behavior of these products in cold environments depends on both the yields and the distribution of the products.

Finally, considering that the presence of straight-line saturated fatty acids is more responsible for this bad behavior than the presence of unsaturated ones, a preliminary study of the methyl palmitate hydroisomerization using bifunctional Pt/acid meso-microporous zeolites as catalysts was performed.

**Keywords:** Mesoporous zeolites, one-step recrystallization, FAMEs isomerization, catalyst performance and deactivation, biodiesel cold flow properties.

## Résumé

L'intérêt pour la valorisation de la biomasse lipidique pour remplacer les ressources fossiles s'est accru ces dernières années. Dans le présent projet, nous avons choisi, parmi les différentes possibilités de transformation de la biomasse lipidique en produits à haute valeur ajoutée, d'étudier la réaction d'isomérisation catalytique des esters méthyliques d'acides gras en esters méthyliques ramifiés. L'utilisation de zéolithes pour cette réaction semble prometteuse, mais la désactivation rapide des catalyseurs empêche une plus large utilisation de ces matériaux. Comme les limitations de diffusion sont probablement le principal paramètre conduisant à cette désactivation rapide, la stratégie proposée ici consiste à modifier le réseau poreux des zéolithes en générant un réseau de mésopores au sein des cristaux. Deux zéolithes de structures différentes ont été choisies: la ferriérite, avec un système de canaux 2-D, et la zéolithe Y, avec un système de canaux 3-D et des pores plus larges. Un système secondaire de mésopores a été créé par recristallisation, et les matériaux obtenus ont été caractérisés.

Les matériaux issus de la recristallisation de la ferriérite présentent un système de mésopores de forme parallélépipédique le long des canaux 10-MR reliés à la surface externe de la ferriérite par des micropores. Ces matériaux contiennent des sites acides moins nombreux mais plus accessibles que la ferriérite de départ. Les échantillons de zéolithe Y ont donné deux matériaux micro-mésoporeux différents, selon la quantité d'aluminium initiale dans la zéolithe parent. Dans le cas d'un rapport Si/Al élevé (30), le système mésoporeux est vermiculaire avec des pores répartis dans l'ensemble des cristaux et connectés au réseau microporeux, créant une structure hiérarchique qui améliore l'accessibilité aux sites acides. A partir de la zéolithe Y avec un faible rapport Si/Al (6), le matériau obtenu est un composite de domaines microporeux et mésoporeux, qui ne sont pas bien connectés.

La performance catalytique des matériaux a été évaluée dans l'isomérisation de l'oléate de méthyle en batch et en réacteur continu en comparant les matériaux zéolithiques recristallisés et les zéolithes parents sous forme H. L'utilisation des ferriérites recristallisées en réacteur batch a permis d'obtenir de légères améliorations du rendement en produits ramifiés à toutes les températures testées par rapport aux matériaux initiaux. En réacteur continu, le réseau mésoporeux a amélioré le comportement du catalyseur en permettant aux précurseurs de coke de diffuser des micropores aux mésopores, ce qui retarde les processus de désactivation. Ce nouveau système catalytique utilisé en flux continu donne des rendements en produits ramifiés jusqu'à 50% et des conversions stables, au moins pendant les huit premières heures de fonctionnement. Dans le cas de la zéolithe Y, la

présence de mésopores n'a pas amélioré les performances catalytiques, même dans le cas d'un faible rapport Si/Al, qui amène à un nombre de sites acides équivalent à celui de la ferriérite. La stabilité de ces catalyseurs lors d'expériences en réacteur continu a été la seule amélioration constatée. Ces résultats montrent que, même si le réseau mésoporeux modifie la sélectivité et la stabilité des catalyseurs, les performances du système catalytique restent fortement dépendantes de la structure microporeuse du matériau zéolithique utilisé comme catalyseur.

Les points de congélation des produits obtenus par ces réactions ont été mesurés par DSC, car les produits branchés pourraient améliorer les propriétés d'écoulement à froid du biodiesel synthétisé à partir de l'huile de palme. Le comportement de ces produits dans les environnements froids dépend à la fois des rendements obtenus et de la distribution des produits.

Enfin, une étude préliminaire d'hydroisomérisation du palmitate de méthyle utilisant des matériaux zéolithiques méso-microporeux Pt/acide bifonctionnels comme catalyseurs a été réalisée.

**Mots clés :** Zéolithes mésoporeuses, recrystallisation, isomérisation d'esters méthyliques d'acides gras, performances et désactivation du catalyseur, propriétés d'écoulement à froid du biodiesel.

# Content

	Pag.
Abstract.....	VII
Résumé.....	IX
List of Figures.....	XV
List of tables .....	XXII
List of symbols and abbreviations.....	XXIII
Introduction .....	1
1. State of the art.....	7
1.1 LIPIDS AS GREEN RAW MATERIALS .....	7
1.1.1 <i>Biodiesel</i> .....	8
1.1.2 <i>Cold Flow properties of fatty acid and derivatives</i> .....	10
1.2 BRANCHED FATTY ACIDS AND DERIVATIVES .....	12
1.2.1 <i>Isomerization Reaction</i> .....	13
▪ Hydroisomerization and deoxygenation reactions .....	15
1.2.2 <i>Use of zeolites to obtain branched fatty acids</i> .....	18
1.3 ZEOLITES AS CATALYTIC MATERIALS .....	20
1.3.1 <i>Zeolites: Structural characteristics and properties</i> .....	20
1.3.2 <i>Shape selectivity and diffusion regimes in zeolites</i> .....	22
1.4 ZEOLITE-BASED MESO-MICROPOROUS MATERIALS.....	26
1.4.1 <i>Strategies for obtaining micro-mesoporous materials with zeolitic framework</i> .....	26
1.4.2 <i>Recrystallization of zeolites</i> .....	31
1.5 THE FERRIERITE ZEOLITE.....	34
1.5.1 <i>Ferrierite-based meso-microporous materials</i> .....	37
1.5.2 <i>Recrystallization of ferrierite zeolites</i> .....	40
1.6 ZEOLITE Y .....	43
1.6.1 <i>Meso-microporous materials from zeolite Y</i> .....	45
1.6.2 <i>Zeolite Y recrystallization</i> .....	47
1.7 JUSTIFICATION AND IMPROVEMENT STRATEGY .....	50
1.8 OBJECTIVES.....	51
2. Experimental methodology .....	53
2.1 CATALYTIC MATERIALS PREPARATION.....	53
2.1.1 <i>Recrystallization of ferrierite</i> .....	53

2.1.2	<i>Recrystallization of zeolites Y</i> .....	54
2.1.3	<i>Catalyst shaping &amp; impregnation</i> .....	54
2.2	CATALYTIC MATERIALS CHARACTERIZATION .....	55
2.2.1	<i>Structural and textural characterization</i> .....	55
▪	X-Ray diffraction (XRD) .....	55
▪	Manometry of nitrogen adsorption.....	55
▪	Electronic microscopy analysis .....	56
▪	Magic Angle Spinning Nuclear Magnetic Resonance of <sup>29</sup> Si ( <sup>29</sup> Si MAS NMR) .....	56
▪	Magic Angle Spinning Nuclear Magnetic Resonance of <sup>27</sup> Al ( <sup>27</sup> Al MAS NMR).....	56
2.2.2	<i>Acidic sites characterization</i> .....	57
▪	Ammonia temperature-programmed desorption (TPD-NH <sub>3</sub> ) .....	57
▪	Infrared analysis of adsorption/desorption of pyridine .....	57
2.2.3	<i>Spent catalytic material characterization</i> .....	57
2.3	CATALYTIC PERFORMANCE TESTS .....	58
2.3.1	<i>Reagents and materials</i> .....	58
2.3.2	<i>Batch conditions</i> .....	58
2.3.3	<i>Continuous flow conditions</i> .....	60
2.4	REACTION PRODUCTS CHARACTERIZATION .....	61
2.4.1	<i>Gas chromatography analysis</i> .....	61
2.4.2	<i>Mass spectroscopy analyses</i> .....	63
2.4.3	<i>Differential scanning calorimetry (DSC) analysis</i> .....	63
3.	Synthesis of catalytic materials: micro-mesoporous materials from zeolites by recrystallization .....	65
3.1	RECRYSTALLIZATION OF FERRIERITE ZEOLITE .....	65
3.1.1	<i>Structure, texture and chemical composition of the ferrierite-based H-form zeolitic materials.</i> 66	
3.1.2	<i>FTIR analysis of acidic sites properties on the ferrierite-based H-form zeolitic materials</i> .....	73
3.1.3	<i>Conclusion</i> .....	77
3.2	RECRYSTALLIZATION OF ZEOLITES Y .....	78
3.2.1	<i>High Silica Zeolite Y recrystallization (H-Y-30)</i> .....	78
▪	Structure, texture and chemical composition of the high silica zeolite Y-based H-form zeolitic materials. 78	
▪	FTIR analysis of acidic sites properties on the high silica zeolite Y-based H-form zeolitic materials .....	86
▪	Conclusions .....	89
3.2.2	<i>Low silica Zeolite Y recrystallization</i> .....	90
▪	Structure, texture and chemical composition of the low silica zeolite Y-based H-form zeolitic materials	90
▪	FTIR analysis of acidic sites properties on the high silica zeolite Y-based H-form zeolitic materials .....	98
▪	Conclusions .....	102
3.3	CONCLUSIONS .....	102
4.	Performance test of Ferrierite type catalytic materials in methyl oleate isomerization. 105	
4.1	CATALYTIC PERFORMANCE EVALUATION IN BATCH CONDITIONS.....	105
4.2	CATALYTIC PERFORMANCE EVALUATION IN CONTINUOUS FLOW CONDITIONS .....	111
4.3	PALM BIODIESEL ISOMERIZATION IN BATCH CONDITIONS.....	120
4.4	CONCLUSIONS .....	121



5.	Performances of Zeolite Y catalytic materials in methyl oleate isomerization.....	123
5.1	EVALUATION OF HIGH SILICA ZEOLITES Y (H-Y-30) AS CATALYTIC MATERIALS.....	123
5.1.1	<i>Catalytic performance evaluation in batch conditions</i> .....	123
5.1.2	<i>Catalytic performance evaluation in continuous flow conditions</i> .....	128
5.2	EVALUATION OF LOW SILICA ZEOLITES Y (H-Y-6) AS CATALYTIC MATERIALS .....	132
5.2.1	<i>Catalytic performance evaluation in batch conditions</i> .....	132
5.2.2	<i>Catalytic performance evaluation in continuous flow conditions</i> .....	134
5.3	CONCLUSIONS .....	136
6.	Determination of the cold flow properties of catalytic test products. ....	139
6.1	EXAMPLE OF AN ANALYSIS OF METHYL OLEATE ISOMERIZATION PRODUCTS .....	139
6.1.1	<i>Products of methyl oleate isomerization using ferrierite based catalytic materials</i> .....	143
6.1.2	<i>Products of methyl oleate isomerization using Zeolite Y based catalytic materials</i> .....	145
6.2	BEHAVIOR IN COLD ENVIRONMENTS .....	147
6.2.1	<i>Products of methyl oleate isomerization using ferrierite based catalytic materials</i> .....	149
6.2.2	<i>Products of methyl oleate isomerization using Zeolite Y based catalytic materials</i> .....	153
6.2.3	<i>Palm biodiesel Isomerization</i> .....	156
6.3	CONCLUSIONS .....	157
7.	Prospective work: Hydroisomerization of methyl palmitate using recrystallized zeolites as catalytic materials .....	159
7.1	RESULTS OF PLATINUM IMPREGNATION IN RECRYSTALLIZED MATERIALS .....	159
7.2	HYDROISOMERIZATION OF METHYL PALMITATE USING MICRO-MESOPOROUS ZEOLITIC MATERIALS .....	161
7.3	CONCLUSIONS .....	164
8.	Conclusions and Perspectives.....	165
8.1	CONCLUSIONS .....	165
8.2	PERSPECTIVES.....	169
	REFERENCES.....	171



## List of Figures

	Pag.
Figure 1-1 Production of products with industrial uses from triglycerides (Source: Corma <i>et al</i> , 2007 [7]) .....	8
Figure 1-2 Biodiesel challenges for improving biodiesel competitiveness (source: Anwar, 2016 [33]) .....	9
Figure 1-3 Crystallization of fatty acid esters. (1) Saturated methyl esters. (2) Unsaturated methyl esters. (3) branched alkyl esters (Source: Leng <i>et al.</i> , 2020 [37]) .....	10
Figure 1-4 Determination of crystallization and melting processes of soybean biodiesel by differential scanning calorimetry in heating (A) and cooling (B) scans (Source: Dunn, 1999 [54]) .....	11
Figure 1-5 Commercial process for saturated branched-chain fatty acid production as a by-product in polymerized fatty acids synthesis (Source: Wiedemann <i>et al</i> , 2016 [12]) .....	13
Figure 1-6 Proposed mechanisms for isomerization reaction (Source: Reaume, S.J., 2013 [75]) .....	14
Figure 1-7 Reactions of unsaturated fatty acid methyl esters on porous acid materials. .	15
Figure 1-8 Proposed mechanisms for dehydrogenation reaction on fatty acids. (Adapted from Adlhart & Uggerud, 2007 [83]) .....	16
Figure 1-9 Diffusion process into the zeolite framework during the hydroisomerization reaction (Adapted from Guisnet, M., 2013 [81]). .....	17
Figure 1-10 Reaction pathway of stearic acid deoxygenation (source: Hermida, 2015 [88]) .....	18
Figure 1-11 Reaction of oleic acid isomerization and deactivation by aromatic coke formation (source: Wiedemann, 2015 [105]) .....	19
Figure 1-12 Building units in the Faujasite (FAU) supercage (Source: Demone, 2018 [116]) .....	21
Figure 1-13 Relationship between maximum rate of catalytic reaction and ratio of pore diameter/molecule diameter in hydrotreatment reaction (Source: Galarneau <i>et al.</i> , 2016 [125]) .....	23
Figure 1-14 Diffusion of molecules inside pores of different sizes. a) Diffusion of different size molecules in three different diffusional regimes (Molecular (blue), Knudsen (green) and intracrystalline (yellow). b) Coefficient of diffusivity (left) and activation energy (right) in these diffusional regimes (source: Li <i>et al.</i> , 2014[119]). .....	24
Figure 1-15 Schematic representation of the improvement through the introduction of mesopores in microporous zeolitic materials. A. Diffusion of molecules (green) into the	

microporous network of the zeolite. B. Diffusion of molecules (Green) into the meso-microporous network of the zeolite.....	25
Figure 1-16 Scheme of a zeolite crystal with different types of new macro/mesoporosity. There can be pores closed (C), blind (B), or which go through (T) the crystal, or there can be pores arising from a marked roughness (R), or well interconnected (I) mesoporosity (Based on: Rouquerol, 2014 [148]) .....	26
Figure 1-17 Different synthesis routes towards zeolite materials combining micro- and mesopores (source: Chal et al., 2011[93]).....	27
Figure 1-18 Comparison of top-down and bottom-up synthesis approaches for meso-microporous zeolitic materials [93]. .....	28
Figure 1-19 Desilication of the zeolite framework using a base as a demineralizing agent (source: Chal et al., 2011 [93]). .....	29
Figure 1-20 Example of a di-quaternary ammonium surfactant used as bifunctional structure-directing agent (source: Na et al., 2013 [140]). .....	29
Figure 1-21 Mechanism of desilication/recrystallization leading to micro-mesoporous zeolitic materials (Source: Ivanova et al., 2014 [162]). .....	31
Figure 1-22 Synthetic strategies of recrystallization leading to different types of materials (Source: Sachse & García-Martínez, 2017 [145]) .....	32
Figure 1-23 One-step recrystallization using a base and cationic surfactant as the template (source: Li et al., 2014 [119]).....	34
Figure 1-24 FER network of interconnected channels (Based on: Bonilla et al., 2009 [172]) .....	35
Figure 1-25 Zeolite with large interconnected pores (APZ-4) from zeolite ferrierite (Source: Moliner et al., 2015 [170]) .....	36
Figure 1-26 TEM micrographs of desilicated ferrierite using a solution of NaOH 1.2 M (a) and recrystallized ferrierites using solutions of NaOH of 1.2 M (b) 0.4 M (c) and 1.8 M (d) with a desilication first step followed by recrystallization with CTAB (source: Khitev et al., 2012 [175]).....	40
Figure 1-27 Meso-microporous material obtained through one-step recrystallization from low silica ferrierite. A. SEM micrograph. B. TEM micrograph (Source: Cheng et al, 2018 [13]) .....	42
Figure 1-28 Faujasite (FAU) cubic structure (Source: Database of Zeolite Structures In: <a href="http://www.iza-structure.org/databases/">http://www.iza-structure.org/databases/</a> ). .....	43
Figure 1-29 Synthesis of hierarchical zeolite Y using bottom-up and top-down strategies (source: Verboekend et al., 2016 [154]). .....	45
Figure 1-30 Mesopore surface of hierarchical faujasites prepared by different approaches (Source: Verboekend et al., 2016 [154]).....	46
Figure 1-31 Results reported by García-Martínez for the H-Y-15 recrystallization. Field Emission-SEM micrographs of (A) parent zeolite Y (CBV 720 Si/Al:15) and (B) recrystallized material. TEM micrographs of (C) parent zeolite Y (CBV 720 Si/Al:15) and (D) recrystallized material. NLDFT pore size distribution curves for the recrystallized material obtained with different trimethylalkylammonium-based surfactants (C10-C22) (Source: Sachse et al., 2017[145]).....	47

Figure 1-32 Evolution of the micropore and mesopore volumes of the zeolites Y (A) CBV 720 (Si/Al:15) and (B) CBV 740 (Si/Al:21) during the one-step recrystallization process [14].	49
Figure 1-33 Evolution of the micropore and mesopore volume of the zeolite Y CBV 760 (Si/Al:30) during the one-step recrystallization process [15].	49
Figure 1-34 Evolution of the micropore and mesopore volumes of the zeolite Y CBV 600 (Si/Al: 3.4) during the one-step recrystallization process [14].	50
Figure 2-1 Scheme of the batch reactor	58
Figure 2-2 Scheme of downstream fixed-bed continuous flow reactor (Source: Vaugon, 2017 [15])	60
Figure 2-3 Conditions of temperature and mass flow in the continuous flow experiment.	61
Figure 2-4 Gas Chromatography analysis of the different fractions of the products of the methyl oleate isomerization. A. Chromatogram of the gas fraction. B. Chromatogram of liquid fraction including oligomer products C. Chromatogram of liquid fraction including monomer products D. MS-MS analysis of oligomer products.	61
Figure 3-1 Powder X-ray diffraction patterns of parent (in blue) and recrystallized (in red) with an enlargement of small-angle patterns of 0.5-6° of powder X-ray diffraction patterns of parent (H-FER-PAR) and recrystallized (H-FER-REC) ferrierite materials.	66
Figure 3-2 Transmission electronic microscopy (TEM) images of ferrierite materials with 2.0 $\mu\text{m}$ (1), 200 nm (2), and 100 nm (3) scale bars. A. Parent Ferrierite (H-FER-PAR). B. Recrystallized Ferrierite (H-FER-REC).	68
Figure 3-3 $\text{N}_2$ sorption isotherm curves of H-form ferrierite-based materials.	69
Figure 3-4 Scanning electronic microscopy (SEM) images of ferrierite materials at 3.0 $\mu\text{m}$ (1) and 1.2 $\mu\text{m}$ (2) scale bars. A. Parent Ferrierite (H-FER-PAR). B. Recrystallized Ferrierite (H-FER-REC).	69
Figure 3-5 Temperature-programmed ammonia desorption profiles of the (A) parent exchanged (H-FER-PAR) and (B) recrystallized (H-FER-REC) zeolitic materials.	70
Figure 3-6 $^{27}\text{Al}$ MAS NMR spectrum of H-FER-PAR and H-FER-REC.	72
Figure 3-7 $^{29}\text{Si}$ MAS NMR spectrum of (A) H-FER-PAR and (B) H-FER-REC.	72
Figure 3-8 FTIR spectra of adsorbed $\text{CD}_3\text{CN}$ on ferrierite as a function of the temperature desorption of (A) H-FER-PAR and (B) H-FER-REC with the enlargement of the 3400-3900 $\text{cm}^{-1}$ zone (1) and the enlargement of the 2200-2400 $\text{cm}^{-1}$ zone (2).	74
Figure 3-9 Comparison of the molar density of acidic sites between parent (H-FER-PAR) and recrystallized (H-FER-REC) catalytic materials.	76
Figure 3-10 Powder X-ray diffraction patterns of parent (in blue) and recrystallized (in red) materials obtained from zeolite Y with Si/Al = 30, with an enlargement of the low angle scattering part (1-6° 2 $\theta$ ).	79
Figure 3-11 $\text{N}_2$ sorption analysis of H-form of zeolite Y-based materials with Si/Al: 30. A. Isotherms curves. B. Pore size distributions.	80
Figure 3-12 Transmission electronic microscopy (TEM) images of high silica zeolite Y-based materials with 200 nm (1), 100 nm (2), and 50 nm (3) scale bars. A. H-Y-30-PAR. B. H-Y-30-REC.	82
Figure 3-13 Scanning electronic microscopy (SEM) images of zeolite Y-based materials with 1.20 $\mu\text{m}$ (1) and 0.6 $\mu\text{m}$ (2) scale bars. A. H-Y-30-PAR. B. H-Y-30-REC.	83

Figure 3-14 $^{27}\text{Al}$ MAS NMR spectra of H-Y-30-PAR and H-Y-30-REC.....	85
Figure 3-15 $^{29}\text{Si}$ MAS NMR spectra of (A) H-Y-30-PAR and (B) H-Y-30-REC. ....	85
Figure 3-16 Temperature-programmed ammonia desorption profiles of the (A) parent exchanged (H-Y-30-PAR) and (B) recrystallized (H-Y-30-REC) zeolite Y-based materials. ....	86
Figure 3-17 FTIR spectra of adsorbed $\text{CD}_3\text{CN}$ on high silica zeolite Y as a function of the temperature desorption of (A) H-Y-30-PAR and (B) H-Y-30-REC with the enlargement of the $3400\text{--}3900\text{ cm}^{-1}$ zone (1) and the enlargement of the $2200\text{--}2400\text{ cm}^{-1}$ zone (2).....	87
Figure 3-18 Comparison of the molar density of acidic sites between parent (H-Y-30-PAR) and recrystallized (H-Y-30-REC) H-form of zeolite Y with $\text{Si}/\text{Al} = 30$ . ....	89
Figure 3-19 Enlargement of small-angle X-ray scattering patterns ( $0.5\text{--}6^\circ$ ) of parent and recrystallized materials from low silica zeolite Y ( $\text{Si}/\text{Al}$ : 6.5).....	90
Figure 3-20 Powder X-ray diffraction patterns of low silica parent zeolite Y ( $\text{Si}/\text{Al}$ : 6.5) and of the resulting materials obtained by recrystallization for different times. ....	91
Figure 3-21 $\text{N}_2$ sorption isotherms of H-form of zeolite Y-based materials with $\text{Si}/\text{Al}$ : 6.5. A. Isotherms curves. B. Pore size distributions.....	92
Figure 3-22 Transmission electronic microscopy (TEM) images of low silica zeolite Y-based materials with 200 nm (1) and 50 nm (2) scale bars. A. H-Y-6-PAR. B. H-Y-6-REC-40h. C. H-Y-6-REC-96h. D. H-Y-6-REC-330h. ....	94
Figure 3-23 Scanning electronic microscopy (SEM) images of zeolite Y-based materials with $3.00\text{ }\mu\text{m}$ (1) and $1.20\text{ }\mu\text{m}$ (2) scale bars. A. H-Y-6-PAR. B. H-Y-6-REC-40h. ....	95
Figure 3-24 Evolution of the micropore and mesopore volumes of the zeolite Y CBV 712® ( $\text{Si}/\text{Al}$ :6.5) during the one-step recrystallization process. ....	96
Figure 3-25 $^{27}\text{Al}$ MAS NMR spectra of H-Y-6-PAR and H-Y-6-REC-40h. ....	97
Figure 3-26 $^{29}\text{Si}$ MAS NMR spectra of (A) H-Y-6-PAR and (B) H-Y-6-REC-40h. ....	98
Figure 3-27 Temperature-programmed ammonia desorption profiles of the (A) parent exchanged (H-Y-6-PAR) and (B) recrystallized (H-Y-6-REC-40h) zeolite Y-based materials. ....	99
Figure 3-28 FTIR spectra of adsorbed $\text{CD}_3\text{CN}$ on low silica zeolite Y as a function of the temperature desorption of (A) H-Y-6-PAR and (B) H-Y-6-REC-40h with the enlargement of the $3400\text{--}3900\text{ cm}^{-1}$ zone (1) and the enlargement of the $2200\text{--}2400\text{ cm}^{-1}$ zone (2).....	100
Figure 3-29 Comparison of the molar density of acidic sites between parent (H-Y-6-PAR-40h) and recrystallized (H-Y-6-REC-40h) H-form of zeolite Y with $\text{Si}/\text{Al}$ : 6. i. silanol groups Brönsted acidic sites. ii. Brönsted acid sites of sodalites cages. iii. Brönsted acid sites in supercages. iv. Lewis acidic sites.....	101
Figure 4-1 Methyl oleate isomerization products yields obtained using H-FER-PAR and H-FER-REC as catalysts at different temperatures ( $260, 285^\circ\text{C}$ ) and pressures ( $2.0, 4.0\text{ MPa}$ ). ....	107
Figure 4-2 Evaluation of the effect of a bulky base (triphenylphosphine) and water as additives in the yields of the methyl oleate isomerization products at $260^\circ\text{C}$ and $4.0\text{ MPa}$ using H-FER-Par and H-FER-Rec as catalytic materials.....	108
Figure 4-3 MALDI-TOF spectrum of extracts of dichloromethane extract from A. H-FER-PAR and B. H-FER-REC spent catalytic materials used in methyl oleate isomerization doped with lithium trifluoroacetate. ....	109

Figure 4-4 TGA analysis of parent exchanged (H-FER-PAR) and Recrystallized (H-FER-REC) spent ferrierite-based catalytic materials. ....	110
Figure 4-5 $^{13}\text{C}$ CP MAS NMR spectrums of spent catalysts based on ferrierite materials H-FER-PAR (blue) and H-FER-REC (red) after methyl oleate isomerization i. At 260°C and 2.0 MPa ii. At 260°C and 4.0 MPa iii. At 285°C and 2.0 MPa iv. At 285°C and 4.0 MPa. ....	111
Figure 4-6 Methyl oleate isomerization in a continuous flow reactor at 260°C and 2.0 MPa using as the catalyst A. H-FER-PAR. B. H-FER-REC. ....	112
Figure 4-7 Methyl oleate isomerization in a continuous flow reactor at 260°C and 4.0 MPa using as the catalyst A. H-FER-PAR. B. H-FER-REC. ....	114
Figure 4-8 Methyl oleate isomerization in a continuous flow reactor at 285°C and 2.0 MPa using as the catalyst A. H-FER-PAR. B. H-FER-REC in the first 8h. ....	116
Figure 4-9 Methyl oleate isomerization in a continuous flow reactor at 285, 310, and 325°C with a return point at 285°C with a pressure of 2.0 MPa using as the catalyst A. H-FER-PAR. B. H-FER-REC carried out by 78h. ....	119
Figure 4-10 Palm biodiesel isomerization at 285°C and 2.0 MPa using ferrierite type catalytic materials. ....	121
Figure 5-1 Methyl oleate isomerization products distribution using H-Y-30-PAR and H-Y-30-REC at different conditions of temperature (260, 285°C) and pressure (2.0, 4.0 MPa). ....	125
Figure 5-2 MALDI-TOF spectra of extracts of dichloromethane washing from ferrierite spent catalytic materials used in methyl oleate isomerization doped with lithium trifluoroacetate. ....	126
Figure 5-3 TGA analysis of parent H-Y-30 PAR (PAR) and Recrystallized H-Y-30-REC (REC) spent high silica zeolite Y-based catalytic materials. ....	127
Figure 5-4 Figure 5-5 CP MAS $^{13}\text{C}$ NMR spectra of spent catalysts based on high silica zeolite Y materials H-Y-30-PAR (blue) and H-Y-30-REC (red) after methyl oleate isomerization A. At 260°C and 4.0 MPa, and B. At 285°C and 2.0 MPa. ....	127
Figure 5-6 Methyl oleate isomerization carried out in continuous flow conditions with a temperature of 260°C and a pressure of 4.0 MPa. A. Using as catalyst H-Y-30-PAR. B. Using as catalyst H-Y-30-REC. ....	129
Figure 5-7 Methyl oleate isomerization carried out in continuous flow conditions with a temperature of 285°C and a pressure of 2.0 MPa. A. Using as catalyst H-Y-30-PAR. B. Using as catalyst H-Y-30-REC. ....	130
Figure 5-8 Methyl oleate isomerization products distribution using H-Y-6-PAR at 285°C and a pressure of 2.0 MPa. ....	133
Figure 5-9 TGA analysis of parent (PAR) spent low silica zeolite Y-based catalytic material. ....	134
Figure 5-10 Methyl oleate isomerization carried out in continuous flow conditions with a temperature of 285°C and a pressure of 2.0 MPa. A. Using as catalyst H-Y-6-PAR. B. Using as catalyst H-Y-6-REC-40h. ....	135
Figure 6-1 Chromatogram of the products of methyl oleate isomerization present in the gas phase. ....	140

Figure 6-2 MALDI-TOF mass spectra obtained from liquid products of methyl oleate isomerization using: <b>A.</b> H-FER-PAR and. <b>B.</b> H-FER-REC as the catalyst. ....	140
Figure 6-3 MS-MS analysis done on M/Z peaks of <b>A.</b> $[C_{37}H_{70}O_4+Li]^+ = 585.5$ and <b>B.</b> $[C_{38}H_{72}O_4+Li]^+ = 599.6$ .....	141
Figure 6-4 Chromatogram of the liquid phase obtained after methyl oleate isomerization (GC anlysis done on HP-5ms® column).....	142
Figure 6-5 Chromatogram of the monomer fraction in the liquid product of methyl oleate isomerization (GC-MS anlysis done on ZB-FAMES column).....	143
Figure 6-6 Enlargement of chromatogram of retention times from 47.0 to 56.0 min on elution of branched-chain fatty acid methyl esters of the chromatogram of initial products of methyl oleate isomerization using: <b>A.</b> H-FER-PAR as catalyst. <b>B.</b> H-FER-REC as catalyst ( GC-MS anlysis done on ZB-FAMES® column).....	144
Figure 6-7 Enlargement of chromatogram of retention times from 56.0 to 62.0 min on elution of straight monounsaturated fatty acid methyl esters of the chromatogram of products of methyl oleate isomerization using: <b>A.</b> H-FER-PAR as catalyst. <b>B.</b> H-FER-REC as catalyst ( GC-MS anlysis done on ZB-FAMES® column).....	145
Figure 6-8 Enlargement of chromatogram of retention times from 44.0 to 58.0 min on elution of branched-chain fatty acid methyl esters of the chromatogram of initial products of methyl oleate isomerization using: <b>A.</b> H-Y-30-PAR as catalyst. <b>B.</b> H-Y-30-REC as catalyst ( GC-MS anlysis done on ZB-FAMES® column). ....	146
Figure 6-9 Enlargement of chromatogram of retention times from 58.0 to 62.0 min on elution of straight monounsaturated fatty acid methyl esters of the chromatogram of products of methyl oleate isomerization using: <b>A.</b> H-Y-30-PAR as catalyst. <b>B.</b> H-Y-30-REC as catalyst ( GC-MS anlysis done on ZB-FAMES® column).....	147
Figure 6-10 Comparison of the cooling scans in DSC analysis of the commercial methyl oleate and of the product of the isomerization reaction performed at 285°C on H-FER-REC at 2.0 MPa. ....	148
Figure 6-11 Cooling scans in DSC analysis of the methyl oleate isomerization products using ferrierite-based materials as catalysts in batch conditions. <b>A.</b> Reaction at 4.0 MPa and 260°C. <b>B.</b> Reaction at 2.0 MPa and 285°C.....	149
Figure 6-12 Cooling scans on DSC analysis of the methyl oleate isomerization products using ferrierite-based material as catalysts in continuous flow conditions (WHSV= 3.5 h <sup>-1</sup> ). <b>A.</b> Reaction at 4.0 MPa and 260°C. <b>B.</b> Reaction at 2.0 MPa and 285°C.....	151
Figure 6-13 Cooling scans on DSC analysis of the methyl oleate isomerization products using ferrierite-based material as catalysts in continuous flow conditions (WHSV=3.5 h <sup>-1</sup> ) at 2.0 MPa and 285°C. <b>A.</b> H-FER-PAR as the catalyst. <b>B.</b> H-FER-REC as the catalyst. ...	152
Figure 6-14 Cooling scans on DSC analysis of the methyl oleate isomerization products using Zeolite Y-based material as catalysts in batch conditions. <b>A.</b> Reaction at 4.0 MPa and 260°C. <b>B.</b> Reaction at 2.0 MPa and 285°C.....	154
Figure 6-15 Cooling scans on DSC analysis of the methyl oleate isomerization products using zeolite Y-based material as catalysts in continuous flow conditions (WHSV=3.5 h <sup>-1</sup> ), 2.0 MPa and 285°C.....	155
Figure 6-16 Cooling scans on DSC analysis of the palm biodiesel isomerization products using ferrierite-based material as catalysts in batch conditions at 2.0 MPa and 285°C.	156



Figure 7-1 Transmission electronic microscopy (TEM) images of ferrierite materials impregnated with Platinum at 50 nm. A. Parent Ferrierite (H-FER-PAR). B. Recrystallized Ferrierite (H-FER-REC). .....	160
Figure 7-2 Transmission electronic microscopy (TEM) images of zeolite Y materials impregnated with Platinum (100 nm scale bar). A. Parent zeolite Y (H-Y-30-PAR). B. Recrystallized zeolite Y (H-Y-30-REC). .....	161
Figure 7-3 Methyl palmitate hydroisomerization products distribution using ferrierite and high silica zeolite Y materials as the catalysts (T: 285°C; P: 4.0 MPa; t: 18h Cat: 10 %wt.). .....	162
Figure 7-4 MALDI-TOF spectrum of methyl palmitate hydroisomerization products (Catalyst: H-Y-30-PAR, 4.0%wt; 285°C; 18h). .....	163

## List of tables

	Pag.
Table 1-1 Palm biodiesel properties [35] .....	9
Table 1-2 Major uses and applications of branched-chain fatty acids and its derivatives (Source: Wiedemann,2016 [12]) .....	12
Table 1-3 Main industrial catalytic processes using zeolites [113]. .....	22
Table 1-4 Characteristics of recrystallization processes and properties of recrystallized zeolitic materials [143,156]. .....	33
Table 1-5 Synthesis and use of nano-sized ferrierite materials. ....	37
Table 1-6 Synthesis and use of stacked meso-microporous nano-sized ferrierite materials .....	39
Table 1-7 Main properties of high silica recrystallized ferrierites treated with NaOH solution at different concentrations and yield in isobutene [175,201]. ....	41
Table 1-8 Commercial zeolites Y from Zeolist® (Source: Verboekend et al., 2016 [154])	44
Table 2-1 Experimental conditions of recrystallization procedures on zeolites Y with different Si/Al ratios .....	54
Table 3-1 Properties of the parent and recrystallized H-form-ferrierite materials .....	67
Table 3-2 Properties of the parent and recrystallized H-Y-30 zeolitic materials .....	81
Table 3-3 Properties of the parent and recrystallized H-Y-6 zeolitic materials .....	93
Table 3-4 Brief of properties of the parent and recrystallized zeolitic materials obtained by one-step recrystallization using a base and CTAB as meso-pore structure directing agent .....	103
Table 4-1 Methyl oleate isomerization conversion, selectivity, and yield in branched product values (Cat. amount: 5%wt.; reaction time: 8h; N <sub>2</sub> atmosphere). .....	106
Table 5-1 Methyl oleate isomerization conversion, selectivity, and yield in branched product values using high silica zeolite Y material as catalysts (Cat. amount: 5%wt.; reaction time: 8h; N <sub>2</sub> atmosphere). .....	124
Table 5-2 Methyl oleate isomerization conversion, selectivity, and yield in branched product values using low silica zeolite Y material as catalysts (Cat. amount: 5%wt.; reaction time: 8h; N <sub>2</sub> atmosphere). .....	132
Table 7-1 Tests of methyl palmitate hydroisomerization done in a batch reactor using micro-mesoporous zeolitic materials (T: 285°C; P: 4.0 MPa). ....	161

## List of symbols and abbreviations

### Symbols

Symbol	Term	SI unit
T	Tone	Mg
Ha	Hectare	10000 m <sup>2</sup>
S <sub>total</sub>	Total surface area	
S <sub>micro</sub>	Surface area of micropores	
S <sub>meso</sub>	Surface area of mesopores	m <sup>2</sup> /g
S <sub>ext</sub>	External surface area	
V <sub>total</sub>	Total pore volume	
V <sub>micro</sub>	Pore volume of micropores	
V <sub>meso-intra</sub>	Pore volume of intracrystalline mesopores	cm <sup>3</sup> /g
V <sub>meso-inter</sub>	Pore volume of intercrystalline mesopores	
T <sub>oF</sub>	Onset temperature of freezing peaks in cooling scans in DSC analysis.	°C
Y <sub>bc</sub>	Yield in branched-chain fatty acids or fatty acid methyl esters	%
WHSV	Weight hourly space velocity	h <sup>-1</sup> (g <sub>raw material</sub> /g <sub>catalyst</sub> )

### Abbreviations

Abbreviations	Term
MTOE	Millions of tons of oil equivalent
FAMEs	Fatty acid methyl esters
CP	Cloud point
PP	Pour Point
CFPP	Cold filtering plugging point
DSC	Differential scanning calorimetry
HVO	Hydrotreated vegetable oils
IZA	International Zeolite Association
BBU	Basic building unit
SBU	Structural building unit
CBU	Composite building unit
FAU	Faujasite
FER	Ferrierite
SOD	Sodalite
GIS	Gismondine
USY	Ultrastable zeolite Y
#-MR	Ring of # T-sites
SDA	Structure-directing agent
MTBE	Methyl-tert-butyl-ether
CTAB	Cetyl trimethyl ammonium bromide

TMAOH	Tetramethylammonium hydroxide
CMPip	cetylmethylpiperidinium bromide
DMP	N,N-diethyl- <i>cis</i> -2,6-dimethylpiperidinium
NMP	n-methylpyrrolidine
C <sub>16</sub> dMImz	1,2-dimethyl-3-hexadecyl-1H-imidazol-3-ium bromide
TPOAC	3-(trimethoxysilyl)propyloctadecyldimethyl ammonium chloride
TMCAH	Trimethylcetylammmonium hydroxide
DME	Dimethylether
LDPE	Low-density polyethylene
HSE	Health, safety & environment
XRD	X-ray diffraction
EDS	Energy dispersive X-ray
SEM	Scanning electronic microscopy
TEM	Transmission electronic microscopy
TPD-NH <sub>3</sub>	Ammonia temperature-programmed desorption
IR	Infrared
TGA	Thermo-gravimetical analysis
DCM	Dichloromethane
H-FER-Par	H-form of parent ferrierite
H-FER-Rec	H-form of recrystallized ferrierite
H-Y- ## -Par-XXh	H-form of parent zeolite Y. ## = Si/Al XX= time
H-Y- ##-Rec-XXh	H-form of Recrystallized zeolite Y. ## = Si/Al XX=time
EFAL	Extraframework Al species
MAS-NMR	Magic angle spinning nuclear magnetic resonance
CP-MAS-NMR	Cross polarized Magic angle spinning nuclear magnetic resonance
MALDI-TOF	Matrix-assisted laser desorption/ionization coupled to time of flight detector

## Introduction

The interest in using porous functional materials as catalysts in processes involved in the valorization of biomass for producing chemical commodities, fuels, and other high added-value products has increased in the last years. The replacement of fossil oil supplies has been defined as an important goal for some countries [1]. The reasons to establish policies and mandates to develop renewable sources include environmental aspects ( $\text{CO}_2$  emission reduction), sustainability, and reduced dependence towards fossil fuel producer countries [2–4]. In order to reduce fossil resources, biomass has been encouraged as a renewable source of carbon [5,6]. However, the complex nature of biomass represents a challenge for its conversion [6]. As observed in Figure 1, intermediate building blocks can be obtained through different chemical routes from saccharides, lignocellulosic materials, proteins, triglycerides, and terpenes, which are present in different biomasses [7,8]. In this context, the use of porous materials like zeolites as catalysts in processes of conversion of the complex molecules that compose biomass has gained much interest. Zeolite based-materials have shown an important selectivity in catalytic reactions such as splitting, condensation, isomerization, or deoxygenation of fossil oil [8,9].

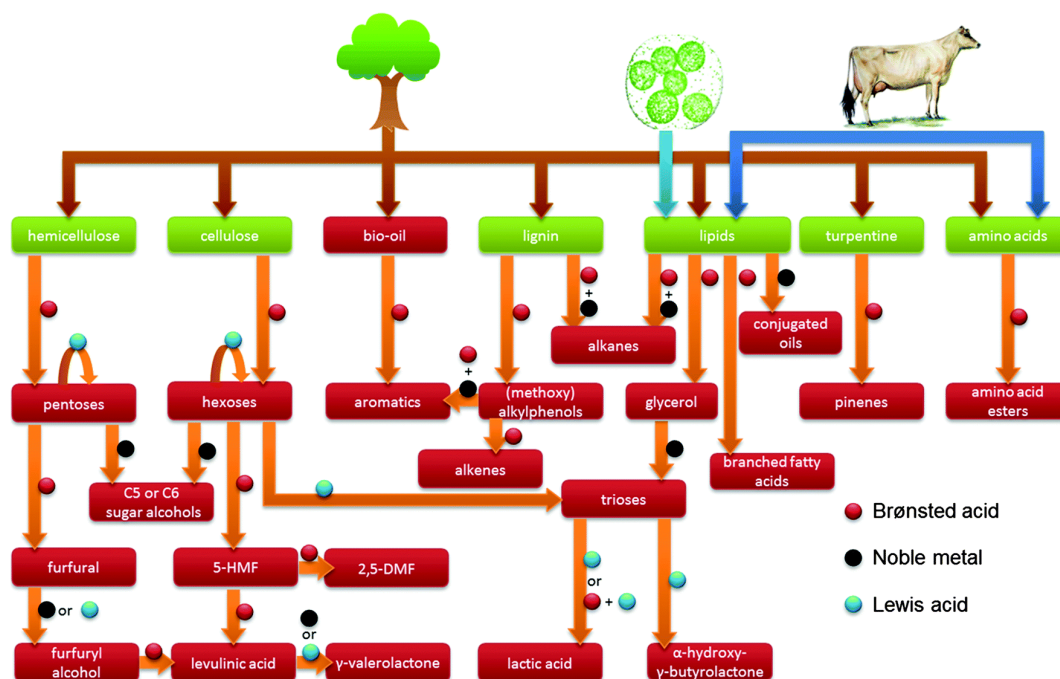


Figure 1. Overview of the use of porous catalysts with different types of active sites in biomass transformation (Source: Ennaert *et al.*, 2015 [8])

Considering the above, valorization of lipid biomass as a replacement of fossil oil supply has been considerably developed in the last years and has led to an increase in fat and oil production. The production of vegetable oils has been increased as a response to the demand for biofuels and oleochemical production, representing 23% of the global demand [10]. Among the different ways to transform this lipid biomass into high added-value products, the synthesis of alkyl-branched fatty acids is one of the significant routes to added-value compounds. Alkyl-branched fatty acids exhibit improved properties that include higher solubility, better hard water tolerance, and oxidative stability, lower melting/freezing points, lower viscosity as well as good spreadability, among others, therefore they are currently used as boundary additives in biodegradable lubricants, emollient in personal care products, and more recently as cold flow properties improver additives in biodiesel [11,12].

Current commercial branched-chain fatty acids are present in the market as low purity (<70%wt) mixtures obtained as by-products of oleic acid polymerization on montmorillonite clays [12]. The use of zeolites, porous acid materials with a well-defined network of micropores, has played an essential role in the development of the production of branched-chain fatty acids by isomerization reaction. This breakthrough was possible since zeolites allowed to overcome the main issue, namely favoring the skeletal ramification process while limiting polymerization processes. However, the fast loss of catalytic activity due to diffusion limitations in zeolites represents an important disadvantage for implementing the use of zeolite-based catalysts in processes of branched-chain fatty acids production.

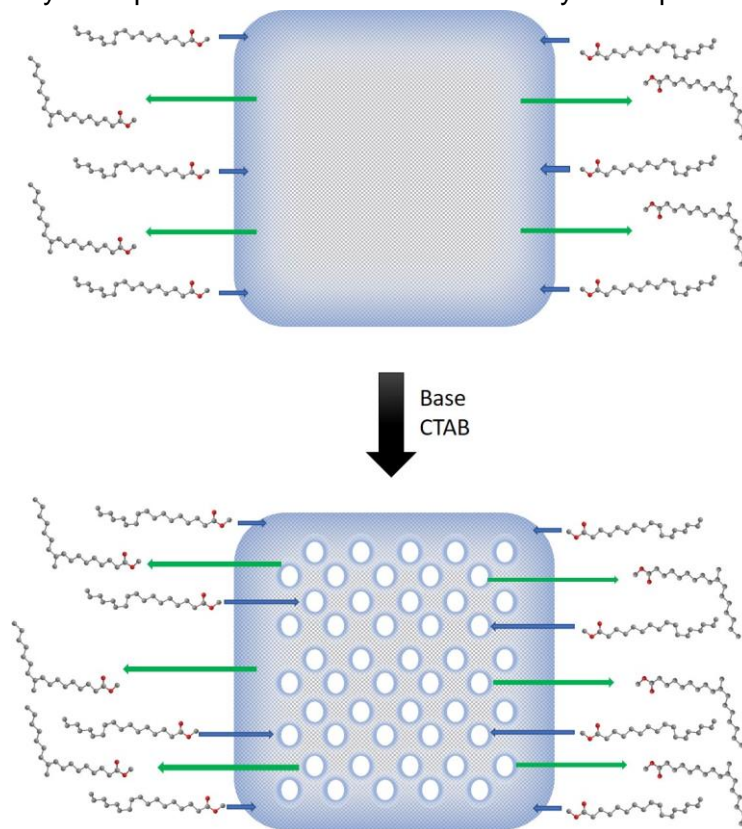


Figure 2. Schematic representation of the strategy adopted to improve the catalytic performance of zeolitic materials through mesopore generation recrystallization.

In order to overcome the diffusion limitations, which accelerate the catalyst deactivation, the strategy that we proposed (see Figure 2) was the preparation of zeolitic materials with meso-microporous systems obtained by recrystallization routes. For this purpose, we adapted procedures that were previously developed in our research group and which consist in generating intracrystalline mesopores in zeolite crystals by applying a hydrothermal treatment in the presence of a base and a surfactant. Then, the main objective of this work was to evaluate the catalytic performances of the recrystallized zeolite materials in comparison with those of the parent ones, and determine whether they could lead to an increase of the yield in branched-chain fatty acid products, and ultimately to the improvement of the crystallization properties of the isomerization reaction products in cold environments.

The results obtained in this work were described based on three activities: (i) the synthesis of micro-mesoporous zeolitic materials from ferrierite and zeolite Y, (ii) the evaluation of the catalytic materials in methyl oleate isomerization reaction in batch and continuous flow conditions, and (iii) the study of the composition of the isomerization products and the characterization of their crystallization properties at low temperatures. Finally, a preliminary study of the materials performance as bifunctional catalysts in the hydroisomerization of methyl palmitate is shown as a perspective to improve the yields in branched fatty acid products and thus increase their potential uses as fuel additives or in other uses.

The first chapter presents the state of the art. It is divided into two parts. The first part describes the potential of lipid biomass as raw material, it also introduces biodiesel, its properties, as well as the high potential of the branched-chain fatty acid compounds, and the methods for their synthesis. This part ends by presenting the isomerization and hydroisomerization reactions, showing how the use of ferrierite as a catalyst has been a breakthrough, leading to higher yields in branched-chain products but with low stability of the catalytic activity caused by a fast catalyst deactivation. The second part presents generalities about zeolites, their applications as catalysts, their advantages, and their main drawback: the diffusion limitations. The alternatives to enhance diffusion are also presented, focusing on the preparation of mesoporous zeolites. Among the alternatives, a special section is dedicated to the approach used in this work: zeolite recrystallization. Moreover, a detailed description of the zeolitic materials used here is given: Ferrierite and Zeolite Y. It includes the description of their properties, uses, advantages, and disadvantages, as well as the routes for obtaining mesoporous zeolitic materials from them.

In the second chapter, a brief description of the materials, methodologies, and characterization techniques used during the development of this work is given. First, the methods of preparation of the catalytic materials, including the one-step recrystallization procedures used for obtaining micro-mesoporous materials from ferrierite and zeolite Y, as well as the different characterization techniques used for the analysis of structural, textural and the acidic properties of the catalytic materials. Moreover, there is a brief description of the procedures and techniques used to characterize the spent catalytic materials. Secondly, the procedures for the catalytic performance tests in the isomerization and

hydroisomerization reactions in batch and continuous flow conditions are explicated, and the techniques and methods of reaction product characterization by gas chromatography, mass spectroscopy, and differential scanning calorimetry are finally described.

Thereafter, the description of the synthesis of micro-mesoporous zeolitic materials from ferrierite and zeolite Y is done in chapter 3. The preparation of these materials was done by one-step recrystallization, consisting of a hydrothermal treatment with a base and CTAB as the surfactant to allow the generation of a new mesopore system. The micro-mesoporous materials were synthesized by using the physicochemical parameters such as temperature, amounts of reagents, and treatment time, that were optimized by our research group. The ferrierite-based materials were obtained following the methodology developed by Cheng et al. [13]. The zeolite Y-based materials were obtained from low and high silica faujasite based on Chal [14] and Vaugon's work [15], respectively. The obtaining of low silica mesoporous materials from CBV 712 zeolite Y (Si/Al: 6.0) is proposed here for the first time. These characterizations allowed us to corroborate the lab previous research results and deepen the knowledge on these materials, especially in the properties related to their catalytic activity and stability.

Afterwards, the evaluation of the catalytic performance of the obtained micro-mesoporous zeolitic materials and the parent microporous zeolites in methyl oleate isomerization in batch and continuous flow conditions of the ferrierite and zeolite Y is presented in chapters 4 and 5, respectively. In these chapters, the catalytic performance was evaluated through parameters like the activity, conversion, selectivity, yield and stability with time-on-stream. As observed in chapter 3, the mesoporous systems generated in the different zeolites were very different depending on the nature of the zeolite and of its Si/Al ratio, which led to important differences in the catalytic performances of the materials.

Chapter 4 describes the catalytic isomerization of methyl oleate using ferrierite-based materials in batch and continuous flow conditions. The tests in batch conditions were done with temperature conditions ranging from 260°C to 285°C and pressures from 2.0 to 4.0 MPa. The spent solid catalytic materials were analyzed by solid state  $^{13}\text{C}$  CP MAS NMR and TGA to have some insight into the coke nature and its amount. Besides, the liquid phases obtained by washing the spent catalysts were analyzed by mass spectroscopy techniques to identify the nature of the coke precursors. The methyl oleate isomerization was then carried out in a downstream fixed-bed continuous flow reactor using ferrierite-based materials catalysts with temperature conditions between 260°C and 285°C, and pressures between 2.0 and 4.0 MPa to evaluate the catalyst stability with time-on-stream.

Chapter 5 describes the catalytic isomerization of methyl oleate using high and low silica zeolite Y-based materials in batch and continuous flow conditions. The tests using high silica micro-mesoporous and microporous zeolite Y-based materials were done in batch and continuous flow conditions at 260°C and 4.0 MPa, as well as 285°C and 2.0 MPa. The tests using low silica micro-mesoporous and microporous zeolite Y-based materials were done in batch (only with the parent material) and continuous flow conditions at 285°C and



2.0 MPa. The analysis of the spent catalytic materials from tests in batch conditions was done by TGA to gain some insight into the coke amounts produced during the reaction.

Ongoing with the last activity proposed in this project, beyond the maximization of yields in branched products obtained in methyl oleate isomerization, the distribution of branched and straight geometrical and positional isomers is analyzed in chapter 6. The study was focused on the reaction products obtained with the highest yield in branched chain-products using as catalysts the micro-mesoporous (recrystallized) zeolites and the microporous (parent) zeolitic materials from ferrierite and zeolite Y. On the other hand, the crystallization behavior of the products in cold environments was evaluated through Differential Scanning Calorimetry (DSC) experiments in order to determine their potential in the research of improved cold flow properties of biodiesel with high levels of saturated fatty acids.

Finally, in chapter 7, a preliminary study of the methyl palmitate hydroisomerization using bifunctional metal/acid meso-microporous zeolitic materials as catalysts is shown. It was proposed after considering the worsening of the behavior in cold environments shown by the isomerization products. Moreover, straight-line saturated fatty acids are more responsible for this lousy behavior than the presence of unsaturated ones, therefore they have to be modified to improve it.

The last part of the manuscript is dedicated to the general conclusion of this work together with some perspectives.



# 1.State of the art

## 1.1 Lipids as green raw materials

The development of alternatives to replace fossil supplies has gained interest in recent years [1]. It is caused mainly by the necessity of decreasing carbon dioxide emissions, estimated at 33.4 Gt in 2017, which will increase around 7% to 2040 [16]. Energy worldwide demand is estimated to be 583.9 Exajoules in 2019 [17], which will increase 725 EJ to 2050 [18]. Fossil fuels supplied 85% of it [16]. 7.5% of fossil fuel consumption is used for the production of chemicals [16], mainly for the production of fertilizers, thermoplastic, elastomers, solvents, additives, and others [19]. Biomass has been encouraged as a renewable source to replace fossil supplies [5]. Building blocks intermediates can be obtained through different chemical routes from saccharides, lignin, triglycerides, and terpenes [7].

Taking this into account, the interest in the valorization of lipid biomass as a green renewable replacement of fossil oil supply has been increasing in the last years [11,20]. It has led to an increase in fat and oil production. The main source for oleochemicals is vegetable oils. Their production has increased of 15% from 2014 to 2018 [21], reaching values between 204 and 208 Mt/year [22,23]. Considering it, an additional increase of more than 20% is expected in the next years [10]. Although around 77 % of these oils are used for food production, biofuels and oleochemical production reached 23% of this demand [10]. Moreover, the valorization of lipid biomass is increasing [20]. Glycerol and fatty acids from triglycerides, as well as other components of lipids, have been identified as precursors of building blocks for different uses [7,24].

Different reactions can be done on the carboxyl head or side alkyl chain of fatty acids [7]. Figure 1-1 represents the different ways to convert them into valuable products. The production of fatty acid derivatives has gained special attention [7]. Moreover, the synthesis of chiral molecules from fatty acids or the use of biochemical routes to improve these products has gained attention recently [25]. Among the products with industrial potential, there are diols and polyols, linear and functionalized fatty poly-acids, hydroxyl, and amino fatty acids; branched fatty acids, among others [20]. Despite general uses in food, soaps, and detergents [26], they can also be used to produce biofuels and other high value-added products [11]. So, the production of biofuels like biodiesel [27] and green diesel [28] has increased recently, among essential products like biodegradable and bio-safe fungicides,

surfactants, monomers, plasticizers additives, cosmetics, personal care products, lubricants, etc. [10,11,20,24].

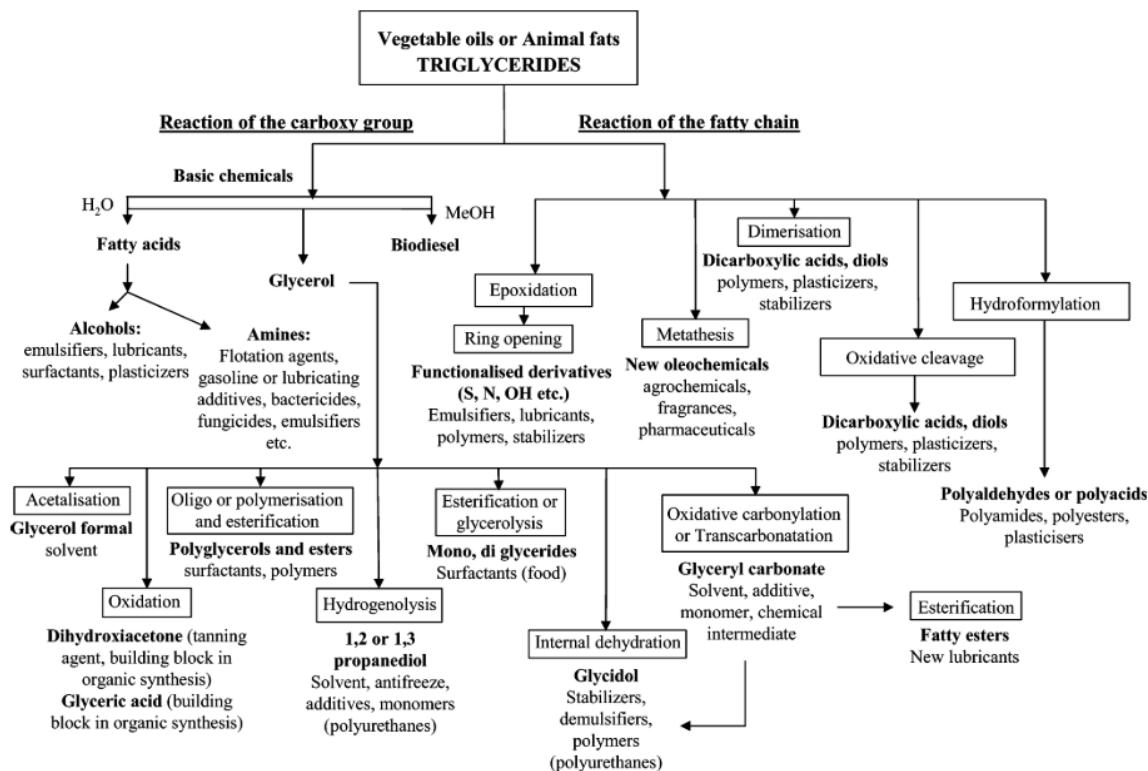


Figure 1-1 Production of products with industrial uses from triglycerides (Source: Corma *et al*, 2007 [7])

### 1.1.1 Biodiesel

Among the different uses of lipids, the biofuels production has been positioned as one of the fastest-growing alternatives to fossil fuels. It is because they can merge well with the existing distribution infrastructure [29]. According to some estimations of organisms like the "Organization of the Petroleum Exporting Countries", worldwide diesel demand will grow around 3% in the next thirteen years [30] as well as biofuel mandates around the world, global biodiesel demand will increase in more than 117% [22]. Fatty acid methyl esters (FAMEs) compose conventional biodiesel. It is produced from vegetable oils to improve the behavior of pure oils into conventional diesel engines as these cannot be used unmodified [31,32]. However, some drawbacks associated with biodiesel must be improved in the next years to make biodiesel competitive in current market conditions. Among these challenges are included the availability of feedstocks, the economic feasibility, the quality requirements, and the sustainability factors (see Figure 1-2) [33]. The recent development of the biorefinery concept to get added-value products from wastes and by-products could improve the competitiveness of the biodiesel sector [29]. On the other hand, the quality requirements for biodiesel used in standard diesel engines requires that properties of biodiesel from vegetable oils must be improved to accomplish the expected demand

increase of this fuel. The complicated relationship among biodiesel properties, as well as the importance of the feedstock price, render the choice of the vegetable oil used as raw material critical [29,31,33].

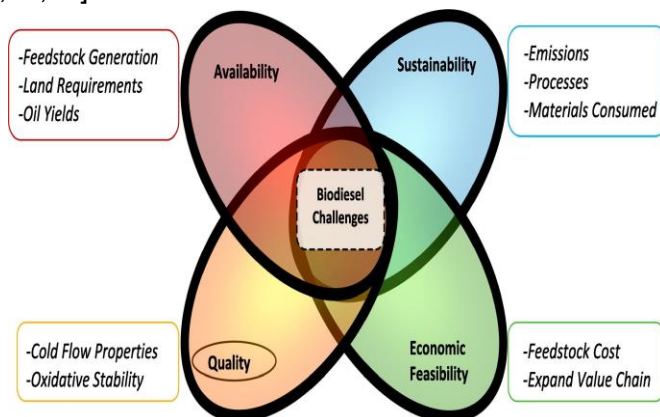


Figure 1-2 Biodiesel challenges for improving biodiesel competitiveness (source: Anwar, 2016 [33])

Biodiesel from palm oil has been, in recent years, one of the main supplies to this demand, representing about one-third of the total worldwide production, estimated at 35.81 million of tons in 2017 [34] due to the fact it has an economic appeal represented by its lowest price on the market (US\$ 640/ton) and its highest yield per cultivated area (3.6 ton/ha) [25]. The properties of palm biodiesel are shown in Table 1-1. Although this biodiesel meets international specifications, one of its main disadvantages is that it does not have an acceptable behavior as fuel at low temperatures especially concerning its flow properties [35]. This fact does not allow an increase in its amount in blending to diesel engines in countries with cold seasons [36] where palm oil low price can represent an economic advantage. In the next section, the relationship between FAMEs characteristics composition and cold flow properties will be discussed in detail

Table 1-1 Palm biodiesel properties [35]

Property	Palm BD	Specification to meet (EN 4214:2012)
Kinematic Viscosity at 40°C (mm <sup>2</sup> /s)	4.33	3.5-5.0
Density (g/mL)	0.8642	0.86-0.9
Oxidation stability index (h)	25.7	3 min
Cloud Point (°C)	16.0	Location & season dependant
Pour Point (°C)	12.0	
Cold Filtering Plugging Point(°C)	12.0	

### 1.1.2 Cold Flow properties of fatty acid and derivatives

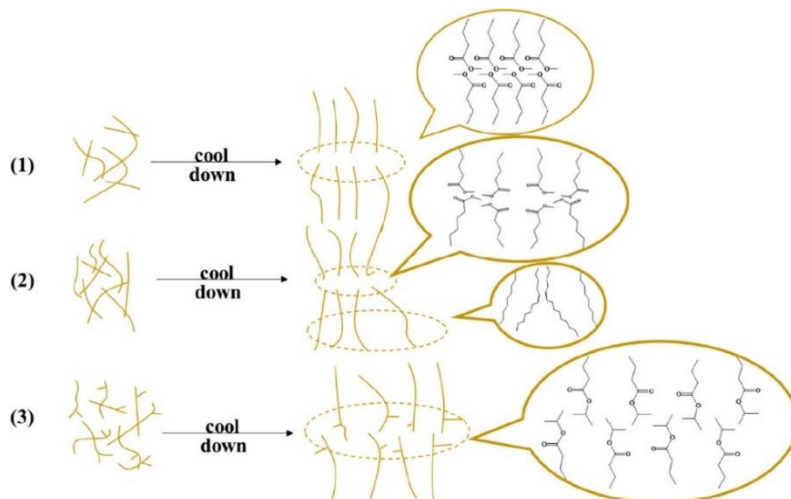


Figure 1-3 Crystallization of fatty acid esters. (1) Saturated methyl esters. (2) Unsaturated methyl esters. (3) branched alkyl esters (Source: Leng *et al.*, 2020 [37])

The behavior of biodiesel and other products obtained from fatty acids in cold environments is due to the presence of straight-line shape fatty acids, which crystallize at temperatures higher than the temperatures required for the biodiesel to function in cold environments [31,37,38]. There is a strong relationship between their properties and the fatty acid methyl ester characteristics [39] like molecular weight (chain length), number, and configuration of double bonds, as well as the presence of aliphatic chain ramifications or heteroatoms [39–43]. Hence, although saturated FAMES like those issued from palm oil show higher stability [44–46], a good heat of combustion and high cetane numbers, these straight-line shaped high molecular weight molecules can “pack” closer, and consequently crystallize at higher temperatures than unsaturated FAMES (see Figure 1-3) [39,47,48]. Taking into account that palm biodiesel contains about 50% (40 to 55% depending on the origin of palm oil) of saturated FAMES [36,40,49], this biofuel presents good oxidative stability and combustion properties but detrimental cold flow properties, at least to be used in areas where “winter” biodiesel are required (Europe or North America for example) [31,50].

There are different techniques for studying the behavior of fatty acid and derivatives at low temperatures, which include manual and automatic procedures based on optical or rheological measurements. Among them, the use of sub-ambient differential scanning calorimetry (DSC) has gained attention in the last years [50,51]. Through this measurement, it is possible to study the transition between solid and liquid states in a highly reproducible way [52]. Figure 1-4 shows the expected behavior of biodiesel (from soybean oil) in cold environments. Several parameters have been established to evaluate the cold flow properties of oils and fuels from the scans from DSC. Among them, we can observe in DSC heating scan (Figure 1-4-A) the melting point (MP) as the onset temperature ( $T_{OM}$ ) of the observed melting peak. Other parameters as the maximum (critical) point of the peak (P1) as well as the completion (COM) of the melting peak were studied as parameters to describe the cold flow properties. In the DSC cooling scan (Figure 1-4-B), it is possible to

see the freezing point (FP) as the onset temperature ( $T_{OF}$ ) of the usually observed freezing peak. Another parameter used to describe these properties was the maximum (critical) point of the peak (P2). The differences observed in the values between the melting point (MP), determined by heating, and the freezing point (FP) determined by cooling of mixtures of esters from fatty acids are due to the supercooling where oils stay in a liquid state below the standard freezing point value unless a nucleation center is present [52]. The large width of more than 10°C, which can be observed, even for isolated esters, in both crystallization and melting processes is due to the transformation between crystallization forms of these compounds [53].

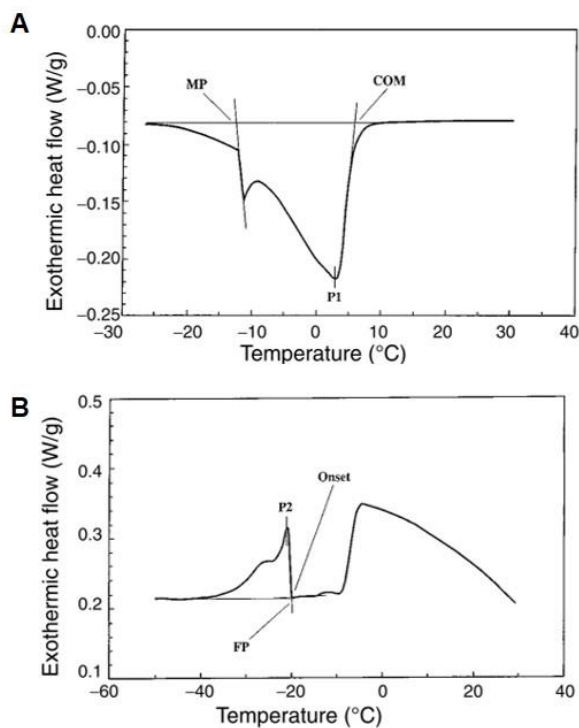


Figure 1-4 Determination of crystallization and melting processes of soybean biodiesel by differential scanning calorimetry in heating (A) and cooling (B) scans (Source: Dunn, 1999 [54]).

The behavior of fatty acids and their derivatives in low-temperature environments is fundamental to define their utility in some products like biodiesel, lubricants, cosmetics, among others [12,55]. Although the analysis of the behavior of oil derivatives in cold environment is not possible using only the melting/freezing points, due to the complexity of the mixtures, it has been studied in indirect ways. The behavior of one fuel at low temperatures is indeed represented by several "cold flow properties" [31,50,56–58]. All of these properties make it possible to define the behavior of diesel mixtures in standard diesel engines [3,56,59]. Three of them are the most used properties: cloud point, pour point, and cold filtering plugging point. Cloud point (CP) is the temperature at which the smallest observable cluster first occurs upon cooling under prescribed conditions a liquid sample [60]. In biodiesel, it is due to the crystallization of the highest melting point esters [31,48]. Pour point (PP) is the lowest temperature at which movement of the liquid sample

is observed under the prescribed conditions of the test [61]. Cold filtering plugging point (CFPP) is the highest temperature at which a given volume of fuel fails to pass through a standardized filtration device (45  $\mu\text{m}$ ) in a specified time (60 s) [62]. These properties can be adequately described from the use of DSC analysis. Parameters previously described in the DSC scans are shown to be directly proportional to cold flow properties [52–54,63].

Considering that biodiesel has usually worse cold flow properties than conventional fossil diesel, different ways have been proposed to improve its cold flow properties. Solutions range from blending different types of oils with different levels of saturation, oil fractionation, use of additives as pour point depressants or crystalline wax modifiers, or modification of fatty acid alkyl ester through transesterification with high molecular weight alcohols as well as reactions over fatty acid chain [31,37]. Among them, the use of Branched fatty acids derivatives obtained through isomerization or hydroisomerization of fatty acids has been proposed as an alternative to improve these properties. This solution led, for example, to improve the cloud and pour point of respectively 4.2 and 6.0°C in the case of palm biodiesel [64]. Furthermore, the use of branched-chain fatty acid alkyl esters as additives has been used to improve the cold flow properties of biodiesel [63].

These results led to increase the interest in branched-chain fatty acids alkyl esters in the last years. The next section describes in detail the synthesis method used to obtain them, their properties and uses.

## 1.2 Branched Fatty acids and derivatives

The use of branched-chain fatty acids and their derivatives is widely studied currently [65,66]. Wiedemann *et al.* did a description of the primary uses of branched-chain fatty acid and derivatives (see: Table 1-2) [12]. Due to their high cost, they are included in formulations in which their improved properties are highly valued [12]. So, they have been used as boundary additive in biodegradable lubricants [11,67], emollients in personal care products [65,66,68], and more recently as cold flow properties improver additives in biodiesel [31,63,69]. They have improved properties like a higher solubility, a better tolerance to water, oxidative stability, lower melting/freezing points, lower viscosity as well as good spreadability, among others [11,12,65,70].

Table 1-2 Major uses and applications of branched-chain fatty acids and its derivatives  
(Source: Wiedemann,2016 [12])

Use	Applications	Key properties
Lubricants	Metalworking, gear oils, friction modifiers, engine lubricant formulation	Oxidative and thermal, stability, low toxicity, lubricity and spreadability, and cold flow properties
Cosmetic and personal care	Skin and hair care, color cosmetic, sun creams toiletries	Odor and color, stability, skin feel, substantivity, water resistance, spreadability and emulsifying, and cold flow properties
Industrial	Textile softening, metal paste, paper sizing	Rewettability, spreadability, lubricity, and water resistance



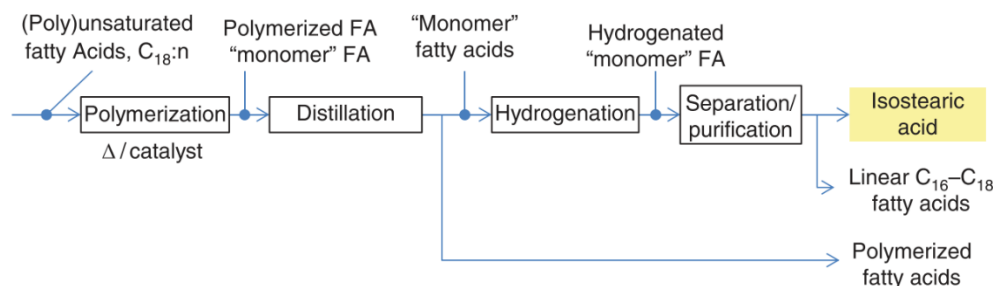


Figure 1-5 Commercial process for saturated branched-chain fatty acid production as a by-product in polymerized fatty acids synthesis (Source: Wiedemann *et al*, 2016 [12])

The branched-chain fatty acids can be obtained from several unsaturated fatty acids by Guerbet reaction, oxo synthesis, and Koch synthesis, fatty acid skeletal ramification or the addition of alkyl radicals to double bonds, co-oligomerization, or by the use of alkyl chloroformates [12,65,66]. Currently, a low purity (<70%wt) branched-chain fatty acid is commercially produced as a by-product of oleic acid polymerization on montmorillonite clay (see Figure 1-5), where the yield in branched-chain products is under 50wt% [65,71]. These commercially available branched-chain fatty acids are hydrogenated and purified to obtain the product known as isostearic acid [12].

The key point to improve the production of branched-chain fatty acids would favor the skeletal ramification processes while limiting as much as possible polymerization. It is possible through the use of porous acid materials as heterogeneous catalysts [65,66,68]. Several acid porous materials like sulfated zirconia with metal promoters, acidic alumina-supported noble metals, silica-supported phosphotungstic heteropolyacids [72]; and more recently, aluminosilicates (zeolites) and silicoaluminophosphates [11,70] have been tested to get higher selectivity to branched-chain products in fatty acids isomerization.

### 1.2.1 Isomerization Reaction

The isomerization reaction has been widely carried out on unsaturated hydrocarbon chain molecules for improving the combustion properties of heavy fractions of fuel oil through branching [73,74].

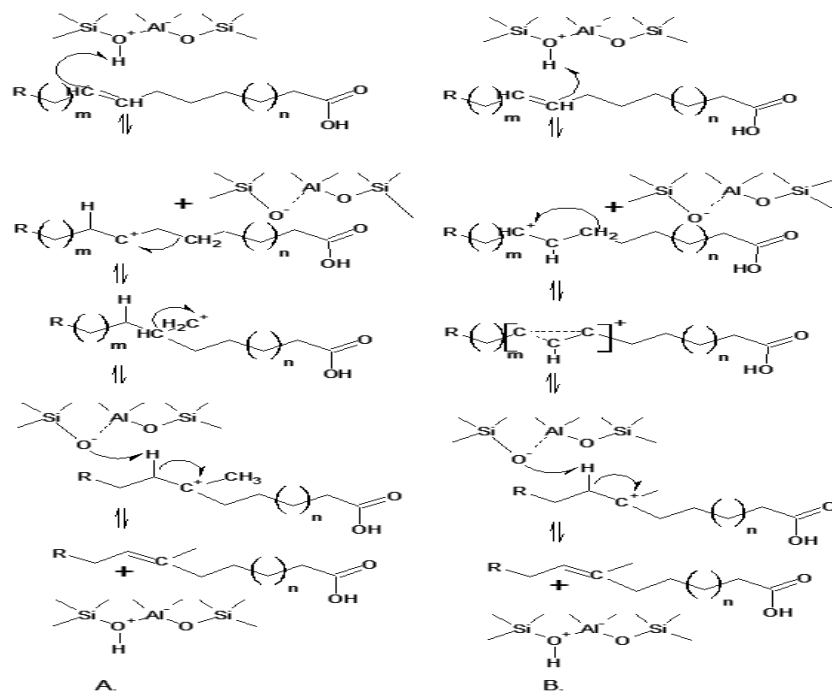


Figure 1-6 Proposed mechanisms for isomerization reaction (Source: Reaume, S.J., 2013 [75])

Isomerization reaction starts when a double bond suffers an electrophilic attack from Brønsted acidic sites in order to lead to carbenium ion rearrangement. Although the formation of a primary carbenium ion is difficult if the acid catalyst has enough strong acidity, this step is followed by skeletal rearrangement by hydride and alkyl shift (Figure 1-6-A) or via protonated cyclopropane (Figure 1-6-B) [73,75]. The formation of the branching in the hydrocarbon chain happens when this carbocation ring breaks [69].

The isomerization reaction is complex and leads to the formation of a wide variety of by-products. In Figure 1-7 is shown how from chain propagation of carbenium ion on the hydrocarbon chain can form different by-products from fatty acids. Among them, the reaction produces several double bond positional isomers of the straight mono-unsaturated substrate as well as positional isomers of the mono-alkyl branched molecules.

Additionally, some products as hydroxylated and saturated fatty acids, gamma, and delta lactones, as well as a high amount of oligomers like dimers or estolides are produced [68,76]. On the other hand, catalytic cracking by  $\beta$ -scission [77] happens quickly on poly-alkyl branched molecules at higher pressures and temperatures [73,77]. Intermolecular polyunsaturated carbocation attack reactions can happen in these experimental conditions and lead to alkylbenzenes formation [76]. Excess of them can lead to carbonaceous deposits leading to “coke” formation, which cannot desorb from active sites, blocking pores and ultimately deactivating the catalyst [76],[73].

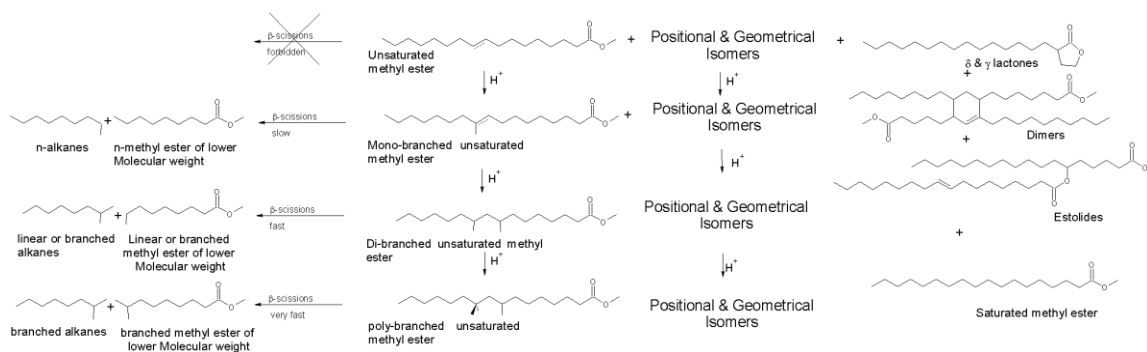


Figure 1-7 Reactions of unsaturated fatty acid methyl esters on porous acid materials.

### ▪ Hydroisomerization and deoxygenation reactions

Considering that behavior of fatty acids and their derivatives in cold environments depends mainly on the presence of saturated molecules, they must be removed or modified to improve biodiesel properties [45,46]. Although yields up to 80% in branched fatty acids through isomerization of unsaturated fatty acids have been obtained [78,79], hydroisomerization yields on saturated fatty acids have reached just 46% (285°C, 4.0 MPa, 16 h) [75] with a fast deactivation of the catalysts in both processes [48,80]. Hydroisomerization yields must be improved to get high levels of alkyl-branched fatty acids to improve cold flow properties in biodiesel

The hydroisomerization allows obtaining branched-chain fatty acids from saturated fatty acids and their derivatives. The low yields on this reaction can be attributed to the high stability of the saturated alkyl chain. However, although alkane chains are unreactive, catalytic conversions to branched isomers are thermodynamically favored [73]. As shown before, the first step to carry out alkyl-branching is the carbenium ion formation. Even if the use of superacid solids to get it by abstracting a hydride ion is possible [73], a bifunctional metal-acid catalyst is often used to carry out the hydroisomerization reaction of the saturated compounds [73,81,82]. The first step of this reaction consists of one hydrogenation on a metallic center [48,75]. As shown in Figure 1-8, the dehydrogenation reaction starts from a saturated fatty acid through 1,1-elimination or 1,2-elimination of hydrogen [83]. In a second step, an unsaturated fatty acid is obtained by isomerization [73,75]. After creating the double bond on the alkyl chain, one isomerization reaction on an acidic site can lead to the obtainment of branched-chain compounds [48,75].

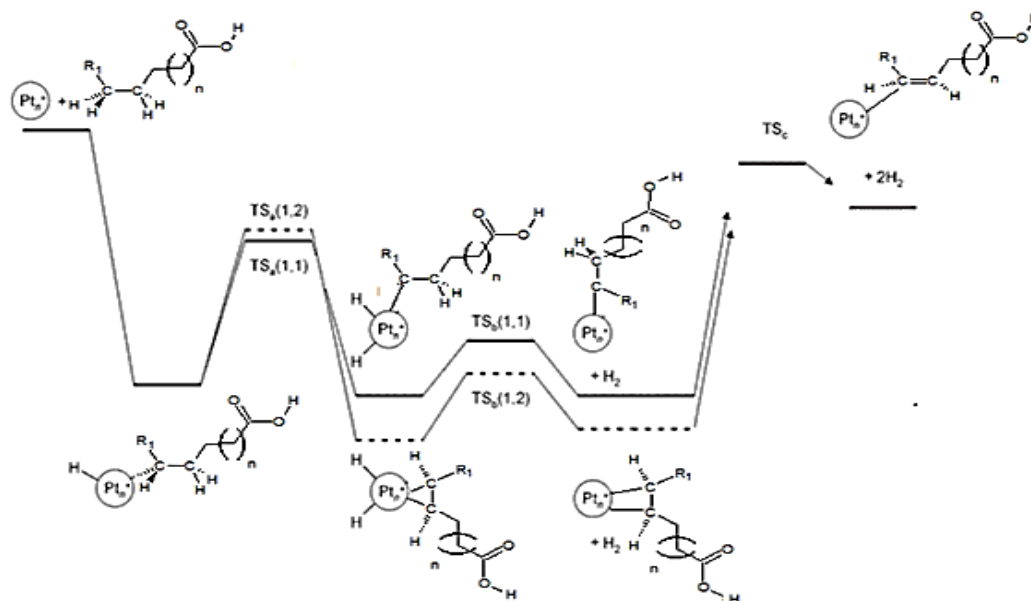


Figure 1-8 Proposed mechanisms for dehydrogenation reaction on fatty acids. (Adapted from Adhart & Uggerud, 2007 [83])

As was previously described for the hydroconversion of hydrocarbons [81,82], there are significant relationships between the amount and location of acid and metal sites into the catalyst framework. Although the hydroisomerization has been described as a two-step reaction, there are at least seven successive steps involved in this reaction [81]. As shown in Figure 1-9 this reaction includes the diffusion of saturated molecules to metallic sites to carry out the dehydrogenation reaction. It is followed by the intra-micropores diffusion of the straight unsaturated moiety to acidic sites where the isomerization reaction happens as it was previously described. The branched-chain molecules then need to diffuse to other metallic sites to be hydrogenated and then diffuse again to the bulky liquid phase. The idea of an “ideal catalyst” to carry out the hydroconversion of hydrocarbons has been discussed for years [77,81]. A bifunctional metal/acid catalyst with 3-D large pores, as the zeolite Y (see section 1.6), with a ratio of metallic-acid functions around 0.17 has been described as the ideal catalyst [81]. However, to increase the selectivity in branched-chain molecules, the presence of a well-constrained pore system that could lead to avoid the excess of successive transformations of branched molecules is crucial [81,82,84]. The use of zeolites containing 10-membered ring channels as TON (ZSM-22) [81,84], coated with alumina [82,85], or the reduction of diffusion length of reaction intermediates has shown to improve this selectivity [81,82].

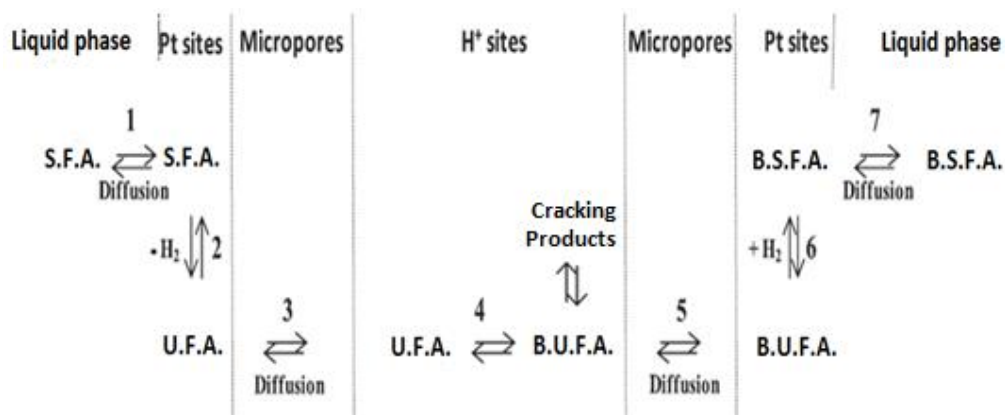


Figure 1-9 Diffusion process into the zeolite framework during the hydroisomerization reaction (Adapted from Guisnet, M., 2013 [81]).

Moreover, parameters as temperature and pressure affect the diffusion process and equilibrium between isomerization and cracking [73,86,87]. These reactions need high temperatures to reach activation energies of alkanes moieties. However, lower temperatures favor mono-branched products and avoid the excess of dehydrogenation, which can conduct to the formation of poly-branched products followed by cracking processes [87], or formation of polyaromatic products, which lead to coke formation [73].

Notwithstanding the potential of the hydroisomerization reaction to improve fatty acid derivatives properties, it has not been studied in depth. In contrast, the studies have been focused on the obtainment of diesel-like fuel products [88,89]. They are known as Hydrotreated vegetable oils (HVO) or green diesel [28,90]. The most relevant pathway is the deoxygenation reaction. It consists in removing the carboxyl group of the fatty acid using bifunctional catalysts [88]. As observed in Figure 1-10, in the deoxygenation of stearic acid, it is possible to get a mixture of hydrocarbons mainly composed of  $C_{17}$  hydrocarbons [88]. These products usually are obtained from triglycerides [89,91], methyl esters [90], or fatty acids [88,92]. This reaction is usually done at conditions of higher temperature (300-420°C) and pressure (3.5-9.2 MPa) than the hydroisomerization reaction (285°C, 4.0 MPa) using noble metals supported on C,  $Al_2O_3$  zeolites and zeolite-type materials [89].

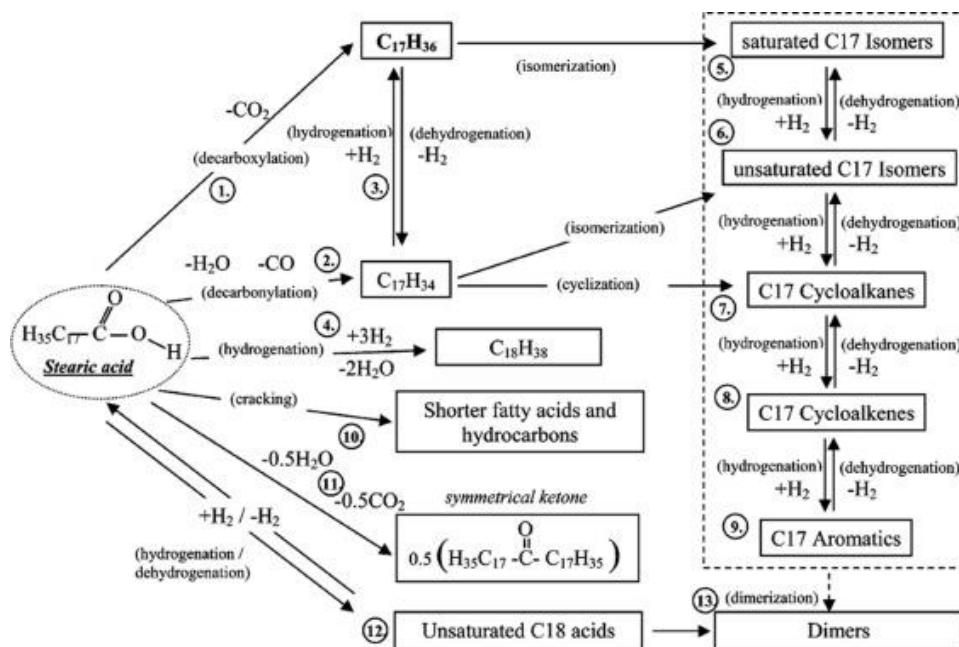


Figure 1-10 Reaction pathway of stearic acid deoxygenation (source: Hermida, 2015 [88])

### 1.2.2 Use of zeolites to obtain branched fatty acids

Even though the zeolites' primary use is in the fluid catalytic cracking process [93,94], they have been investigated to improve yields to branched products in the isomerization of fatty acids [11]. In the last years, zeolites with large pores like  $\beta$ -zeolite (yield: 50% [69,95,96]), Zeolite L (yield: 51%[97]), and Mordenite (yield: 66.5%[78]) has been used in methyl oleate or oleic acid isomerization[98,99]. On the other hand, the use of ferrierite as a catalyst has been a breakthrough [12], leading to getting a yield in branched products up to 74% [99].

Additionally, the use of additives, along with the use of ferrierite, has shown to improve conversion values over 97 % and yield ones up to 80% [70,100]. Ngo et al. studies in oleic acid isomerization show that water as an additive improves conversions value because it helps to the formation of new Brönsted acidic sites from Lewis ones [78]. At the same time, the addition of bulky hindered Lewis base molecules (i.e., triphenylphosphine) improves the selectivity to branched products because it neutralizes selectively external surface acidic sites which are responsible for oligomerization reactions [72,76,101]. They have been used as well with other zeolite as mordenite, showing similar results of improved selectivity in branched products [102]. Recently, the impregnation of magnesium oxide in ferrierite suppressed the dimer byproducts formation [103].

On the other hand, the works by Weckhuysen *et al.* and Ngo *et al.* have shown that the distribution of products depends on the architecture of channels and nature of acidic sites of the zeolites [68,70,78]. From the study of different commercially available ferrierites it was shown that a ferrierite with a low Si/Al ratio and few Brönsted acidic sites of high strength in the 10-Membered rings (10-MR) promotes yields to branched products [79].

Finally, the evaluation of more realistic substrate mixtures like methyl oleate instead of oleic acid have been carried out. Lower conversions and yields were found. A yield of 40% was obtained using a larger pore size  $\beta$ -zeolite [69], while conversion of 72% and yield of 42% was obtained using smaller pore size ferrierite [76]. In that case, the selectivity to branched products was higher using triphenylphosphine, while water led to higher conversions but just because of lactones formation [76]. Recently, the work of Bolshakov et al. showed that hierarchical porous ferrierite obtained by the transformation from a faujasite precursor had enhanced catalytic performance on oleic acid isomerization [104]. Although the synthesis of micro-mesoporous materials obtained by recrystallization from ferrierite has been previously reported in our laboratory (see section 1.5.1), these recrystallized materials have not been tested in this reaction or another reaction. Although a regeneration method was developed [99], the fast deactivation of the more expensive ferrierite catalytic materials, in comparison with the montmorillonite clays during oleic acid isomerization is the main reason why this process is less economically competitive than the commercial process of oleic acid dimerization (see Figure 1-5) [76].

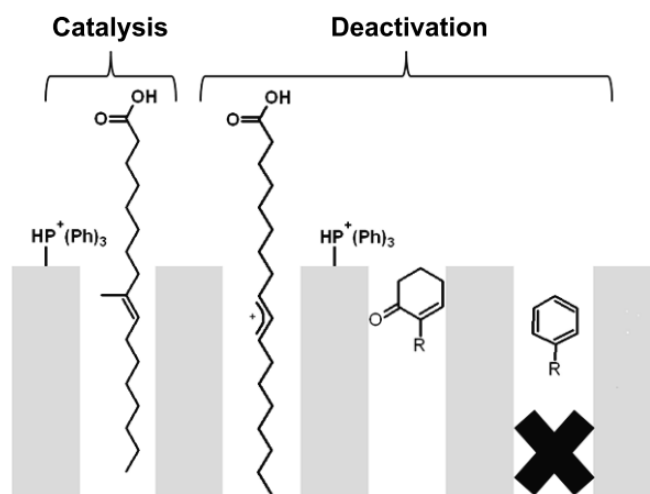


Figure 1-11 Reaction of oleic acid isomerization and deactivation by aromatic coke formation (source: Wiedemann, 2015 [105]).

Although the fast-initial blockage of the channels is one of the reasons why high yields are obtained in isomerization reaction using this zeolite, it leads to final deactivation of the catalysts. This fast initial channel blockage [80] allows that the catalytic activity for this reaction is performed just in the acidic sites of the pore mouth of the 10-membered ring (MR) channels (phenomenon known as pore mouth catalysis) [79], which represents less than 20% of the total Brönsted acidic sites in this zeolite [106]. These pore mouths are non-connected, whereby the chance of successive reactions decreases, increasing the selectivity in the reaction [79]. On the other hand, acidic site poisoning happened too during isomerization reaction by strong adsorption of polyenylic species which lead to deactivation processes previously described. It causes a low diffusion of raw materials inside the zeolite network (see Figure 1-11) as well as low diffusivity of them by smaller or obtruded channels. The catalyst particles are underused [107], reaction rates are lower [15,108], and coke formation [77,109] bringing to faster deactivation of catalysts [105]. So, although a large

pore size would improve the diffusion of the reagents into the zeolite crystalline network, the importance of zeolites in isomerization reaction is that they can decouple isomerization and oligomerization reactions by shape-selectivity in smaller pores [76].

In order to better understand the nature of this kind of catalytic materials, in the next section, a brief introduction to zeolitic materials, structure, properties, and uses is done.

## 1.3 Zeolites as catalytic materials

### 1.3.1 Zeolites: Structural characteristics and properties

Zeolites are aluminosilicates with a crystalline structure constituted of  $\text{SiO}_4$  and  $\text{AlO}_4$  tetrahedrons ( $\text{TO}_4$ ), which create a network of a well-defined interconnected system of pores [110,111]. They have high surface areas as well as a considerable acidity, which both can be tuned by different treatments [15,107,112,113]. According to IUPAC guidelines, zeolites can be defined as “a subset of microporous or mesoporous materials containing voids arranged in an ordered manner and with a free volume larger than a 0.25 nm diameter sphere” [114,115]. The general formula for zeolites is given as:

$$|M_x(H_2O)_y|[Al_xSi_{t-x}O_{2t}] - IZA \quad (1)$$

Where:

- $M$  represents a univalent charge balancing cation.
- $x$  is the number of Al atoms in the unit cell
- $y$  is the number of adsorbed water molecules in the unit cell
- $t$  is the number of T ( $T=\text{Si} + \text{Al}$ ) atoms in the unit cell
- $IZA$  is the code for the framework type assigned by the International Zeolite Association (IZA) [114,115].



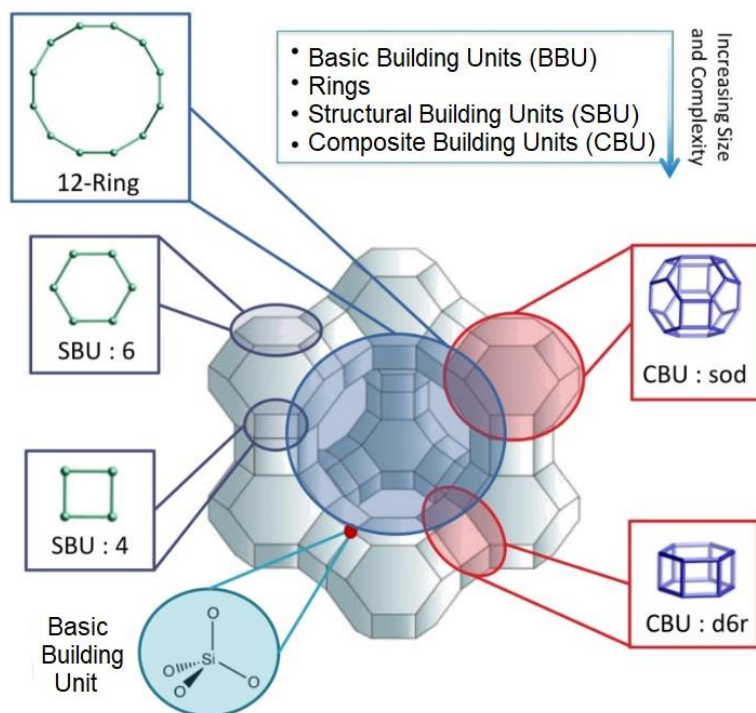


Figure 1-12 Building units in the Faujasite (FAU) supercage (Source: Demone, 2018 [116])

The 3D framework structure is defined by the specific way the  $\text{TO}_4$  are linked [113,115]. Also called basic building (BBU) units, they come together to form more complex structural building units (SBU) [116]. Forming more complex units from SBUs, polyhedral composite building units (CBU) can be common in multiple frameworks, being useful in identifying relationships among the framework types [114–116]. In Figure 1-12 it is possible to see how the arrangement of these building units form the 3D crystalline framework structure of the Faujasites (FAU). Here it is possible to see how some SBUs define the face of the CBUs. These structures are  $n$ -member rings (MR), with  $n$  the number of T-sites [115]. In the FAU structure (see Figure 1-12), there are three kinds of rings: 4-, 6- and 12-MR.

The network of interconnected pores is differentiated by the position and the ordering of these rings [115]. So, polyhedral CBUs with all of faces smaller than 6-MR are called cages. If the CBU has at least one face larger than 6-MR, it is called cavity. When these rings of more than six members are infinitely ordered in one dimension, the pores are called channels [115,116]. This arrangement of interconnected cages, cavities, and channels defines the porous system of the zeolites, and the size of the rings, which forms those, determines the accessibility of molecules to the crystallite [107,115,116]. The porosity of the zeolite is classified as microporosity ( $<2.0$  nm). The zeolitic pore system is typically constructed from channels of 8- to 12-MR with pore size from 0.4 to 0.8 nm [113,115]. These materials generate a high selectivity in the processes caused by these continuous channels, which have a dimension similar to those of reactant molecules [108].

The zeolite crystalline frameworks and, to a lesser extent, their chemical compositions determine the properties and potential uses of the zeolitic materials [117]. Zeolite worldwide consumption was around 2990 KTon in 2016 [118]. They were used mainly as ionic exchangers (66.6 %) in detergent builders as well as size exclusion adsorbents (18.0 %) in purification processes [94,107]. However, their more important use is as catalysts in different industrial processes (14.0 %) [112], especially in the petrochemical industry in the fluid catalytic cracking process (FCC) [93,94,119]. Although more than 200 zeolite frameworks have been synthesized, just a few of them are used as catalysts in industrial applications [107,111,113]. In Table 1-3 are reported the main industrial chemical processes that use zeolitic materials as catalysts. Zeolitic materials are used especially as acid catalysts because they have a strong acidity and well-defined micropore system, which allows getting high conversions and selectivities [87,120].

Table 1-3 Main industrial catalytic processes using zeolites [113].

<b>Zeolite</b>	<b>Modifications</b>	<b>Process</b>
<b>Y (FAU)</b>	USY, LaH-Y CaH-Y	Fluid catalytic cracking
	--	Isomerization, Alkylation, Disproportionation
<b>ZSM-5 (MFI)</b>	Silicalite	Beckmann rearrangement
	Me-MF1	Pyridine bases synthesis
	(dispersed)	Hydration of cyclohexane
	Me(Cu, Fe, Co)-MFI	Diethanolamine synthesis
	Mo-MFI	NO reduction
<b>Mordenite (MOR)</b>		Aromatization of methane
	(modified)	Trans-alkylation, isomerization, disproportionation
<b>MCM-22 (MWW)</b>		Methylamine synthesis
<b>B (BEA)</b>		Alkylation of benzene
<b>L (LTL)</b>	Pt-L	Alkylation of benzene, Acylation with acetic anhydride
<b>SAPO-34</b>		Aromatization
<b>titanosilicate</b>		Methanol to olefin
		H <sub>2</sub> O <sub>2</sub> oxidation

### 1.3.2 Shape selectivity and diffusion regimes in zeolites

The performance of zeolites as catalytic materials is a function of the size and shape of their pore systems. On one hand, the pore size is responsible for the effect known as shape selectivity, where the constrain on the diffusion of the molecules improves the selectivity, especially in complex reactions [113,121–123]. On the other hand, the small pore of the zeolites may be the cause of intracrystalline diffusion limitations [122], limiting the reaction rate [107,108,121]. Although a large pore size improves the diffusion of the reagents into the zeolite crystalline network, the adequate pore size for each reaction must be used to keep the selectivity of shape (see Figure 1-13) [15,124].

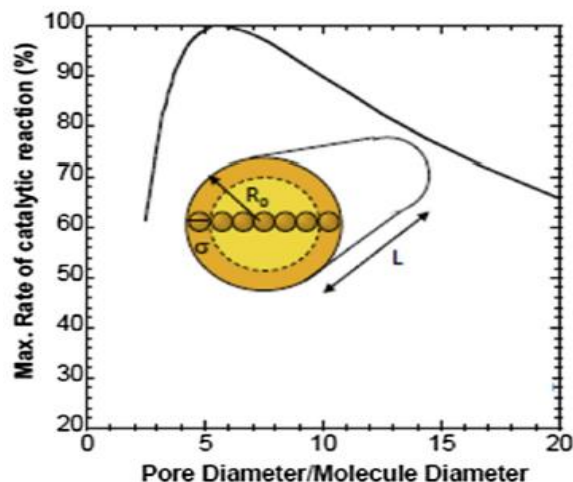


Figure 1-13 Relationship between maximum rate of catalytic reaction and ratio of pore diameter/molecule diameter in hydrotreatment reaction (Source: Galarneau *et al.*, 2016 [125])

In an average catalytic process, the molecules pass through three different regimes of the diffusion to arrive at catalytic sites (Figure 1-14) [119,126]. In the first place, known as molecular diffusivity, the molecules diffuse from the bulk of the raw material flow through the biggest pores [126,127]. This diffusion is ruled by intermolecular collisions [122], and it can be of the order of  $10^{-4} \text{ m}^2/\text{s}$  [119]. Then, the molecules are affected by the regime known as Knudsen diffusion [122]. Here, the diffusion is ruled by both molecule-molecule and pore wall-molecule collisions. This diffusion is from one to four magnitude orders lower than the molecular one [119]. Finally, molecules have to diffuse through the crystalline structure of the zeolites [126,127]. This change in the diffusion regime leads to a drastic drop in the diffusivity from five to ten orders of magnitude [119,120]. At this point, the diffusional regime is ruled exclusively by the interaction between the molecules and the pore walls. As mentioned before, the pore sizes of these materials are of the same order of magnitude as some molecules; therefore only molecules with a smaller size and in some position can move through the pores [113], leading to shape selectivity. Thus, it can be expressed in three ways: avoiding that the larger molecules can diffuse into the pores (reagent selectivity), avoiding that one bulkier transition state happens (transition state selectivity), or avoiding that the bigger byproducts cannot go out of the crystalline network until they are reconverted (product selectivity) [8,122].

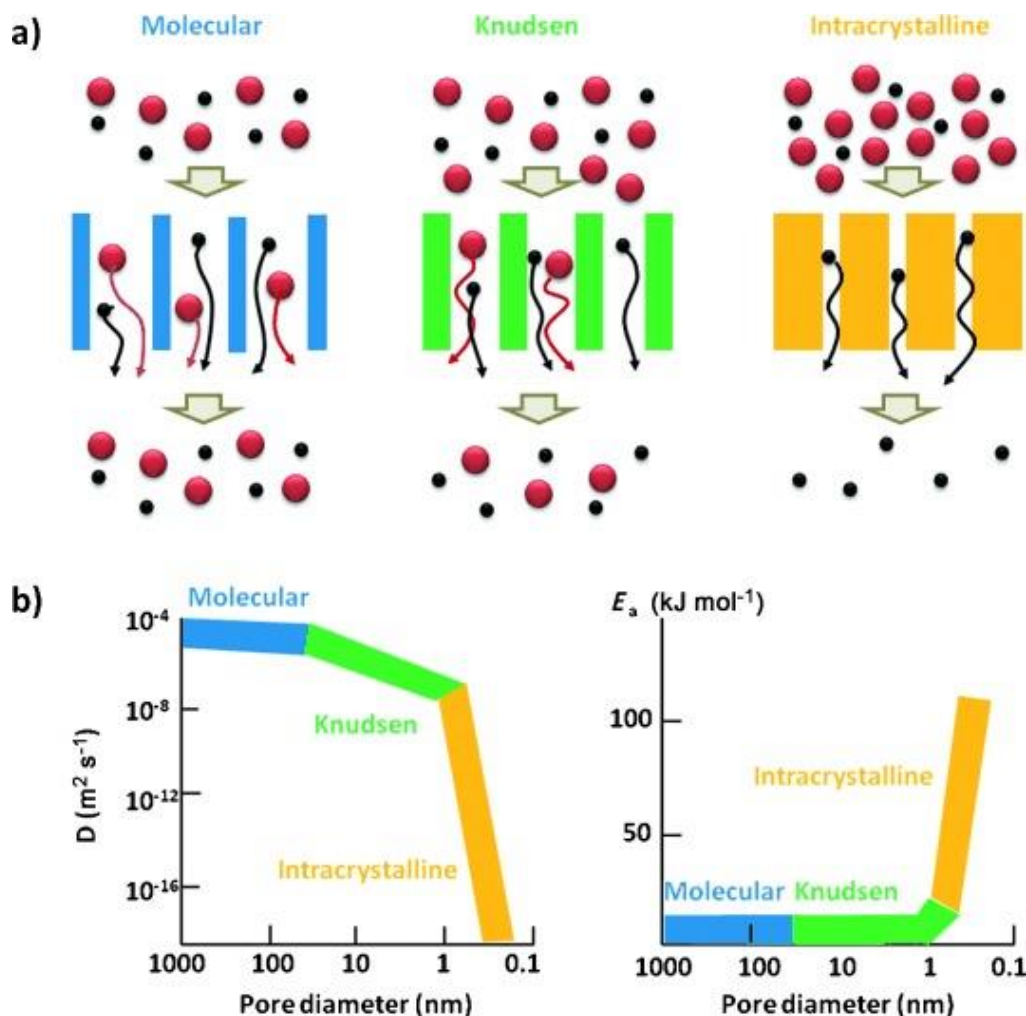


Figure 1-14 Diffusion of molecules inside pores of different sizes. a) Diffusion of different size molecules in three different diffusional regimes (Molecular (blue), Knudsen (green) and intracrystalline (yellow)). b) Coefficient of diffusivity (left) and activation energy (right) in these diffusional regimes (source: Li *et al.*, 2014[119]).

Considering the critical effect of the micropore system on the diffusion in the zeolites, the kinetics of catalytic processes are usually determined by this diffusion limitation. Microporous zeolitic diffusion involves narrow confinements (responsible for shape selectivity) and high concentrations of raw materials [122,126]. Moreover, the presence of additional barriers in zeolites can negatively affect the diffusion. Among them, there are surface barriers by adsorption on the external surface of the particles [122], barriers in the interface between intergrowth building blocks as well as steric hindrance among the molecules in the channels [122]. All these factors lead to the drop of the diffusivity. In these conditions, catalyst particles are underused [107], reaction rates are lower [15,108], and coke is often formed in isomerization/cracking reactions [77,109] leading to a faster deactivation of catalysts [105].

Keeping in mind the need to improve the efficiency of the catalytic processes when these diffusion problems are present, different developments have been made. They have been

done in the reactor design [128], through the use of structured supports, in the control of shape and size of the particles [129,130], and the transformation of the texture of the zeolite catalytic materials [121,131].

In order to improve the diffusion of large molecules by the transformation of the zeolites, the developments consist mainly in reducing the distance that the molecules have to travel along the crystals (diffusion length) [122]. They include the widening of the micropore channels, the reduction of crystal size, and the introduction of mesopores in the zeolite crystals [107,131–138]. The widening of the micropore channels has been obtained by the modification of the zeolite synthesis conditions as well as the use of larger structure directing agents [138]. Such developments concerned about ten types of framework [138], enhancing the effective diffusivity [122] but with considerable losses in catalytic activity and thermal stability [123]. On the other hand, the reduction of the particle size to get nanosized zeolites have been studied extensively [139,140], but the technical problem of the handling of nanomaterial powders at an industrial scale reduces their opportunities to scale-up [123]. The last alternative of the obtaining of meso-microporous materials has been shown to improve the diffusion of large molecules inside zeolite particles [123].

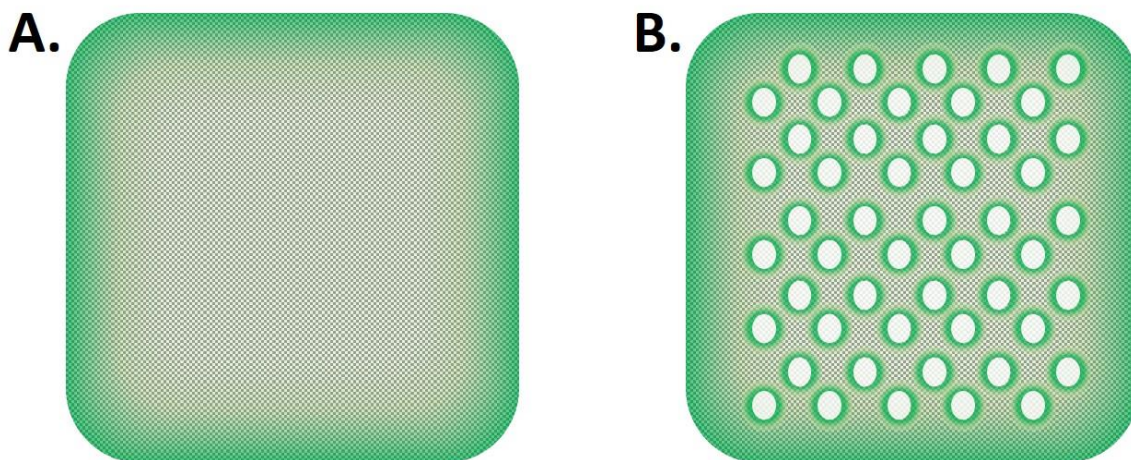


Figure 1-15 Schematic representation of the improvement through the introduction of mesopores in microporous zeolitic materials. A. Diffusion of molecules (green) into the microporous network of the zeolite. B. Diffusion of molecules (Green) into the meso-microporous network of the zeolite.

Diffusion of molecules through zeolite crystals is schematized in Figure 1-15. In green are represented the radial flow from the external surface to the microporous structure of the zeolites represented in gray grid. Here in Figure 1-15-A it is possible to see how the inner part of the zeolite is not used because the molecules do not arrive there. It results in the following fact : only a very small part of the active sites are used [107,126]. Additionally, these active sites start to lose activity with the course of the reaction by processes of poisoning or blocking [117,141,142]. Then, the activity and life-cycle of the catalyst decrease while these inner active sites are not used. On the other hand, in Figure 1-15-B it is possible to see how the introduction of the mesopores into the zeolite structure decreases



the diffusion length of the molecules, allowing some of the inner part of the zeolite to be used. It leads to enhancement of the accessibility of the active sites and decrease of the catalyst deactivation rates [143]. As a consequence of those considerations, meso-microporous materials have shown better performance in the activity, stability, and catalyst lifetime in reactions like alkylation, isomerization, aromatization, condensation, and cracking [130,144,145]. Keeping this idea in mind, a brief description of the methods for preparing meso-microporous materials from zeolites is discussed in the next section.

## 1.4 Zeolite-based meso-microporous materials

### 1.4.1 Strategies for obtaining micro-mesoporous materials with zeolitic framework

The synthesis of micro-mesoporous materials [143], in some cases with hierarchical porosity [121,131,146,147], is one of the most promising alternatives to improve diffusion into zeolites. However, it is essential to notice that not just the increase in the volume of mesopores is significant, but the connectivity of them to the surface and with the micropores is important too. In Figure 1-16 it is possible to see the different types of pores according to their connectivity. There are closed pores (C), not accessible from the external surface, blinded (B) by one side to the surface, pores which just go through (T) the crystal, or are present as rough external surface (R), or they go through the crystal, but they are well interconnected (I) [148].

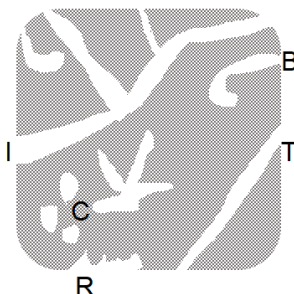


Figure 1-16 Scheme of a zeolite crystal with different types of new macro/mesoporosity. There can be pores closed (C), blind (B), or which go through (T) the crystal, or there can be pores arising from a marked roughness (R), or well interconnected (I) mesoporosity (Based on: Rouquerol, 2014 [148])

The integration of an ordered and well-interconnected network of mesopores in zeolitic microporous materials has shown to significantly improve the diffusion of the molecules more than the addition of disordered mesopores [123]. Moreover, the improvement on the mass transfer as well as on the efficiency in the reactions is depending more of the topology of the meso- and microporous phases than the increase in the mesopore volume, especially when this topology is hierarchical [121–123,131]. In order to develop the best catalytic material, this and other aspects should be taken into account. In Figure 1-17, there is an

overview of the various synthesis routes towards zeolite materials combining micro- and mesopores done by Chal *et al.* [93].

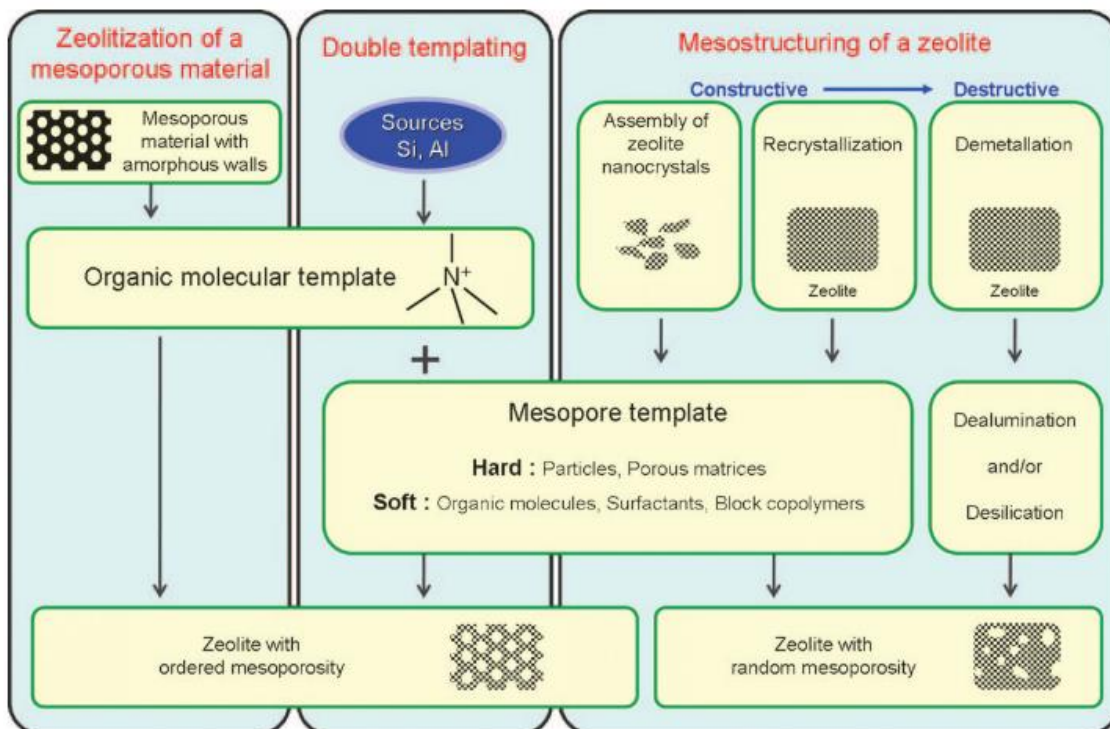


Figure 1-17 Different synthesis routes towards zeolite materials combining micro- and mesopores (source: Chal *et al.*, 2011[93]).

There are several approaches to obtain this kind of materials, these can be top-down (destructive) or bottom-up (constructive) strategies [93,111,131,133,145,149]. In Figure 1-18 the comparison of top-down and bottom-up synthesis approaches for meso-microporous zeolitic materials is shown based on the work of Chal *et al.* [93]. The approaches were evaluated in different aspects: production costs, health, safety and environment (HSE) issues, hydrothermal stability, flexibility in Si/Al ratio, predestination to get an ordered mesoporous architecture (topological aspect), and the possibility of a breakthrough development which can boost its use. The evaluation was done with a grade of five for the most positive evaluation, and a grade of one for the worst.

The top-down (destructive) approaches consist in the demetallation of zeolite microstructure by different agents (see Figure 1-17). The dealumination consists in the hydrolysis of Al-O-Si bonds by calcination, steaming, or using acids or other chemical agents. Using a similar approach, the desilication consists in the extraction of silicon atoms using mineral or organic bases [150–152]. This leads to a significant increase in the pore volume [143,153]. It is known that desilication starts preferentially at boundaries or defect sites of the zeolite crystals, which leads to a decrease in the crystallinity of the zeolitic materials [93,120,154]. Desilication procedure may lead to a considerable amount of mass loss (40-90%) [93]. This procedure can be applied in zeolites with Si/Al ratios from 15 to 50

(see Figure 1-19) to generate mesopores [111,143]. It is because the aluminum atoms in the zeolite framework protect clusters close to them from desilication, limiting the mesopore formation [155]. On one hand, if there are few Al atoms ( $\text{Si/Al} > 50$ ), desilication could be excessive. To avoid it, the use of some surfactants or tetraalkylammonium hydroxides can help to control the desilication process [143,156]. On the other hand, an excess of Al atoms ( $\text{Si/Al} < 10$ ) can limit the desilication process, avoiding mesopore formation. In order to work with a broader Si/Al ratio range [93], two-step desilication-dealumination procedures have been proposed to improve zeolite properties [107,157,158].

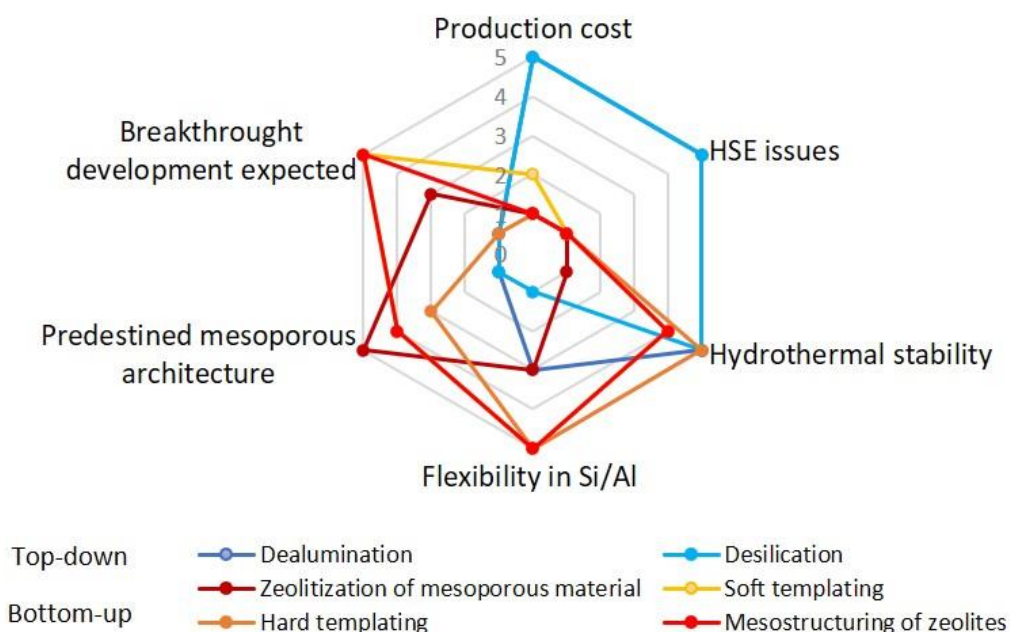


Figure 1-18 Comparison of top-down and bottom-up synthesis approaches for meso-microporous zeolitic materials [93].

The demetallation processes have been applied in industrial applications for a long time because they are low cost and easily applicable processes [133]. Their main disadvantages are the amorphization of the zeolite framework, a lower number of acidic sites as well as the random distribution of the different size mesopores [93].



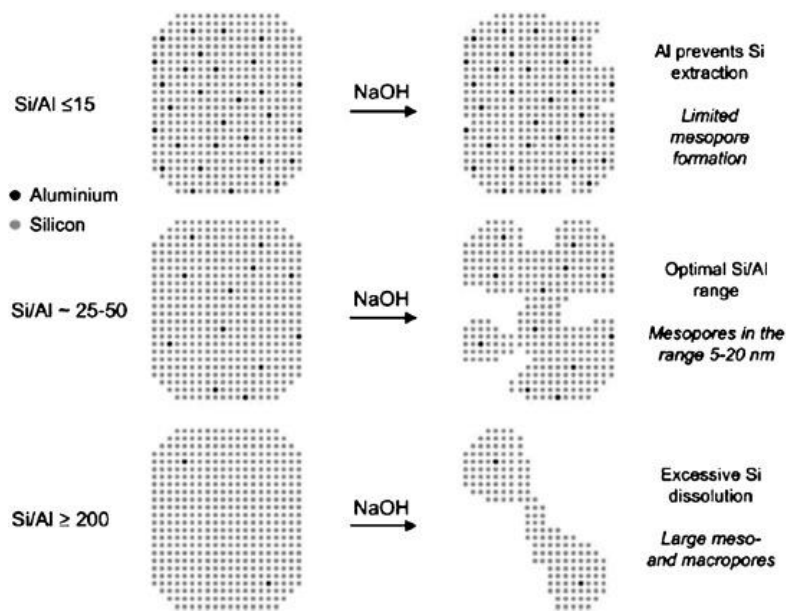


Figure 1-19 Desilication of the zeolite framework using a base as a demineralizing agent (source: Chal *et al.*, 2011 [93]).

On the other hand, bottom-up approaches consist in synthesizing a specific phase into another (see Figure 1-17) [93,111,131,145]. They have as main advantages the potential to tune the different characteristics of the pores. So, such processes allow to get a zeolitic microporous network in ordered mesoporous materials, to get mesopores into zeolite framework, or to get both pore systems simultaneously using the adequate structure-directing agent (SDA) [133,140,145].

Obtaining zeolitic structures in mesoporous materials is possible by crystallization with hydrothermal treatments using molecular micropore-SDA or introducing zeolite “seeds” in the material. It can lead to composites of micro and mesoporous regions or mesoporous materials with coatings of zeolitic frameworks [150]. The main disadvantage of this alternative is that the synthesis of ordered mesoporous materials needs high amounts of organic mesopore-SDA (30-70% wt.), which along with the use of micropore-SDA, can increase the costs [93,135,146]. Indeed, most of these SDAs are expensive. Moreover, such processes, including the SDA removal steps, should include the evaluation of the associated HSE risks.

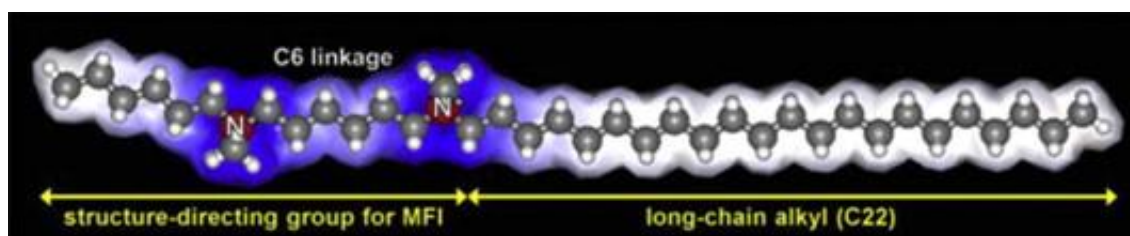


Figure 1-20 Example of a di-quaternary ammonium surfactant used as bifunctional structure-directing agent (source: Na *et al.*, 2013 [140]).

On the other hand, obtaining these zeolitic materials by the simultaneous synthesis of the micro- and mesoporous systems has been studied. Their convenient and versatile way to tune the size, shape, and interconnection of the pores is desired to develop catalytic materials [149,159]. The main way to obtain them is through the addition of micro- and meso-SDA or bifunctional SDA along with alumino-silicate precursors in the crystallization medium [93,131,133]. Among the SDA used in these procedures, we can mention carbon-based “soft” and “hard” templates as well as silylated alkyl chains [133]. The soft templates usually are organic compounds that tend to form micelles, which act as templates [93]. The hard templates are usually well-defined carbon-based solids like polymers, carbon black, carbon nanotubes, nanofibers, aerogels, among others [93,133]. The research group of Ryoo proposed the use of SDA, which can act on two different length scales [133,140]. In Figure 1-20 is presented an example of alkyl multi-ammonium surfactant which acts as bifunctional SDA. The di-ammonium group acts as a structure-directing group for zeolitic microporous structure, while the long-chain alkyl group acts as a meso-porogen agent by forming assemblies by hydrophobic interactions [140]. As previously described, the cost of these expensive SDAs is one of the main drawbacks of these procedures [93,135]. The development of these or other cheaper or recyclable SDA may lead to promising breakthrough processes to the industry.

Finally, another way to get these micro-mesoporous materials is the meso-structuring of zeolites. It can be done by creating inter-particle mesopores by stacking nanocrystals of zeolites or delamination and reassembly, or it can be done by generating intra-particle mesopores by recrystallizing microporous zeolitic materials in the presence of a base and a mesopore-SDA [93]. A microporous zeolitic material with inter-crystalline mesopores can be obtained by controlling the stacking nano-size zeolite structure with voids between them too [111,130,133]. The process of delamination and reassembly is based on structural degradation of the zeolite framework by exfoliation by selective hydrolysis followed by reassembly by pillaring with organic, inorganic, or mixed chemical compounds [160]. Again, using these expensive SDA or selective exfoliant is one of the main drawbacks [93,135]. On the other hand, the recrystallization process, also known as pseudomorphic transformation or riving [154], allows obtaining zeolitic materials with intracrystalline mesopores [143]. It consists in the transformation of microporous zeolite crystals into mesopore-containing zeolite ones [93]. They are obtained using a demineralizing agent for desilication and a cationic surfactant as mesopore-SDA. The cetyltrimethylammonium bromide (CTAB) is the most common used surfactant [143,156,161]. Advantages of the recrystallization process are the use of commercially available zeolites, as well as the capacity to tune the pore structure under relatively mild conditions. This opens the opportunity of developing processes easily applicable to an industrial scale. Keeping it in mind, a brief description of the zeolite recrystallization process is discussed in the next section.

### 1.4.2 Recrystallization of zeolites

The recrystallization of zeolitic materials allows the introduction of organized mesopores using mild conditions [139,156]. The process consists in one or two-step hydrothermal treatment in which a strong base or alcohol, such as glycerol, is used as a structural degradation agent along with surfactants used as mesopore-SDA [143,156]. In the case of the use of alcohols, the process for structural degradation is the depolymerization of the zeolite [156]. In the case of using the bases, the degradation of the zeolite framework occurs by desilication [143].

The proposed mechanism by Ivanova *et al.* [162] for the recrystallization of zeolitic materials is shown in Figure 1-21. In general terms, the reaction starts with a fast-ionic exchange followed by desilication caused by the alkali attack to siliceous structures, creating some porosity[162,163]. It is followed by the diffusion of the surfactant inside the zeolite framework and undergoing an ion exchange with the cations present in the new pores. After it, micelles of the surfactants are formed inside the zeolite framework, followed by the recrystallization of siliceous structure around them. It leads to the formation of organized mesopores [145]. Finally, the surfactant is removed by calcination to obtain the recrystallized mesoporous material [111].

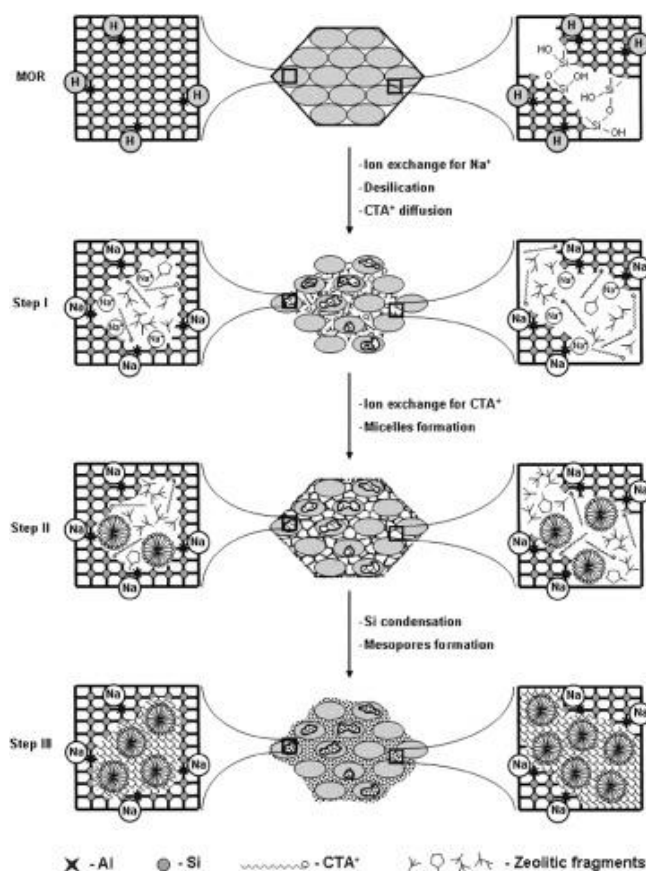


Figure 1-21 Mechanism of desilication/recrystallization leading to micro-mesoporous zeolitic materials (Source: Ivanova *et al.*, 2014 [162]).

Extensive studies of Ivanova et al. on two-step recrystallizations showed that depending on the dissolution level, the recrystallization leads to three different types of micro-mesoporous materials (see Figure 1-22). The first ones (RZEO-1) are mesostructured zeolitic materials which can be coated with films of mesoporous materials. They were obtained in the mildest conditions. The mesoporosity, in this case, is formed from the highly siliceous species in thin layers on the crystal surface. The acidity and textural properties of such materials are similar to those of parent zeolites, but they have an accessibility improved by the presence of the mesopores [143,156]. The second ones (RZEO-2) are composite materials consisting of two co-crystallized zeolitic and mesoporous ordered phases. They are formed in more severe recrystallization conditions. Although their total number of acid sites decreases and there is a higher proportion of Lewis-type acidic sites than Bronsted ones, the acid strength of these last ones does not change while the accessibility is further improved [143,156]. The third ones (RZEO-3) are mesoporous materials containing small zeolitic fragments in the walls. They are obtained by completed recrystallization in the strongest conditions. They have the structure, texture, and morphology of ordered mesoporous materials. These mesoporous materials have lost their zeolitic porosity and acidity [143,156]. In Table 1-4, are briefed the conditions necessary for recrystallization to obtain each kind of material as well as the properties of each kind of material.

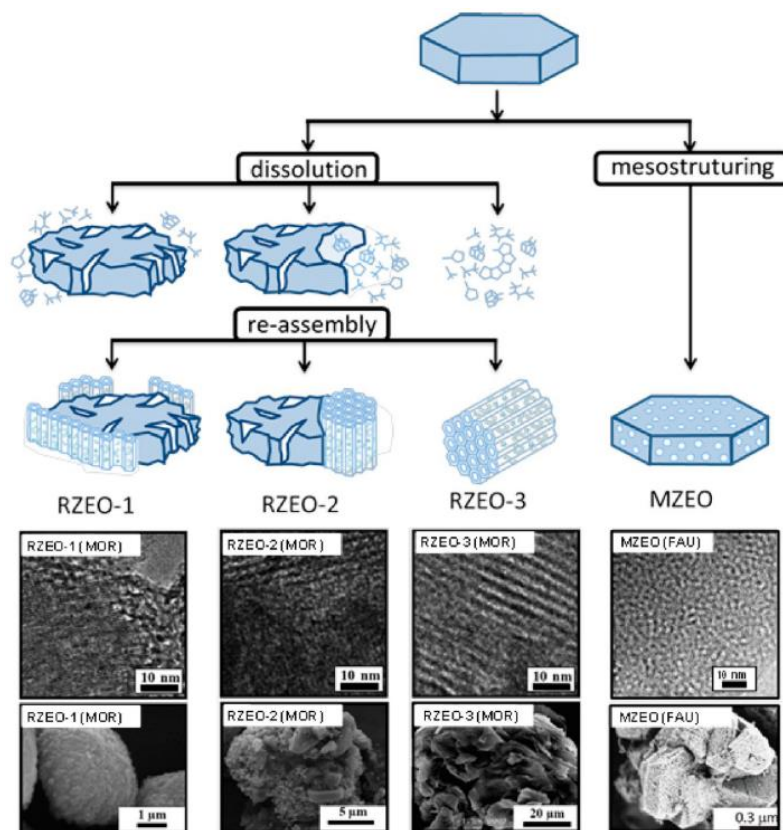


Figure 1-22 Synthetic strategies of recrystallization leading to different types of materials  
(Source: Sachse & García-Martínez, 2017 [145])

Table 1-4 Characteristics of recrystallization processes and properties of recrystallized zeolitic materials [143,156].

		RZEO-1	RZEO-2	RZEO-3
<b>Desilication Step</b>	<b>Demineralizing agent</b>	Weak base + surfactant	Strong base	Strong base
	<b>OH/Zeo (mmol/g)</b>	2-5	6-12	10-12
	<b>Temperature (°C)</b>	20-40	20-40	Up to 80
	<b>Time (H)</b>	0.5-1.0	Up to 3	Up to 3
<b>Recrystallization step</b>	<b>Surf/Zeo (mmol/g)</b>	1-6	1-6	2-8
	<b>Hydrothermal treatments steps</b>	1: pH=12	1: pH=12 2: pH=8-9	1: pH=8-10.5
	<b>Temperature (°C)</b>	100-150	100-150	100-110
	<b>Si/Al</b>	10-100	10-50	10-50
	<b>Phase composition</b>	As in the parent zeolites	The mixture of zeolitic and mesostructured	Mainly mesostructured
	<b>Morphology</b>	Crystals as in the parent zeolite but coated with a worm like mesoporous films	Co-crystallized zeolite crystals and mesoporous particles	Spheroid or lamellar particles of mesoporous materials
<b>Local structure</b>	<b>Al coordination</b>	Tetrahedral	Tetrahedral and octahedral	Tetrahedral and octahedral
	<b>Si coordination</b>	Tetrahedral, Q <sub>4</sub>	Mainly Q <sub>4</sub> , a small contribution of Q <sub>3</sub>	Q <sub>4</sub> /Q <sub>3</sub> ratio higher than in MCM-41
	<b>Framework vibrations (FTIR)</b>	As in the parent zeolites	As in the parent zeolites	Evidence for zeolitic fragments
<b>Textural properties</b>	<b>V<sub>micro</sub></b>	As in the parent zeolites	Reduced by 20-60%	Reduced by 70-100%
	<b>V<sub>micro/total</sub></b>	0.5-0.9	0.1-0.5	<0.1
	<b>Mesopore size (nm)</b>	2.9-3.3; 4-20	2.7-3.3; 4-20	2.3-3.5
<b>Acid Sites</b>	<b>Content</b>	As in the parent zeolites	Reduced by 5-55%	Reduced by 60-80%
	<b>Bronsted/Lewis Accessibility index</b>	1-10 0.4-0.8	0.5-4 0.6-1.0	0.1-2 ~1.0
	<b>Hydrothermal stability</b>	As in the parent zeolites	Stable in boiling water during 336 h	Stable in boiling water during 120 h

On the other hand, there are discussions about the reaction pathway in zeolite recrystallization when it is done in one-step. It usually is done under stronger hydrothermal treatment conditions [117]. Although Ivanova *et al.* [143] reported that one-step recrystallization occurs according to previously described ways, García-Martínez *et al.* [111,119,145,164] has proposed that these one-step processes occur differently. It is referred to as pseudomorphic transformation [155,165] or crystal rearrangement [119,145], giving a different mesostructured zeolite.

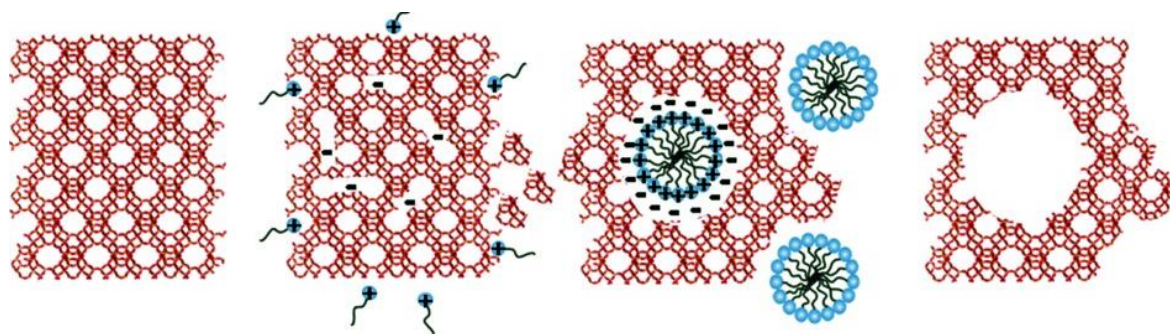


Figure 1-23 One-step recrystallization using a base and cationic surfactant as the template (source: Li *et al.*, 2014 [119])

In contrast with the mechanism proposed by Ivanova *et al.*, García-Martínez *et al.* [111,119,145,164] have proposed a mechanism for one-step recrystallization based on the “crystal rearrangement” concept (see Figure 1-23). The process starts with some desilication by the base and the diffusion of the surfactant inside of the zeolite framework. After it, when there is enough surfactant amount, the formation of the micelles occurs in these conditions, the flexible zeolite framework is rearranged to accommodate the micelles. If there are enough micelles, they become to be ordered in hexagonal or cubic ways. After the removal of surfactants by calcination, a well-ordered system of regular size mesopores appears. In contrast with meso-microporous zeolite materials obtained with two-step recrystallization, the materials obtained by the one-step process are single-phase crystalline zeolites with intracrystalline mesopores [117]. This mechanism is subject of controversy, mainly due to the unlikely step of migration of isolated surfactant molecules to the interior of crystals until they reach the right concentration for forming micelles.

## 1.5 The Ferrierite zeolite

The ferrierite (FER) is a zeolite with a platelet like crystal morphology as well as an anisotropic framework of small and medium pore size that contain two intersected channel systems [13,166–168]. One of them is formed by 8-MR (0.35 x 0.48 nm) along the [010] direction and the other one is formed by 10-MR (0.43 x 0.55 nm) along the [001] direction [166,167,169,170]. Additionally, FER has cavities at the intersection of the 8- and 10-MR only accessible through the 8-MR [169,170]. The scheme of these channels is shown in Figure 1-24. This material has a high stability against water or other chemical agents at high temperatures [13,166].

The most common way to synthesize this zeolite is the hydrothermal synthesis using tetramethylammonium molecules as SDA at high temperatures [166]. In this way, ferrierite, especially the low silica one ( $\text{Si}/\text{Al} < 10$ ), can be produced industrially at a low cost [13]. Moreover, it can be synthesized by other routes, using one or more organic templates or without the use of them. Depending on these conditions, ferrierite can be obtained with different  $\text{Si}/\text{Al}$  ratios, acidic sites distributions [171], particle size, even with heteroatoms [166,170].



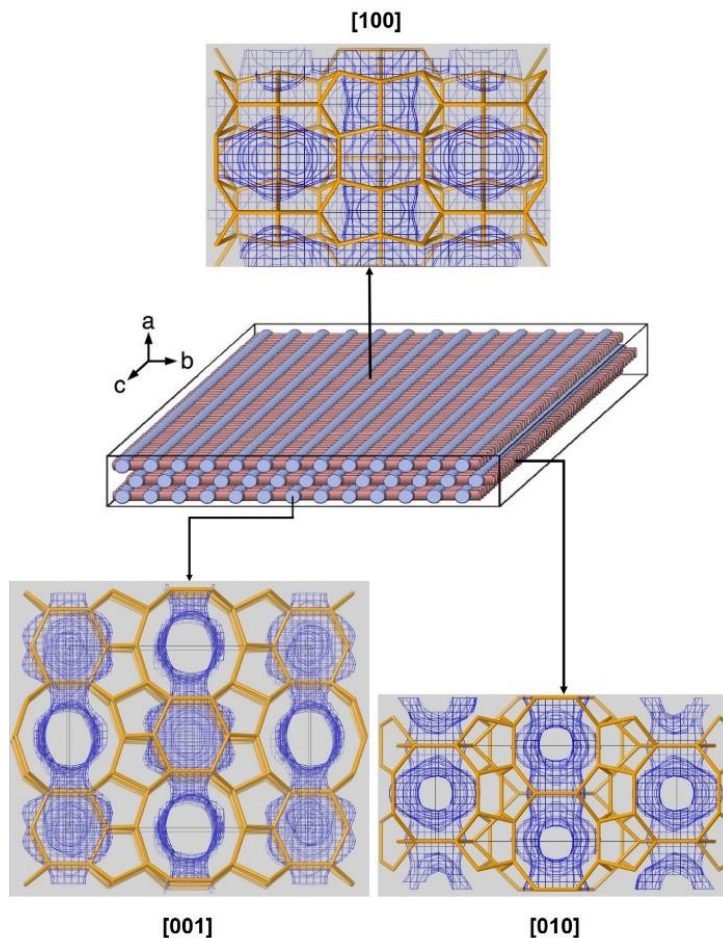


Figure 1-24 FER network of interconnected channels (Based on: Bonilla *et al.*, 2009 [172])

This zeolite material is used as a solid acid catalyst in the following applications: CO<sub>2</sub> hydrogenation, methanol to olefin, N<sub>2</sub>O decomposition, alcohol dehydration, dimethyl ether carbonylation, isomerization of short alkenes, among others [13,166]. The most important application of ferrierite is for the isomerization of n-butene to produce branched compounds [166,170,173] used as precursors on methyl-tert-butyl ether (MTBE) synthesis [174]. Usually, this zeolite is used in reactions where the selectivity induced by the porous network is fundamental. According to different works, these pore systems can produce the effect known as the pore mouth catalysis. In the reaction conditions, just the acidic sites in the pore mouth of the channels are accessible for the reagents, while the inner section of the crystal is filled with slowly diffusing species [169]. These pore mouths are non-connected, therefore the chance of successive reactions decreases, increasing selectivity in the reactions [11,79,175–177]. However, this leads to the fact that the inner part of the crystals are underused and this reduces the lifetime as catalysts of the ferrierite materials [169]. In order to improve the characteristics of ferrierite as a catalyst, FER-based materials with varying properties have been developed. The approaches to prepare them include changes in the elementary composition, morphology, porosity and acid strength [166].

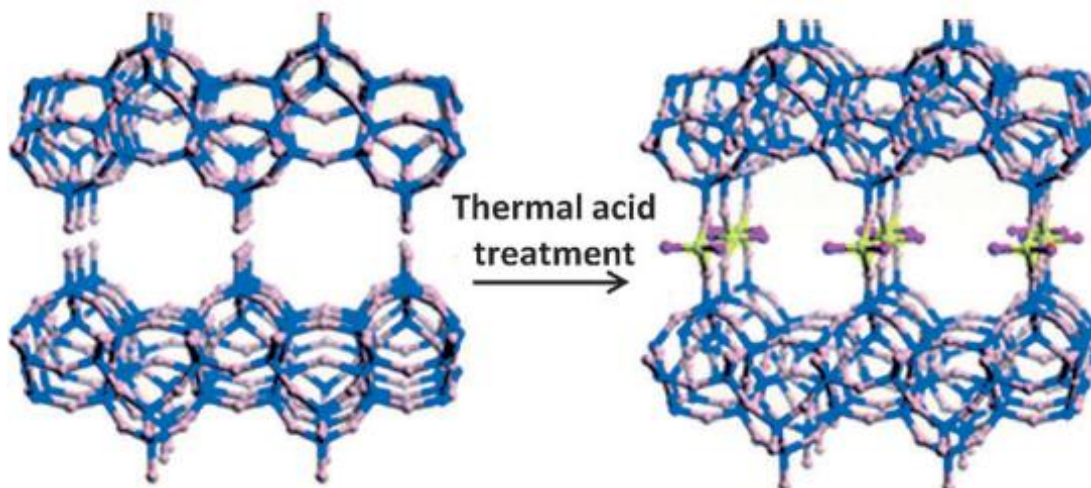


Figure 1-25 Zeolite with large interconnected pores (APZ-4) from zeolite ferrierite (Source: Moliner *et al.*, 2015 [170])

The synthesis of new zeolitic phases using ferrierite as precursors has been developed recently [167,170]. A zeolite phase (APZ-4) of large interconnected pores among layers of 2D FER structures has been synthesized by pillaring. The APZ-4 (see Figure 1-25) phase was obtained by acid treatment of nanosized FER structures (exfoliation) followed by pillaring using alkoxysilanes to form silica bridges [178]. This formed 12-MR interconnected with FER layers. However, these structures have been obtained in a pure siliceous form, therefore their applications as catalysts have not been developed yet [167,170,178].

On the other hand, some important efforts have been made to decrease the particle size with the objective to decrease the diffusion length without affecting selectivity properties [129,166]. The most basic approach to reduce the crystal size is adjusting the SDA concentration in the hydrothermal synthesis process [166,179]. Another strategy consists in the hydrothermal synthesis of nano-sized ferrierite by adding surfactants [166] or bulky alcohols [177]. The use of organic surfactants as cetyltrimethylammonium bromide (CTAB) [180] and cetyltrimethylammonium bromide (CTAB) [181] has shown an effect in decreasing the particle size [129,166]. The use of other organic compounds to only one SDA (*N,N*-diethyl-*cis*-2,6-dimethyl piperidinium (DMP) [182]) which can reduce the particle size additionally has been developed but with some changes obtained in the morphology [182,183]. In Table 1-5 there is a brief summary of the improvements obtained in several catalytic reactions using nano-sized ferrierite. In general, the reduction of the crystal size leads to an improvement in the activity and stability of reactions of isomerization of isobutene and conversion of methanol to dimethyl ether.



Table 1-5 Synthesis and use of nano-sized ferrierite materials.

Synthesis Process	SDA	Co-SDA	Catalytic test	Remark	REF.
H.T. <sup>a</sup> 175°C 55 h	Pyrrolidine	TMAOH	Isomerization of n-butane	- Higher activity and stability	[177]
H.T. 150°C 48 h	Piperidine	CTAB			[181]
H.T. 140°C 48 h	DMP	--		- Nanosheets - Higher conversion and selectivity	[182]
H.T. 150°C 336 h	Choline	--		- Nano needles - Higher conversion	[183]
H.T. 180°C 75 h	Pyrrolidine	Sodium lauryl sulfate	Methanol to dimethyl ether	- Higher conversion and selectivity to DME	[184]

<sup>a</sup>H.T.: Hydrothermal treatment

Finally, considering that the introduction of mesoporosity may improve the use of inner acidic sites [169,175], we will discuss in the next section the synthesis of mesoporous ferrierite-based materials.

### 1.5.1 Ferrierite-based meso-microporous materials

The introduction of mesopores in the ferrierite structure has been proposed to improve the diffusion of bulky molecules, avoiding the problem of affecting the selectivity generated by its confined structure. As discussed before (see section 1.4), there are different top-down and bottom-up strategies to get meso-microporous materials from zeolites.

Among the top-down strategies, dealumination and desilication as consecutive demetallation processes have been applied to ferrierite structure to get meso-microporous materials. The conventional dealumination processes applied to FER zeolites include treatments with steam and inorganic acids [166]. Both dealumination processes lead to non-ordered mesopores as well as redepositing of extra-framework-Al structures [166,185]. However, these processes have shown to improve the catalytic performance of ferrierite materials. Both steam [186,187] and acid [176,186,188] dealumination processes applied on ferrierite materials have improved yields to isobutene in the n-butane isomerization process. Some researchers have used  $(\text{NH}_4)_2[\text{SiF}_6]$  to eliminate these extra-framework structures, which reduces the selectivity in the process [188,189]. It has improved catalytic material performance [176] as long as the acid concentration was not excessive [188]. On the other hand, the dealumination process, through 0.25 M HCl solutions, has shown to improve the conversion in  $\alpha$ -pinene isomerization [190] and m-xylene conversion, enhancing the selectivity towards p-xylene [191,192].

Considering the high stability of ferrierite structure against chemical agents, desilication processes require harsher conditions than other zeolites, even more when the process is

done over low silica zeolites [13,166]. Usually, basic desilication leads to obtaining disordered and non-uniform mesopores [172]. Desilicated materials obtained from high silica ferrierites ( $\text{Si}/\text{Al} = 27$ ) by using sodium hydroxide solutions ( $< 0.5 \text{ M}$ ) have higher surfaces and mesopore volumes while preserving a part of their original microporous structure [172,193]. However, as previously said (see section 1.4), the desilication process leads to high mass losses. Nevertheless, these materials have shown superior activity in catalytic cracking of low-density polyethylene (LDPE) [172], isomerization of butene [175], and propylene conversion [193] in comparison with parent ferrierite. In the case of low silica ferrierites ( $\text{Si}/\text{Al} = 9$ ), the use of solutions of higher concentrations of sodium hydroxide ( $< 0.5 \text{ M}$ ) led to the loss of the ferrierite crystalline structure [13]. In order to obtain mesoporous materials without structure loss from low silica ferrierite, it was necessary to perform a hydrothermal treatment at  $130^\circ\text{C}$  for 72h with a less concentrated ( $0.25\text{M}$ ) solution of sodium hydroxide [13].

In order to improve the mesopore generation process on ferrierite, consecutive processes of dealumination-desilication have been applied. Brylewska *et al.* [194] got a micro-mesoporous material with mesopores preferentially formed in the 8-MR through a dealumination step with nitric acid followed by a desilication step with lithium hydroxide. This material showed an improvement in ethanol dehydration. A multiple-step process that includes desilication with sodium aluminate, followed by an acid chloride dealumination and a final sodium hydroxide desilication has been developed to obtain ferrierites with a high intracrystalline mesopore volume [158,195]. Verboekend *et al.* [195] showed that with a higher mesopore area ( $99 \text{ m}^2/\text{g}$ ), the dispersion of metals on the ferrierite surface is improved. Catizzzone *et al.* [158] showed that with the increase of mesopore volume, ferrierite materials lead to higher conversion and selectivity to light hydrocarbons in methanol dehydration. Recently, the use of mixtures of  $\text{HF-NH}_4\text{F}$  in proper concentrations allowed to improve the conversion of chloromethane to propylene with high selectivity to ethylene formation [196].

On the other hand, among the bottom-up strategies tested to shorten the diffusion length through the obtaining of meso-microporous materials, the following approaches have been developed : the pillaring of FER structures [197,198], the transformation to FER from zeolites with bigger porosity [104], synthesis of the meso and microporous phases simultaneously [199,200], the synthesis of nano-stacked ferrierite crystals [139], as well as recrystallization processes on commercial zeolitic phases [13,201].

The swelling of layered aluminosilicate precursors of FER zeolitic (PREFER) structures using CTAB followed by pillaring using TEOS as a pillar precursor allows getting materials with 2D layers of ferrierite, whose pillared structure generates mesopores of around  $3 \text{ nm}$  [160,198]. These processes imply the prior expensive obtaining of PREFER lamellar structures using as SDA the 4-amino-2,2,6,6-tetramethylpiperidine[202]. With a similar method, Fuentes-Ordoñez *et al.* got a micro-mesoporous material (ITQ-6) with a high mesopore volume ( $1.255 \text{ cm}^3/\text{g}$ ), which, after impregnation with Pt, improves its catalytic activity in polystyrene hydrocracking. Following another strategy, Bolshakov *et al.* work [104] showed that hierarchically porous ferrierite could be obtained by the transformation

from a faujasite precursor. This material was obtained starting from zeolite Y (CBV-600®) using n-methylpyrrolidine (NMP) and 1,2-dimethyl-3-hexadecyl-1H-imidazol-3-ium bromide (C<sub>16</sub>dMImz) as co-structure-directing-agents. It had a better catalytic performance than parent ferrierite in the isomerization reaction of oleic acid skeletal. In a similar way, Xu *et al* [199,200] synthesized MCM-22/FER and MCM-49/FER composites using as SDA the hexamethyleneimine and hexamethyleneimine/cyclohexamine, respectively. The MCM-22/FER composite showed a better catalytic performance on the olefin aromatization reaction in comparison to MCM-22 or FER materials. It could be due to some synergistic effect among both phases, possibly allowed by integrating the phases [199].

Table 1-6 Synthesis and use of stacked meso-microporous nano-sized ferrierite materials

Synthesis Process	Co-SDA	$V_{\text{tot}} - V_{\text{micro}}$ (cm <sup>3</sup> /g)	Catalytic test	Remark	REF.
H.T. <sup>a</sup> 150°C 168 h	Piperidine/ CMPip <sup>b</sup>	0.43	Oligomerization of n-pentene	- Higher conversion, stability, and selectivity	[180]
H.T.150°C 336 h	Piperidine/ TMAOH	0.34	Pyrolysis of LDPE	-Higher catalytic performance	[203]
H.T. 160°C 96 h	Pyrrolidine/ TPOAC <sup>c</sup>	0.23	Benzylation of toluene	-FER nanosheets -A superior catalytic activity	[204]
H.T. 120°C 96 h <sup>d</sup>	Pyrrolidine	0.46	Isomerization of butene	-Higher selectivity and catalysts stability	[205]
H.T.160°C 144 h	TMCAH <sup>e</sup>	0.13	DME carbonilation reaction	- Higher catalytic activity and stability	[206]

<sup>a</sup> H.T.: Hydrothermal treatment

<sup>b</sup> CMPip: cetyltrimethylpiperidinium

<sup>c</sup> TPOAC: 3-(trimethoxysilyl)propyloctadecyldimethyl ammonium chloride

<sup>d</sup> Under rotation (60 rpm)

<sup>e</sup> TMCAH: trimethylcetylammonium hydroxide

The obtaining of mesopores through the ordered-stacking of nanoparticles of ferrierite has been widely studied because it allows shortening the diffusion length without affecting the microporous structure [139]. These materials are usually synthesized by hydrothermal processes using micro-SDA and surfactants as co-structure-directing-agents or the use of bulky bifunctional molecules. In the work of Chu *et al.* [205], they proposed the obtaining of this kind of material using a single micro-SDA (Pyrrolidine), but the hydrothermal treatment was done under dynamic conditions (rotation at 60 rpm). Table 1-6 presents a summary of the improvements obtained in several catalytic reactions using stacked meso-microporous nano-sized ferrierite materials. In general, the reduction of the size of the microporous domains leads as well as the incorporation of a mesopore system in a highly hierarchized way to an improvement in the activity and stability of these catalysts.

Finally, the application of recrystallized micro-mesoporous materials has been reported only in the case of ferrierites with Si/Al ratio of 27 [143]. These meso-microporous materials were obtained by two-step recrystallization procedures using sodium hydroxide and CTAB [175,201,207]. These meso-microporous ferrierite materials improve conversion, selectivity, and stability parameters in the skeletal isomerization of 1-butene into iso-butene [175,201], and butanol dehydration to get butenes [207]. Recently, our research group has

developed this recrystallization process in the case of a ferrierite with a low Si/Al ratio and obtained a micro-mesoporous material, which has parallelepiped-shaped mesopores along the 10-MR channel direction [13].

Taking into account that we obtained the meso-microporous ferrierite materials by one-step recrystallization, we will discuss in detail the characteristics of these materials in the next section.

### 1.5.2 Recrystallization of ferrierite zeolites

Recrystallization treatments of ferrierite have been performed on high (Si/Al=27.5) [201] and low (Si/Al 9.2) [13] silica ferrierite zeolites using sodium hydroxide as a demineralizing agent and CTAB as a mesopore template.

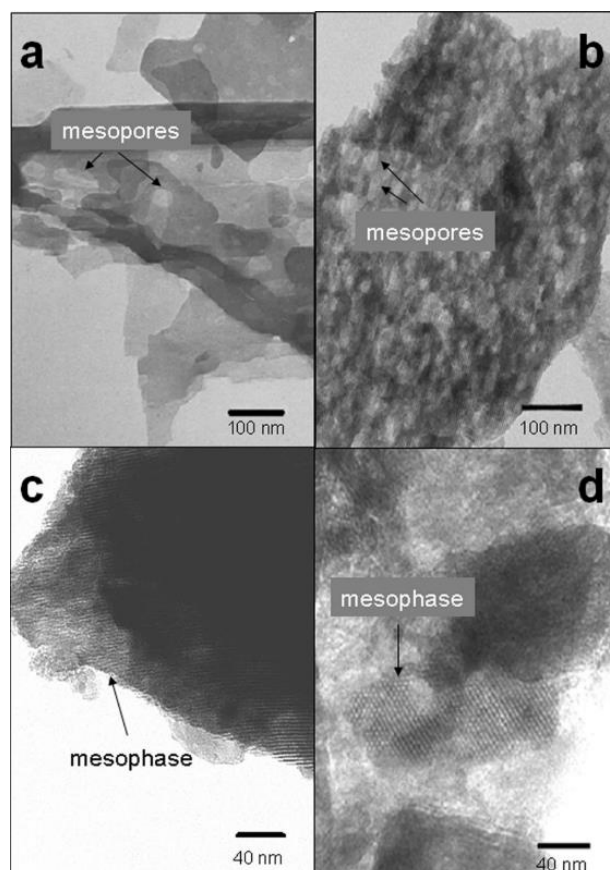


Figure 1-26 TEM micrographs of desilicated ferrierite using a solution of NaOH 1.2 M (a) and recrystallized ferrierites using solutions of NaOH of 1.2 M (b) 0.4 M (c) and 1.8 M (d) with a desilication first step followed by recrystallization with CTAB (source: Khitev *et al.*, 2012 [175]).

Let us first consider the case of high silica ferrierite (Si/Al=27.5). The procedure to get meso-microporous zeolitic materials was composed of two steps: a desilication step done at room temperature for 24h in NaOH solution from 0.4 to 1.8 M followed by a

recrystallization step through a hydrothermal treatment at 110°C for 24 h using CTAB as mesoporous template [175,201]. In Figure 1-26 it is possible to see that, while desilication leads to randomly distributed and disordered pores (Figure 1-26-a), recrystallization leads to the formation of an ordered mesoporous phase with pore size around 10 nm (Figure 1-26-b,c,d) [175,201]. It can be due to the drilling effect of the surfactant caused by the ion exchange of  $\text{CTA}^+$  which protects the ferrierite from undesirable destruction. It allows zeolitic fragments to be reordered in mesoporous structures around surfactant micelles [175]. As it was mentioned before (see section 1.4.2), the variation of dissolution level is the most crucial parameter for defining the characteristics of the meso-microporous zeolite. Although FER crystalline phase was the only phase observed in XRD analysis, the crystallinity decreased with the degree of dissolution [201].

Additionally, the small-angle analysis revealed the presence of a hexagonal mesoporous phase, defined as MCM-41. The amount of this phase increased proportionally with the degree of dissolution [201] for forming composites of micro and mesoporous phases. In concordance with the mechanism described by Ivanova et al. [143], the mesoporous phase was initially observed as a phase growing in zeolite crystal walls. Then, the use of a low NaOH concentration (0.4 M) solution led to lower dissolution degrees (Figure 1-26-c) while a higher concentration of NaOH (1.8 M) led to higher dissolution degrees, the mesoporous phase being immersed in the residual zeolite fragments (Figure 1-26-d) [175,201]. Although the Si/Al ratio of the recrystallized material was kept unchanged compared to parent ferrierite, the total acidity decreased when the degree of dissolution was very high due to the loss of crystallinity [175,201]. In order to evaluate the improvement of the accessibility to acidic sites (shortening of the diffusion length), Khitev *et al.* defined [175] the accessibility index as the ratio between the intensity of the adsorbed pyridine at 130 and 300°C. According to the results briefed in Table 1-7, they concluded that the accessibility increased with the degree of dissolution [175,201]. The evaluation of these materials as catalysts in 1-butene isomerization showed that they had a better performance than parent or just desilicated ferrierites. The best yield in isobutene in the isomerization reaction of butene was achieved with an intermediate degree of dissolution-recrystallization. This was because the right balance could be reached between accessibility given by the mesoporous phase and activity given by the microporous phase [175].

Table 1-7 Main properties of high silica recrystallized ferrierites treated with NaOH solution at different concentrations and yield in isobutene [175,201].

Exp.	$C_{\text{NaOH}}$ (M)	Relative crystallinity	$V_{\text{mic}}/V_{\text{Tot}}$	Accessibility Index (%)	Yield in Isobutene (%)
Parent FER	--	1.0	0.91	21	24
1	0.4	1.1	0.80	40	34
2	1.2	0.7	0.34	59	40
3	1.8	0.4	0.14	97	34

Let us now consider the case of low silica ferrierite. Considering that low silica ferrierite has a higher stability than high silica one, the use of classical desilication procedure does not lead to mesopore formation [13]. In our research group, Cheng *et al.* [13,208] have generated mesopores by desilication through a hydrothermal treatment at 130°C. They used CTAB for protecting ferrierite from the undesirable destruction, which led to GIS or SOD phase appearance. Based on that, they established the adequate parameters of sodium hydroxide concentration, temperature, and time to get meso-microporous materials from low silica ferrierite in a one-step recrystallization procedure. They found that the obtaining of a microporous material with just the FER crystalline phase can be achieved using NaOH concentration between 0.25 and 0.5 M, temperatures between 130 and 150°C, and performing the hydrothermal process from 24 h to 72 h [13].

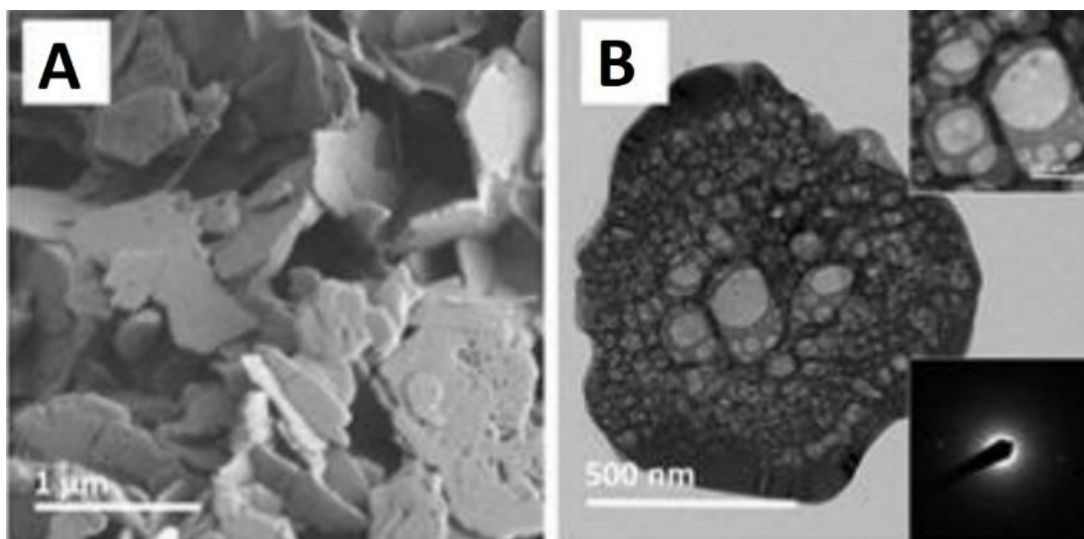


Figure 1-27 Meso-microporous material obtained through one-step recrystallization from low silica ferrierite. A. SEM micrograph. B. TEM micrograph (Source: Cheng *et al.*, 2018 [13])

Unlike the meso-microporous materials obtained from high silica ferrierite, which are composed of meso and microporous composites, the authors claimed the obtaining of a microporous material with parallelepiped-shaped mesopores embedded into the ferrierite crystals (Figure 1-27). These embedded mesopores, with a wide distribution of sizes lower than 50 nm, go along the 10-MR channels in the [001] direction, but they are occluded with respect to the external surface of the crystals [13]. This fact can limit the improvement expected from the shortened diffusion length of the reagents in these meso-microporous crystals. The difference in the mesoporous system topology can be explained by the recrystallization mechanism. This kind of porosity would be produced in accordance with the mechanism of crystal rearrangement in which the simultaneous steps of demineralizing together with migration and exchange of CTA<sup>+</sup> species, would direct the phenomenon of mesopore creation [117]. Until the writing of this document, these materials had not been tested as catalysts.

## 1.6 Zeolite Y

Zeolite Linde type Y is a less acidic zeolitic variant (Si/Al over 2.2 ) of the Faujasite (FAU) zeolitic framework (see Figure 1-28) [154,157]. Faujasite shows a cubic structure (space group:  $Fd3M$ ) formed by linking sodalite CBU connected through double 6-MR hexagonal prisms (see Figure 1-12) [15,110]. It allows the formation of a 3-D channel structure formed by four 12-MR windows (0.74 nm), which lead to a super-cage of 1.12 nm of diameter surrounded by ten sodalite units [14,15,119,132]. This framework allows the diffusion of voluminous molecules with a remarkable shape selectivity [14,15,154].

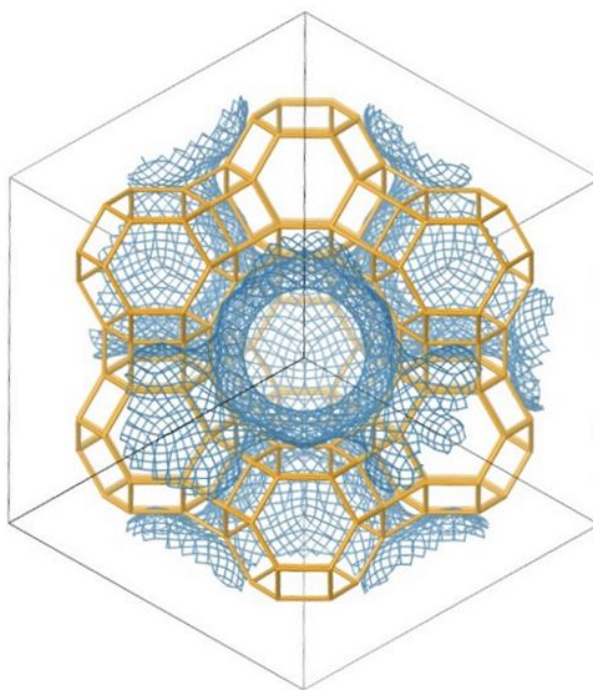


Figure 1-28 Faujasite (FAU) cubic structure (Source: Database of Zeolite Structures In: <http://www.iza-structure.org/databases/>).

A free-SDA hydrothermal synthesis commonly leads to the obtainment of this zeolitic material with a final Si/Al ratio of around 2.5, a composition of  $\text{NaAlO}_2 \cdot 2.5\text{SiO}_2$  and a cell a parameter of 24.72 Å [15,154,157,209,210]. This material is not usually used due to its low thermal stability [157]. However, higher silica faujasites could be obtained by different post-treatments and they were shown to keep their crystalline structure [154,157]. Considering that different dealumination procedures like acid extraction, isomorphous Al/Si substitution ionic exchanges, and thermal treatments have been applied on these materials to improve the faujasite thermal stability [157], the obtaining of an ultrastable zeolite Y (USY) was possible by steaming and a subsequent acid leaching [154]. It led to the improvement of the thermal stability and the enhancement of its catalytic performance in fluid catalytic cracking process [113,117,154].

Since the introduction of USY zeolite in the fluid catalytic cracking process decades ago, the consumption of more than 385 thousand tons per year of zeolite Y [211] represents the largest consumption of zeolite catalyst on the market [117]. Apart from its use in the FCC process, the zeolite Y is used to hydrodearomatization, toluene disproportionation, selective benzene hydroalkylation, hydroisomerization, among others [15,154].

Table 1-8 Commercial zeolites Y from Zeolist® (Source: Verboekend et al., 2016 [154])

CBV code	Si/Al	Cation	Unit cell size (Å)	Treatment
<b>100</b>	2.6	Na <sup>+</sup>	24.65	Fresly synthesized
<b>300</b>		NH <sub>4</sub> <sup>+</sup>	24.68	I.E. <sup>a</sup>
<b>400</b>		H <sup>+</sup>	24.50	I.E. + L.St. <sup>b</sup>
<b>500</b>		NH <sub>4</sub> <sup>+</sup>	24.53	I.E. + M.St. <sup>c</sup>
<b>600</b>		H <sup>+</sup>	24.35	I.E. + M.St.
<b>712</b>	6	NH <sub>4</sub> <sup>+</sup>	24.35	I.E. + M.St. + A.L. <sup>d</sup>
<b>720</b>	15	H <sup>+</sup>	24.28	I.E. + S.St. <sup>e</sup> + A.L.
<b>760</b>	30		24.24	
<b>780</b>	40		24.24	
<b>901</b>	40		24.24	I.E. + S.St. <sup>e</sup> + A.L. + H.T. <sup>f</sup>

<sup>a</sup> Ionic exchange; <sup>b</sup> Light or mildly Steaming; <sup>c</sup> Medium steaming; <sup>d</sup> Acid leaching

<sup>e</sup> Several steaming; <sup>f</sup> Heat treatment

The process for obtaining USY zeolite involves the steaming of low silica zeolite Y (Si/Al ~2.5), which leads to the formation of 5-50 nm defect domains removed in a subsequent acid leaching to form non-ordered intercrystalline mesopores [120,154]. Variations of operational conditions including temperature or time of dealumination treatment in the steaming process allow preparing zeolites with different aluminum amounts [154,157]. Typically, the acid leaching allows removing the amorphous materials produced during steaming, improving the crystallinity and thermal stability of the zeolite Y. As it can be observed in Table 1-8, this procedure leads to a change in the cell parameter proportional to the decrease of the aluminum amount [212]. Moreover, there are changes in silanol groups and Lewis acidity, as well as a pore volume increase, present as mesopores from 5 to 50 nm in the zeolite Y crystals [14,15]. However, some recent studies have shown that the presence of these mesopores does not improve the diffusivity of bulky molecules significantly [154,157]. For this reason, the improvement of diffusion in these materials is one of the most critical targets [117], which has been widely studied [154,213].

An excellent overview of the alternatives for preparing hierarchical faujasites was presented in the review article of Verboekend et al. [154]. In Figure 1-29 it is possible to see the different strategies reported to get hierarchical zeolites Y. Those different approaches will be shortly described in the next section with their advantages and disadvantages.



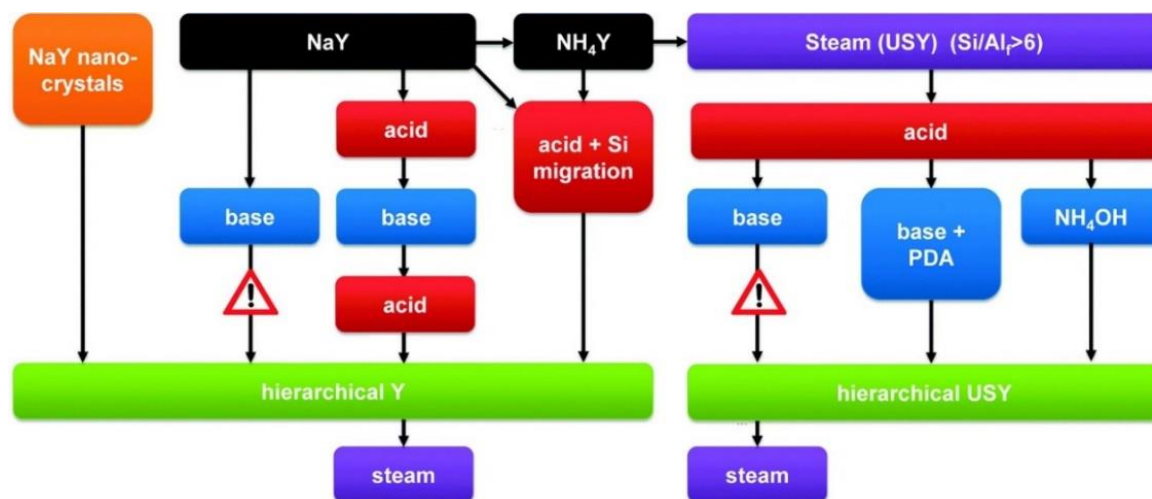


Figure 1-29 Synthesis of hierarchical zeolite Y using bottom-up and top-down strategies (source: Verboekend et al., 2016 [154]).

### 1.6.1 Meso-microporous materials from zeolite Y

The bottom-up strategies include the formation of NaY nanocrystals [154] or the synthesis simultaneously of meso and microporous phases from proto-zeolitic seeds and organic surfactants [145]. On one hand, the synthesis of nano-sized crystals is possible, by changing the hydrothermal conditions for avoiding aggregation, and giving rise to intercrystalline porosity. The use of nano-sized zeolite Y has been shown to improve the selectivity to medium range hydrocarbons in the FCC process [145]. Although it is a free SDA strategy, the limitation to only low silica zeolite Y, the low yields, and the subsequent presence of large amounts of amorphous species should be improved to be competitive [145,154].

On the other hand, the formation of both pore systems simultaneously was possible by using surfactants together with co-solvents and lead to mesopores with different shapes and sizes and microporous domains in the mesoporous walls [119,145]. The use of carbon aerogels as templates allows the generation of well-ordered interparticle mesopores in zeolite Y [120]. Using CTAB, tert-butanol and trimethylbenzene as SDA, it was possible to get one material with superior catalytic activity in the catalytic dehydration of 2-propanol [119]. The use of a silylated quaternary ammonium surfactant (N,N-dimethyl-N-octadecyl-(3-triethoxy-silylpropyl)ammonium) allows getting a zeolite Y micro-mesoporous material, which showed an improved catalytic performance in hydrodesulfurization reaction [119]. However, the expensive and non-environment-friendly organic SDA used in this strategy as well as the lower thermal stability of the synthesized materials than that of USY zeolite are critical drawbacks of this approach [154,164].

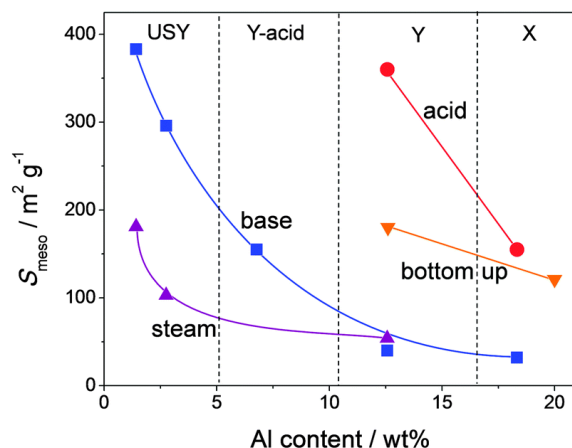


Figure 1-30 Mesopore surface of hierarchical faujasites prepared by different approaches (Source: Verboekend *et al.*, 2016 [154]).

Since the synthesis of an ultrastable zeolite Y (USY) by steaming and subsequent acid leaching of an  $\text{NH}_4$ -form of low silica zeolite [154], top-down strategies for the synthesis of hierarchical zeolites have been widely developed. As it was mentioned before (see section 1.4), the approach to form the mesopore system strongly depends on the desired Si/Al ratio, i.e. the aluminum content necessary for the desired application. In Figure 1-30 it is possible to see that bigger mesopore surfaces can be obtained in high silica faujasite zeolitic materials from destructive approaches [154].

On one hand, acid dealumination is not the usual process which is used to get hierarchical zeolites from faujasites. This treatment is usually used to remove undesired species from dealuminated faujasites obtained from the steaming procedure or to reduce aluminum amount before desilication processes [154,157,195]. Acid treatments of zeolite Y produce Si/Al gradients inside the crystals with Al-rich and Al-depleted zones [154]. More selective acid treatments have included acid treatments with ammonium hexafluorosilicate, silicon tetrachloride, and  $\text{H}_4\text{EDTA}$ , leading to stable frameworks with extended mesopore formation [120,154,157,214].

On the other hand, the desilication procedure on zeolite Y is very sensitive to the aluminum content (see Figure 1-30). So, as it is described by Verboekend *et al.* (see Figure 1-29), direct desilication in zeolites does not lead to the formation of hierarchical meso-microporous materials of faujasite structures [154]. In the case of low silica zeolite Y desilication, a high concentration of alkaline ( $\text{NaOH} > 3\text{M}$ ) and high temperatures are necessary [107,132]. Besides, desilication is inefficient because there are significant losses of microstructure without the formation of mesopores [154]. Si/Al ratio should be raised to carry out desilication processes [154]. In the case of high silica zeolites Y ( $\text{Si/Al} > 6$ ), which have already been hydrotreated, their high sensitivity to alkaline desilication leads to large pore formation and a fast amorphization. Alkaline treated high silica zeolite Y ( $\text{Si/Al}: 30$ ) showed better selectivity in kerosene gasoline-range hydrocarbons than parent zeolite in the hydrocracking of vacuum gas oil [154,215]. The same material showed a higher yield in branched-chain compounds in the hydroisomerization of hexadecane [15,216].

As observed in Figure 1-29, consecutive steps of steaming, acid leaching, and desilication have been proposed to get hierarchical zeolites Y [107,154]. Acid pretreatments with citric acid, H<sub>4</sub>EDTA, HCl usually preceded desilication treatments [119,154]. These treatments have allowed working with low silica zeolite Y because they generate Al-depleted zones prone to desilication [119,195]. Alkaline treatments have been done with mineral bases as NaOH or organic ones as TMAOH or TPAOH [119,214]. However, these materials have not significantly improved the catalytic performance of the zeolite Y [119,154]. Additional mild acid treatments were done to get better crystallinity and acidity properties [214]. These materials showed to increase by 55% the catalytic activity on the alkylation of benzyl alcohol with toluene [119]. Other approaches as the depolymerization-recrystallization using glycerol and CTAB have led to the formation of a mixture of zeolitic nanocrystals and an amorphous mesoporous phase [119,217]

As it was mentioned before, the use of some surfactants or tetraalkylammonium hydroxides can help to control the desilication process [143,154,156]. The generalities about the recrystallization are described in section 1.4.2. The development of the recrystallization of zeolite Y materials will be described in the next section.

### 1.6.2 Zeolite Y recrystallization

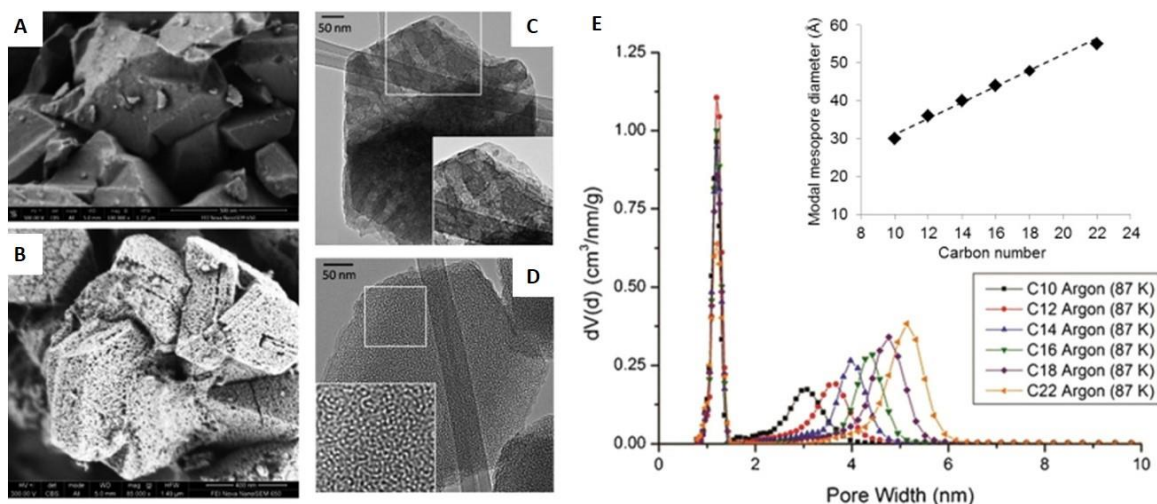


Figure 1-31 Results reported by García-Martínez for the H-Y-15 recrystallization. Field Emission-SEM micrographs of (A) parent zeolite Y (CBV 720 Si/Al:15) and (B) recrystallized material. TEM micrographs of (C) parent zeolite Y (CBV 720 Si/Al:15) and (D) recrystallized material. NLDFT pore size distribution curves for the recrystallized material obtained with different trimethylalkylammonium-based surfactants (C10-C22) (Source: Sachse *et al.*, 2017[145])

The process for the high silica zeolite Y recrystallization was patented and reported by García-Martínez *et al.* [218,219]. The one-step recrystallization procedure was done on steamed-acid leaching zeolite Y with Si/Al around 15 (Zeolyst CBV 720®) with a solution of CTAB 0.37M and NH<sub>4</sub>OH or TMAOH 0.09M. Treatment was done at 150°C for 10-20h.

According to the claim of García-Martínez et al. [119,213], the introduction of a mesoporous ordered system (see Figure 1-31-B and D) occurred according to the crystal-rearrangement mechanism (Figure 1-23). In an independent work of our laboratory, Fajula *et al.* [155,165] corroborated the fact that the recrystallization led to the disappearance of initial larger mesopores that commercial CBV720® zeolite exhibits (see Figure 1-31-A and C). They showed that these materials have a complicated relationship between the micro and mesoporous domains, which is strongly dependent on the concentration of the base [220]. Some studies have shown that organic bases such as TMAOH improved the crystallinity of the obtained zeolitic materials [14,15,154]. The recrystallized zeolite materials prepared using CTAB (C16) as trimethylalkylammonium-based surfactant presented a MCM-type ordered 2D hexagonal organization of small mesopores with a diameter of around 4 nm [155,219]. García-Martínez et al. found that the pore size of the mesostructured system is proportional to the number of carbons of the alkyl chain of the trimethylalkylammonium-based surfactant (see Figure 1-31-E) [145]. The micro-mesoporous material obtained by this process from CBV 720 (Si/Al:15) was scaled up in a commercial zeolite manufacturing and successfully used in one refinery [119]. Taking into account that the use of expensive organic surfactants which are lost after their removal by calcination represents the main disadvantage, the use of a recoverable structuring agent can be a breakthrough alternative. In our laboratory, Chal et al. [14] proposed the use of polyether amines as thermosensitive recyclable SDA to carry out the one-step recrystallization procedure. The removal of those recyclable SDA after hydrothermal treatment allowed to use the SDA in at least four recrystallization cycles.

These meso-microporous materials have shown improved catalytic performance in different reactions. Although there was just a slight improvement in the catalytic activity in the cracking of triisopropylbenzene compared to parent zeolite (CBV 720®) [119], the selectivity in 1,3-diisopropylbenzene was increased, and deactivation by coke formation was slowed down [119]. This material also showed an improved selectivity in medium-range hydrocarbons than parent material in VGO hydrotreatment [219]. More recently, Vaugon *et al.* [15,216] found that an increase in mesopore volume architecture of this material improved the selectivity to isomers fraction in hydrocracking of n-hexadecane and of squalene.

In the work developed in our laboratory, Chal et al. [14] made the optimization of one-step recrystallization parameters for the zeolite Y CBV 720 (Si/Al: 15) and CBV 740 (Si/Al: 21), as well as the evaluation of the evolution of the textural properties as a function of time in these processes (see Figure 1-32). On the other hand, Vaugon et al. [15] optimized the one-step recrystallization parameters for the zeolite Y CBV 760 (Si/Al: 30) and evaluated the evolution of the textural properties as a function of time of this process (see Figure 1-33). In these one-step recrystallization processes, at least four different stages were distinguished. In the first stage, the dissolution of the zeolite structure occurs together with the filling by the redeposited dissolved species of the mesopores already present in the material. It is followed by the second stage, when a wormlike mesoporous structure is created by dissolution-reprecipitation. After it, the third stage corresponds to the growth of a mesostructured structure while the microporous structure is destroyed, it is characterized

by the relation  $V_{\text{micro}} \text{ lost} = V_{\text{meso}} \text{ created}$ , and it ultimately can lead to a 100% organized mesoporous material after several hours. Finally, during the fourth stage, an anarchic dissolution was observed, leading to bigger mesopores and the loss of any structure. The evolution of each stage depends on the zeolite aluminum content and the presence of the mesopores produced during the previous steaming. So, during the recrystallization with CTAB and TMAOH 0.09M of the zeolite Y with Si/Al of 15 (Figure 1-32-A), it took at least eight hours to start the wormlike mesopore formation, and a loss of microporosity was not observed in the first 24 hours. In contrast, during the recrystallization with CTAB and TMAOH 0.045M of the zeolites Y with Si/Al of 21 (Figure 1-32-B) and Si/Al of 30 (Figure 1-33), it took less than one hour to start the wormlike mesopore formation, and an important loss of microporosity was observed just after four hours [14,15].

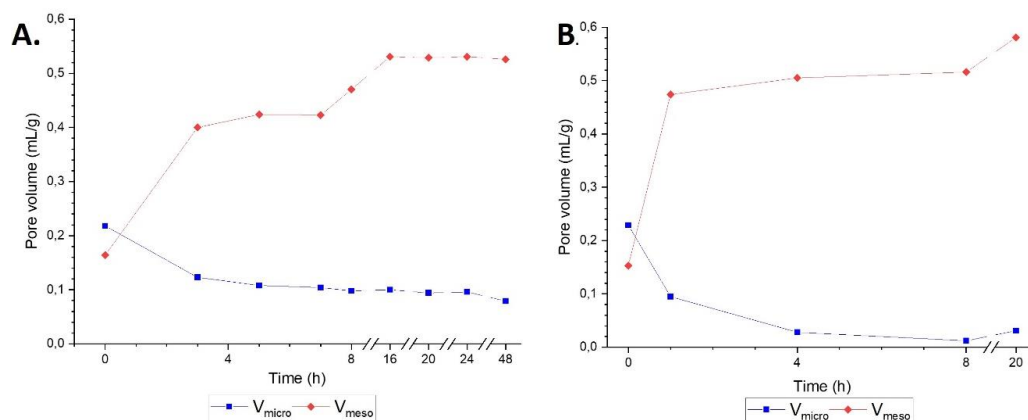


Figure 1-32 Evolution of the micropore and mesopore volumes of the zeolites Y (A) CBV 720 (Si/Al:15) and (B) CBV 740 (Si/Al:21) during the one-step recrystallization process [14].

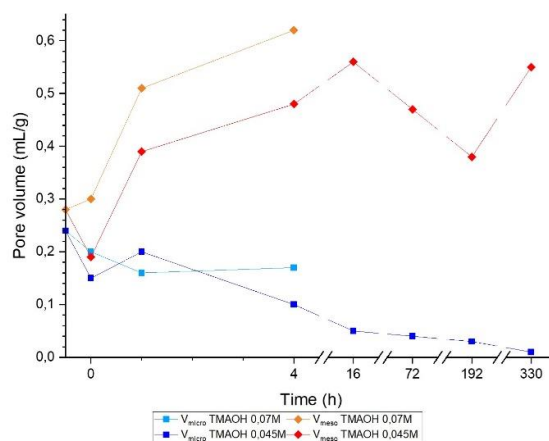


Figure 1-33 Evolution of the micropore and mesopore volume of the zeolite Y CBV 760 (Si/Al:30) during the one-step recrystallization process [15].

The recrystallization was done on low silica zeolite Y (as-synthesized) as well, but a previous acid leaching step was necessary before the hydrothermal treatment [14,221]. García-Martínez *et al.* [221] claimed that acid washing pretreatment with citric acid of the

zeolite Y CBV 500 helped to carry out the recrystallization of the material with ammonium hydroxide. The obtained material presented a considerable mesoporosity keeping part of the microporosity, but it was not homogeneously distributed as it was described for high silica zeolites Y. In the work of Chal et al. [14] the optimization of one-step recrystallization parameters was done for the zeolite Y CBV 600 (Si/Al: 3.4) as well as the evaluation of the evolution of the textural properties as a function of time of the process (see Figure 1-34). It is essential to notice that the commercial supplier already steamed this material (see Table 1-8). As it is observed in Figure 1-34, it was possible to get a significant amount of mesopores just after 330 h of hydrothermal treatment. The microporosity was non-significantly lost during this hydrothermal treatment.

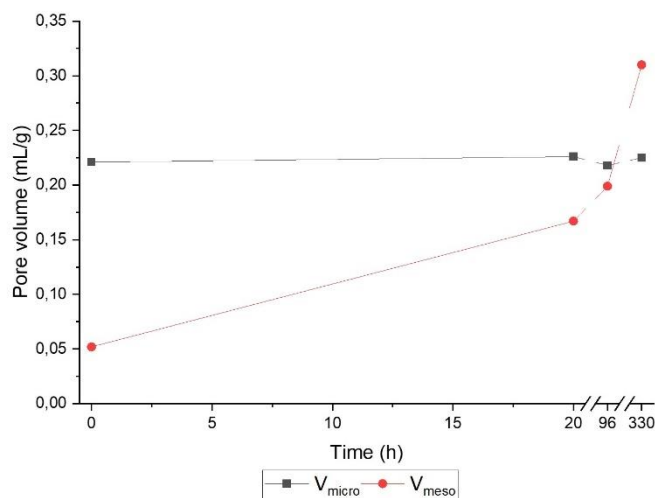


Figure 1-34 Evolution of the micropore and mesopore volumes of the zeolite Y CBV 600 (Si/Al: 3.4) during the one-step recrystallization process [14].

## 1.7 Justification and improvement strategy

Considering that one of the main problems of the use of zeolitic materials is the diffusion limitation of large molecules, the underuse of zeolite crystals is expected in the reaction of skeletal isomerization of fatty acids and derivatives. It can lead to lower yields and a fast deactivation of the catalytic materials. The strategy proposed here to improve yield and catalyst lifetime in skeletal isomerization of fatty acid methyl esters is the use of zeolitic materials with meso-microporous systems as catalysts.

In this work, two zeolites with different frameworks were used. The first one is the ferrierite, which has a small (0.35 x 0.48 nm) and medium (0.42 x 0.54 nm) pore size (see section 1.5), which presented the best catalytic performance in the isomerization of fatty acids (see section 1.2.2). The second zeolitic material selected as catalyst was the zeolite Y, which has larger pores (0.74 x 0.74 nm) (see section 1.6), which has been extensively studied for the isomerization of large hydrocarbons for FCC process. A new mesopore system was

created in each of them through one-step recrystallization. It consisted in a hydrothermal treatment with a base and Cetyl Trimethyl Ammonium Bromide (CTAB) as mesostructure-directing agent. It allowed us to form meso-microporous materials used as catalysts. We evaluated if this new porosity helped to improve the diffusion of methyl esters inside the crystalline network. We evaluated the catalytic performance of these materials in methyl oleate isomerization in batch and continuous flow experiments and we compared the results using recrystallized materials and parent zeolites, evaluating the effect of the presence of the mesopores in ferrierite and high and low silica zeolite Y.

## 1.8 Objectives

The main objective of this work was the evaluation of the catalytic performance of meso-microporous zeolitic materials in the reaction of skeletal isomerization of methyl oleate.

The specific objectives were:

- Synthesis of micro-mesoporous zeolitic materials from ferrierite and zeolite Y.
- Evaluation of the micro-mesoporous zeolitic materials as catalysts in the methyl oleate isomerization reaction performed in batch and continuous flow conditions.
- Study of the cold flow properties of methyl oleate isomerization products.





## 2. Experimental methodology

### 2.1 Catalytic materials preparation

In this study, two kinds of materials (with & without secondary mesopore system) were obtained from two kinds of zeolites (Ferrierite & Zeolite Y). On one hand, recrystallization treatments of the zeolites were performed by hydrothermal treatment using a base (demineralizing agent) and a surfactant (CTAB) followed by an ionic exchange with  $\text{NH}_4\text{NO}_3$  1.0 M (when it was necessary) and calcination at  $550^\circ\text{C}$ . On the other hand, parent zeolites were treated through ionic exchange (when it was necessary) with  $\text{NH}_4\text{NO}_3$  1.0 M followed by calcination at  $550^\circ\text{C}$ . These materials were tested on isomerization reaction of methyl oleate and palm biodiesel, as well as, in the hydroisomerization of methyl palmitate (after Pt wetness impregnation).

#### 2.1.1 Recrystallization of ferrierite

In a typical synthesis, according to Cheng *et al.* [13] methodology, 4.89 g of Na, K –Ferrierite (HSZ-720 KOA® Tosoh Si/Al: 9.2), and 2.49 g of CTAB were mixed with 150 mL of 0.2 M NaOH solution and the mixture was stirred for 30 min at room temperature. The suspension was hydrothermally treated at  $130^\circ\text{C}$  in a Teflon-lined stainless autoclave for 72 h. After cooling the autoclave in an ice-water bath until room temperature, the solid was filtered under vacuum and washed with deionized water repeatedly until pH 7. Then, the product was dried overnight at  $80^\circ\text{C}$ , it was milled, and it was ion-exchanged in 150 mL of a 1.0 M  $\text{NH}_4\text{NO}_3$  solution for six hours at room temperature. Then the solid was filtered under vacuum and washed with deionized water repeatedly until pH 7 and drying under the at same conditions. Later, the ferrierite  $\text{NH}_4$ -form with CTAB sample was calcined in air flow (200 mL/min) in a tubular furnace with the heating program set as follow: from room temperature to  $550^\circ\text{C}$  with a heating ramp of  $120^\circ\text{C}/\text{h}$  and the plateau was of sixteen hours. H-form recrystallized ferrierite (H-FER-REC) (mass yield: 65.4%) was obtained. On the other hand, steps of ion-exchange, drying, and calcination were performed in the same conditions directly on Na, K –Ferrierite to get the H-form of parent zeolite (H-FER-PAR) or just mentioned hereafter as parent ferrierite.

## 2.1.2 Recrystallization of zeolites Y

Two different zeolite Y samples of Si/Al ratios of 6.5 and 30 were used as precursors. They were recrystallized in the presence of CTAB as the structure-directing agent and tetramethylammonium hydroxide (TMAOH) as demineralizing agent. Recrystallization conditions were summarized in Table 2-1. In each experiment, zeolite Y was mixed with CTAB in 250 ml Erlenmeyer. After it, the solution of TMAOH was added, and the mixture was kept stirring at 500 rpm for 20 min. The mixture was added to one metallic autoclave equipped with a polytetrafluoroethylene vessel of 220 mL. The autoclave is closed and heated at 150°C for the stipulated procedure time. After it, recrystallization was quenched using an ice-water bath; the solid was filtered and washed with water until neutral pH. The solid was dried overnight at 80°C. Then, it was milled and calcined under airflow (200mL/min) with the following heating program: from room temperature to 550°C at 120°C/h, held for 16h. It allowed to get the recrystallized zeolite Y based materials (abbreviated as: H-Y-##-REC-XXh; ##: nominal Si/Al ratio; XX: recrystallization time). On the other hand, steps of calcination were performed in the same conditions directly on commercial zeolites to get the H-form of parent ones (H-Y-##-PAR; ##: nominal Si/Al ratio).

Table 2-1 Experimental conditions of recrystallization procedures on zeolites Y with different Si/Al ratios

Zeolite	Si/Al ratio	Zeolite amount (g)	CTAB amount (g)	Solution TMAOH		Hydrothermal treatment time (h)	Mass yield (%)
				Amount (mL)	Conc. (M)		
CBV 712 (NH <sub>4</sub> -form)	6.0	3.06	1.52	91.7	0.09	40	77.6
						96	63.2
						330	76.4
CBV 760 (H-form)	30	5.01	2.49	150	0.07	1	76.9

## 2.1.3 Catalyst shaping & impregnation

The catalytic materials previously prepared were shaped into particles of the desired size by compressing the powder under 196 Mpa in a laboratory pellet press, crushing into an agate mortar, and sieving into consecutive test sieves No. 40 (425 µm) and No. 60 (250 µm). The solid collected into both sieves was used in catalytic tests in continuous flow conditions while the bottoms (particle size <250 µm) were used in catalytic test in batch conditions.

In order to do hydroisomerization tests of methyl palmitate (see chapter 7), the bifunctional metal/acid catalytic materials were obtained by wetness impregnation with H<sub>2</sub>PtCl<sub>6</sub> (Pt 0.5%wt). Each zeolitic material was put into an oven at 80°C overnight. The dried powder was weighted into a glass petri dish, and it was put into a desiccator in which there was a saturated solution of NaCl. According to the amount of zeolite, one milliliter per zeolite gram of a solution of hexachloroplatinic acid hexahydrate (H<sub>2</sub>PtCl<sub>6</sub>·6H<sub>2</sub>O) of 0.0125 g/mL was

prepared. This solution was added drop by drop homogeneously distributed on the powder surface. The desiccator was sealed, and each impregnated zeolite material was kept in it for three hours and 30 minutes. After it, the powder was recovered and put into a round flask. It was then put in a rotary evaporator at room temperature and pressure overnight. The day after, the powder was milled and calcined under airflow (200mL/min) with the following heating program: from room temperature to 550°C at 120°C/h, followed by a plateau at 550°C for 16h.

## 2.2 Catalytic materials characterization

### 2.2.1 Structural and textural characterization

According to Cheng *et al.* characterization methodology [13], the crystal structure was analyzed by powder X-Ray diffraction (XRD). The surface area and pore volumes were calculated from the analysis of the adsorption-desorption isotherms of nitrogen. The compositions of the samples (Si/Al) were determined by energy-dispersive X-ray (EDS). Particle size and morphology of materials were observed on a scanning electronic microscopy (SEM). Transmission electron microscopy (TEM) determined the distribution, size, and orientation of the intracrystalline mesopores.  $^{27}\text{Al}$  MAS NMR analysis was done to study the local environments of aluminum atoms.

- **X-Ray diffraction (XRD)**

Crystal structure was analyzed by powder X-Ray diffraction (XRD) on a Bruker AXS D8 ADVANCE diffractometer with Bragg- Brentano geometry and  $\text{CuK}\alpha$  radiation ( $\lambda=0.15406$  nm) as incident beam and 1D solid detector LYNX EYES®. Data were recorded by continuous scanning in the range of  $2\theta$  values of  $0.5 - 6^\circ$  and  $4 - 50^\circ$  for analyzing the ordered mesoporous structures and crystalline zeolite structures with an angular step of  $0.0197^\circ$  and a counting time of 0.2 s per step, respectively.

- **Manometry of nitrogen adsorption**

Surface area and pore volumes were calculated from the analysis of the adsorption-desorption isotherms of nitrogen recorded at 77 K using a Micromeritics TriStar 3000. Prior to the isotherm acquisition, the H-form samples were degassed under vacuum at 250°C for 12 h.

The total surface area was determined by the Brunauer-Emmett-Teller (BET) method. The external surface area was calculated using the  $\alpha_s$  plot method applied to the desorption branch of the isotherm at  $P/P_0$  of 0.5. Mesopore surface plus the external surface area was calculated using the  $\alpha_s$  plot method applied to the fraction of the isotherm below  $P/P_0$  of 0.3. Mesopore surface area was calculated as the difference between both values. The micropore surface was calculated as the difference between total surface area and mesopore surface + external surface area. The micropore volume was calculated using the

$\alpha_s$  plot method applied to the fraction of the isotherm below  $P/P_0$  of 0.3. The volume of micropores plus intracrystalline mesopores was calculated using the  $\alpha_s$  plot method applied to the desorption branch of the isotherm at  $P/P_0$  of 0.5. The total pore volume (including micropore volume, the volume of intracrystalline mesopores, and volume of intercrystalline mesopores) was calculated from the total amount adsorbed at a relative pressure  $P/P_0$  of 0.95.

- **Electronic microscopy analysis**

The compositions of the samples were determined by elemental analysis using the energy-dispersive X-ray (EDS) analysis method on a SEM FEI QUANTA 200F with accelerating voltage of 15 kV (PT MEA-UM). The particle size and morphology of materials were observed by using a SEM HITACHI 4800S (PT IEM) with accelerating voltage of 5 kV. The distribution, size and orientation of the intracrystalline mesopores were determined by Transmission Electron Microscopy (TEM). The samples were embedded in the resin Acrylique LR White® cut with a ultramicrotome in slices of 50 nm of thickness and deposited on a carbon coated formvar 200 mesh copper grid. TEM observations were done using a JEOL 1200-1400 Plus EXII electron microscope with accelerating voltage of 100 kV (PT MEA -UM).

- **Magic Angle Spinning Nuclear Magnetic Resonance of  $^{29}\text{Si}$  ( $^{29}\text{Si}$  MAS NMR)**

The Magic Angle Spinning Nuclear Magnetic Resonance of  $^{29}\text{Si}$  ( $^{29}\text{Si}$  MAS NMR) analysis of the zeolitic materials was done on a 300 MHz Varian VNMRS300 spectrometer (UM) using a Varian T3 MAS (Magic Angle Spinning) probe with 7.5 mm  $\text{ZrO}_2$  rotors.  $^{29}\text{Si}$  MAS NMR spectra have been acquired using the quantitative Single Pulse technique with  $^1\text{H}$  decoupling with a recycle delay of 60 s, a  $\pi/6$  pulse of 2  $\mu\text{s}$ , and a spinning rate of 5 kHz. Q8M8H (octakis(dimethylsiloxo)octasilsesquioxane) has been used as a secondary reference (left peak at -2.25 ppm). The width of the spectral window is 50 kHz and the line broadening is 50 Hz.

- **Magic Angle Spinning Nuclear Magnetic Resonance of  $^{27}\text{Al}$  ( $^{27}\text{Al}$  MAS NMR)**

The Magic Angle Spinning Nuclear Magnetic Resonance of  $^{27}\text{Al}$  ( $^{27}\text{Al}$  MAS NMR) analysis of the zeolitic materials was done on a 600 MHz Varian VNMRS® spectrometer (UM) using a Varian T3 MAS (Magic Angle Spinning) probe with 7.5 mm  $\text{ZrO}_2$  rotors.  $^{27}\text{Al}$  MAS NMR spectra were acquired using the quantitative Single Pulse technique with  $^1\text{H}$  decoupling with a recycle delay of 1 s, a  $\pi/6$  pulse of 2  $\mu\text{s}$ , and a spinning rate of 22 kHz. Aluminum nitrate has been used as a secondary reference (peak at 0.0 ppm). The width of the spectral window is 192 kHz and the line broadening is 50 Hz.

### 2.2.2 Acidic sites characterization

Acidic sites characterization was done by ammonia temperature-programmed desorption (TPD-NH<sub>3</sub>) for the quantification of the total number of acidic sites and by the infrared analysis of adsorption/desorption of acetonitrile for the discrimination of the acidic sites.

- **Ammonia temperature-programmed desorption (TPD-NH<sub>3</sub>)**

Ammonia temperature-programmed desorption (TPD-NH<sub>3</sub>) was performed using an AutoChem II® apparatus from Micromeritics. The solids (30–50 mg) were calcined in flowing air up to 550°C (10°C/min) cooled to 100°C and saturated with ammonia (10 mL/min flow of a mixture of 95% He, 5% NH<sub>3</sub>, 45 min). The physisorbed base was swept in He flow (50 mL/min, 2 h) while chemisorbed ammonia was desorbed by increasing the temperature (10 °C/min) up to 700°C. The amount of base adsorbed was quantified by a calibrated Thermal Conductivity Cell.

- **Infrared analysis of adsorption/desorption of pyridine**

Infrared (IR) spectra were recorded on a Bruker EQUINOX 55 spectrometer with DTGS detector in transmission mode, with a resolution of 2 cm<sup>-1</sup> over 64 scans in the range 400-4500 cm<sup>-1</sup>. The band areas were computed by the Fityk software upon assuming the Gaussian function for IR bands, and then were normalized to the optical path. All the IR analyses were performed at room temperature. The influence of atmospheric CO<sub>2</sub> was reduced by flushing the spectrometer with dry nitrogen (Air Liquide, N<sub>2</sub> > 99.9%) during the analysis. The infrared analysis of adsorbed CD<sub>3</sub>CN (Aldrich, 99.8% D atoms) was performed in a quartz low-pressure transmission cell with KBr windows. The catalyst was pressed into a self-supporting wafer (5000 kg·cm<sup>-2</sup>, 30 mg, 18 mm in diameter) and then pre-treated in the IR cell under a dynamic vacuum (10<sup>-5</sup> mbar) at 250°C for 16 h before cooling down to room temperature. Deuterated acetonitrile was then adsorbed at an equilibrium pressure of 1.0 mbar on the catalyst. Afterward, it was desorbed for three hours under a dynamic vacuum in order to remove the physisorbed acetonitrile. Four desorption temperatures (25, 50, 100, and 150°C) were studied by increasing the catalyst wafer temperature for 15 min under a dynamic vacuum. After each desorption treatment, the catalyst was cooled down to room temperature before the IR measurement. The molar density of acid sites was calculated using Beer-Lambert law and extinction coefficients of 3.60 cm·μmol<sup>-1</sup> to Lewis acidic sites (2321 cm<sup>-1</sup>) and 2.05 cm·μmol<sup>-1</sup> to Brønsted acidic sites (2306 - 2275 cm<sup>-1</sup>)[222].

### 2.2.3 Spent catalytic material characterization

Each spent catalytic material saved (0.5 g) was washed with 10 mL of acetone, centrifuged and dried at 60°C. Then, a 24-hour Soxhlet treatment with dichloromethane was done. The obtained solids were dried and analyzed by XRD (see section 2.2.1), TGA, and <sup>13</sup>C CP MAS NMR.

On one hand, the total coke amount of each sample was determined by thermogravimetric analyses using the TGA analyzer (PerkinElmer TGA 4000). The analyses were done from 40 °C to 900 °C with a ramp of 5 °C/min in airflow (60 mL/min). The coke amount was calculated from TGA results as the sum of mass losses from 250 to 700°C.

On the other hand, the  $^{13}\text{C}$  Cross Polarization Magic Angle Spinning (CP MAS) NMR spectra were taken on a 300 MHz Varian VNMR300® spectrometer ("Wide Bore" magnet at 7.05 Tesla). A Varian T3 MAS probe was used with 3.2 mm zirconia rotors and a spinning speed of 12 kHz. The spectra were acquired using the non-quantitative CPMAS technique with  $^1\text{H}$  decoupling with a recycle delay of 3 s, a  $\pi/2$  pulse of 5  $\mu\text{s}$  and a contact time of 0.5 ms. The width of the spectral window is 50 kHz, the acquisition time is 40 ms and the line broadening is 50 Hz. Adamantane has been used as a secondary reference (left peak at 38.5 ppm).

## 2.3 Catalytic performance tests

### 2.3.1 Reagents and materials

Reagent grade oleic acid (91.6 %wt. C18:1; 3.7 % wt. C18:2; 2.6 % wt. C18:0; 1.4 % wt. C16:0; 0.7 % wt. others), palm oil, sulfuric acid 98% Heptane, methyl arachidate, and methanol were purchased from Sigma-Aldrich.

Methyl Oleate was synthesized by acid esterification by reflux at 60°C for 3h with  $\text{H}_2\text{SO}_4$  at 2% and oleic acid – methanol molar ratio of 6:1. Palm biodiesel was prepared from palm oil through basic transesterification by reflux at 60°C for 1h with NaOH at 0.5% and Palm Oil – methanol molar ratio of 6:1. In both cases, the product was purified through consecutive washings with water at 40°C followed by vacuum distillation at 60°C.

### 2.3.2 Batch conditions

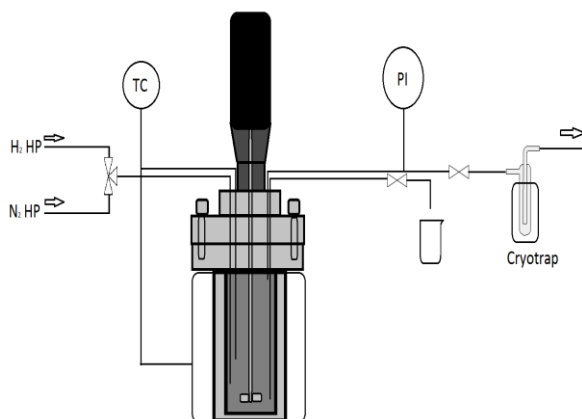


Figure 2-1 Scheme of the batch reactor

Evaluation of catalytic materials on isomerization and hydroisomerization reactions in batch conditions was done in a 200 mL flange autoclave shown in Figure 2-1. For each reaction, parameters of temperatures, pressures, and reaction times were evaluated.

The isomerization tests of methyl oleate in batch conditions were performed with a catalyst charge of 5wt.%, under N<sub>2</sub> atmosphere, working at temperatures between 260 and 285°C and pressures between 2.0 and 4.0 MPa. In a typical experiment, 50 g of methyl oleate and 2.5 g of the catalytic material of particle size under <250 µm (see section 2.1) were mixed and put into a 200 mL flange autoclave. The system was purged with nitrogen flow during 30 s thrice, and the pressure was adjusted to near 1.0 MPa. The reactor was heated until obtaining the desired temperature, after which the pressure was adjusted to the desired value. This is considered as the starting point of the reaction, which is carried out for 8 hours. After the reaction, the system was cooled down until room temperature, and the gas exit valve was opened to collect gas samples in a cryotrap. After opening the reactor, the reaction mixture was taken out and filtered at room temperature. The liquid extract was sent to GC analyses. Finally, 0.5 g of spent catalytic material was washed with 10 mL acetone, centrifuged and dried at 60°C. A second step of washing by Soxhlet extraction during 24 hours with dichloromethane was performed. These solids were dried and analyzed by TGA and CP MAS <sup>13</sup>C NMR (see section 2.2.3). The liquid phase extracted from both acetone and dichloromethane, were analyzed by GC-MS and MALDI-TOF (see section 2.4).

The hydroisomerization tests were done in a mixture of nitrogen-hydrogen as an atmosphere. In a typical experiment, catalytic material (2.5 g particle size <250µm) was first added to the reactor. The reactor was then closed and sealed. It was purged with a flow of H<sub>2</sub> during 30 s thrice. Then, the catalyst is pre-treated by heating the reactor at 285°C during 8h. The reactor was then allowed to cool down to room temperature. The day after, the reactor was opened, the methyl ester (50g) (preheated at 50°C) was added, and the reactor was closed carefully. It was purged with hydrogen flow during 30s thrice, and after this, it was partially depressurized until a pressure below 10 bar is attained. The reactor was then heated until the desired temperature, and then pressure and atmosphere composition were fixed according to the experiment. This is considered as the starting point of the reaction. After the reaction, the system was cooled down to 50°C. After the stirring was stopped, the reactor was cooled down to room temperature, and the exit valve was open to collect gas samples in cryotrap. Once opened, the reactor was heated at 50°C to liquefy the reaction mixture, which was then taken out and filtered at the same temperature. Finally, the spent catalytic material and reaction products were saved for posterior analysis.

### 2.3.3 Continuous flow conditions

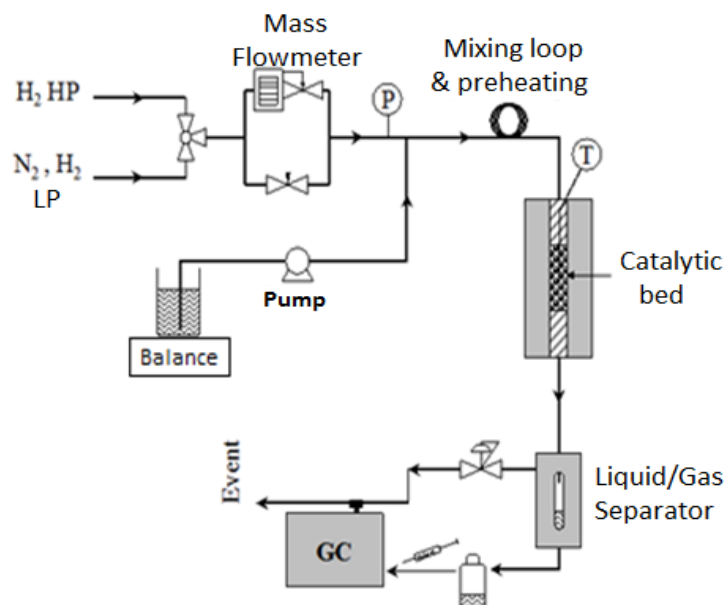


Figure 2-2 Scheme of downstream fixed-bed continuous flow reactor (Source: Vaugon, 2017 [15])

The isomerization of methyl oleate in continuous flow conditions was performed in a downstream fixed-bed continuous flow reactor (6 mm ID) (see Figure 2-2) using 1–1.3 g of catalytic material (see section 2.1) with particle size ranging from 250 to 425  $\mu\text{m}$  prepared by the method described above, and mixed with quartz with particle size ranging from 150 to 250  $\mu\text{m}$ . The quantity of quartz is adjusted to keep a total volume of 3.7  $\text{cm}^3$  of the catalytic bed constant. The catalyst was activated in situ under a hydrogen flow of 50 mL/min at 400°C for 18h (heating rate: 120°C/h). The reaction procedure was adapted from Kenmogne et al. [223]. Methyl oleate was pumped at a flow rate of 4.0 mL/h, allowing a WHSV of 3.5  $\text{h}^{-1}$  in the reactor and mixed with the carrier gas ( $\text{N}_2$ ) at the desired pressure (between 1.0 and 4.0 MPa). The reaction temperature was varied between 260 and 325°C within the course of one reaction. Lighter gaseous reaction products were analyzed online by GC, while liquid heavier products were collected periodically to be analyzed separately (see section 2.4). At the end of an experiment, the reactor was depressurized under nitrogen flow, and the temperature decreased to room temperature. When the experiment took more than one day, the flow of raw material was reduced, allowing a WHSV of 1.2  $\text{h}^{-1}$  during the nights. The day after, the flow was normalized to previous conditions, and the new temperature condition was fixed. This procedure was repeated each day during the course of a typical experiment (see Figure 2-3).



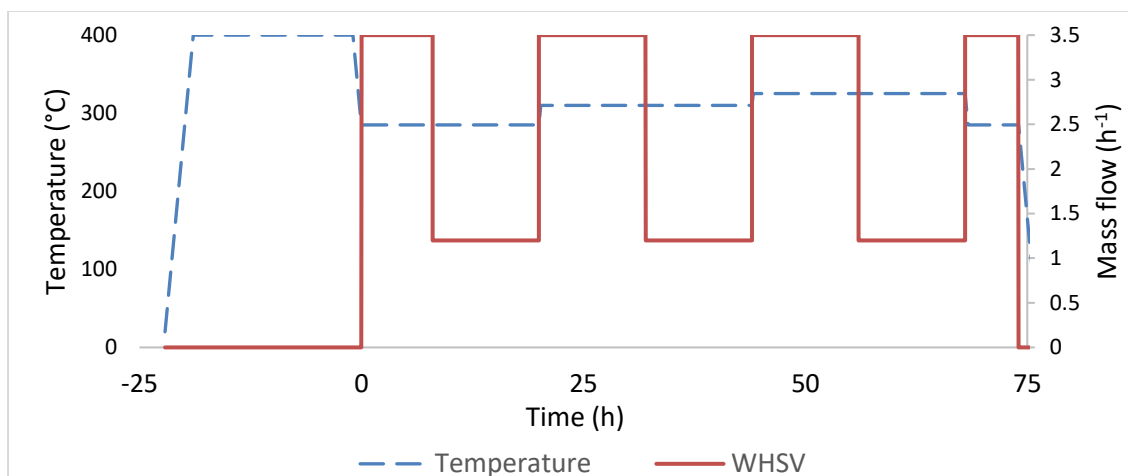


Figure 2-3 Conditions of temperature and mass flow in the continuous flow experiment.

## 2.4 Reaction products characterization

### 2.4.1 Gas chromatography analysis

The products of the methyl oleate isomerization are a complex mixture of compounds in gas and liquid phases due to the complexity of the reaction (see Figure 1-7).

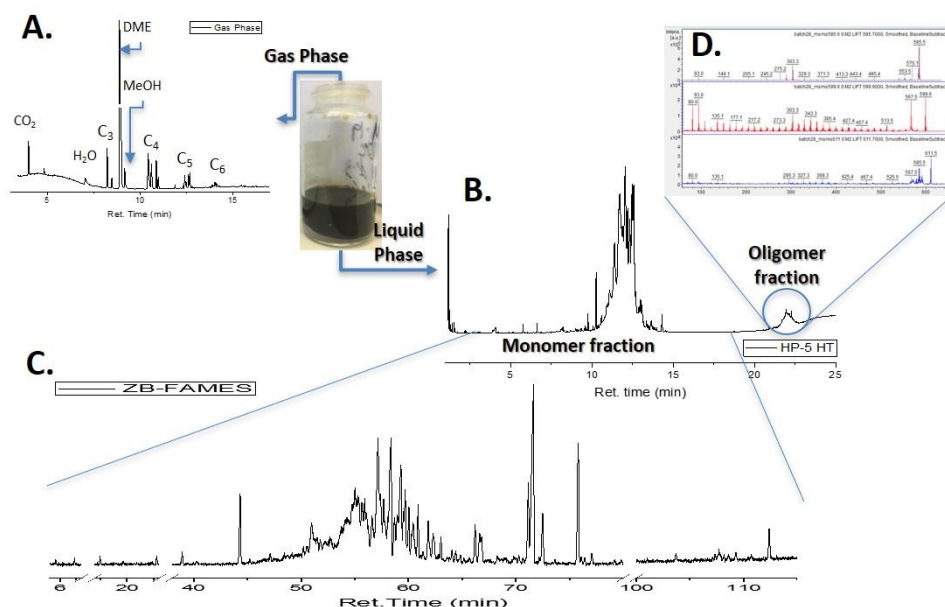


Figure 2-4 Gas Chromatography analysis of the different fractions of the products of the methyl oleate isomerization. A. Chromatogram of the gas fraction. B. Chromatogram of liquid fraction including oligomer products C. Chromatogram of liquid fraction including monomer products D. MS-MS analysis of oligomer products.

The gas fraction products of methyl oleate isomerization (see Figure 2-4-A) was analyzed using a gas chromatograph GC equipped with an FID detector (Agilent 7890A). The chromatographic separation was performed on a Rt-Q-Bond Plot capillary column (30m x 0.25 mm x 8  $\mu$ m) coupled in series with a HP-5-ms capillary column (30m x 0.25 mm x 0.25  $\mu$ m). A linear velocity of 31 cm s<sup>-1</sup> was chosen for the Hydrogen carrier gas. The injector was set at 250°C, with a split ratio of 10. The oven temperature program was set as follows: a plateau at 40°C is held for 2.0 min; then heated to 80°C with a rate of 15°C/min, then heated to 250°C with a rate of 20°C/min and held for 7.0 min, and finally increased to 255°C at 10°C/min and held for 4.0 min.

The liquid fraction was analyzed through two different GC methodologies. For both analyses, samples were prepared by mixing 10  $\mu$ L of the liquid phase products with 50  $\mu$ L of internal standard solution (methyl arachidate) and diluted to 1.0 mL of heptane. 1.0  $\mu$ L of that mixture was injected. In the first type of GC analysis allowed determining the oligomers amount in the samples (see Figure 2-4-B). The products were analyzed using a GC (Varian 3900) equipped with a HP-5HT® capillary column (15 m x 0.32 mm x 0.10  $\mu$ m). The carrier gas flow (H<sub>2</sub>) was set at 2.6 mL/min. The injector was set at 330°C, with a split ratio of 30. FID detector was set at 335°C. The oven temperature program was set to an initial temperature of 50°C held for 1.0 min, then increased to 160°C at a ramp rate of 15°C/min, and increased to 230°C at a ramp rate of 7°C/min, and increased to 380°C at a ramp rate of 30°C/min and held for 10 min. In the second method, all the compounds of the liquid fraction (except the oligomers) were identified and quantified (see Figure 2-4-C). The samples were prepared by the method previously described, and the analysis was performed using a gas chromatograph coupled to a mass spectrometer GC-MS (Shimadzu QP-2010plus). The chromatographic separation was performed on a ZB-FAMES® capillary column (60m x 0.25 mm x 0.20  $\mu$ m). The carrier gas (He) was set at a linear velocity of 29 cm s<sup>-1</sup>. The injector was set at 250°C, with a split ratio of 10. The oven temperature program was set to an initial temperature of 100°C, held for 3.0 min, and then it was increased to 215°C at 1°C/min; and increased to 250°C at 15°C/min and held for 1.6 min. The detector transfer line and source temperature were set at 250°C and 200°C. Equivalent Chain Length (ECL) of the products were calculated using retention time of saturated straight fatty acid methyl esters: C14:0 (30.40 min), C16:0 (43.85 min), C18:0 (57.51 min), C20:0 (71.09 min), and C22:0 (83.18 min).

Conversion ( $C$ ) was defined as  $C = 100 \left( 1 - \frac{Q_{in-t i}}{Q_{in-t 0}} \right)$  where  $Q_{in-t i}$  is the concentration of remaining substrate  $i$  at a time  $i$ , and  $Q_{in-t 0}$  is the initial concentration of the substrate in the raw material. Due to the significant complexity of products, they are classified in different families of products in the liquid phase: branched C18 isomer products, linear-saturated FAME product (methyl stearate), Straight C18 isomers of methyl oleate, cracking products, oligomer and other products. The yield of a  $j$  family of compound ( $Y_j$ ) is defined as:  $Y_j = 100 \left( \frac{Q_{j-t i}}{Q_{in-t 0}} \right)$  where  $Q_{j-t i}$  is the concentration of  $j$  kind of compound and  $Q_{in-t 0}$  is the concentration of substrate in the raw material.

Finally, the chromatographic GC-MS analysis of the extracts from spent catalytic materials were carried out using the same instrument equipped with a HP-5-ms capillary column (30m x 0.25 mm x 0.25  $\mu$ m). The injector was set at 250°C, with a split ratio of 10. The oven temperature program was set to an initial temperature of 45°C, held for 1.0 min; then it was increased to 110°C at 5°C/min, increased to the final temperature of 250°C at 20°C/min and held for 6 min. The transfer line and source temperatures of the MS detector were set at 250 and 200 °C, respectively. Each liquid extract was diluted to 1.0 mL of the respective solvent.

### 2.4.2 Mass spectroscopy analyses

Oligomers were analyzed in liquid fraction products by MALDI-TOF MS and MS/MS analyses. Moreover, the dichloromethane liquid extracts from Soxhlet procedures from the washing of the spent catalysts were also analyzed by the same method. The samples were dissolved at 5 mg/mL in dichloromethane. The matrix used was DHB (2,5-dihydroxybenzoic acid) dissolved at 10 mg/mL in acetone. The cationization agent was lithium chloride (5 mg/mL in acetone). First, 1  $\mu$ L solution LiCl was spotted on the MALDI plate followed by 0.5  $\mu$ L of matrix and 0.5  $\mu$ L of the sample solution. It was left to dry before analysis.

Full scan mass spectra and MS/MS spectra were performed on a MALDI-TOF/TOF Bruker Rapiflex using a nitrogen laser for MALDI( $\lambda$ =337nm). All spectra were recorded in positive ionization mode. Mass spectra of 3000 shots were accumulated for the spectra at a 25 kV acceleration voltage and reflectron lens potentials at 26.3 KV. A mixture of peptides was used for external calibration. For MS/MS mode, the transmission of precursor ions into the collision cell was optimized using decelerating lens of 18 kV and MS/MS pulse of 2.9 kV.

### 2.4.3 Differential scanning calorimetry (DSC) analysis

In order to study the thermal behavior of the methyl oleate isomerization samples as well as the isomerization products obtained from palm biodiesel differential scanning calorimetry experiments were performed. The analysis was carried out in a DSC4000, PerkinElmer® calorimeter. 5 mg of each sample was put in a hermetically sealed aluminum pan. The analysis was done under a nitrogen flow of 50 mL/min. The analysis was conducted from an initial temperature that was set at -60°C, held for 5 min. After it, heating with a ramp of 5°C/min to +60°C, held for 2 min, followed by cooling with a ramp of 10°C/min to -60°C.



## **3.Synthesis of catalytic materials: micro-mesoporous materials from zeolites by recrystallization**

The synthesis of the micro-mesoporous zeolitic materials, further used as catalysts, was done by one-step recrystallization, consisting of a hydrothermal treatment with a base and CTAB as the surfactant to allow the formation of a new mesopore system (see section 1.4.2). The physico-chemical parameters of the recrystallization treatment, including temperature, amounts of reagents and treatment time, were set according to the procedures previously established in our laboratory. On one hand, the ferrierite-based materials were obtained following the methodology developed by Cheng et al. [13]. On the other hand, the zeolite Y-based materials were obtained from low and high silica faujasite, following procedures established by Chal et al. [14] and Vaugon et al. [15], respectively (see section 2.1.2). The preparation of the micro-mesoporous materials from CBV 712 (Si/Al=6.0) is proposed here for the first time. Materials were characterized according to the methodologies described in section 2.2. Analyses results allowed us to corroborate the laboratory previous results and also to deepen our knowledge on these materials, on the recrystallization processes, and especially on the relations between their properties and their catalytic activity and stability.

### **3.1 Recrystallization of ferrierite zeolite**

The recrystallization of a low silica ferrierite was performed. The ferrierite structure presents a highly-constrained anisotropic microporous framework which is constituted of two intersected channels of 8-MR (0.35 x 0.48 nm) and 10-MR (0.43 x 0.55 nm), which run along the [010] and [001] directions, respectively. The commercial ferrierite Na, K-Ferrierite (HSZ-720 KOA® Tosoh Si/Al: 9.2) used in this work was a powder with a particle size around 20 µm. Due to its low Si/Al ratio, this parent ferrierite has a high stability to the attack using basic chemical agents. The recrystallization treatment was done at 130°C for 72h using sodium hydroxide in a high concentration (0.2 M) and CTAB as meso-structure directing agent (see section 2.1.1). Taking into account the high amounts of charge-balancing cations, i.e. sodium (1.0%) and potassium (4.6%), a step of ionic exchange with  $\text{NH}_4\text{NO}_3$  1.0 M was necessary prior the calcination to get the H-form of the recrystallized material, labeled as H-FER-REC.

The different properties of this material were analyzed, and compared with the properties of the H-form of the parent material, labeled as H-FER-PAR. As it was mentioned before, due to high amounts of Na and K, the commercial ferrierite was treated with  $\text{NH}_4\text{NO}_3$  1.0 M to get a  $\text{NH}_4$ -form which was calcined to get this material. In the next sections will be compared the different properties of H-FER-PAR and H-FER-REC: their structural, textural, and chemical characteristics as well as their acidic properties.

### 3.1.1 Structure, texture and chemical composition of the ferrierite-based H-form zeolitic materials.

Following recrystallization conditions for highly stable low silica ferrierite established by Cheng *et al.* [13], it was possible to prepare a ferrierite-based material that presents an added mesopore system and that keeps its crystalline structure.

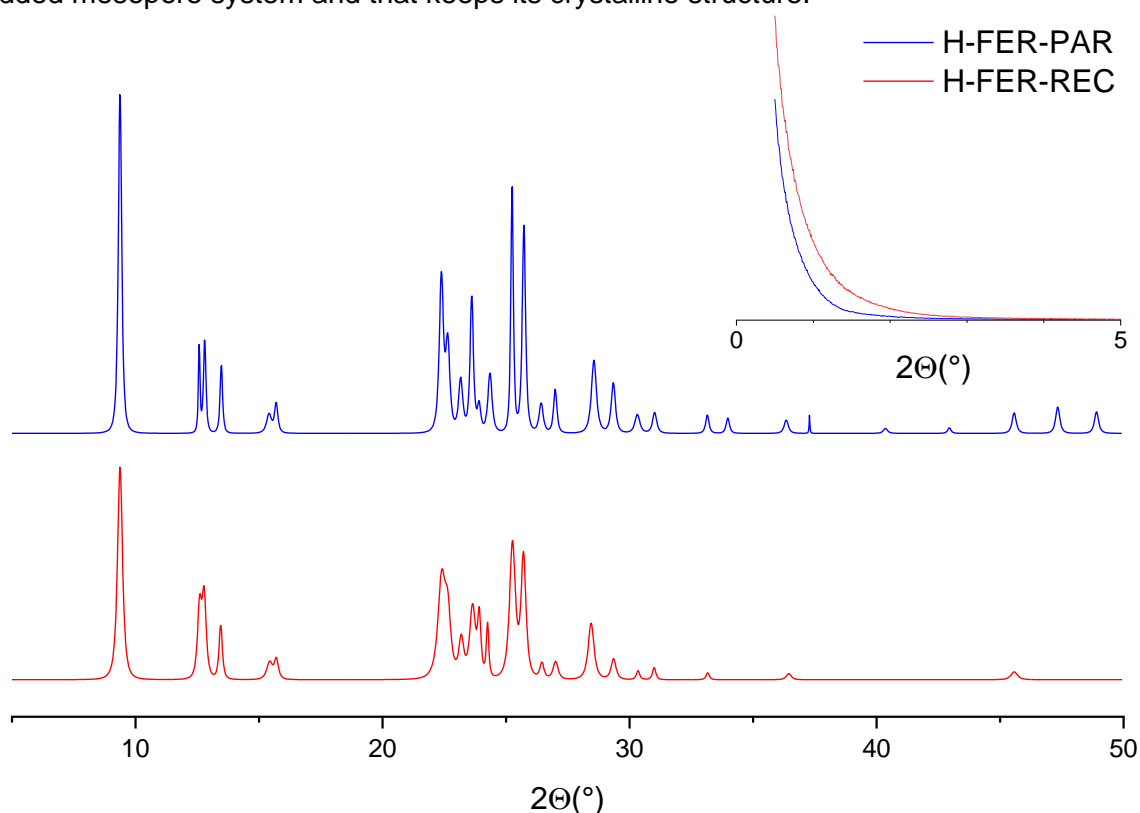


Figure 3-1 Powder X-ray diffraction patterns of parent (in blue) and recrystallized (in red) with an enlargement of small-angle patterns of 0.5-6° of powder X-ray diffraction patterns of parent (H-FER-PAR) and recrystallized (H-FER-REC) ferrierite materials.

Figure 3-1 shows XRD patterns of parent and recrystallized ferrierite materials. Although both showed typical diffraction peaks of highly crystalline ferrierite, the recrystallized material has less intense and broader peaks; this reflects a loss of crystallinity and smaller crystallite size, respectively, due to some framework breakage [13] upon recrystallization. No peaks are observed in the small-angle scattering domain (see Figure 3-1), indicating no

ordered mesopore structure. On the other hand, no other crystalline phases (SOD, GIS) or lamellar materials were formed; such phases were previously reported in the case of the use of more severe conditions of recrystallization [13].

Table 3-1 Properties of the parent and recrystallized H-form-ferrierite materials

Properties		Parent			Recrystallized		
Surface area (m <sup>2</sup> /g)	<b>S<sub>total</sub></b>	379	±	24	406	±	15
	<b>S<sub>micro</sub></b>	340	±	24	248	±	14
	<b>S<sub>meso</sub></b>	18	±	2	76	±	16
	<b>S<sub>ext</sub></b>	21	±	7	82	±	14
Pore Volume (cm <sup>3</sup> /g)	<b>V<sub>total</sub></b>	0.20	±	0.02	0.38	±	0.03
	<b>V<sub>micro</sub></b>	0.13	±	0.01	0.10	±	0.01
	<b>V<sub>més0-intra</sub></b>	0.01	±	0.00	0.13	±	0.02
	<b>V<sub>meso-inter</sub></b>	0.06	±	0.02	0.15	±	0.04
<b>Si/Al</b>		9.7	±	0.3	6.6	±	0.3
<b>Total acidity (μmol/g STP)</b>		1050	±	31	720	±	56

The transmission electronic microscopy (TEM) micrographs of the H-form ferrierite-based zeolitic materials are shown in Figure 3-2. TEM images of H-FER-PAR and H-FER-REC at 2.0 μm scale bar (Figure 3-2-A1 and B1, respectively) were compared: the width on [100] plane of the FER crystals looked smaller, less than 0.3 μm, in the recrystallized material than in the parent H-form material, where more crystals with a width above 0.4 μm are observed. The H-FER-PAR has platelet-like crystals with very few small pores (Figure 3-2-A2), not previously observed in parent Na,K-Ferrierite [13], certainly due to the demetallation process occurring upon ionic exchange. A slight increase in the Si/Al ratio from 9.2 in Na,K-FER to 9.7 in H-FER-PAR confirmed it (See Table 3-1).

TEM images of H-FER-REC showed a large number of parallelepiped-shaped mesopores with blunt borders (Figure 3-2-B2). There is a wide distribution quasi-square pores with pore sizes from 10 to 50 nm. Some bigger pores presented a rectangular shape with lengths above 100 nm. They can be a consequence of the merging of adjacent pores. According to Figure 3-2-C2, the mesopores have thicknesses from 1.5 to 20 nm. By comparing Figure 3-2-B2 and Figure 3-2-C2, it is possible to see that the mesopores are oriented along the crystal c-axis, along the direction of 10-MR channels, and located in different layers from surface to interior of the crystals (Figure 3-2-C2).

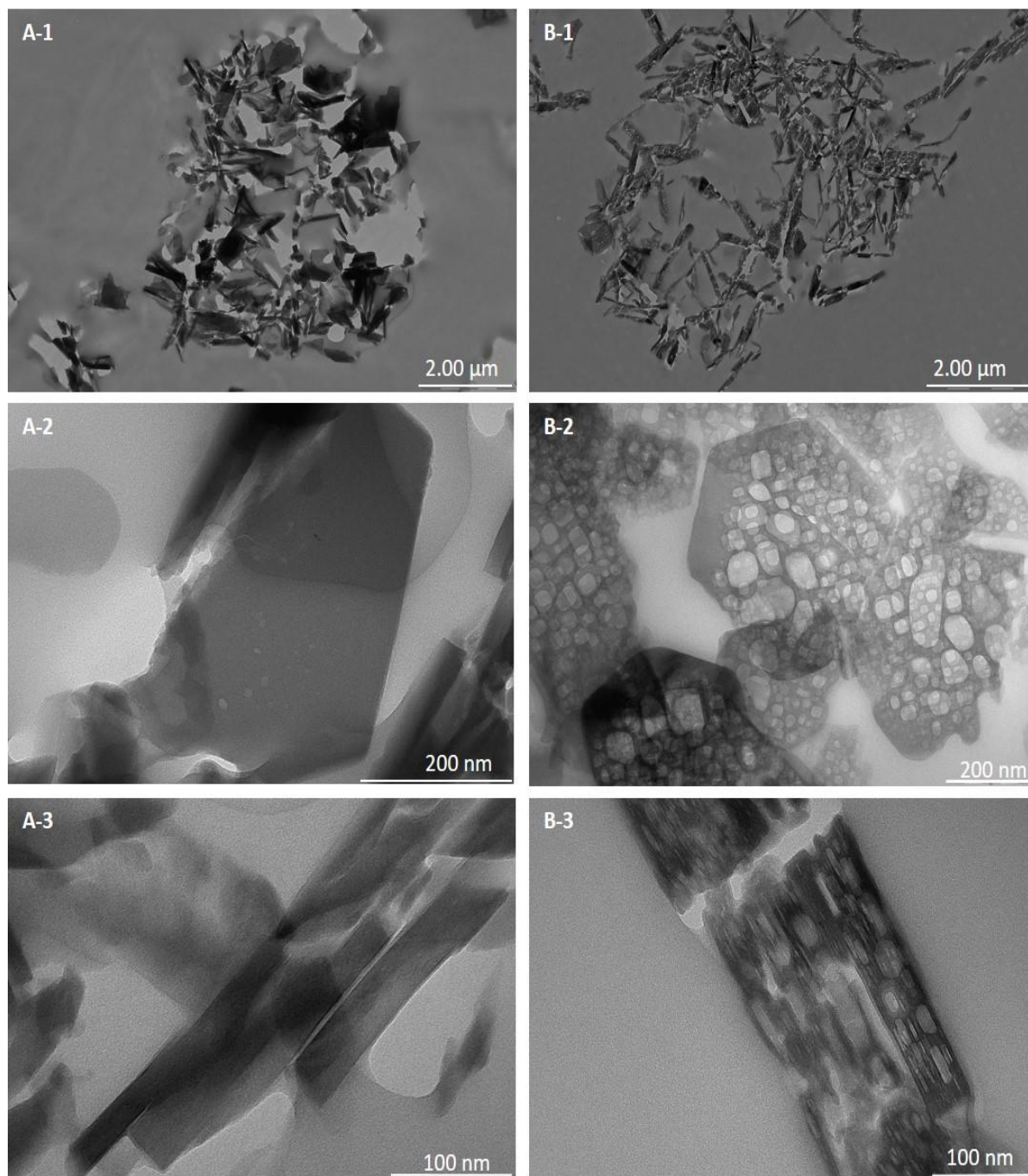


Figure 3-2 Transmission electron microscopy (TEM) images of ferrierite materials with 2.0 μm (1), 200 nm (2), and 100 nm (3) scale bars. A. Parent Ferrierite (H-FER-PAR). B. Recrystallized Ferrierite (H-FER-REC).



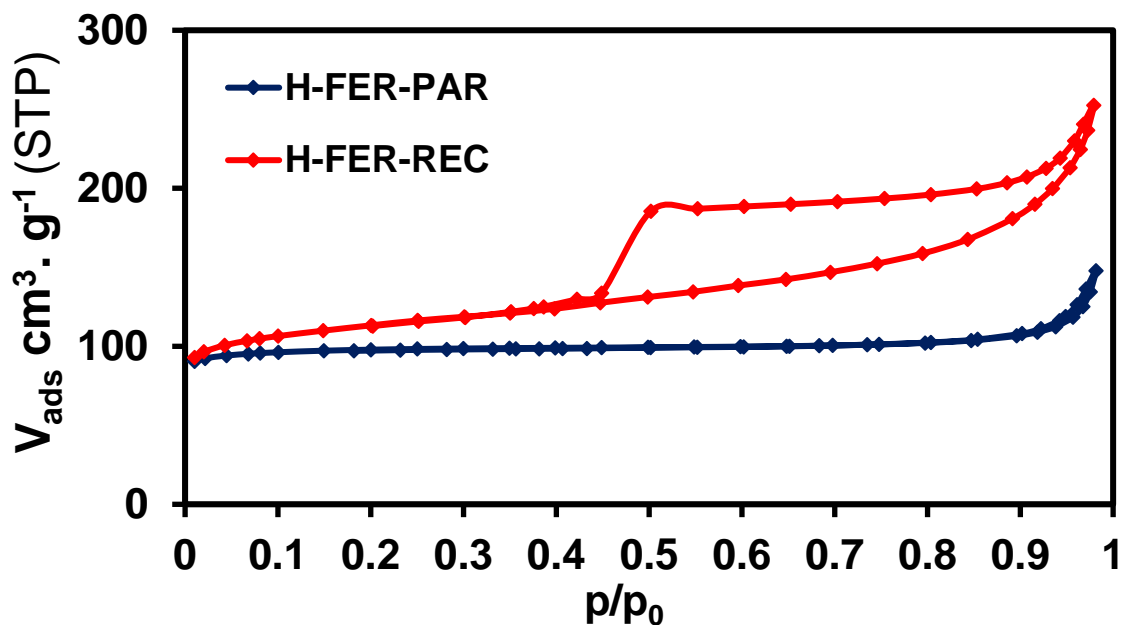


Figure 3-3 N<sub>2</sub> sorption isotherm curves of H-form ferrierite-based materials.

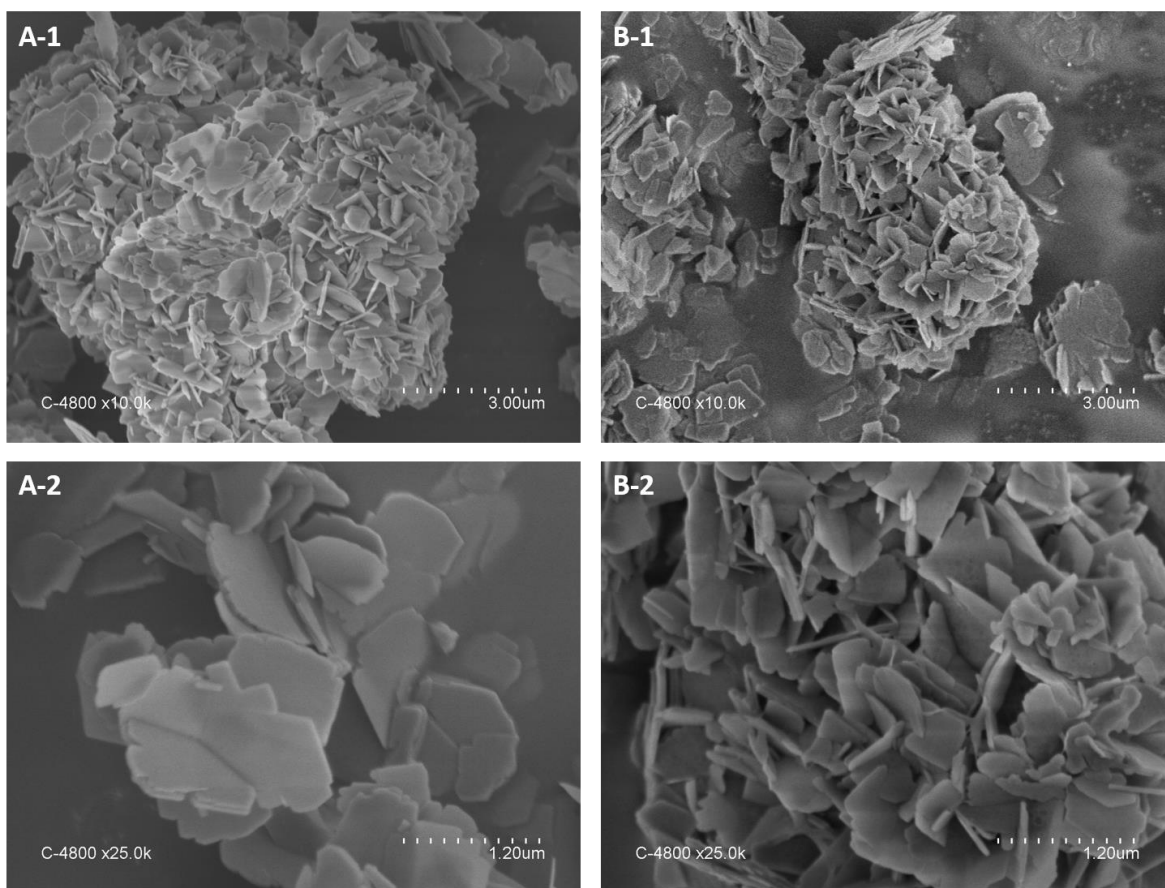


Figure 3-4 Scanning electronic microscopy (SEM) images of ferrierite materials at 3.0  $\mu\text{m}$  (1) and 1.2  $\mu\text{m}$  (2) scale bars. A. Parent Ferrierite (H-FER-PAR). B. Recrystallized Ferrierite (H-FER-REC).

According to the information summarized in Table 3-1, an increase in intracrystalline mesopore volume from 0.01 in H-FER-PAR to 0.13 cm<sup>3</sup>/g in the recrystallized material, as well as in the intercrystalline mesopore volume from 0.06 to 0.11 cm<sup>3</sup>/g, confirms the presence of a new system of mesopores. The surface area of mesopores increased from 18 to 76 m<sup>2</sup>/g. The presence of a large hysteresis loop of N<sub>2</sub> sorption isotherms of H-FER-REC (see Figure 3-3) in contrast to the isotherms of parent FER confirms the presence of large mesopores, as previously reported by Cheng et al. [13]. These mesopores are connected to the external surface of the crystals via restrictions. Although the surface area is only slightly increased from 379 to 406 m<sup>2</sup>/g, and the micropore volume is slightly decreased from 0.13 to 0.10 cm<sup>3</sup>/g, the external surface area increased significantly from 21 to 82 m<sup>2</sup>/g. It is consistent with the smaller size of recrystallized ferrierite crystals compared to that of the parent ferrierite, as observed on SEM images (Figure 3-4), and also clearly on TEM images (Figure 3-2 A-1 and B-1).

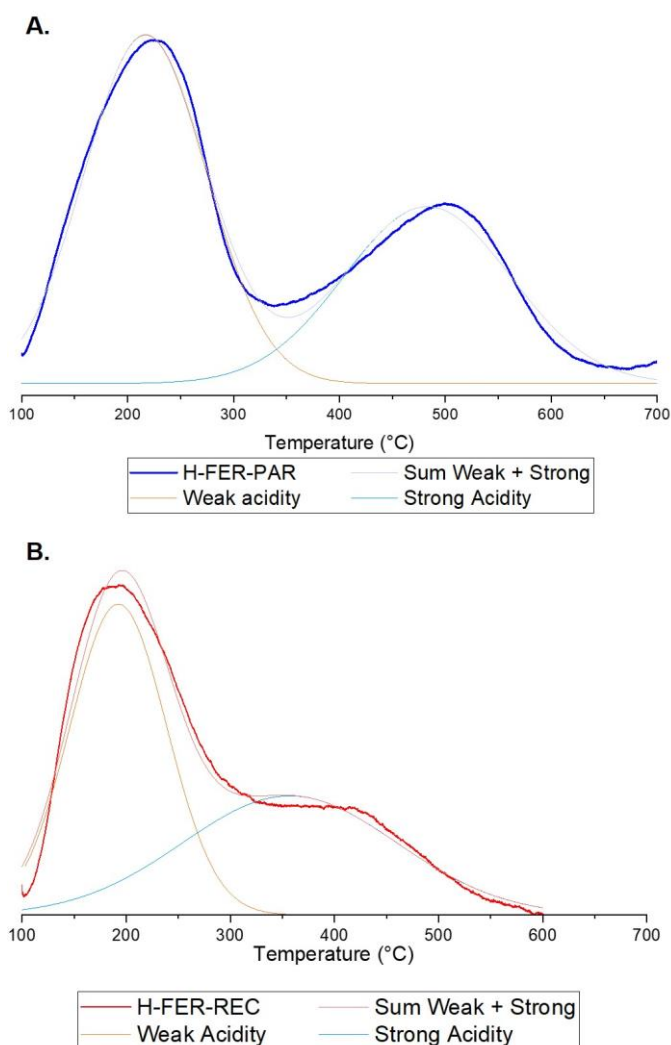


Figure 3-5 Temperature-programmed ammonia desorption profiles of the (A) parent exchanged (H-FER-PAR) and (B) recrystallized (H-FER-REC) zeolitic materials.

On the other hand, the Si/Al ratio significantly decreased from 9.7 to 6.6 in parent and recrystallized samples, respectively, due to the desilication process promoted by the base attack. This can indicate, considering this Si/Al ratio change, that the recrystallization mechanism does not correspond to the mechanism proposed by Ivanova et al. [162] for two-step recrystallization, where the Si/Al ratio does not change upon recrystallization. In contrast, the behavior of this one-step recrystallization can be explained better for the mechanism of crystal rearrangement proposed by García-Martínez *et al.* [213] (see section 1.4.2).

As observed in the ammonia TPD profiles (Figure 3-5), the most important change from H-FER-PAR to H-FER-REC was the decrease in the peak corresponding to the strong acidity. Minor changes were observed in the maximum temperature of the peaks and in the total area related to the total acidity of the samples. The significantly higher amount of aluminum in recrystallized ferrierite did not lead to an increase in acidity. The total acidity even decreased from 1050  $\mu\text{mol/g}$  in H-FER-PAR to 720  $\mu\text{mol/g}$  in H-FER-REC with a larger fraction of strong acidic sites. This can be related to the partial destruction of the microporous crystalline structure during the desilication process [143].

In order to confirm it, solid-state NMR analyses of silicon and aluminum nuclei were done on H-FER-PAR and H-FER-REC zeolitic materials. The spectra were deconvoluted using the DMFIT® software. The deconvolution of the  $^{27}\text{Al}$  MAS NMR spectra using this software is still under process. So only qualitative evolutions will be given here.

On the one hand,  $^{27}\text{Al}$  MAS NMR spectra of parent and recrystallized ferrierite were compared in Figure 3-6. The following differences were observed: the integration of the signal around 0 ppm associated with octahedral extra-framework aluminum (EFAL) species was increased from H-FER-PAR to H-FER-REC. It is a consequence of the dissolution of the crystalline structure and the subsequent formation of aluminum hydroxide-based amorphous phase. Furthermore, the integration of the signal around 55 ppm was decreased from H-FER-PAR to H-FER-REC, indicating a smaller amount of tetrahedral aluminum species being part of the microporous crystalline network of the zeolite. The width of the tetrahedral Al signal increased revealing an increase of the disorder in the zeolite phase, as a result of a distribution of chemical environments and / or distances. As expected, the amount of tetrahedral aluminum lost during the recrystallization was proportional to acidity loss. Additionally, the appearance of a small peak around 30 ppm, showed the presence of pentahedral aluminum species related to defaults in the crystalline network of the ferrierite.

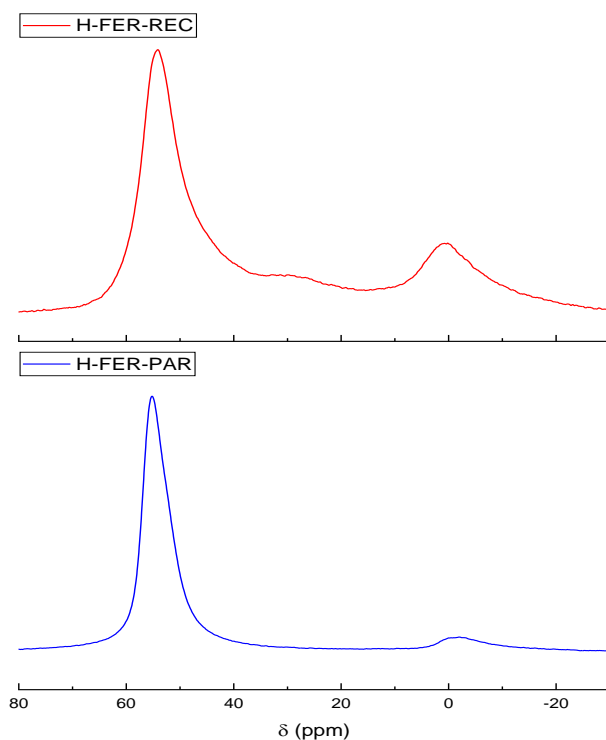


Figure 3-6  $^{27}\text{Al}$  MAS NMR spectrum of H-FER-PAR and H-FER-REC.

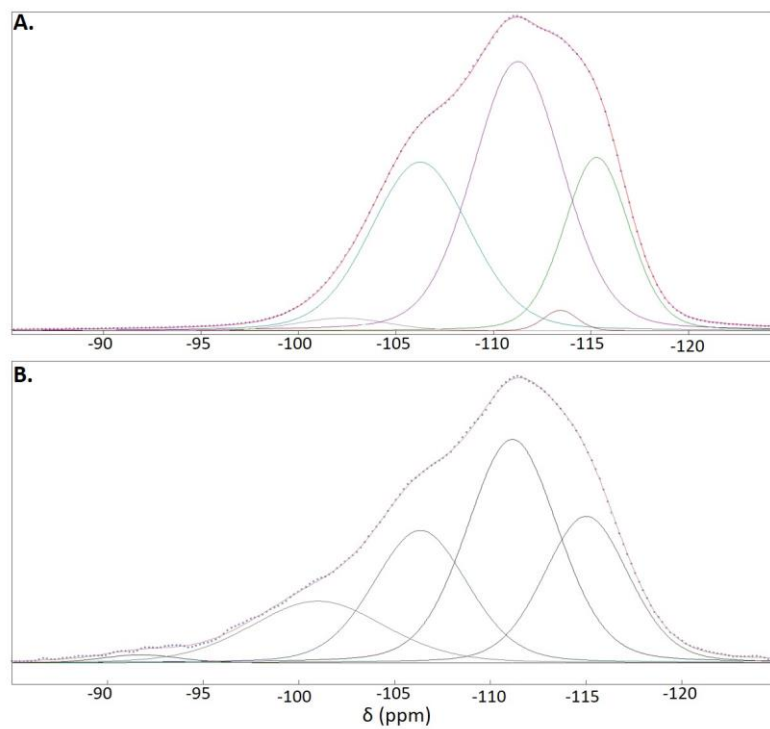


Figure 3-7  $^{29}\text{Si}$  MAS NMR spectrum of (A) H-FER-PAR and (B) H-FER-REC.

On the other hand,  $^{29}\text{Si}$  MAS NMR spectra of parent and recrystallized ferrierite were compared in Figure 3-7. The amount of Si sites of  $\text{Q}_4$  type, ie. having only Si atoms in the second coordination sphere (chemical shift ( $\delta$ ) from -113 to -120 ppm) does not change significantly between H-FER-PAR (22.2%) and H-FER-REC (23.0%) materials. However, the amount of Si atoms of  $\text{Q}_4$  type attached to one Al atom ( $\delta$  at -111 and -106 ppm) decreased from 75.6% in H-FER-PAR to 60.7% in H-FER-REC. This means that the Al tetrahedral sites are less numerous, relative to Si sites. This can be related to the destruction of part of the zeolite framework during the recrystallization treatment, leading to silicon environments less rich in aluminum in the zeolite phase. This is consistent with the observation of Al extra-framework species as six-fold coordinated sites. The amount of Si sites with a chemical environment whose NMR signature appears below -106 ppm ( $\delta$  at -102 and -101 ppm), increased from 2.2% in H-FER-PAR to 16.4% in H-FER-REC. These signals could be associated with Si atoms  $\text{Q}_4$  attached to one aluminum atom or to  $\text{Q}_3$  Si sites, ie. Si atoms presenting an OH group in the coordination sphere. These  $\text{Q}_3$  Si sites could be related to the formation of an amorphous aluminosilicate phase in the sample. To sum up, the  $^{27}\text{Al}$  and  $^{29}\text{Si}$  NMR experiments revealed thus the presence in H-FER-REC of an Al-poorer ferrierite phase coexisting with an extra-framework Al-rich hydroxide phase and an amorphous aluminosilicate phase. Moreover, the chemical environments of Si and Al(IV) sites in the FER phase appear as more distributed, as shown by the increase of the linewidths.

### 3.1.2 FTIR analysis of acidic sites properties on the ferrierite-based H-form zeolitic materials

In order to better understand the changes in acidity properties upon recrystallization, infrared analysis of adsorbed deuterated acetonitrile was done on each of these materials. The use of  $\text{CD}_3\text{CN}$ , a weak base, as a probe of acidity on the surface appears to be relevant to identify the Lewis and Brönsted acid sites and to differentiate and quantify the strength of the different Brönsted acid sites on the catalysts [224]. Figure 3-8 shows the FTIR spectra of both parent and recrystallized ferrierite samples before and after adsorption of  $\text{CD}_3\text{CN}$  and at different temperatures during the desorption procedure.

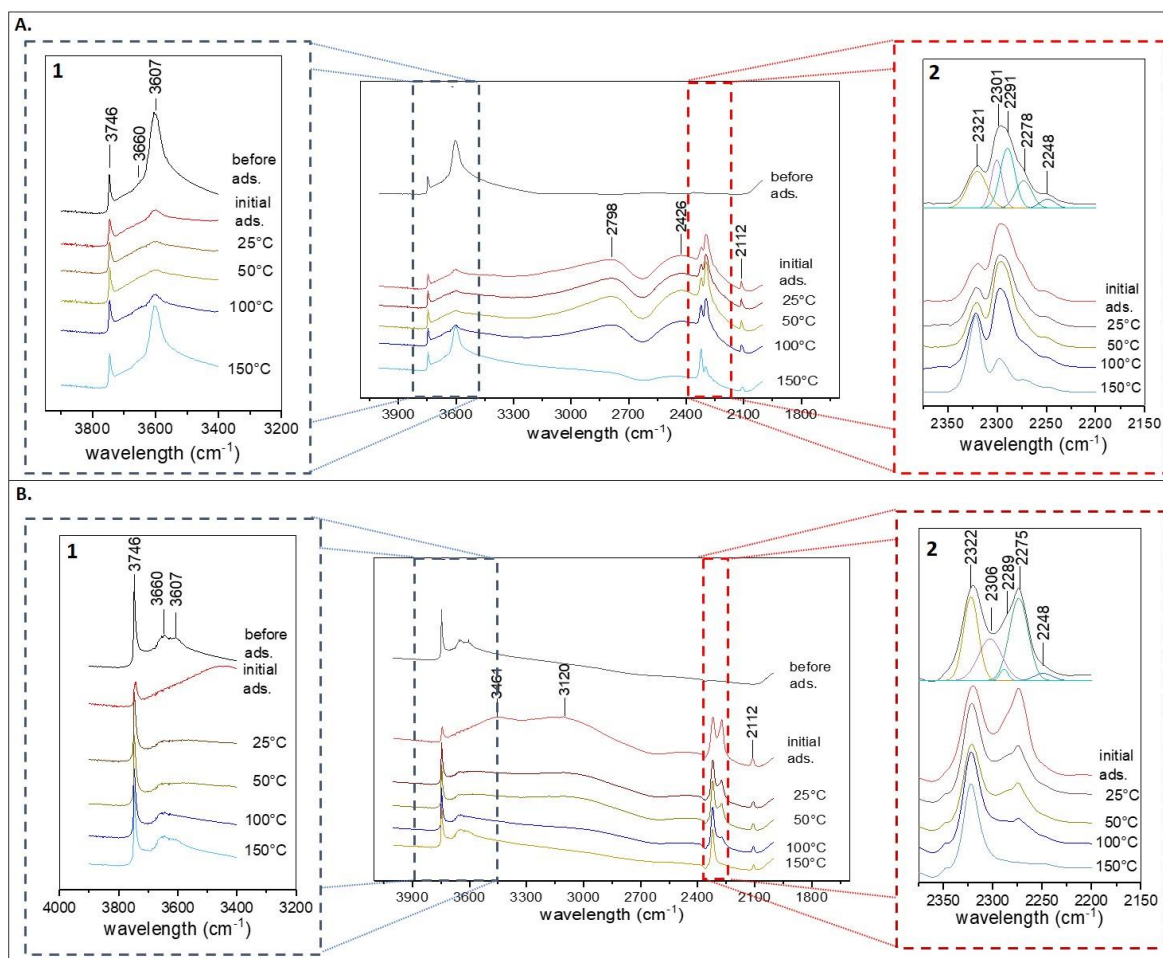


Figure 3-8 FTIR spectra of adsorbed  $\text{CD}_3\text{CN}$  on ferrierite as a function of the temperature desorption of (A) H-FER-PAR and (B) H-FER-REC with the enlargement of the  $3400\text{--}3900\text{ cm}^{-1}$  zone (1) and the enlargement of the  $2200\text{--}2400\text{ cm}^{-1}$  zone (2).

FTIR spectra of both parent and recrystallized zeolites before  $\text{CD}_3\text{CN}$  adsorption are very similar, the only differences being in the intensity of several bands. Three bands can be seen in the spectral region of  $\text{--OH}$  stretching. The first band at  $3746\text{ cm}^{-1}$  can be assigned to the  $\nu(\text{OH})$  of the terminal silanol groups ( $\text{Si--OH}$ ) [222,225,226]. The  $3746\text{ cm}^{-1}$  band is more intense in H-FER-REC, indicating a higher amount of terminal silanols in this material. Silanol groups are expected to be produced during the formation of an amorphous phase upon recrystallization. This band is consistent with the observation of more numerous  $\text{Q}_3$  Si sites in H-FER-REC. The band at  $3660\text{ cm}^{-1}$  can be assigned to  $\nu(\text{OH})$  present in extra-framework species, it is often associated in the literature to a band at  $3780\text{ cm}^{-1}$ , characteristic of acidic OH groups linked to extra-framework aluminum, which is not observed in the present spectra [222]. The last band present in both spectra at  $3607\text{ cm}^{-1}$  corresponds to the bridged hydroxyl groups ( $\text{Si--OH--Al}$ ) on the ferrierite framework [106,225,226]. The band at  $3607\text{ cm}^{-1}$  is large and asymmetric due to the fact that several kinds of bridging hydroxyls are present, in various environments, as it was already demonstrated by several studies [106,227]. Although the attribution of this band is still

controversial in the literature, considering that more confined acidic sites tend to present lower wavenumbers [228], they could be assigned as follows: 10-MR channels ( $3609\text{ cm}^{-1}$ ), 8-MR cages ( $3601\text{ cm}^{-1}$ ), 8-MR channels ( $3587\text{ cm}^{-1}$ ), and 6-MR channels ( $3565\text{ cm}^{-1}$ ) [106,227]. Even if the spectra are similar for both materials, the intensity of the band assigned to bridging hydroxyl groups (Si-OH-Al) is significantly lower in the recrystallized sample, certainly as a result of the loss of part of the microporous crystalline framework of ferrierite during recrystallization. This is consistent with the lower amount of  $Q_4(1Al)$  silicon sites, as observed by  $^{29}\text{Si}$  NMR. According to the literature [227], the Brönsted acid sites on terminal silanol groups correspond to weak acid sites, while the acid sites on bridging hydroxyl groups are stronger, and the strength of Brönsted acid sites increases with lower OH stretching frequency (if no H bonds are present). The parent ferrierite sample seems to have more stronger Brönsted acid sites (related with acidity in the zeolitic framework) than the recrystallized sample.

The adsorption of  $\text{CD}_3\text{CN}$  led on both samples to a slight decrease of the terminal silanol band at  $3746\text{ cm}^{-1}$  and the quasi disappearance of the bands from  $3730$  to  $3550\text{ cm}^{-1}$  corresponding to bridged hydroxyls (see Figure 3-8-A1 and B1). Concomitantly, two broad bands appeared between  $2400$  and  $2200\text{ cm}^{-1}$ , which correspond to acetonitrile bands in OH-NCCD<sub>3</sub> molecular complexes between the bridged hydroxyl groups and acetonitrile on the surface. These bands are typical of strong Brönsted acid sites on the surface [225]. An enlargement of this area is shown for both materials in Figure 3-8-A2 and B2. Two weak bands at  $2112$  and  $2248\text{ cm}^{-1}$ , which are present throughout the whole  $\text{CD}_3\text{CN}$  adsorption process and are not modified by the desorption process, can be attributed to the  $\nu_s(\text{CD}_3)$  and  $\nu_{as}(\text{CD}_3)$  frequencies. In the  $\nu(\text{CN})$  spectral region, the two broad bands obtained, the first one from  $2350$  to  $2310\text{ cm}^{-1}$  and the second one from  $2310$  to  $2250\text{ cm}^{-1}$ , were assigned to Lewis and Brönsted acidic sites, based on the data found in the literature [192,222,225,229,230]. These bands are composites with at least five components identified in both materials after a computer modeling of the spectra. Apart from the  $2248\text{ cm}^{-1}$  band relative to the  $\nu_{as}(\text{CD}_3)$  frequency, the other four bands are attributed to the  $\nu(\text{CN})$  modes of acetonitrile adsorbed on different acid sites. The first band ( $2278\text{ cm}^{-1}$  on H-FER-PAR and  $2275\text{ cm}^{-1}$  on H-FER-REC) corresponds to the adsorption on the silanols, which are weak Brönsted acids, in accordance with previous studies on the literature [229,231]. The second ( $2291\text{ cm}^{-1}$  on H-FER-PAR and  $2289\text{ cm}^{-1}$  on H-FER-REC) and third ( $2301\text{ cm}^{-1}$  on H-FER-PAR and  $2306\text{ cm}^{-1}$  on H-FER-REC) bands are attributed to the adsorption of  $\text{CD}_3\text{CN}$  adducts with acidic sites on the bridged hydroxyl groups present inside the 8-MR and 10-MR channels, and they correspond to strong Brönsted acid sites. The fourth band ( $2322\text{ cm}^{-1}$  on H-FER-PAR and  $2321\text{ cm}^{-1}$  on H-FER-REC) corresponded to acetonitrile adsorbed on the Lewis acidic sites [192,222,225,229,230]. When comparing H-FER-PAR and H-FER-REC in the CN spectral region (Figure 3-8-A2 and B2) after desorption at  $25^\circ\text{C}$ , it is noticeable that the ratio between Brönsted and Lewis acid sites decreases upon recrystallization; it was mainly a consequence of the decrease in the amount of strong Brönsted sites, which is not compensated by the increase in the terminal silanols in H-FER-REC. A significant decrease of the signal intensity corresponding to strong Brönsted sites in the zeolite channels is observed after recrystallization. Considering



that in the region associated with the stretching of the hydroxyls ( $3400\text{--}3900\text{ cm}^{-1}$ ), the more constrained acidic sites presented lower wavenumbers, It is reasonable to expect that the adducts with adsorbed deuterated acetonitrile showed a similar behavior. It has been observed for other zeolites as the zeolite Y (see section 3.2), where the assignment of hydroxyl groups correspond to assignments on CN stretching region [228,232]. Then, the deconvoluted band at  $2291\text{ cm}^{-1}$  in H-FER-PAR and  $2289\text{ cm}^{-1}$  in H-FER-REC was attributed to the acidic sites inside the 8-MR channels while the band at  $2301\text{ cm}^{-1}$  in H-FER-PAR and  $2306\text{ cm}^{-1}$  in H-FER-REC was attributed to the acidic sites inside the 10-MR channels. An interesting feature is that the relative content of Bronsted strong acid sites in 8-MR significantly decreases upon recrystallization, relatively to sites in 10-MR environments. This should be related to the modification of the crystal structure upon recrystallization and may give information on the transformation occurring when occluded mesopores are generated in the FER crystals. It suggests that the formation of the occluded mesopores within the crystals affects more the 8-MR channels than the 10-MR channels. Let us study the evolution of the signals as a function of the acetonitrile desorption temperature. In both parent and recrystallized FER materials, the relative intensity of the CN vibrations corresponding to bridging silanols (when considering together OH in 8-MR and 10-MR), decreases less quickly as a function of the desorption temperature than the signal associated with terminal silanols. This is consistent with the higher acidity strength of the bridging silanols in Si-OH-Al groups.

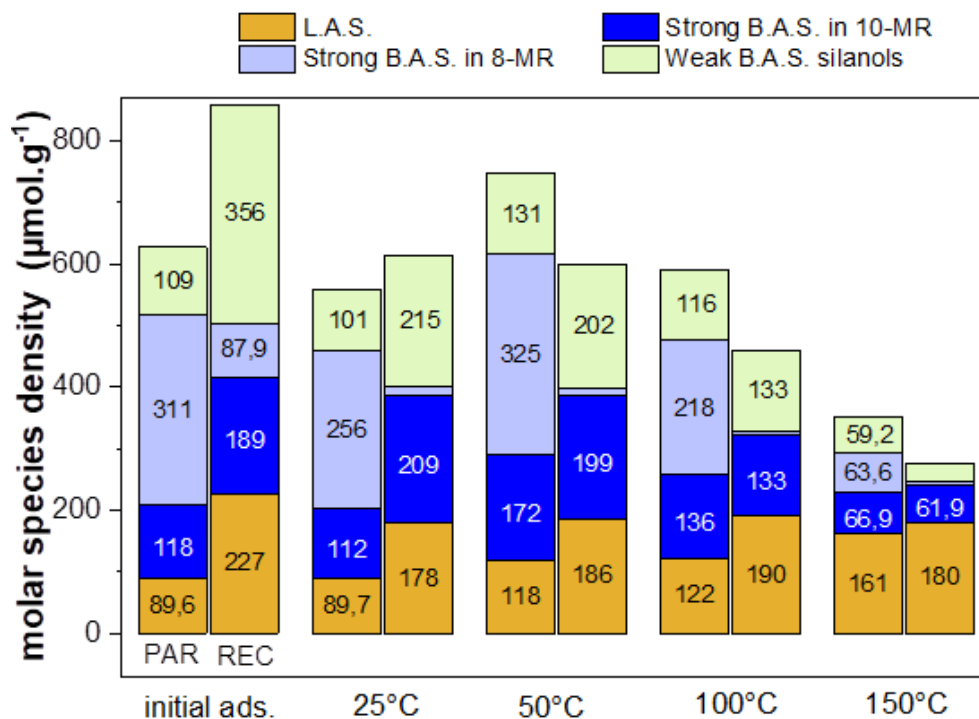


Figure 3-9 Comparison of the molar density of acidic sites between parent (H-FER-PAR) and recrystallized (H-FER-REC) catalytic materials.



The band decomposition enabled us to calculate the molar density of acidic sites and thus, compare their evolution with desorption temperature and between the two samples (Figure 3-9). A higher total acid site amount was observed on the recrystallized ferrierite surface just after adsorption of  $\text{CD}_3\text{CN}$ , mostly as the result of a higher amount of physisorbed  $\text{CD}_3\text{CN}$  on weak Brönsted acid sites at  $2278\text{ cm}^{-1}$  (silanols). Then, it is likely more judicious to discuss the number of acid sites after desorption of the physisorbed  $\text{CD}_3\text{CN}$ .

Considering the extinction coefficients reported for each kind of acid site, the molar density of them was calculated at  $25\text{ }^\circ\text{C}$ . Although there is a higher amount of weak Brönsted acid sites (silanols) in H-FER-REC ( $215\text{ }\mu\text{mol/g}$ ) than in H-FER-PAR ( $101\text{ }\mu\text{mol/g}$ ) at this temperature, the ratio among them decreases significantly. Besides, it is interesting to note that the sum of Lewis and Bronsted acid sites, which come from Al atoms, are proportional to Si/Al ratio variation in these ferrierite-based materials (H-FER-PAR:  $458\text{ }\mu\text{mol/g}$ , H-FER-REC:  $400\text{ }\mu\text{mol/g}$ ). It showed that the number of acidic sites accessible from ferrierite microporous channels keeps in similar values, even if the total acidity decreased by more than 30%. However, there was a significant decrease in the amount of Bronsted acid sites from bridged hydroxyl groups in the ferrierite structure in a similar proportion, which was observed to total acidity loss (H-FER-PAR:  $368\text{ }\mu\text{mol/g}$ , H-FER-REC:  $222\text{ }\mu\text{mol/g}$ ). It was in concordance with the results that showed that the acidity loss was caused by the loss of tetrahedral aluminum, which forms these acidic sites.

According to the advance of the temperature desorption of the  $\text{CD}_3\text{CN}$ , the number of adsorbed molecules are less whereby the global amount of acid sites decreases with the temperature in both materials. At  $150^\circ\text{C}$ , it is worth noting that the molar density of Lewis acid sites is roughly similar for both samples, suggesting the same amount of strong acid sites at the end of  $\text{CD}_3\text{CN}$  desorption. Excluding from the analysis Lewis acid sites, which apparently kept unchanged during the desorption, the number of strong Brönsted acidic sites, even at  $150^\circ\text{C}$ , was higher in the H-FER-PAR ( $131\text{ }\mu\text{mol/g}$ ) than in the H-FER-REC ( $65\text{ }\mu\text{mol/g}$ ).

### 3.1.3 Conclusion

From the analysis of results of characterization of the zeolitic material obtained by one-step recrystallization of low silica ferrierite, it was possible to conclude that it led to the formation of a microporous ferrierite structure with embedded mesopores. In concordance with the results obtained by Cheng *et al.*[13], it was possible to corroborate that this mesopore system is composed of parallelepiped-shaped mesopores of sizes from 10 to 50 nm, and they are connected to the external surface via micropores. It was determined that there was a loss of about one-quarter of micropore volume as well as around one-third of the total acidity of the parent material. This could be related to the dissolution of part of the crystalline structure of ferrierite. It was shown that the loss of acidity was directly proportional to the loss of tetrahedral aluminum species, corresponding to Brönsted acidic sites of ferrierite framework. Additionally, the presence of a higher amount of weaker Brönsted acidic sites associated with terminal silanols in H-FER-REC is certainly associated with the growth of a mesoporous phase onto the zeolite crystals. This new weak Brönsted acidity is surely not

strong enough to participate in acid reactions, therefore the new mesopore system may just allow increasing the accessibility to other efficient Brönsted acidic sites.

## 3.2 Recrystallization of zeolites Y

Micro-mesoporous zeolite Y-based materials were obtained by recrystallization of low (CBV 712®; Si/Al: 6.0) and high silica (CBV 760®; Si/Al: 30) faujasite based on the research work of Chal [14] and Vaugon [15], respectively (see section 2.1.2). The preparation of the meso-microporous materials from CBV 712 (Si/Al: 6.0) is proposed here for the first time. The evolution of the textural properties as a function of the hydrothermal treatment time is discussed, together with the properties of the acidic sites.

### 3.2.1 High Silica Zeolite Y recrystallization (H-Y-30)

The commercial zeolite Y (CBV 760®) was provided in the protonated form due to the ionic exchange, steaming and acid treatment done for its preparation (see Table 1-8) The parent (H-Y-30-PAR) was obtained by calcination of the acquired zeolite at 550°C in airflow in which water and other adsorbed impurities were removed. On the other hand, the recrystallized (H-Y-30-REC) zeolite Y material was prepared by one-step recrystallization; the treatment conditions were chosen following the research work of Vaugon *et al.* [15,216] (see: section 2.1.2) The materials were fully characterized; their structural, textural and acidic properties have been determined and are presented hereafter.

- **Structure, texture and chemical composition of the high silica zeolite Y-based H-form zeolitic materials.**

XRD patterns of parent and recrystallized HY-30 materials are presented in Figure 3-10. They show that both materials kept their crystalline structure typical of the faujasite (FAU) structure. There was not a significant difference in the cell parameter between the H-Y-30-PAR ( $24.29 \pm 0.01 \text{ \AA}$ ) and H-Y-30-REC ( $24.30 \pm 0.01 \text{ \AA}$ ), which suggests that the crystal composition was not significantly modified. However, the crystallite size was calculated using the Deybe-Scherrer equation. The crystal size in the recrystallized material ( $47.4 \pm 15.9 \text{ nm}$ ) was a bit smaller than in the parent zeolite Y H-Y-30-PAR ( $62.6 \pm 10.6 \text{ nm}$ ). Some material loss or slight amorphization during the recrystallization process could be responsible for it. The low angle scattering patterns are also presented in Figure 3-10. As already observed in the literature in the recrystallization of high silica zeolite Y, an intense peak around  $2^\circ 2\theta$  and another less intense peak around  $4^\circ 2\theta$  previously associated with meso-ordered 2D hexagonal structure was observed in the low angle scattering range as in mesoporous MCM-41-type materials [15,155].

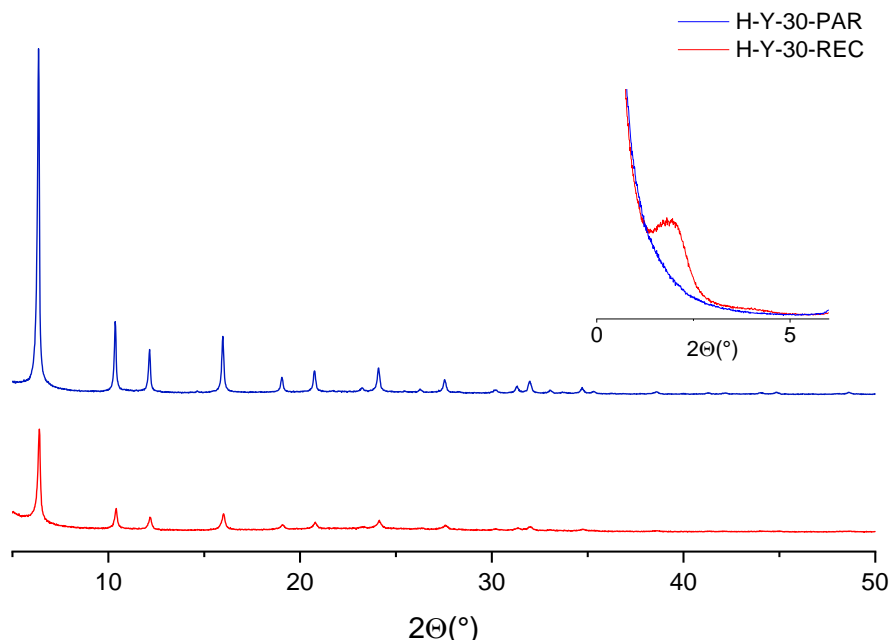


Figure 3-10 Powder X-ray diffraction patterns of parent (in blue) and recrystallized (in red) materials obtained from zeolite Y with Si/Al = 30, with an enlargement of the low angle scattering part (1-6° 2 $\theta$ ).

The acquired zeolite Y (CBV 760®) was in protonated form due to the ionic exchange, steaming and acid treatment done for its obtainment (see Table 1-8). The parent (H-Y-30-PAR) was obtained by calcination of the acquired zeolite at 550 on airflow in which water and other adsorbed impurities were removed. On the other hand, the recrystallized (H-Y-30-REC) zeolite Y material was obtained by one-step recrystallization following the conditions optimized by Vaugon *et al.* [15,216] in the conditions previously described (see: section 2.1.2). XRD patterns (Figure 3-10) show that both materials kept their crystalline structure typical of the faujasite (FAU) structure. There was not a significant difference in the cell parameter between the H-Y-30-PAR ( $24.29 \pm 0.01$  Å) and H-Y-30-REC ( $24.30 \pm 0.01$  Å). However, a smaller crystallite was observed in the recrystallized material ( $47.4 \pm 15.9$  nm) than in the parent zeolite Y H-Y-30-PAR ( $62.6 \pm 10.6$  nm). Some material losses or amorphization during the recrystallization process could be responsible for it. As observed previously in the recrystallization of high silica zeolite Y, one intense peak around 2° and another less intense peak around 4° previously associated with ordered hexagonal was observed in the low angle range mesopores type MCM-41 [15,155].

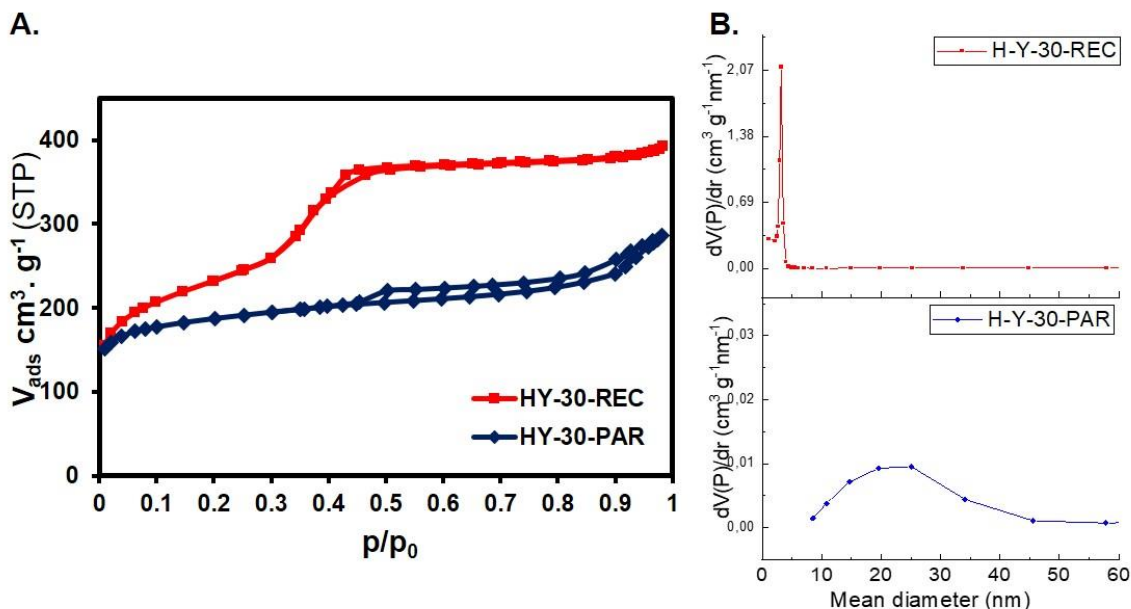


Figure 3-11 N<sub>2</sub> sorption analysis of H-form of zeolite Y-based materials with Si/Al: 30. A. Isotherms curves. B. Pore size distributions.

On the other hand, in the N<sub>2</sub> sorption analysis, both materials presented isotherms classified as type I+IV, characteristic of materials with micro and mesopores (Figure 3-11-A). However, the differences observed in the isotherm hysteresis and the sharp increase in adsorbed volume observed in the isotherm of H-Y-30-REC highlight the change in the size distribution and content of mesopores upon recrystallization of HY-30 parent zeolite. As described previously by Vaugon [15], the parent material H-Y-30 presented a large H4-type hysteresis, characteristic of large pores connected to the external surface by restrictions. Considering the pore size distribution (Figure 3-11-B), H-Y-30-PAR sample has a broader mesopore size distribution extending from 5 to 50 nm. In the recrystallized material, this hysteresis disappeared, and it was replaced by a sharp increase in the adsorbed volume around a  $P/P_0$  value of 0.37. Analysis of pore size distribution (Figure 3-11-B) reveals homogeneous mesopores of regular size around 3.7 nm. The formation of this new mesopore system was evidenced by the increase in intracrystalline mesopore volume from 0.15  $\text{cm}^3/\text{g}$  in H-Y-30-PAR to 0.41  $\text{cm}^3/\text{g}$  in H-Y-30-REC. As it is shown in Table 3-2, there was a decrease in micropore volume from 0.17  $\text{cm}^3/\text{g}$  in H-Y-30-PAR to 0.10  $\text{cm}^3/\text{g}$  in H-Y-30-REC. It corroborates the fact that the micropore system was partially dissolved during recrystallization due to some partial zeolite destruction, while a new mesoporous structure was formed [155]. There was also a decrease in the volume of intercrystalline mesopores from 0.15  $\text{cm}^3/\text{g}$  in H-Y-30-PAR to 0.07  $\text{cm}^3/\text{g}$  in H-Y-30-REC, it is evidenced in the sorption isotherms by the disappearance of the increased adsorbed volume at high  $P/P_0$  value.

Table 3-2 Properties of the parent and recrystallized H-Y-30 zeolitic materials

Properties		Parent			Recrystallized		
Surface area (m <sup>2</sup> /g)	<b>S<sub>total</sub></b>	703	±	14	796	±	14
	<b>S<sub>micro</sub></b>	406	±	22	233	±	29
	<b>S<sub>meso</sub></b>	193	±	17	518	±	43
	<b>S<sub>ext</sub></b>	103	±	5	46	±	9
Pore Volume (cm <sup>3</sup> /g)	<b>V<sub>total</sub></b>	0.45	±	0.01	0.58	±	0.03
	<b>V<sub>micro</sub></b>	0.17	±	0.01	0.10	±	0.01
	<b>V<sub>més</sub>-intra</b>	0.13	±	0.02	0.41	±	0.04
	<b>V<sub>meso</sub>-inter</b>	0.15	±	0.02	0.07	±	0.04
<b>Si/Al</b>		30.2	±	2.0	24.4	±	3.0
<b>Total acidity (μmol/g STP)</b>		254	±	24	239	±	13

TEM micrographs of the zeolite H-Y-30 parent and recrystallized materials are presented in Figure 3-12. They are images taken on ultramicrotome prepared thin slices of 50 nm of thickness. In the parent high silica zeolite Y, mesopores are heterogeneous in size and randomly distributed in location, they coexist with macropores which are connected to the surface (Figure 3-12-A1), and result of the steaming and acid leaching treatments. As described previously, the recrystallization treatment led to the disappearance of the initial large mesopores and to a large decrease of the macropores (Figure 3-12-B1). In H-Y-30-PAR material, the mesopores and macropores were not interconnected with each other (Figure 3-12-A2), neither with the faujasite microporous structure (Figure 3-12-A3). Let us now consider the new mesopores formed upon recrystallization, which were clearly observed on TEM micrographs, as shown in Figure 3-12. A new wormlike mesoporous structure is observed all over the recrystallized zeolite crystals (Figure 3-12-B2), it coexists with the crystalline microporous structure. As observed in Figure 3-12-B2, the mesopore system is well connected with micropore faujasite structure, creating a hierarchical micro-mesoporous zeolite material, as previously described [155,165]. Moreover, a mesoporous phase appeared on the surface of the crystals. It was formed as a consequence of the dissolution of part of the zeolitic material and redeposition of the dissolved matter on the crystal external surface. It was possible to observe that the re-deposited material did not present a crystalline ordered structure (Figure 3-12-B3); we can then conclude that the redeposited material is an amorphous mesoporous phase.

This redeposited material affected the high silica zeolite Y's external surface. Although H-Y-30-PAR and H-Y-30-REC both materials have an octahedral shape (see Figure 3-13-A1 and B1), typical for faujasites, there was a significant difference in the external surface of both materials. On one hand, H-Y-30-PAR crystals had a rough surface with sharp and well-defined edges (see Figure 3-13-A2), in which it was possible to observe some porosity connected to the external surface. On the other hand, H-Y-30-REC crystals had a smoother surface with blunt borders (see Figure 3-13-B2), caused by the presence of the redeposited amorphous phase.

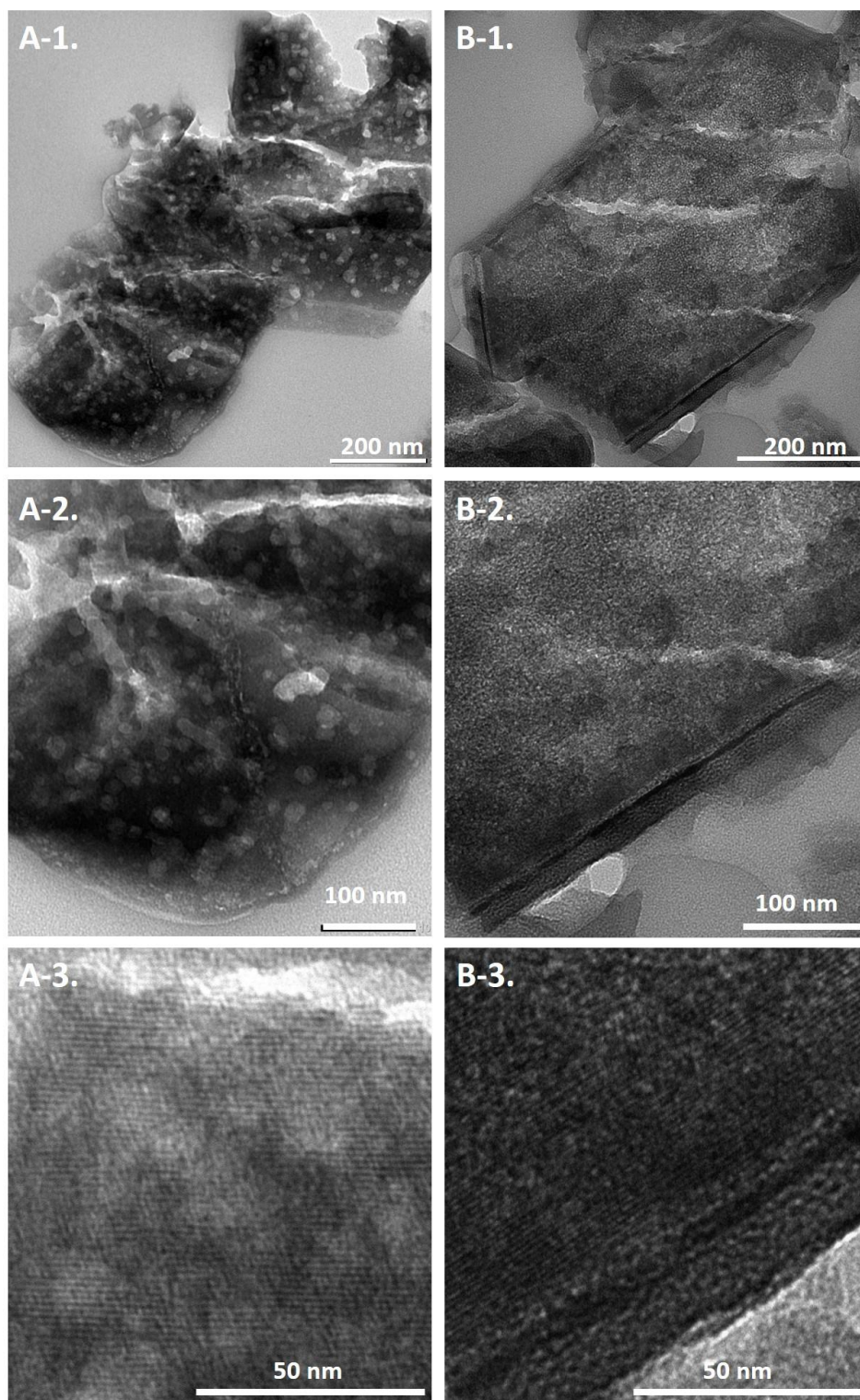


Figure 3-12 Transmission electron microscopy (TEM) images of high silica zeolite Y-based materials with 200 nm (1), 100 nm (2), and 50 nm (3) scale bars.

A. H-Y-30-PAR. B. H-Y-30-REC.



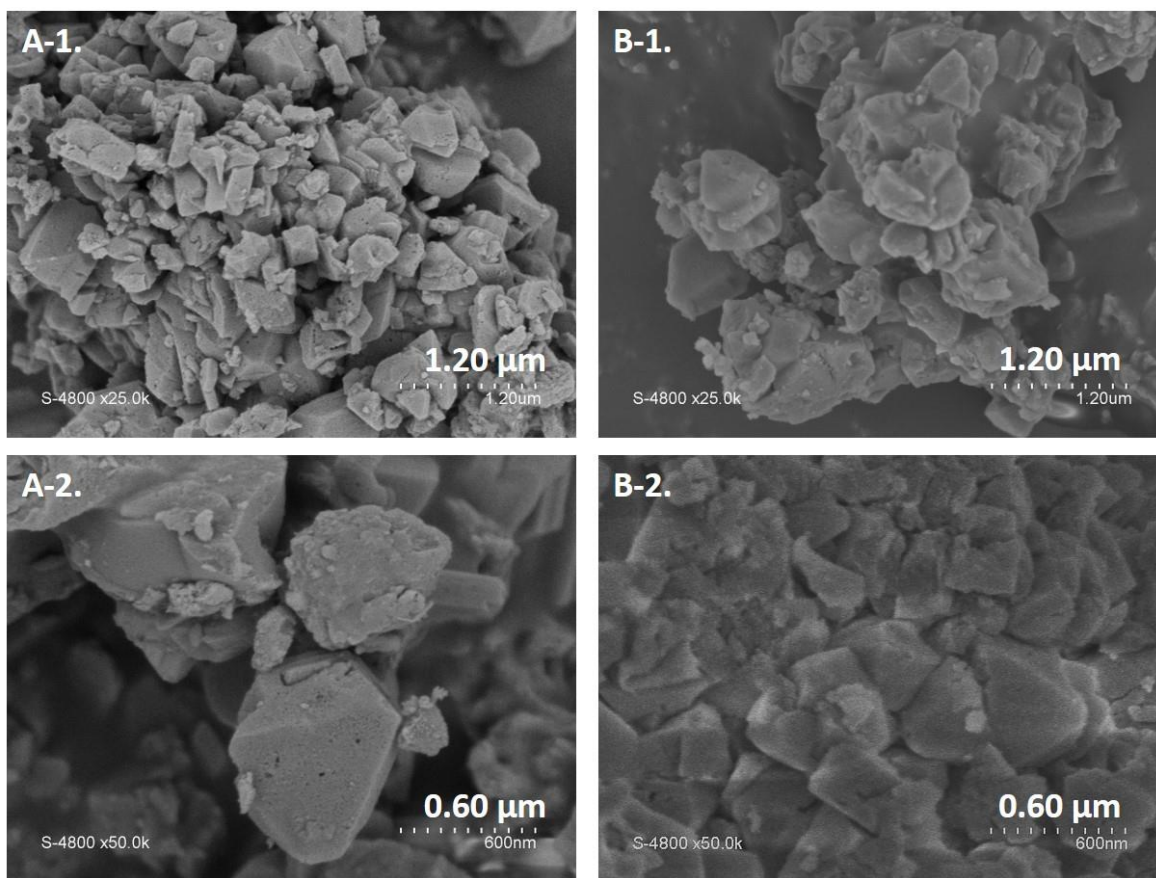


Figure 3-13 Scanning electron microscopy (SEM) images of zeolite Y-based materials with 1.20  $\mu\text{m}$  (1) and 0.6  $\mu\text{m}$  (2) scale bars. A. H-Y-30-PAR. B. H-Y-30-REC.

On the other hand, Si and Al contents of parent and recrystallized materials were determined. The Si/Al ratio value exhibited a slight but significant change from  $30.2 \pm 2.0$  in H-Y-30-PAR to  $24.4 \pm 3.0$  in the recrystallized sample, due to the desilication process promoted by the base attack. Although part of the dissolved material was redeposited, some of it was leached. It led to a loss of material during the hydrothermal treatment, corresponding to a final mass yield of the process of 76.9% wt. These observations were not in concordance with the mechanism proposed by Ivanova et al. [162] for two-step recrystallization processes, where the Si/Al ratio does not change and which is evidenced by the presence of micro- and mesoporous separated domains. Besides, the presence of redeposited matter having mesopores but no microporous domains has not been observed in the mechanism involving crystal rearrangement, as proposed by García-Martínez *et al.* [213].

In order to go further in the elucidation of the phenomena occurring upon recrystallization, solid state NMR analysis of aluminum and silicon nuclei were done on H-Y-30-PAR and H-Y-30-REC materials. The spectra were deconvoluted using the DMFIT® software. The deconvolution of the  $^{27}\text{Al}$  MAS NMR spectra using this software is still under process. So only qualitative evolutions will be given here.

The  $^{27}\text{Al}$  NMR signal due to six-fold coordinated Al sites is due to Al atoms present in domains which do not belong to the zeolite phase, ie. EFAL entities, while the signal associated to four-fold coordinated Al sites can be due to Al sites belonging to the zeolite framework or to amorphous aluminosilicate phases.

Contrarily to ferrierite materials, the high silica zeolite Y suffered a pretreatment necessary for its preparation; therefore, the fraction of non-tetrahedral Al sites is significant in the parent material. The whole Al VI signal is constituted of two components: a sharper signal centered at -0.7 ppm and a wider signal centered at about 4 ppm. The sharper signal is due to some highly mobile species such as oligomeric aluminum hydroxide species, while the wider one is due to more condensed polymeric Al hydroxide phase, known as EFAL phase. The  $^{27}\text{Al}$  MAS NMR spectra of parent and recrystallized high silica zeolite Y (Si/Al: 30) were compared in Figure 3-14. The following differences were observed: the integration of the signal of Al VI sites associated with octahedral extra-framework aluminum (EFAL) species increased from parent zeolite Y (H-Y-30-PAR) to the recrystallized material (H-Y-30-REC). This change was due to the formation of more EFAL species upon recrystallization. Moreover, the signal is wider in the recrystallized material, suggesting some more distributed Al chemical environments in this EFAL phase. On the other hand, the area of the signal corresponding to tetrahedral Al environments decreased from the PAR material to the REC material, with a total integration of Al IV sites, indicating a loss of tetrahedral aluminum species. The Al IV signals are constituted also of two components, one sharper centered at 60.5 ppm and another one, wider, centered at 55 ppm. The sharper one is due to Al IV sites in the zeolitic phase, while the wider one corresponds to Al IV sites in an aluminosilicate amorphous phase, consistently with the larger width of the signal. The fraction of the Al IV sites in the zeolitic phase decreases from the PAR zeolite Y to the REC zeolite Y. This can be related to the decrease of the zeolitic phase fraction, as revealed by the decreased microporous volume and the smaller XRD intensity of the zeolite peaks, and in concordance also with the loss of from the PAR zeolite to the REC zeolite, which is also consistent with the formation of more abundant EFAL species. Additionally, the existence of a signal around 30 ppm showed the presence of pentahedral aluminum species related to defaults in the crystalline network of the zeolite Y material. This signal is present in both PAR and REC materials, and its intensity increases after recrystallization, consistently with the formation of more defaults in the zeolite crystals.



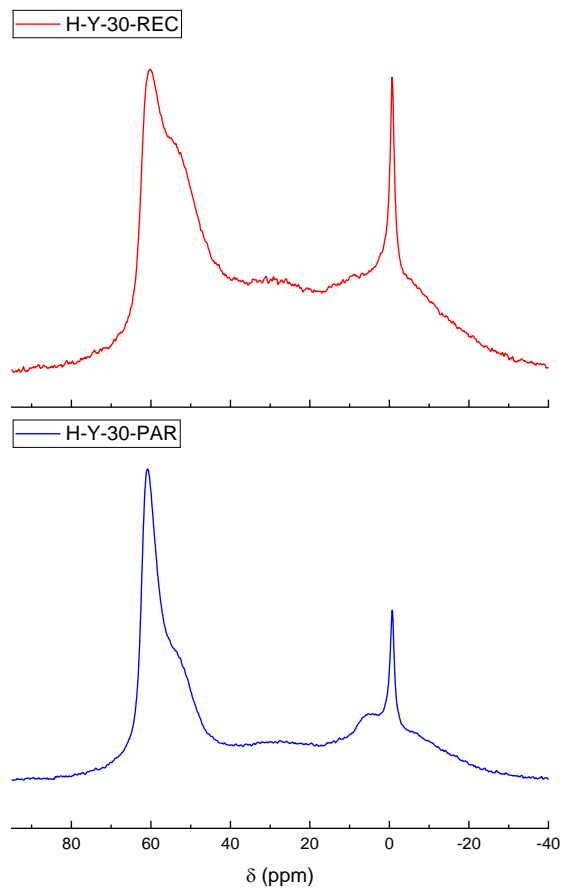


Figure 3-14  $^{27}\text{Al}$  MAS NMR spectra of H-Y-30-PAR and H-Y-30-REC.

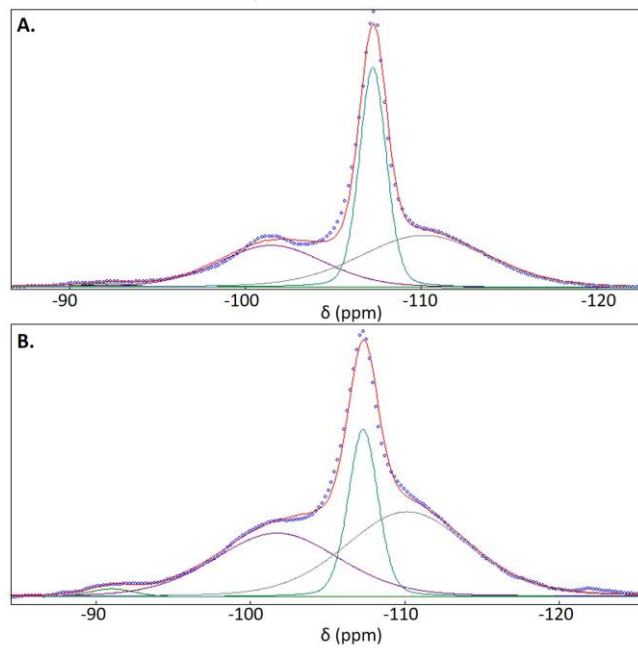


Figure 3-15  $^{29}\text{Si}$  MAS NMR spectra of (A) H-Y-30-PAR and (B) H-Y-30-REC.

On the other hand,  $^{29}\text{Si}$  MAS NMR spectra of parent and recrystallized high silica zeolite Y (Si/Al: 30) were compared in Figure 3-15. The amount of  $\text{Q}_4$  type Si atoms attached to just Si atoms of a non-zeolitic phase (signals at -111 ppm) increased from 38.8% in H-Y-30-PAR to 44.2% in H-Y-30-REC, probably due to the appearance of the highly siliceous redeposited material. A decrease in signal at -107 ppm, assigned to  $\text{Q}_4$  type Si atoms attached to just Si atoms of a -zeolitic phase from H-Y-30-PAR (34.5%) to H-Y-30-REC (20.9%) can corroborate it. However, the amount of Si atoms  $\text{Q}_4$  attached to one Al atom (peak centered at -101 ppm) increased from 25.8% in H-Y-30-PAR to 33.4% in H-Y-30-REC. This showed that the zeolite framework in the REC sample is richer in Al atoms, probably due to the Si migration to new redeposited areas. The change of the amount of Si atoms with a chemical environment that is associated to the signals at -92 ppm did not significantly change, it varied from 1.0% in H-Y-30-PAR to 1.4% in H-Y-30-REC. These signals could be associated with  $\text{Q}_4$  Si atoms attached to two aluminum atoms or  $\text{Q}_3$  Si atoms attached to one hydroxyl. This signal could be related to the redeposited amorphous aluminosilicate phase which is present on the zeolite Y crystals

▪ **FTIR analysis of acidic sites properties on the high silica zeolite Y-based H-form zeolitic materials**

The acidic properties of parent and recrystallized H-Y-30 materials were determined. from the ammonia TPD profiles (see Figure 3-16). There was no significant difference in the total acidity values of H-Y-30-PAR ( $254 \pm 24 \mu\text{mol/g}$ ) and H-Y-30-REC ( $239 \pm 13 \mu\text{mol/g}$ ). Through the peak deconvolution of these TPD profiles was possible to observe that there were not changes in the proportion of Brönsted acidity upon recrystallization (H-Y-30-PAR: 46.0% and H-Y-30-REC: 47.5%).

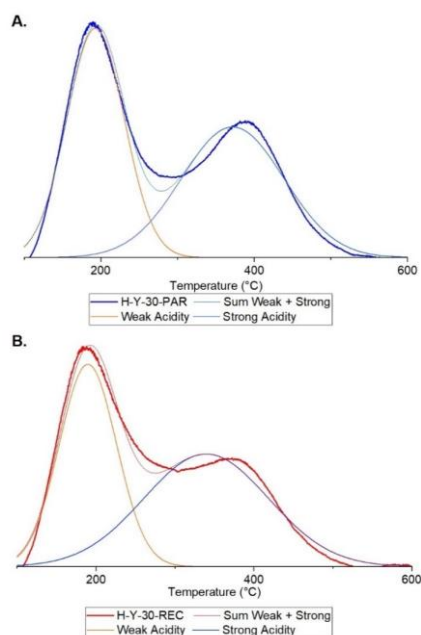


Figure 3-16 Temperature-programmed ammonia desorption profiles of the (A) parent exchanged (H-Y-30-PAR) and (B) recrystallized (H-Y-30-REC) zeolite Y-based materials.

In order to understand better the changes in acidity properties upon recrystallization, infrared analysis of adsorbed deuterated acetonitrile was done on each of these materials in order to identify the Lewis and Brönsted acid sites as well as to differentiate and to quantify the strength of the different Brönsted acid sites on the catalysts [224]. Parent and recrystallized zeolite Y-based zeolitic materials both revealed three bands in the spectral region of O-H stretching (Figure 3-17-A1 and B1) in IR spectra before CD<sub>3</sub>CN adsorption. The band around 3740 cm<sup>-1</sup> was assigned to the  $\nu(\text{OH})$  of the terminal silanol groups (Si-OH). It is essential to notice that this band has a higher intensity in the H-Y-30-REC material, indicating more numerous terminal silanol groups in the recrystallized material. On the other hand, bands of 3629 and 3564 cm<sup>-1</sup> were assigned to the  $\nu(\text{OH})$  of bridged hydroxyl groups (Si-OH-Al) in the supercage and in the sodalite cages of the faujasite framework, respectively [233,234]. No significant differences were observed in these two signals between H-Y-30-PAR and H-Y-30-REC materials.

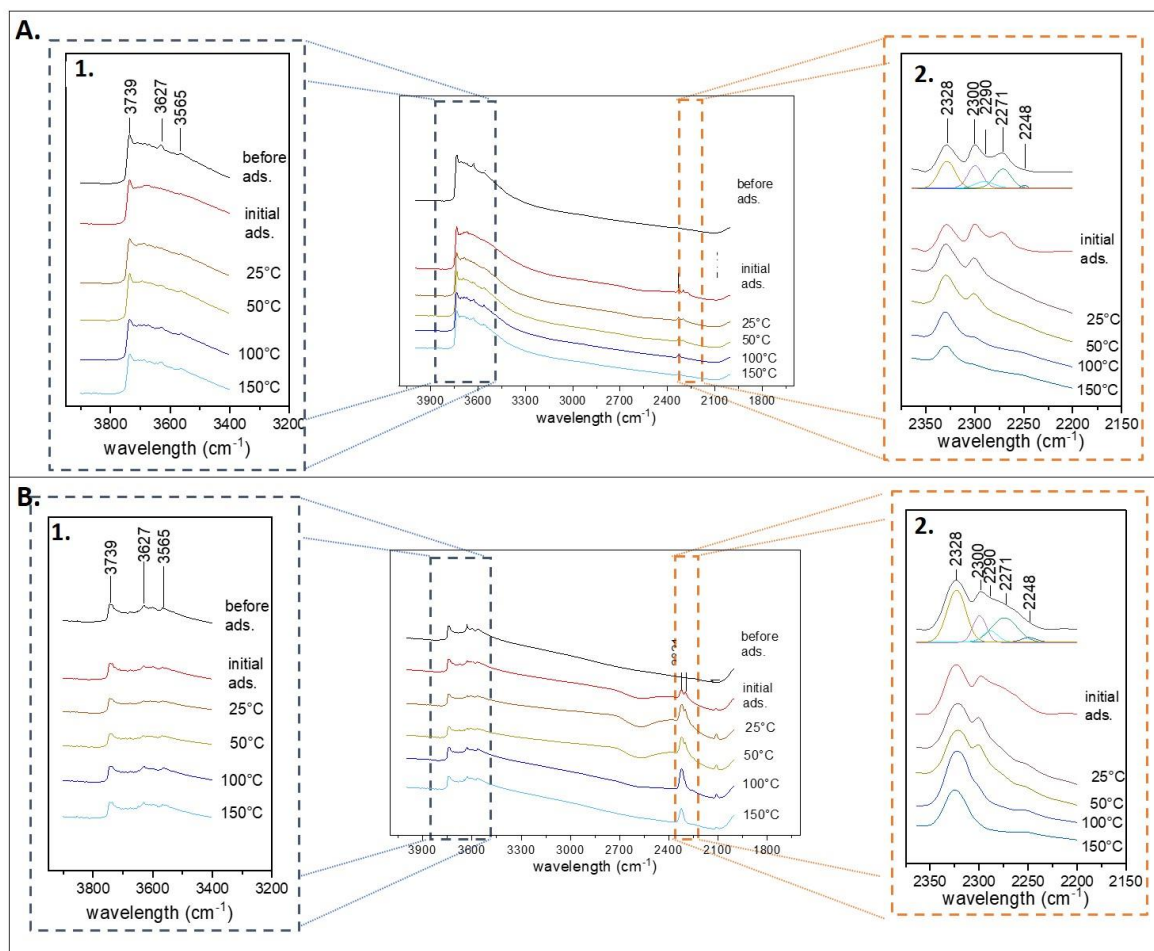


Figure 3-17 FTIR spectra of adsorbed CD<sub>3</sub>CN on high silica zeolite Y as a function of the temperature desorption of (A) H-Y-30-PAR and (B) H-Y-30-REC with the enlargement of the 3400-3900 cm<sup>-1</sup> zone (1) and the enlargement of the 2200-2400 cm<sup>-1</sup> zone (2).

FTIR spectra of adsorbed CD<sub>3</sub>CN of parent and recrystallized high silica zeolite Y are shown in Figure 3-17, respectively. In the OH stretching region of both materials (Figure

3-17-A1 and B1), the adsorption of  $\text{CD}_3\text{CN}$  led to a slight decrease of the band around  $3740\text{cm}^{-1}$  and the *quasi* disappearance of the bands from  $3730$  to  $3550\text{ cm}^{-1}$ . On the other hand, bands from  $2200$  to  $2400\text{ cm}^{-1}$  appeared related to the  $\nu(\text{CN})$  of the adsorbed acetonitrile. In this spectral region (Figure 3-17-A2 and B2), the signal is a composite with at least five components in both materials [224,232]. Apart from the  $2248\text{ cm}^{-1}$  band relative to the  $\nu_{\text{as}}(\text{CD}_3)$  frequency, the other four bands are attributed to the  $\nu(\text{CN})$  mode of acetonitrile adsorbed on different acid sites. The first band ( $2271\text{ cm}^{-1}$  in H-Y-30-PAR and  $2274\text{ cm}^{-1}$  in H-Y-30-REC) is associated with acetonitrile adsorbed on silanols, weak Brönsted acids. Second ( $2290\text{ cm}^{-1}$ -parent and  $2292\text{ cm}^{-1}$ -recrystallized) and third ( $2300\text{ cm}^{-1}$  H-Y-30-PAR and  $2301\text{ cm}^{-1}$ -recrystallized) bands have been attributed to deuterated acetonitrile adsorbed on the bridged hydroxyl Si-OH-Al Brönsted acidic sites inside the supercage and sodalite cages, respectively. The fourth band (at  $2328\text{ cm}^{-1}$  in parent and  $2325\text{ cm}^{-1}$  in recrystallized materials) corresponded to acetonitrile adsorbed on the Lewis acid sites. Comparing H-Y-30-PAR and H-Y-30-REC in the CN spectral region after initial  $\text{CD}_3\text{CN}$  adsorption (Figure 3-17-A2 and B2), it is possible to say that the Brönsted-Lewis acidic sites ratio decreased upon the recrystallization procedure. According to NMR analysis, the recrystallized material has more silanols and more EFAL species which are produced, which could explain the more numerous acidic sites in the recrystallized material. However, as observed for ferrierite-based materials, the large amount of acidic sites just after acetonitrile adsorption was mainly due to physisorbed  $\text{CD}_3\text{CN}$ . In a more pronounced way, this difference disappeared instantaneously when the temperature of the IR analysis increased, and the amounts of adsorbed  $\text{CD}_3\text{CN}$  dropped quickly.

The band decomposition enabled us to compare quantitatively the parent and recrystallized materials and determine the molar density of the different acidic sites when considering the extinction coefficients reported for each kind of site (Figure 3-18). Although a higher total acid site amount was observed on the H-Y-30-REC surface just after adsorption of  $\text{CD}_3\text{CN}$ , we confirm that it was mostly due to a higher amount of weak Brönsted acidic sites at  $2278\text{ cm}^{-1}$  of silanol groups as well as Lewis acidic sites. It could be a result of the presence of the redeposited, highly siliceous phase in the recrystallized material. The amount of bridged hydroxyl Si-Al-OH strong Brönsted acidic sites was slightly superior in H-Y-30-REC. However, when the temperature was increased to start the desorption process, these weakly adsorbed molecules were removed. At  $25^\circ\text{C}$ , the total IR band areas were similar in both catalysts suggesting a similar total acid site amount.

As mentioned before, there is a higher amount of Brönsted acid sites in H-Y-30-PAR ( $40.4\text{ }\mu\text{mol/g}$ ) than H-Y-30-REC ( $24.8\text{ }\mu\text{mol/g}$ ) at this temperature. When the temperature was increasing, the number of adsorbed molecules decreased fast because they are not so numerous and not strong enough. The increase in desorption temperature affected more the Brönsted than the Lewis sites. There were no major differences between both materials when the temperature was increased, indicating no big differences in number or accessibility of acidic sites, at least for a small molecule probe as  $\text{CD}_3\text{CN}$ . When comparing H-Y-30-PAR and H-Y-30-REC, it is nevertheless shown that strong Brönsted acid sites in SOD cavities and in supercages are more numerous in the parent than in the recrystallized sample, which confirms again that recrystallization lead to a loss in zeolite crystallinity and

the associated strong acid sites. Again, similarly to what was observed in the ferrierite based materials, the number of strong Brönsted acidic sites that had adsorbed  $\text{CD}_3\text{CN}$  molecules still at  $150^\circ\text{C}$ , was higher in the H-Y-30-PAR ( $8.0 \mu\text{mol/g}$ ) than in the H-Y-30-REC ( $0 \mu\text{mol/g}$ ).

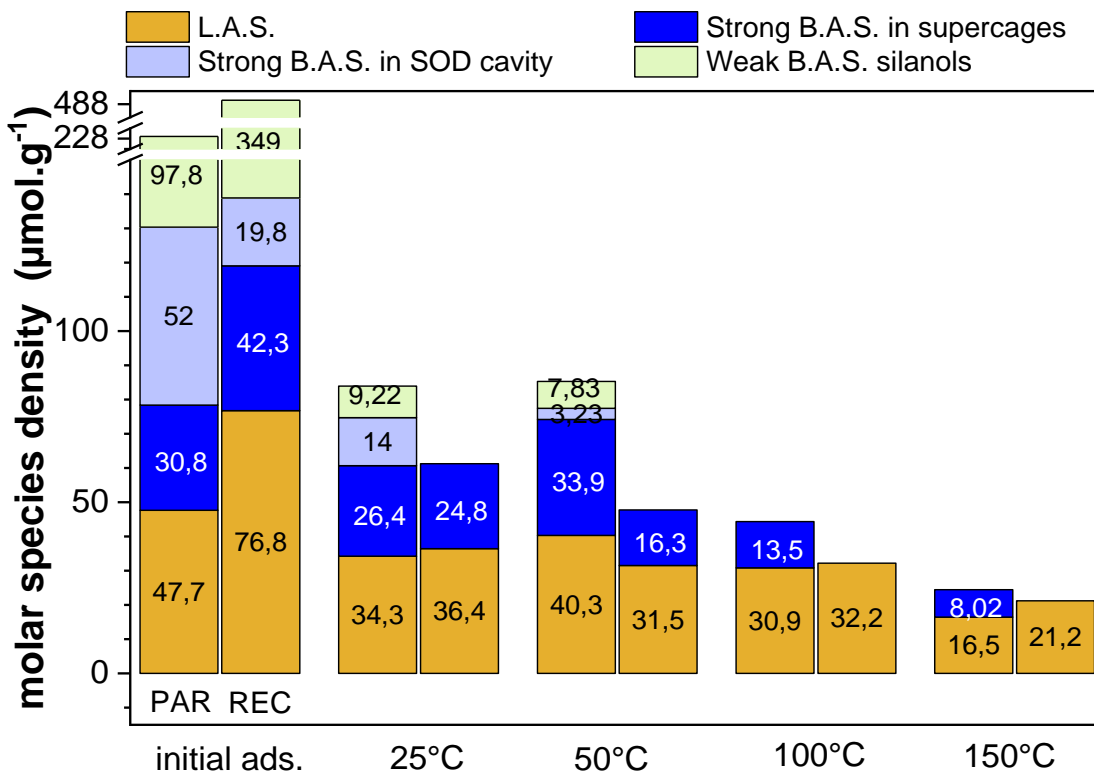


Figure 3-18 Comparison of the molar density of acidic sites between parent (H-Y-30-PAR) and recrystallized (H-Y-30-REC) H-form of zeolite Y with  $\text{Si/Al} = 30$ .

### ▪ Conclusions

From the analysis of results of the characterization of the material obtained by one-step recrystallization of high silica zeolite Y ( $\text{Si/Al} = 30$ ), it was possible to conclude that a hierarchically porous ordered structure of zeolite Y material was formed, exhibiting interconnected mesopores and micropores. In concordance with the results obtained by Vaugon *et al.*[15,216], it was concluded that a wormlike mesoporous structure was formed. This wormlike mesoporous texture was embedded in the zeolite crystalline framework in the whole crystals, as shown by the images of the ultramicrotomed crystal slices. An extra mesopore system was also formed, it is a short-range ordered hexagonal mesoporous structure of MCM-41 type. This more organized mesoporous phase is an aluminosilicate phase which presents short-range ordered cylindrical mesopores with some MCM-41 type organization in small domains; this redeposited mesoporous aluminosilicate phase does not present any zeolite ordering. The formation of this redeposited amorphous phase can

be related to the higher amount of weaker Brönsted acidic sites associated with terminal silanols in H-Y-30-REC. Finally, the content of the zeolite crystalline phase decreases upon recrystallization, it corresponds to a loss of about 40% of micropore volume. Moreover, the REC material lost some strong Brönsted acidity compared to the parent zeolite.

### 3.2.2 Low silica Zeolite Y recrystallization

The preparation of mesoporous zeolitic materials from low silica zeolite Y CBV 712® (Si/Al: 6.5) is proposed here for the first time. The one-step recrystallization was done using TMAOH at a concentration of 0.09M and CTAB as the surfactant (see Table 2-1) at 150°C. The choice of these conditions was based on Chal *et al.*'s work [14] done for steamed zeolite Y CBV 600 (Si/Al: 2.6) (see section 1.6.1). This procedure was tested with three different times of hydrothermal treatment: 40, 96, and 330 h. It was followed by a calcination step for removing the surfactant and obtaining the H-form of the recrystallized material. On the other hand, knowing that the commercial parent zeolite Y was provided under the NH<sub>4</sub>-form as obtained by steaming and acid treatment (see Table 1-8), it was calcined to get the protonated form. The materials obtained at different times of treatment were characterized according to the methodologies described in section 2.2.

- **Structure, texture and chemical composition of the low silica zeolite Y-based H-form zeolitic materials**

The XRD patterns of the materials in the small-angle scattering (0.5-6° 2 $\theta$ ) (Figure 3-19) and long-angle scattering (Figure 3-20) obtained from zeolite Y CBV 712® show that they kept their crystalline structure typical of the faujasite (FAU) structure whatever the treatment time. In contrast with the recrystallization process of high silica zeolite Y, no clear peak was observed in the small-angle scattering patterns of 0.5-6° 2 $\theta$  of these materials (Figure 3-19), indicating that there is no ordered secondary meso-structure. Only the pattern of the sample obtained after 330 hours of treatment presents a very weak signal between 0.5 and 1° appearing as a slope different from what is observed with shorter durations.

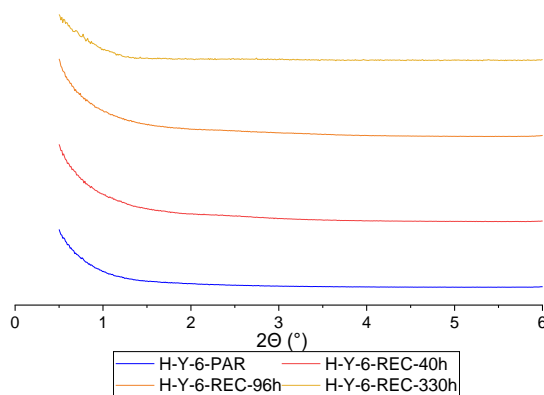


Figure 3-19 Enlargement of small-angle X-ray scattering patterns (0.5-6°) of parent and recrystallized materials from low silica zeolite Y (Si/Al: 6.5).

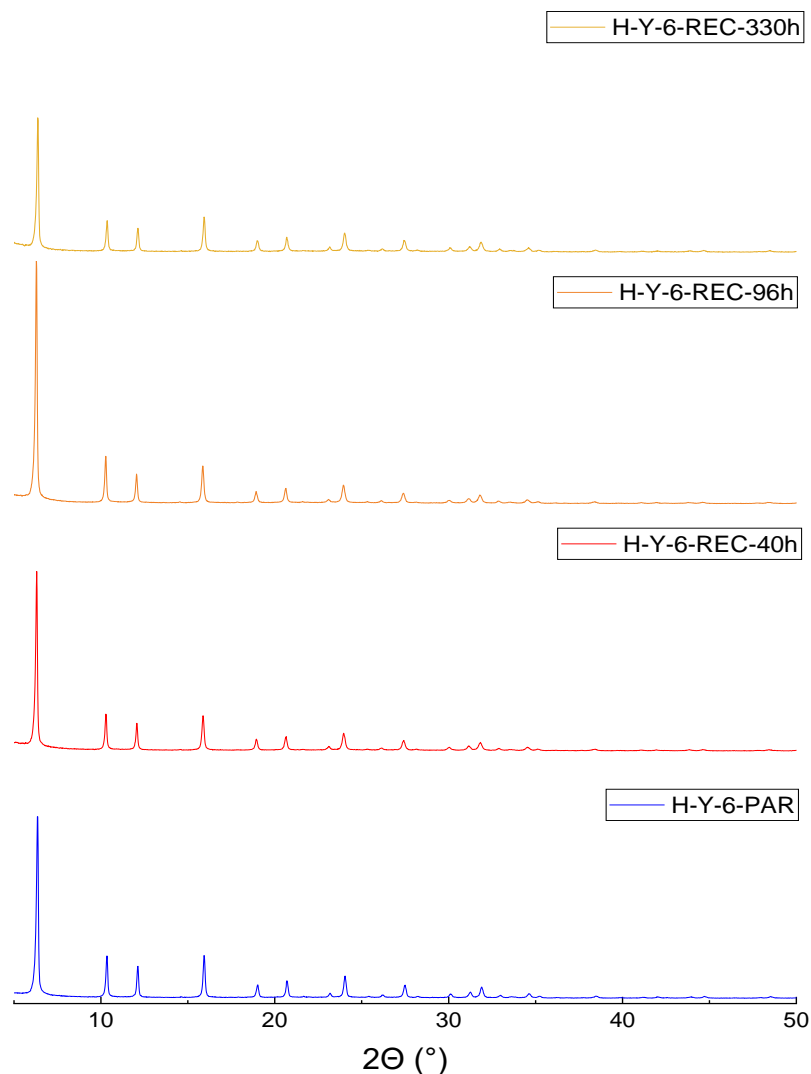


Figure 3-20 Powder X-ray diffraction patterns of low silica parent zeolite Y (Si/Al: 6.5) and of the resulting materials obtained by recrystallization for different times.

On the other hand, the  $N_2$  sorption isotherms of recrystallized materials can be classified as Type I+IV, characteristic of materials with micro and mesopores (Figure 3-21-A). The differences in the isotherm shape and the increase in total adsorbed volume from H-Y-6-PAR to recrystallized materials reveal the change in the mesoporosity of the H-Y-6 materials. As described previously, the parent material H-Y-6 presents a large H4-type hysteresis on a wide range of relative pressure, characteristic of large pores connected to the external surface by restrictions. In contrast with the case of high silica zeolite Y recrystallization, a hysteresis was maintained in the present recrystallized materials. The difference in the total adsorbed volume and the hysteresis extent reveals the evolution of the mesoporosity upon recrystallization: according to the pore size distribution (Figure 3-21-B), the H-Y-6-PAR material has a very broad pore size distribution from 5 to 50 nm. In the recrystallized materials, this broad pore size distribution disappeared, but it was not replaced by an intense and narrow pore size distribution, as it could be observed in the



case of high silica Y zeolite. Weak peaks appear in the pore size distributions centered at about 2.5 and 3.2 nm. This indicates that the obtained mesopores are not very numerous and they do not have a perfectly defined size, contrarily to what was observed in H-Y-30-REC.

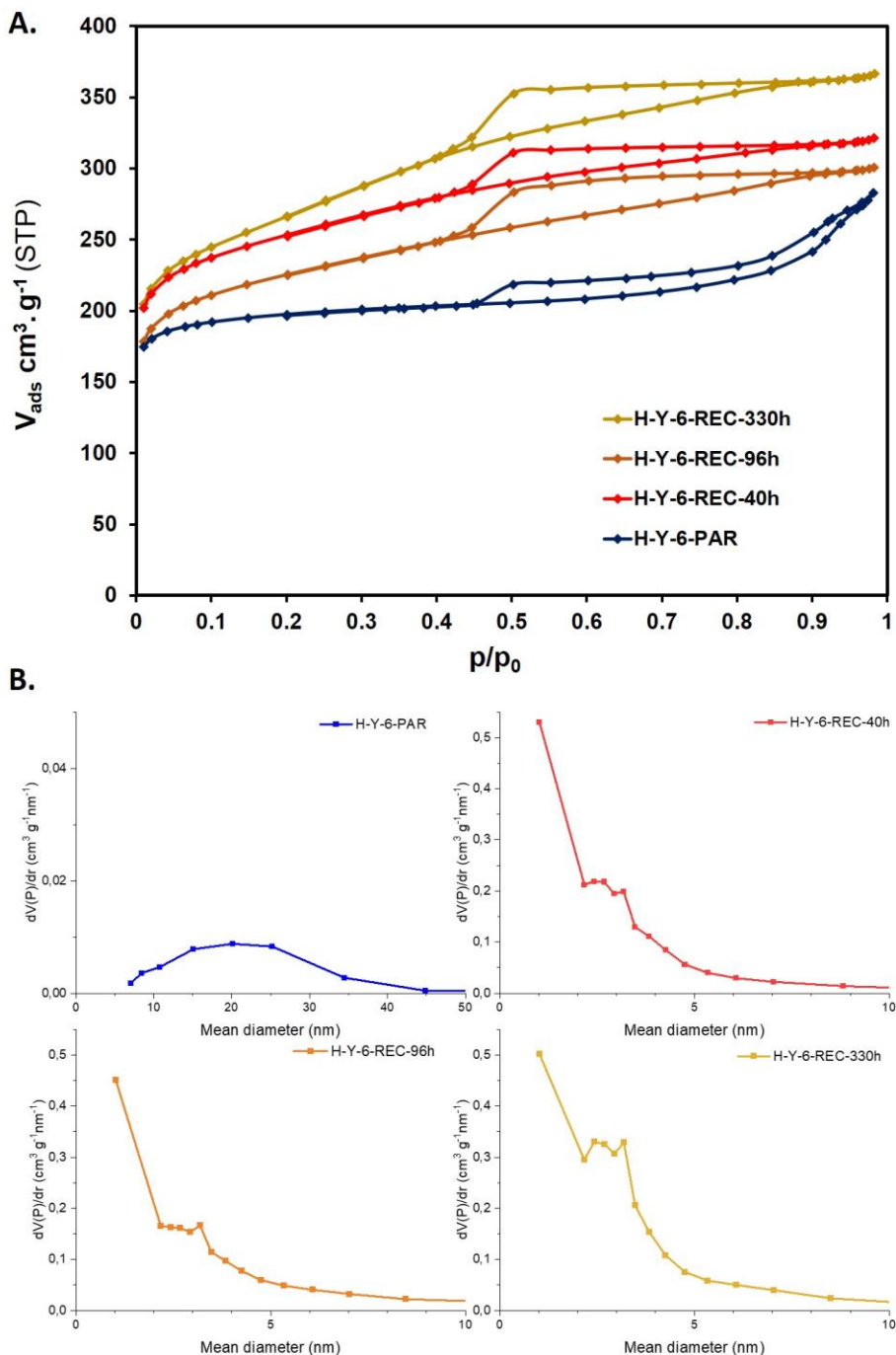


Figure 3-21 N<sub>2</sub> sorption isotherms of H-form of zeolite Y-based materials with Si/Al: 6.5.  
A. Isotherms curves. B. Pore size distributions.



The recrystallization process of low silica zeolite Y yielded a material with a significant mesoporosity while maintaining a large part of the microporosity. As it is possible to see in Figure 3-22-A-1, the parent zeolite presents some mesoporosity and macroporosity, which are produced by the steaming process done by the supplier. Figure 3-22-A-2 shows that the microporous framework is well distributed in all the crystals. The analysis of the nitrogen sorption results shows that the porosity of the H-Y-6-PAR material (see Table 3-3) is mainly composed of micropores ( $0.23 \text{ cm}^3/\text{g}$ ) and intercrystalline mesopores ( $0.13 \text{ cm}^3/\text{g}$ ). In contrast with high silica recrystallized zeolite Y, the spatial distribution of mesopores was not homogeneous in the crystals of the present low silica recrystallized materials; the materials exhibit areas of zeolitic domains and other mesoporous areas, especially in the border of the crystals. As observed in Table 3-3, Si/Al ratio and total acidity of the recrystallized materials were affected by the recrystallization procedure.

Table 3-3 Properties of the parent and recrystallized H-Y-6 zeolitic materials

Properties		Parent	Recrystallized		
			40 h	96 h	330h
Surface area (m <sup>2</sup> /g)	S <sub>total</sub>	776	945	840	976
	S <sub>micro</sub>	579	569	483	515
	S <sub>meso</sub>	106	361	343	460
	S <sub>ext</sub>	91	15	14	15
Pore Volume (cm <sup>3</sup> /g)	V <sub>total</sub>	0.44	0.50	0.47	0.57
	V <sub>micro</sub>	0.23	0.23	0.20	0.21
	V <sub>méso-intra</sub>	0.08	0.24	0.25	0.33
	V <sub>meso-inter</sub>	0.13	0.03	0.02	0.03
Si/Al		6.5	6.8	6.5	6.9
Total acidity (μmol/g STP)		847	889	763	908

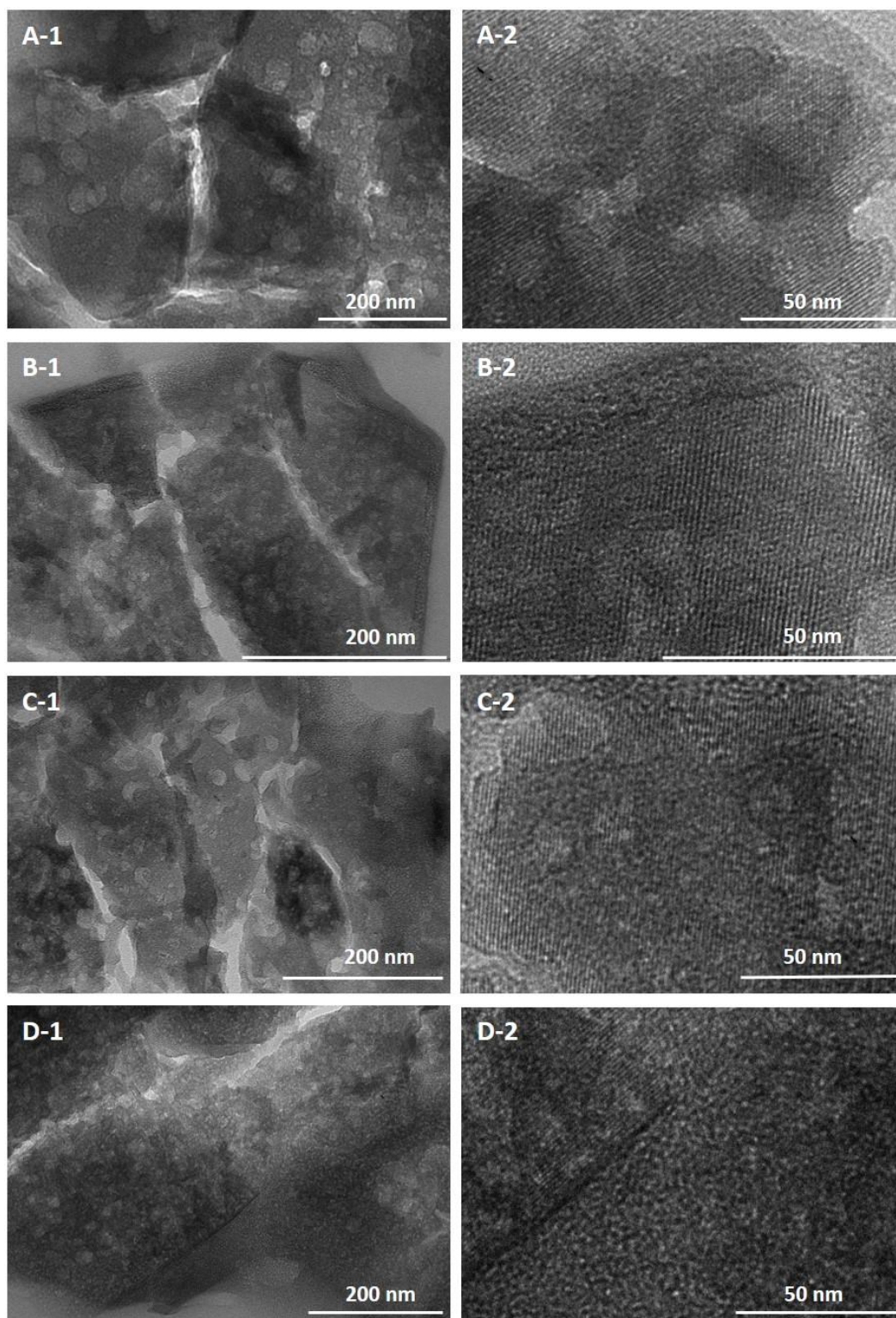


Figure 3-22 Transmission electron microscopy (TEM) images of low silica zeolite Y-based materials with 200 nm (1) and 50 nm (2) scale bars. A. H-Y-6-PAR. B. H-Y-6-REC-40h. C. H-Y-6-REC-96h. D. H-Y-6-REC-330h.

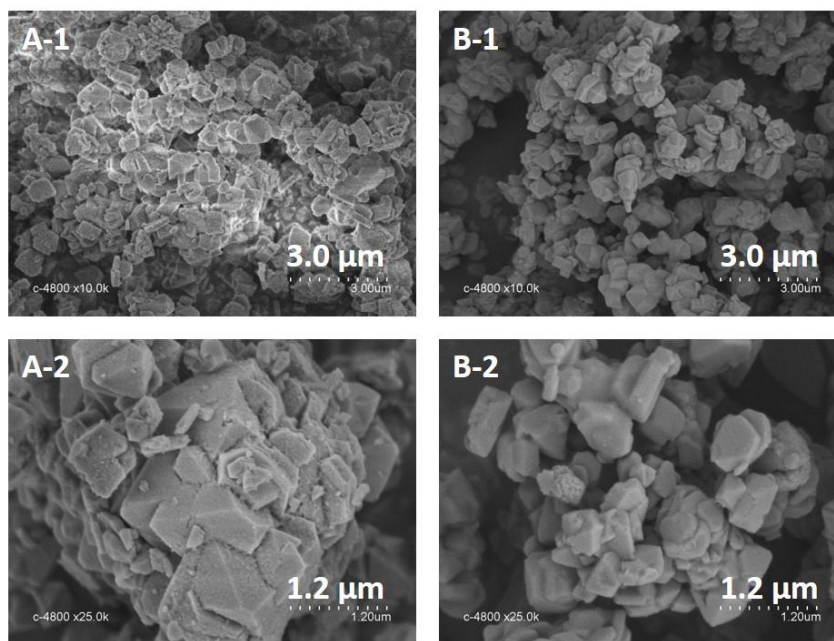


Figure 3-23 Scanning electron microscopy (SEM) images of zeolite Y-based materials with 3.00  $\mu\text{m}$  (1) and 1.20  $\mu\text{m}$  (2) scale bars. A. H-Y-6-PAR. B. H-Y-6-REC-40h.

In the material obtained after 40h of hydrothermal treatment, H-Y-6-REC-40h (Figure 3-22-B-1), some new large mesopores are observed, they may result from the desilication of parts of the disordered zeolitic areas which were produced during the steaming Figure 3-22-B-2 shows the presence of zeolitic domains and mesopores present in the crystals. One can also observe new domains of non-zeolitic material redeposited on the crystals. As observed in Figure 3-24, a large drop in the intercrystalline mesoporous volume ( $0.03 \text{ cm}^3/\text{g}$ ) was observed while the intracrystalline mesopore volume was increased ( $0.24 \text{ cm}^3/\text{g}$ ). The micropore volume in H-Y-6-REC-40h was similar to that in H-Y-6-PAR material. When the hydrothermal treatment was done for a longer time, in the H-Y-6-REC-96h, the presence of big mesopores is less evident, whereas mesoporous domains become more predominant, leading to some clear separation between the zeolitic and mesoporous domains in the H-Y-6-REC-96h (see Figure 3-22-C-2). Moreover, layers of redeposited matter around the crystals were less present. (see Figure 3-22-C-1). As observed in Figure 3-24, there was a similar amount of inter- ( $0.02 \text{ cm}^3/\text{g}$ ) and intracrystalline mesopores ( $0.25 \text{ cm}^3/\text{g}$ ) in samples after 40 or 96h of hydrothermal treatment. The micropore volume ( $0.20 \text{ cm}^3/\text{g}$ ) decreased slightly, showing the destruction of a small part of the zeolitic structure. Finally, in the material obtained after 330 hours of recrystallization, H-Y-6-REC-330h, the filling of the larger pores was effective (see Figure 3-22-D-1), and a small number of big mesopores was observed. This material showed areas of mesoporous domains and zeolitic domains which are certainly connected, as one can see from the 70nm thick ultramicrotome-obtained slices. (see Figure 3-22-D-1). After 330 h treatment, the intercrystalline mesopore volume ( $0.02 \text{ cm}^3/\text{g}$ ) kept a similar value as before, but the amount of intracrystalline mesopore volume was significantly increased ( $0.33 \text{ cm}^3/\text{g}$ ). However, after this long treatment, the micropore volume was similar as before ( $0.21 \text{ cm}^3/\text{g}$ ), showing the very high resistance to attack of low silica zeolite Y despite the

recrystallization process. Finally, as it can be seen from the sorption isotherms and also from the graph of Figure 3-24, it was evidenced that the recrystallization process of low silica zeolite Y proceeds through, first, a transformation of the inter-crystalline mesoporous volume into intra-crystalline mesopore volume, and secondly some further generation of intracrystalline mesopore while maintaining the zeolitic crystalline structure, as it can be seen from the constant microporous volume. This last step evidences the capacity of low silica zeolite Y to truly recrystallize into micro-mesoporous material without scarifying the zeolitic structural order.

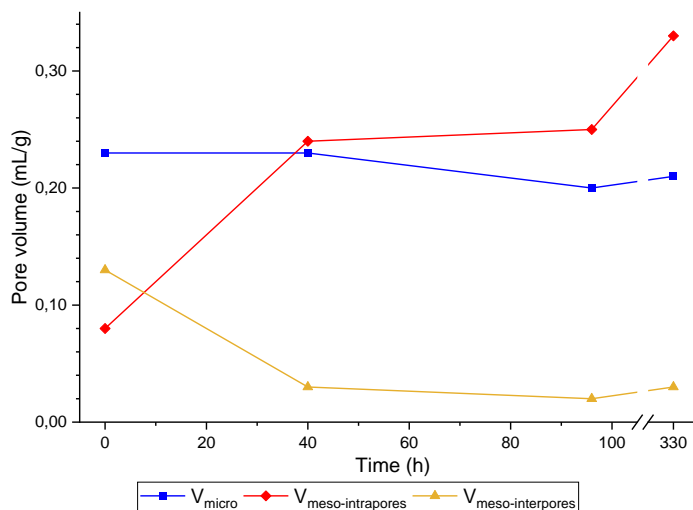


Figure 3-24 Evolution of the micropore and mesopore volumes of the zeolite Y CBV 712® (Si/Al:6.5) during the one-step recrystallization process.

In order to better understand the changes that the one-step recrystallization produced on the low silica zeolite Y materials (Si/Al: 6.5), solid state NMR analysis of aluminum and silicon nuclei was done on H-Y-6-PAR and H-Y-6-REC-40h zeolitic materials. The deconvolution of the  $^{27}\text{Al}$  MAS NMR spectra using the DMFIT® software is still under process. So only qualitative evolutions will be given here.

The  $^{27}\text{Al}$  MAS NMR spectra of parent and 40 hour-recrystallized low silica zeolite Y (Si/Al: 6.5) were compared in Figure 3-25. As mentioned before for the high silica zeolite Y, H-Y-6-PAR showed signals associated with octahedral aluminum sites in EFAL domains. These Al VI sites are present in two different environments, as shown by the two different peaks, one sharper at -1.4 ppm and one wider at 5.4 ppm. The sharp peak at -1.4 ppm is due to highly labile Al species, in small oligomeric entities, while the wider peak at 5.4 ppm is due to bigger species in extra-framework aluminum hydroxide-type phases. The following differences between parent and recrystallized materials were observed: The signals associated with octahedral Al species showed a small change in intensity: Al VI sites become slightly less abundant in recrystallized material (H-Y-6-REC-40h) compared to parent zeolite Y (H-Y-6-PAR). Indeed, while the fraction of the sharpest signal around 0 ppm increased, the wider signal decreased in intensity upon recrystallization. This change was due to some removed aluminum-hydroxide-type EFAL species upon recrystallization.

On the other hand, the signal centered at 60 ppm, due to Al IV sites, in H-Y-6-REC-40h is slightly wider than the signal due to tetrahedral sites in H-Y-6-PAR, indicating more dispersity in the Al local environments in the zeolite framework upon recrystallization. This peak is the signature of Al sites in the zeolite framework. The fraction of these tetrahedral aluminum species is quite constant upon recrystallization; this result is in concordance with the fact that the loss of acidity was not significant. Additionally, the signal around 30 ppm, assigned to pentahedral aluminum species and which is related to defaults in the zeolite crystalline network is evidenced clearly in H-Y-6-REC-40h, while it was not significant in H-Y-6-PAR. This change was probably caused by the desilication process, which occurred during the first 40h of the one-step recrystallization.

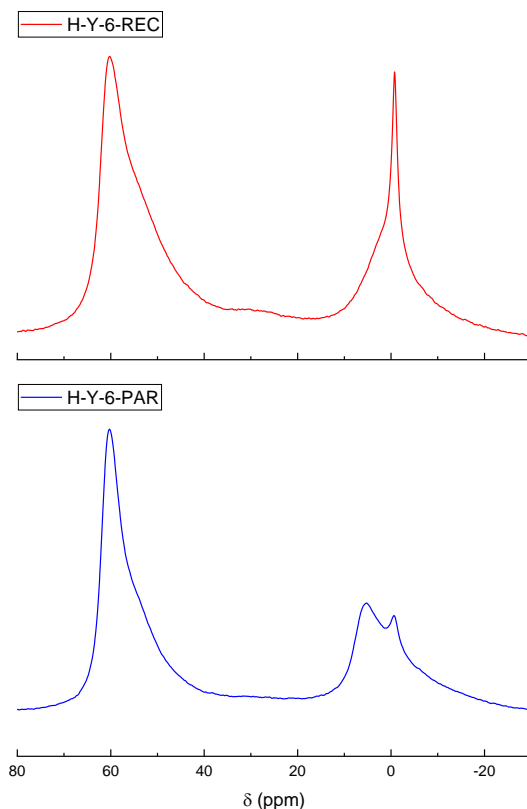


Figure 3-25  $^{27}\text{Al}$  MAS NMR spectra of H-Y-6-PAR and H-Y-6-REC-40h.

On the other hand,  $^{29}\text{Si}$  MAS NMR spectra of parent and recrystallized low silica zeolite Y (Si/Al: 6.5) were compared in Figure 3-26. The amount of  $\text{Q}_4$  type Si atoms attached to just Si atoms (signals at -111 ppm and at -107 ppm) did not show a significant difference between H-Y-6-PAR (65.6%) and H-Y-6-REC-40h (67.0%) materials. However, the amount of Si atoms  $\text{Q}_4$  attached to one Al atom (peak centered at -102 ppm) decreased from 29.4% in H-Y-6-PAR to 24.5% in H-Y-6-REC-40h. This shows that the zeolite framework in the REC sample is less rich in Al atoms, this result could be related to the destruction of part of the zeolite framework during recrystallization, in accordance with  $^{27}\text{Al}$  MAS NMR data. The amount of Si atoms with a chemical environment that is associated to the signals below -97 ppm increased from 5.0% in H-Y-6-PAR to 8.4% in H-Y-6-REC-40h. These signals could be associated with  $\text{Q}_4$  Si atoms attached to two aluminum atoms or  $\text{Q}_3$  Si atoms attached



to one hydroxyl. This signal could be related to the redeposited amorphous aluminosilicate phase which is present in the low silica zeolite Y.

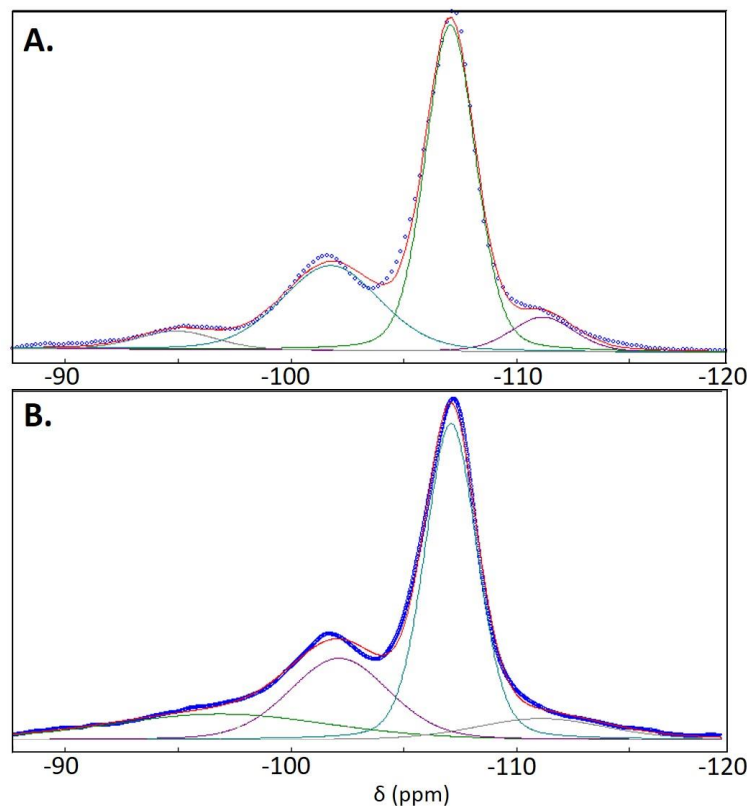


Figure 3-26  $^{29}\text{Si}$  MAS NMR spectra of (A) H-Y-6-PAR and (B) H-Y-6-REC-40h.

- **FTIR analysis of acidic sites properties on the high silica zeolite Y-based H-form zeolitic materials**

As observed in Figure 3-27, there were not observed a significant difference in the total acidity values of H-Y-6-PAR (847  $\mu\text{mol/g}$ ) and H-Y-6-REC-40h (889  $\mu\text{mol/g}$ ), as well as the distribution of weak or strong distribution acidic sites upon recrystallization. To evaluate in deep infrared analysis of adsorbed deuterated acetonitrile was done on each of these materials to identify the Lewis and Brönsted acid sites as well as to differentiate and to quantify the strength of the different Brönsted acid sites on the catalysts [224].

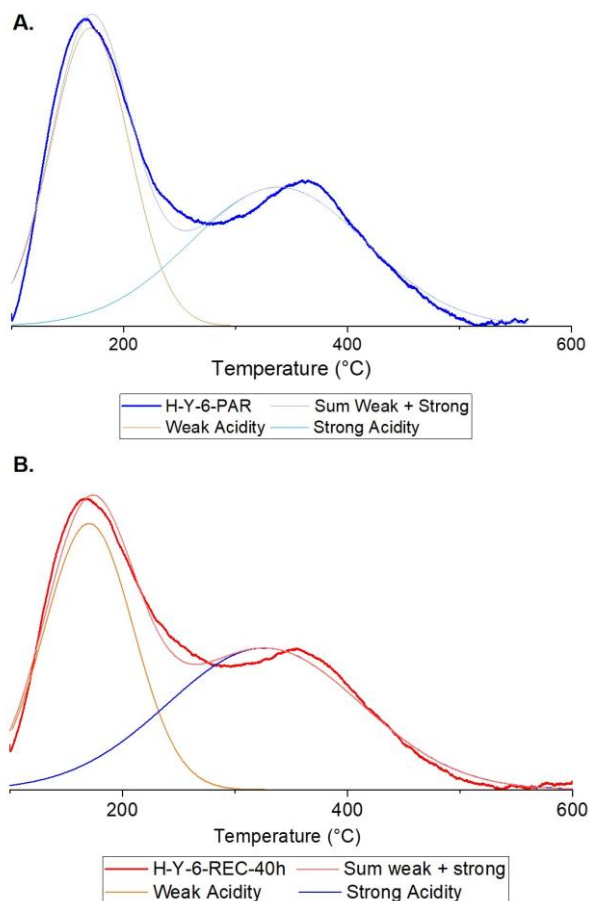


Figure 3-27 Temperature-programmed ammonia desorption profiles of the (A) parent exchanged (H-Y-6-PAR) and (B) recrystallized (H-Y-6-REC-40h) zeolite Y-based materials.

Parent and recrystallized low silica zeolite Y-based materials both revealed the three bands in the spectral region of O-H stretching (Figure 3-28-A1 and B1) described previously for the high silica zeolite Y materials. For the low silica zeolite Y, H-Y-6-PAR and H-Y-6-REC-40h, the band around  $3739\text{ cm}^{-1}$  was assigned to the  $\nu(\text{OH})$  of the terminal silanol groups (Si-OH). In contrast with the case of the H-Y-30-REC material, the intensity of the silanol band in H-Y-6-REC-40h was not more intense than in H-Y-6-PAR. On the other hand, the bands assigned to the  $\nu(\text{OH})$  of bridged hydroxyl groups (Si-OH-Al) in the supercage ( $3627\text{ cm}^{-1}$ ) and in the sodalite cages ( $3565\text{ cm}^{-1}$ ) were observed in H-Y-6-PAR and H-Y-6-REC-40h. Additionally, two supplementary bands at  $3669$  and  $3600\text{ cm}^{-1}$  were observed in these materials. They have been assigned to hydroxyl groups present in extra-framework phases [232]. A significant decrease in their intensity was observed between H-Y-6-PAR and H-Y-6-REC-40h materials; this is consistent with the decrease of the amount of EFAL species as revealed by  $^{27}\text{Al}$  MAS NMR.

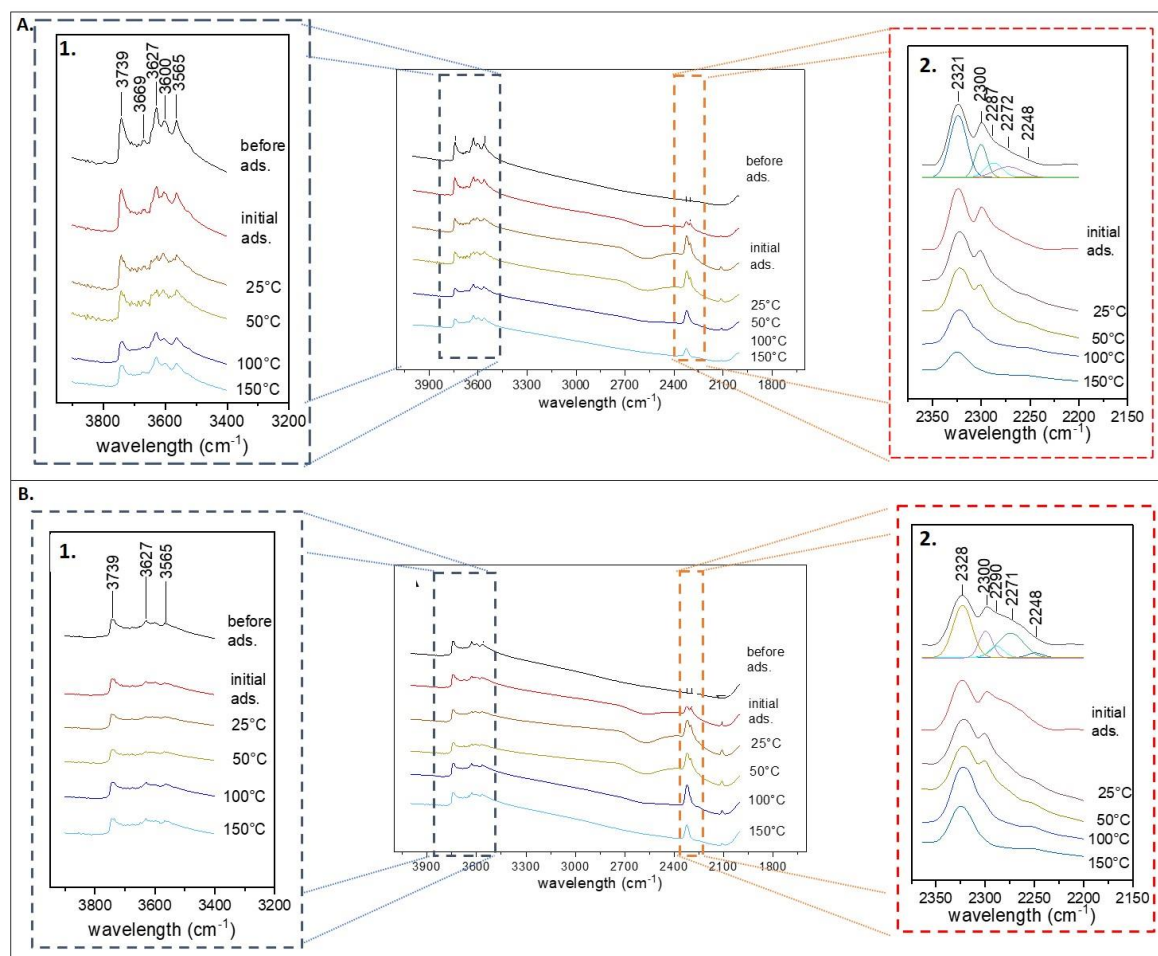


Figure 3-28 FTIR spectra of adsorbed  $\text{CD}_3\text{CN}$  on low silica zeolite Y as a function of the temperature desorption of (A) H-Y-6-PAR and (B) H-Y-6-REC-40h with the enlargement of the 3400-3900  $\text{cm}^{-1}$  zone (1) and the enlargement of the 2200-2400  $\text{cm}^{-1}$  zone (2).

FTIR spectra of adsorbed  $\text{CD}_3\text{CN}$  of parent and recrystallized low silica zeolite Y are shown in Figure 3-28. In the OH stretching region of both materials (Figure 3-28-A1 and -B1) the adsorption of  $\text{CD}_3\text{CN}$  led to a slight decrease of the band around  $3739\text{cm}^{-1}$  and a significant decrease of the bands from  $3730$  to  $3550\text{ cm}^{-1}$ . On the other hand, bands from  $2200$  to  $2400\text{ cm}^{-1}$  appeared related to the  $\nu(\text{CN})$  of the adsorbed species. The signal is a composite with at least five components in both materials in this spectral region (Figure 3-28-A2 and B-2) [224,232]. Apart from the  $2248\text{ cm}^{-1}$  band relative to the  $\nu_{\text{as}}(\text{CD}_3)$  frequency, the other four bands are attributed to the  $\nu(\text{CN})$  mode of deuterated acetonitrile adsorbed on different acid sites. The first band ( $2272\text{ cm}^{-1}$  H-Y-6-PAR and  $2271\text{ cm}^{-1}$  H-Y-6-REC-40h) corresponds to the adsorption on silanol. Second ( $2287\text{ cm}^{-1}$ - parent and  $2290\text{ cm}^{-1}$ - recrystallized) and third ( $2300\text{ cm}^{-1}$  H-Y-6-PAR and H-Y-6-REC-40h) bands have been attributed the adsorption of  $\text{CD}_3\text{CN}$  on the bridged hydroxyl Si-OH-Al Brönsted acidic sites inside the supercage and sodalite cages, respectively. The fourth band ( $2321\text{ cm}^{-1}$ -parent and  $2328\text{ cm}^{-1}$ -recrystallized) corresponded to acetonitrile adsorbed on the Lewis acid sites. Comparing H-Y-6-PAR (Figure 3-28-A-2) and H-Y-30-REC (Figure 3-28-B-2) in the  $\nu(\text{CN})$



spectral region, it is possible to say that the Brönsted-Lewis acidic sites ratio was almost the same in both materials. The presence of the redeposited materials led to a slight increase of the amount of weak Brönsted acid sites related to these groups. The amount of bridged hydroxyl Si-OH-Al strong Brönsted acidic sites was similar in both materials.

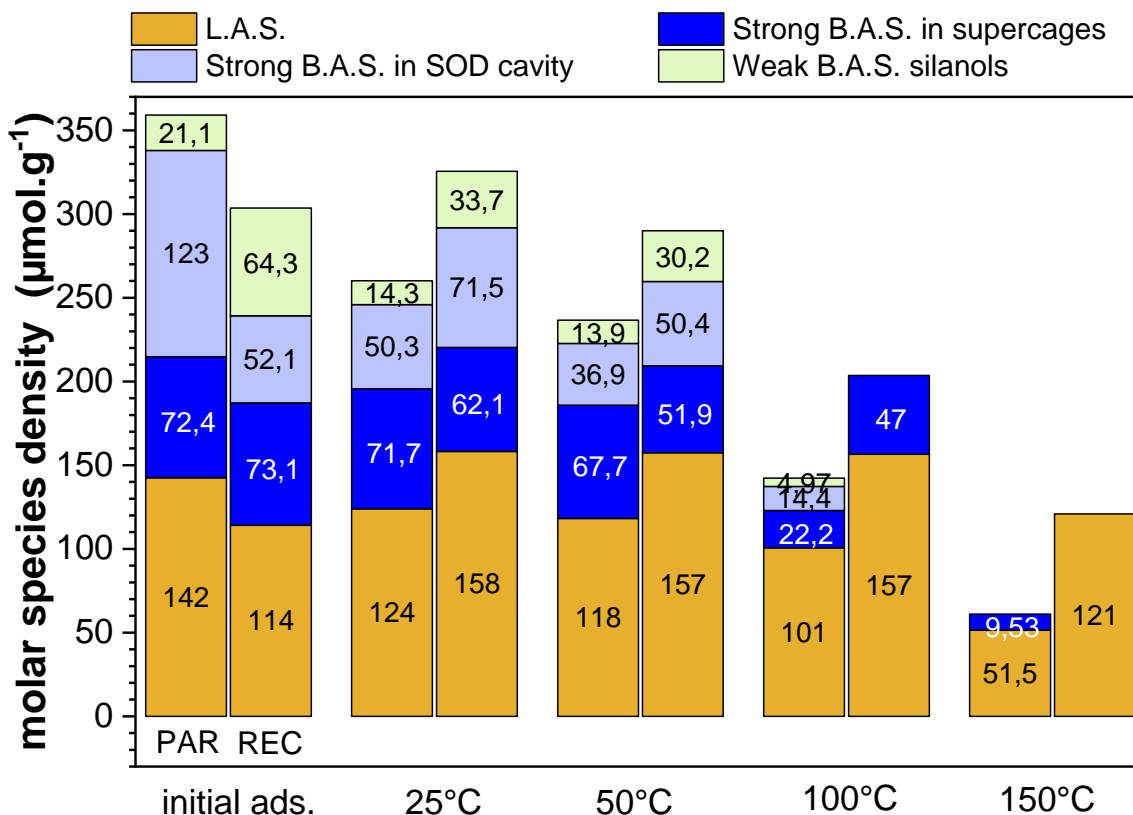


Figure 3-29 Comparison of the molar density of acidic sites between parent (H-Y-6-PAR-40h) and recrystallized (H-Y-6-REC-40h) H-form of zeolite Y with Si/Al: 6. i. silanol groups Brönsted acidic sites. ii. Brönsted acid sites of sodalites cages. iii. Brönsted acid sites in supercages. iv. Lewis acidic sites.

The band decomposition and the analysis considering the extinction coefficients reported for each kind of acid site enabled us to compare the molar density of different acidic sites (Figure 3-29). As previously described, the analysis of the values reported at 25°C, showed that the total IR band areas were similar in both catalysts suggesting a similar total acid site amount. There is a slightly higher amount of Brönsted acid sites in H-Y-6-REC-40h (150.3  $\mu\text{mol/g}$ ) than in H-Y-6-PAR (136.1  $\mu\text{mol/g}$ ) at this temperature. While the temperature was increased, the number of adsorbed molecules decreased fast because they are not enough or are not strong enough. There were no significant differences among both materials when the temperature was increased, indicating no differences in number or accessibility of acidic sites, at least for a small molecule probe as the  $\text{CD}_3\text{CN}$ .

### ▪ Conclusions

The analysis of the results of characterization of the zeolitic materials obtained by the one-step recrystallization of low silica zeolite Y (Si/Al: 6.5), showed the synthesis of micro-mesoporous zeolitic materials by hydrothermal treatment for 40 to 330h. A significant increase in the amount of intracrystalline mesopore volume while maintaining the majority of the micropore volume allowed us to conclude that in the described conditions, it was possible to get a mesoporous low silica zeolite.

However, in contrast with the recrystallization of high silica zeolite Y, due to the higher stability of the low silica material to base attack, it was necessary to apply long duration recrystallization treatment in order to generate intracrystalline mesopores with a significant volume. Moreover, the intracrystalline mesopores seem to be organized on a shorter distance. No well-defined homogeneous wormlike mesoporous texture is observed on TEM images, but rather mesoporous domains distributed heterogeneously along the crystals. It cannot be easily confirmed that some interconnexions exist between micropores and mesopores in the crystals.

Nevertheless, a noticeable feature is the generation of a considerable intracrystalline mesopore volume while the zeolite microporous volume was not decreased; this could be associated with a true recrystallization mechanism at long treatment times. The results also showed that some EFAL species were removed during the recrystallization process, and the appearance of a redeposited amorphous aluminosilicate phase on the low silica zeolite Y crystals did not significantly affect the acidic properties of the materials. In conclusion, the total acidity of the material was not significantly affected by the recrystallization process, the number of strong Bronsted acid sites was slightly increased, as the number of weak Bronsted sites and the number of Lewis acid sites.

## 3.3 Conclusions

The synthesis of the micro-mesoporous zeolitic materials was done by one-step recrystallization, consisting of a hydrothermal treatment with a base and CTAB as the surfactant. It allowed the synthesis of mesoporous zeolite-based materials from two different frameworks: ferrierite and faujasite (zeolite Y). The brief of the properties of the materials prepared in this work has been done in the Table 3-4.

Table 3-4 Brief of properties of the parent and recrystallized zeolitic materials obtained by one-step recrystallization using a base and CTAB as meso-pore structure directing agent

		FERRIERITE		ZEOLITE Y			
				High silica		Low Silica	
		PAR <sup>a</sup>	REC <sup>b</sup>	PAR	REC	PAR	REC
						40 h	330 h
Base material		HSZ 720KOA® (Si/Al: 9.2)		CBV 760 (Si/Al: 30)		CBV 760 (Si/Al: 6.0)	
Framework		FER				FAU	
Microporous channels		8-MR (0.35 x 0.48 nm) 10-MR (0.42 x 0.54 nm)		12-MR (0.74 x 0.74 nm)			
Preparation conditions		I.E. <sup>c</sup> + Calc. <sup>d</sup>	NaOH (0.25 M) – CTAB – 130°C – 72h	Calc.	TMAOH (0.07 M) – CTAB – 150°C – 1h	Calc.	TMAOH (0.09 M) – CTAB – 150°C 40h 330h
Si/Al		9.7	6.6	30.2	24.4	6.5	6.8 6.9
V <sub>micro</sub> (cm <sup>3</sup> /g)		0.13	0.10	0.17	0.10	0.23	0.23 0.21
V <sub>meso-intra</sub> <sup>e</sup> (cm <sup>3</sup> /g)		0.01	0.13	0.13	0.41	0.08	0.24 0.33
V <sub>meso-inter</sub> <sup>f</sup> (cm <sup>3</sup> /g)		0.06	0.15	0.15	0.07	0.13	0.03 0.03
SAXS <sup>g</sup> peaks (2Θ)		No	No	No	2.0 and 4.0°	No	No 0.5°
Meso-pore system obtained in one-step rec.	Ordered	-	No	-	Like MCM-41 type materials	-	No Ordered on a lower distance
	Size (nm)	-	10 – 50	-	3.7	-	2.5 – 3.2
	Morphology	-	Parallelepiped-shaped	-	Hexagonal	-	Hexagonal
	Distribution	-	Embedded in the crystals. Well distributed along 10-MR channels	-	Embedded in the crystals. Worm-like structure in all the crystal	-	Embedded in the crystals. Worm-like structure in mesoporous domains
	Connectivity	-	Connected with the external surface via micropores	-	Hirearchical micro-mesoporous connectivity	-	Micro and mesoporous domains. Connected with the external surface via micropores
Total acidity (μmol/g) <sup>h</sup>		1050	720	254	239	847	889 908
Acidity interacting with CD <sub>3</sub> CN (μmol/g) <sup>i</sup>	Lewis	90	178	34	36	124	158 -
	Bronsted in Si-Al-OH	368	222	40	25	122	134 -
	Bronsted in Si-OH	101	215	9	0	14	34 -

<sup>a</sup> Parent. <sup>b</sup> Recrystallized <sup>c</sup> Ionic Exchange <sup>d</sup> Calcination at 550°C <sup>e</sup> Intracrystalline mesoporous volume<sup>f</sup> Intercrystalline mesoporous volume <sup>g</sup> Small angle X-ray scattering <sup>h</sup> Values reported from TPD-NH<sub>3</sub> analysis<sup>i</sup> Acidity values reported from the temperature-programmed FTIR analysis of adsorbed CD<sub>3</sub>CN at 25°C.

The ferrierite-based materials were obtained by recrystallization following the methodology developed by Cheng et al. [13]. It was possible to conclude that it led to a micro-mesoporous ferrierite-based structure with embedded mesopores. This mesopore system is composed of parallelepiped-shaped mesopores of sizes from 10 to 50 nm along the 10-MR channel

direction, and they are connected to the external surface via micropores. It was measured that there was a loss of around one-quarter of micropore volume and as well as around one-third part of the total acidity of the parent material, caused by the dissolution of part of the crystalline structure of the ferrierite. It was concluded that the loss of the acidity was directly proportional to the loss of tetrahedral aluminum species, represented in Brönsted acidic sites of ferrierite frameworks. Additionally, the presence of a higher amount of weaker Brönsted acidic sites associated with terminal silanols in H-FER-REC is consistent with the growth of a mesoporous phase onto zeolite crystals.

On the other hand, the zeolite Y-based materials were obtained from high and low silica faujasite zeolites based on the works of Vaugon [15] and Chal [14], respectively. In the case of the recrystallization of the high silica zeolite Y CBV 760® (Si/Al: 30), it was possible to conclude that it led to the formation of a hierarchically porous ordered structure containing mesopores and micropores, in which the mesopore system is constituted of cylindrical mesopores arranged on a short length scale similarly to MCM-41 –type materials, with mesopores of 3.8 nm size. The presence of a higher amount of weaker Brönsted acidic sites associated with terminal silanols in H-Y-30-REC is also in agreement with the growth of a redeposited amorphous phase.

Finally, the preparation of microporous-mesoporous materials from CBV 712 ® Zeolite Y (Si/Al: 6.5) is proposed here for the first time with recrystallization procedures from 40 to 330h. In this case, due to the higher stability of this material to base attack, a long hydrothermal treatment was necessary for obtaining a meso-microporous material with embedded zeolitic and mesoporous domains within the crystals, with no loss in microporous volume neither in acidity. The analysis showed that some EFAL species, present in the parent material, were removed during the recrystallization process. Finally, the appearance of a redeposited amorphous aluminosilicate phase in the low silica zeolite Y did not significantly affect the low silica zeolite Y material acidic properties. In conclusion, the total acidity of the material did not significantly change upon recrystallization, the number of strong Bronsted acid sites was slightly increased, as the number of weak Bronsted sites and the number of Lewis acid sites.

## **4. Performance test of Ferrierite type catalytic materials in methyl oleate isomerization.**

The recrystallized ferrierite and the parent material have been evaluated as catalysts in the methyl oleate isomerization in batch and continuous flow reactor. Different parameters have been evaluated such as activity, conversion, selectivity, and deactivation. Ferrierite zeolites have been chosen according to the literature where they have already been successfully used for the isomerization of oleic acid [70,79]. The main goal here is to evaluate the differences induced by the creation of the mesoporous system in the recrystallized ferrierite on its catalytic performance in methyl oleate isomerization.

### **4.1 Catalytic performance evaluation in batch conditions**

The first experiments of isomerization of methyl oleate have been carried out in batch reactor, in order to evaluate the potentiality of recrystallized ferrierite in this reaction, and also to adjust the best possible reaction conditions. The first tests were done according to the best conditions reported in the literature in isostearic acid production from oleic acid, i. e. temperatures between 260°C and 285°C, pressures of 2.0 and 4.0 MPa and an amount of catalyst of 5 wt% [70]. The results obtained are summarized in Table 4-1 and Figure 4-1. Globally, the use of recrystallized H-FER-REC compared to the parent sample leads to almost equivalent conversions, but to slightly higher selectivities to branched-chain products. The effect of pressure and temperature seems marginal at best, at least in batch reactor, where, in the absence of kinetic monitoring the evolutions of conversion and selectivity vs. time cannot be determined.

The yields in branched-chain products obtained for methyl oleate isomerization in this work in batch conditions were better than values previously reported. The yield values were above 55%. These values are largely superior to the 42% previously reported on methyl oleate isomerization done at 260°C during 6h [76]. The best yield value to C<sub>18</sub> branched-chain products, 62.0%, was found using the recrystallized ferrierite sample as a catalyst at 285°C.

Table 4-1 Methyl oleate isomerization conversion, selectivity, and yield in branched product values (Cat. amount: 5%wt.; reaction time: 8h; N<sub>2</sub> atmosphere).

Temp (°C)	Catalyst	Pressure (Mpa)	Conversion (%)	Branched products		Coke amount in spent catalyst <sup>a</sup> (% wt.)
				Selectivity (%)	Yield (%)	
260	H-FER-PAR	2.0	97.4	60.0	58.4	14.5
		4.0	98.6	56.7	55.9	11.6
	H-FER-REC	2.0	95.9	62.3	59.8	19.3
		4.0	98.3	59.2	58.2	20.3
285	H-FER-PAR	2.0	99.4	55.6	55.3	13.5
		4.0	99.1	56.0	55.5	13.4
	H-FER-REC	2.0	98.8	60.2	59.5	17.9
		4.0	98.7	62.8	62.0	18.9

<sup>a</sup> Calculated from TGA results as the sum of mass losses from 250 to 700°C.

However, this higher temperature, compared to 260°C, leading to a higher yield of branched products also leads to a higher amount of cracking products (see Figure 4-1) because cracking is favored at higher temperatures [235]. The effect of pressure depends on the temperature. The increase of pressure led to a decrease in yields at 260°C, but to a slight increase at 285°C, and the same trends are observed on the parent and the recrystallized materials. Two reasons can explain this effect. The first one is the higher accessibility to the micropore network on H-FER-REC compared to the H-FER-PAR, and this effect is accentuated by the increase of pressure. This could lead to higher yields in branched products as, according to the pore mouth hypothesis [79,201], the isomerization reaction happens just in the pore mouth of 10-MR channels in the zeolite. Although recrystallized materials have less Brönsted strong acidic sites, as evidenced by FT-IR spectroscopy using acetonitrile as a probe (see section 3.1.2), the newly created mesopore system allows a better access to new pore mouths where active sites are located, improving the interaction between the substrate and the inner acidic sites. The second reason is the higher diffusivity of the coke precursors, due to the presence of mesopores. It could retard the deactivation of the acidic sites, allowing them to convert more molecules. The shape selectivity losses which could be expected with the losses of well-constrained ferrierite channels network were not observed. It has been reported before [93,111,149] that the creation of mesoporous network, especially when it is hierarchically organized with micropores, can improve the selectivity because it shortens the diffusion path and it can avoid secondary reactions. Additionally, the mesopores created within the ferrierite network are linked to the external surface only through micropore channels (see chapter 3), preventing the leave of some by-products until they are reconverted. Moreover, the fact that less Brönsted acidic sites of high strength are present compared to the parent sample also decreases the probability of successive reactions, and reinforces the selectivity caused by the pore mouth catalysis.

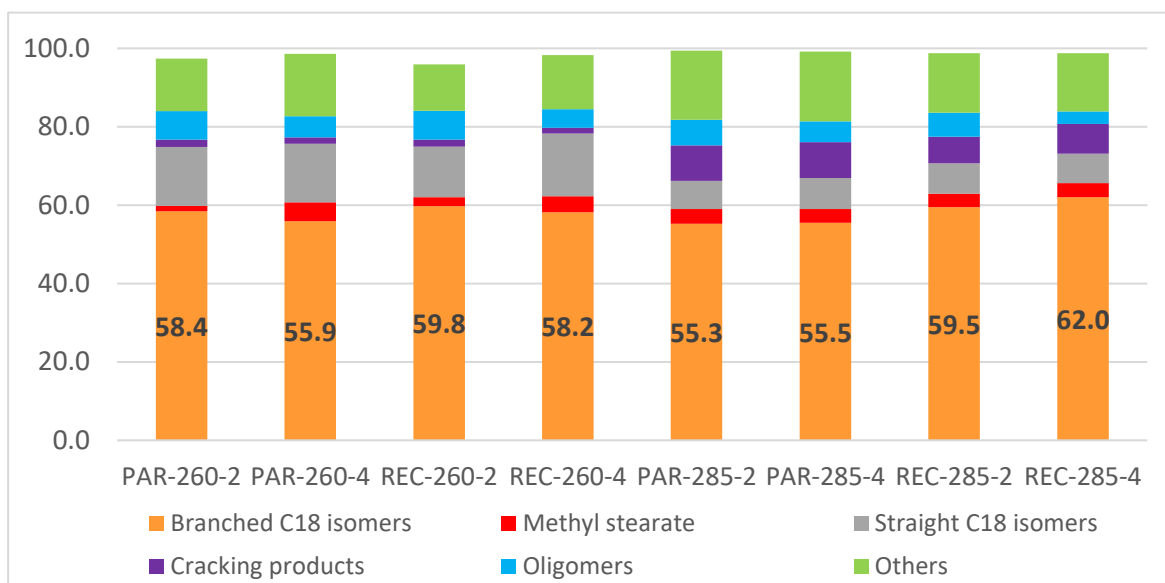


Figure 4-1 Methyl oleate isomerization products yields obtained using H-FER-PAR and H-FER-REC as catalysts at different temperatures (260, 285°C) and pressures (2.0, 4.0 MPa).

Previous work on the isomerization of oleic acid performed by Ngo et al. described the positive influence of triphenylphosphine used as additive (10%wt) on the yield of the reaction [78]. In order to assess the effect of these additives in the present reaction, the experiments at 260°C and 4.0 MPa were repeated, putting as additives a bulky base (triphenylphosphine 10wt.% respect to catalytic material) to prevent the acidic sites on the external surface exterior of ferrierite crystals to be active and water (1.0 mL) to convert some Lewis acidic sites into Brönsted ones.

The results of these reactions compared to the reaction without additives is shown in Figure 4-2. Although lower amounts of by products were obtained with the use of additives, lower conversions and yields in branched products were observed. A significant decrease in oligomer products was observed. The bulky triphenylphosphine base blocks the external acidic sites responsible for the formation of oligomers. However, under these conditions, the excess of blocking of acidic sites also leads to the decrease of yield in branched products, especially when using recrystallized ferrierite samples, as it probably also blocks the access to pore mouth acidic sites. These results are corroborated by the decrease of the amount of coke in the spent catalyst when using the additives. In the case of H-FER-PAR, the amount of coke decreased from 11.6 to 6.7%. In the case of H-FER-REC, the amount of coke decreased from 20.3 to 10.9 % (see below the analysis of coke). This decrease was caused by this blocking of the acidic sites by the bulky base.

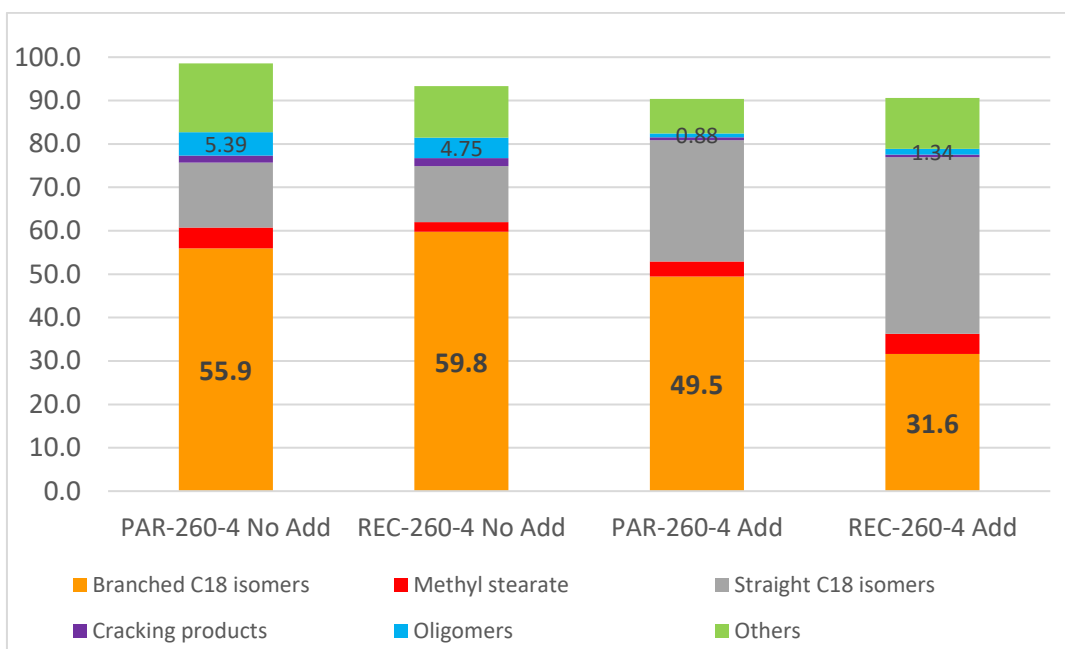


Figure 4-2 Evaluation of the effect of a bulky base (triphenylphosphine) and water as additives in the yields of the methyl oleate isomerization products at 260°C and 4.0 MPa using H-FER-Par and H-FER-Rec as catalytic materials.

In order to have some insights about catalyst deactivation and the nature of the coke causing deactivation, spent catalytic materials were washed and the liquid extracts were analyzed by GC-MS and MALDI-TOF. The solid part of the spent catalytic material was analyzed by TGA to evaluate the amount of coke remaining on the ferrierite, and further CP MAS  $^{13}\text{C}$  NMR analysis was carried out to give insights about the nature of the carbonaceous material present on the spent catalysts.

The spent materials were first washed with acetone, to remove remains of the products and reactants of the reaction, according to the work of Weckhuysen et al. [105]. It was followed by Soxhlet extraction for 24 h with dichloromethane. This procedure has shown to remove the soluble components of the coke which are not inside of the porous network of the spent catalyst [236,237]. GC-MS and MALDI-TOF analysis of the liquid phase extracted after the first step of washing by acetone showed that only traces of products of the reaction that were not removed after filtration remained. Typical MALDI-TOF spectra obtained from the liquid phase extracted in the second step by dichloromethane are shown on Figure 4-3. They first showed minimal remains of products of methyl oleate isomerization detected as lithium adducts like oleic acid ( $[\text{C}_{18}\text{H}_{34}\text{O}_2]\text{Li}^{+}=289$ ), methyl oleate ( $[\text{C}_{18}\text{H}_{36}\text{O}_2]\text{Li}^{+}=303$ ), hydroxy compounds ( $[\text{C}_{18}\text{H}_{36}\text{O}_3]\text{Li}^{+}=319$ ) as well as estolides ( $[\text{C}_{37}\text{H}_{70}\text{O}_4]\text{Li}^{+}=585$ ) and dimers of methyl oleate ( $[\text{C}_{38}\text{H}_{72}\text{O}_4]\text{Li}^{+}=600$ ). In the mass spectrum methyl losses were detected corresponding to the peaks at  $m/z$  269 ( $[\text{C}_{18}\text{H}_{30}\text{O}]\text{Li}^{+}$ ) and at  $m/z=262$  ( $[\text{C}_{18}\text{H}_{30}\text{O}]^{+}$ ). The peak at  $m/z=183$  of formula  $[\text{C}_{12}\text{H}_{15}\text{O}]\text{Li}^{+}$  corresponds to the loss of hexane, while the peak at  $m/z=121$  corresponds to the formula  $[\text{C}_8\text{H}_9\text{O}]^{+}$ , the peak at  $m/z=108$  corresponds to methoxyphenyl  $[\text{C}_7\text{H}_8\text{O}]^{+}$  and the fragment at  $m/z=77$  is the radical phenyl  $[\text{C}_6\text{H}_5]^{+}$ . Finally, the principal peak obtained in all the spectra of MALDI-TOF analysis is related to



intermediates of alkylbenzene production ( $[C_{19}H_{33}O]^+=277$ ) previously observed in the literature as coke precursors [11,76]. This precursor was identified by MS-MS analysis of  $m/z=277$  corresponding to 1-dodecyl-6-methoxycyclohexa-1,3-diene.

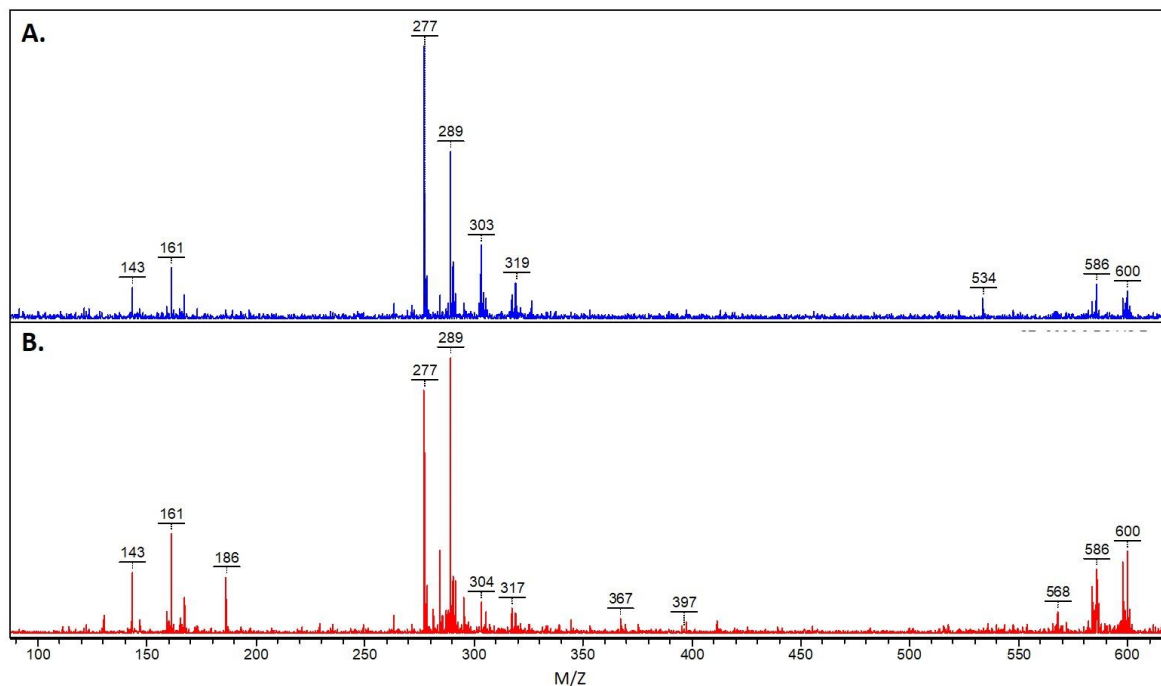


Figure 4-3 MALDI-TOF spectrum of extracts of dichloromethane extract from A. H-FER-PAR and B. H-FER-REC spent catalytic materials used in methyl oleate isomerization doped with lithium trifluoroacetate.

Thermo gravimetrical analysis (TGA) results from spent catalytic materials (Figure 4-4) showed three phases of mass losses previously associated with remain traces of high volatile products (120-250°C), remains of high molecular weight products, non-polyaromatic (250-400°C), and polyaromatic coke (400-700°C)[76], being this last one the highest of them. The amount of coke in the spent catalyst was calculated from TGA results as the sum of mass losses from 250 to 700°C. The amount of coke present in the different samples of spent catalysts is shown in Table 4-1. The amount of coke in the spent catalyst was calculated from TGA results as the sum of mass losses from 250 to 700°C. Mass losses are higher in recrystallized samples than parent one at both temperatures. These higher coke amounts can be explained by the mesopores' presence where more coke can be formed. Although this new mesoporous network could enhance the transport of coke precursors out of the micropore ferrierite structure, the fact that these mesopores were connected to the external surface of the crystals by micropores could avoid that these precursors leave the catalytic material particles. This is also in line with the fact these experiments are carried out in batch reactor (without any possibility to follow the kinetics of the reaction due to too many experimental hurdles), which means that the time at which the maximum conversion is attained is unknown. The remaining reaction time, after the maximum conversion is reached, then can lead to the formation of side-products and/or

coke. This happens probably when the reactants cannot diffuse to catalytic sites anymore, and therefore cannot be transformed inside the zeolite channels due to shape selectivity.

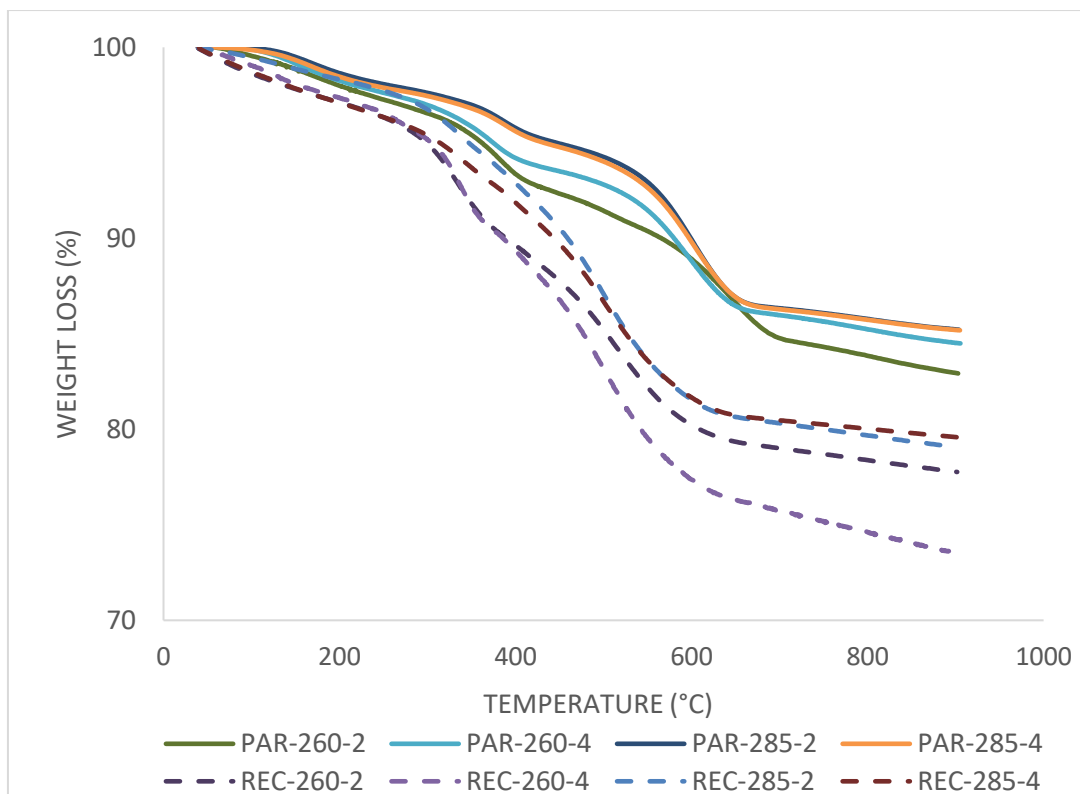


Figure 4-4 TGA analysis of parent exchanged (H-FER-PAR) and Recrystallized (H-FER-REC) spent ferrierite-based catalytic materials.

To go further in the coke analysis,  $^{13}\text{C}$  CP MAS NMR spectrum of the spent catalyst has been registered to give insights on the nature of the carbonaceous material (Figure 4-5). Globally, signals from 0 to 70 ppm were assigned to aliphatic carbons, while the signal at around 130 ppm was assigned to aromatic carbons [238–240]. Among the signals obtained between 0 and 70 ppm, the signals from 10 to 20 ppm were assigned to methyl groups ( $-\text{CH}_3$ ) in aliphatic chains, while signals from 20 to 35 ppm were assigned to methylene groups ( $-\text{CH}_2-$ ) in aliphatic chains [238]. Another signal around 60 ppm was assigned to methylene groups in alpha or beta position to a heteroatom like oxygen [238,240]. The primary signal of this last group in spent recrystallized ferrierite at 260°C (spectra i and ii) could be closer to an aromatic ring, which leads to a downfield displacement in the spectrum. The same phenomenon is observed in the spectra of the spent catalyst used in reaction at 285°C (spectra iii and iv). The signal present around 60 ppm, especially intense in spectra iii, indicates the presence of oxygen in the coke. The broad peak around 130 ppm was assigned to carbons in aromatic rings. More intense signals assigned to aromatic carbons can be observed in the spent catalysts of tests at 285°C. This could be due to a higher aromatization at 285°C. This hypothesis is confirmed by the lower intensity in these spectra of the signal around 60 ppm related to methylene close to oxygen in the

experiments at 285°C, in comparison with experiments done at 260°C, indicating a lower amount of this element in the coke.

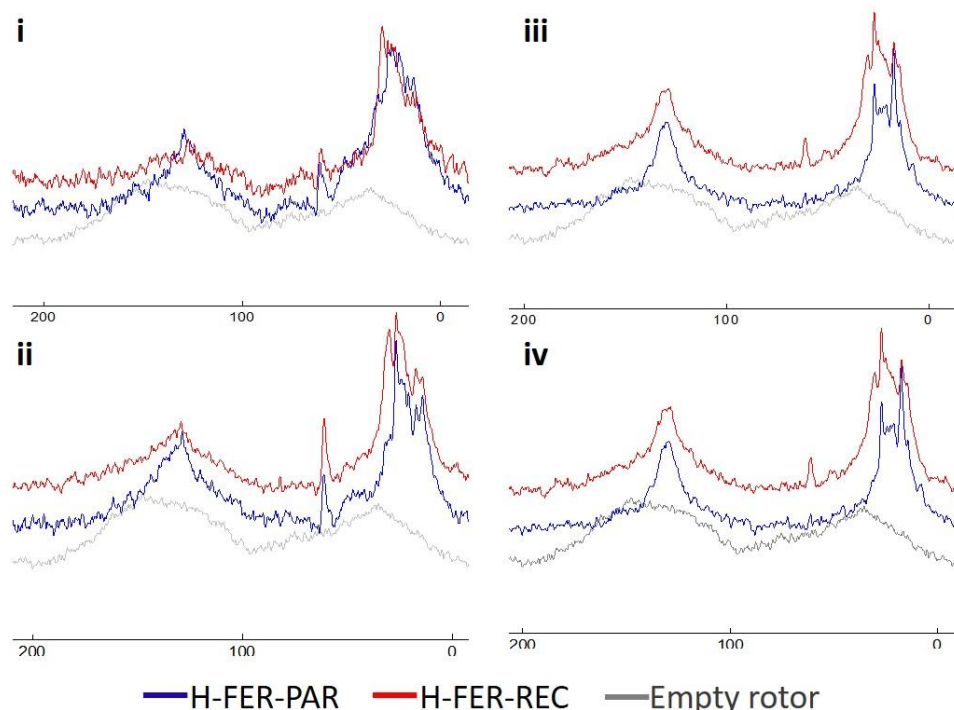


Figure 4-5  $^{13}\text{C}$  CP MAS NMR spectrums of spent catalysts based on ferrierite materials H-FER-PAR (blue) and H-FER-REC (red) after methyl oleate isomerization i. At 260°C and 2.0 MPa ii. At 260°C and 4.0 MPa iii. At 285°C and 2.0 MPa iv. At 285°C and 4.0 MPa.

## 4.2 Catalytic performance evaluation in continuous flow conditions

In order to know more about the catalytic performances of these materials in the face of future industrial applications, and to complete the results already obtained in batch reactor, the methyl oleate isomerization reaction was done in a downstream fixed-bed continuous flow reactor. It is the first time, to the best of our knowledge, that this type of reaction is carried out in a continuous flow reactor, with experiments running for several days. These experiments will allow assessing the behavior and robustness of such catalytic systems. The reaction was carried out using H-FER-PAR and H-FER-REC, both with a weight hourly space velocity (W.H.S.V.) of  $3.5 \text{ h}^{-1}$  at 260 and 285°C as well as pressures of 2.0 and 4.0 MPa, to have conditions comparable to those studied in batch.

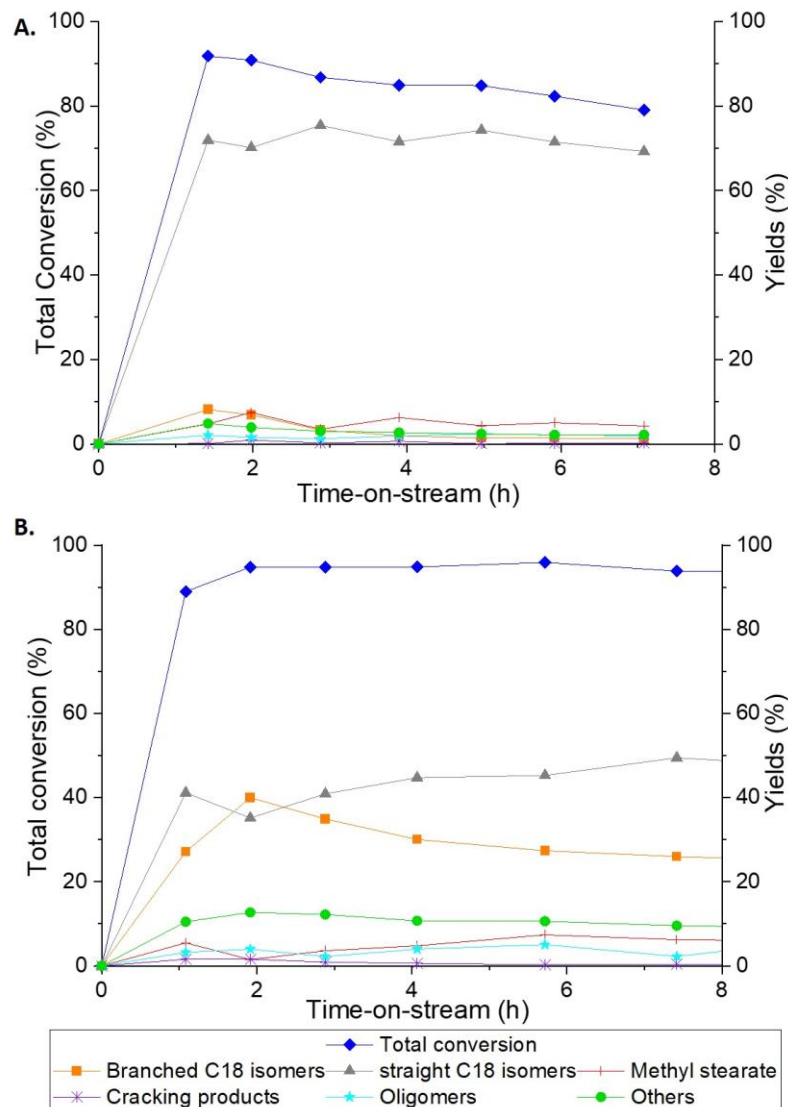


Figure 4-6 Methyl oleate isomerization in a continuous flow reactor at 260°C and 2.0 MPa using as the catalyst A. H-FER-PAR. B. H-FER-REC.

At 260°C and a pressure of 2.0 MPa (Figure 4-6), H-FER-PAR and H-FER-REC catalytic materials showed a similar behavior concerning conversion, with a high and stable value for several hours and a high and quite stable yield (with a slight increase in the case of recrystallized ferrierite) to straight C<sub>18</sub> double bond positional/geometrical (cis/trans) isomers of methyl oleate with ca. 70% for the parent sample, and ca. 40% for the recrystallized sample. These levels of yields were not observed in the batch reactor. Concerning the yields in branched C<sub>18</sub> isomers, which are the desired products, at these conditions of pressure and temperature, they were quite stable (H-FER-PAR  $Y_{bc}$ : 8.2%; H-FER-REC  $Y_{bc}$ : 40.0%) but low compared to the results obtained in batch conditions (H-FER-PAR  $Y_{bc}$ : 58.4%; H-FER-REC  $Y_{bc}$ : 59.8%) especially for the parent sample, for which the difference is huge. This behavior can be explained by shorter contact time between catalytic material particles and methyl oleate, compared to the batch reactor (8h of

reaction), which is not enough to allow consecutive reactions, usually leading to the formation of branched products. And when comparing the levels of branched products yields using parent and recrystallized samples, the difference (ca. 40% with a slow decrease with time-on-stream for recrystallized sample and ca. 8% for the parent one) is striking as they were nearly to the same level in the batch reactor. This is probably due to the shorter time contact in the flow reactor, which illustrated the decisive role played by the mesoporous network created in the recrystallized sample. Indeed, as shown by FT-IR results (see section 3.1.2), although H-FER-PAR has a higher amount of Brönsted strong acidic sites, in these conditions, the mesoporous network allowed increasing the diffusion of the molecules inside the zeolite framework. The contact between the molecules of methyl oleate and the acidic sites present at the mouth of 10-MR channels is then favored. At low pressure, an improvement in the diffusivity of methyl oleate inside the crystalline network of the zeolite can then be obtained by the presence of a new mesoporous network in a downstream fixed-bed continuous flow reactor. When considering more precisely the results obtained with H-FER-PAR, yields in branched-chain products (8.2%) and other by-products were low. Using the parent ferrierite sample, the maximum yield (10%) was reached after one hour of time-on-stream, and its value decreased fast, probably due to the deactivation of Brönsted strong acidic sites located in pore mouths. In contrast, when using recrystallized ferrierite as the catalyst, the maximum yield in branched products (42.5%) was attained after 2h of time-on-stream, and its value decreased slowly until 30%. It can be due to the new mesoporous system that can slow down the pore-blocking phenomenon by allowing precursors in the coke formation to spread from the micropore system to mesopores. Considering that these mesopores are connected to the external surface by micropores, when these precursors grow by oligomerization reaction, they could not leave ferrierite particles, thus retarding the deactivation phenomena. This is confirmed by the increase of production of by-products like methyl stearate, lactones, and oligomers, which started to increase concomitantly to the decrease in branched products production. At this point, due to the blocking of inner acidic sites, the catalytic activity of external acidic sites was more important, leading to a loss of selectivity.

When considering more broadly the catalysts deactivation, shorter contact times in flow reactor are beneficial to the catalyst behavior, as the conversions decrease slowly during the first hours of reaction, and then remain remarkably stable with time-on-stream. This is further supported by the amount of oligomers in continuous flow conditions, which decreases drastically compared to batch conditions, for both catalysts. In these flow conditions, short contact times probably lead to a lower probability for the molecules to be adsorbed on external acidic sites where the shape selectivity is lost.

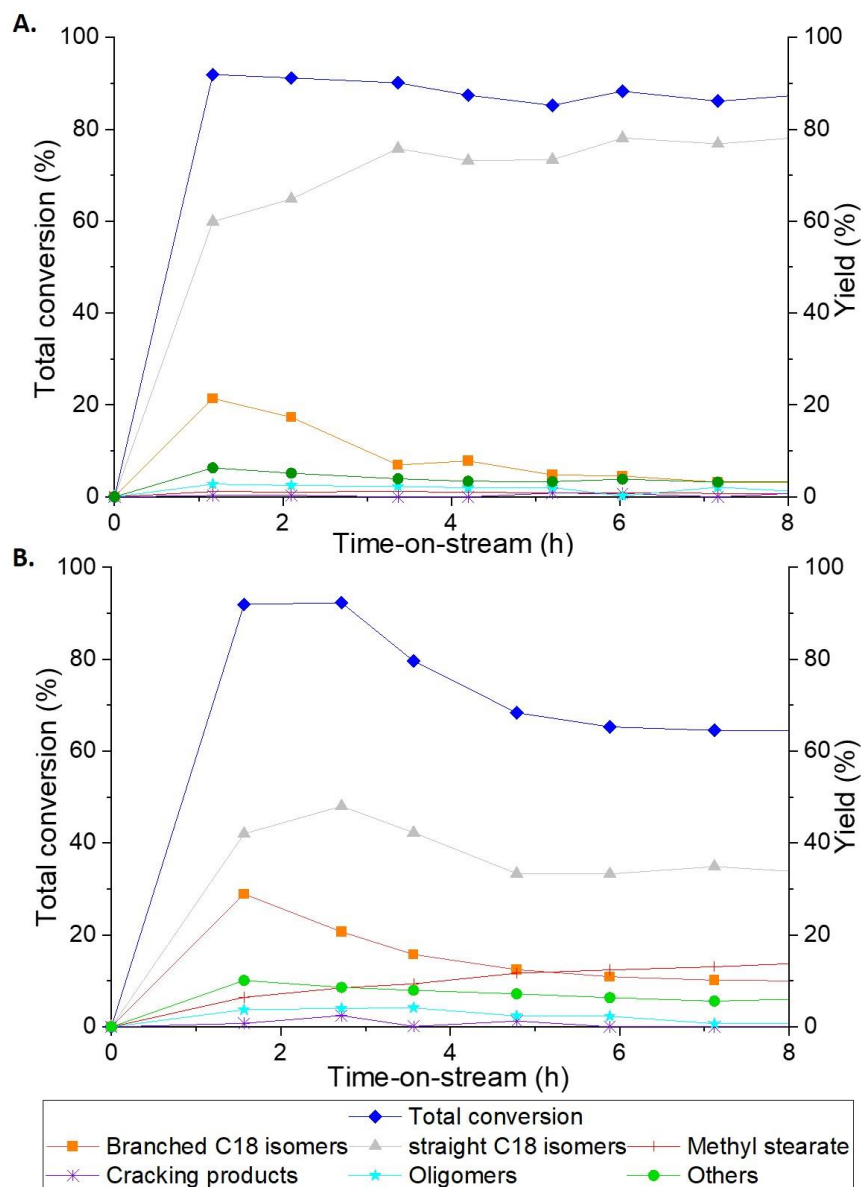


Figure 4-7 Methyl oleate isomerization in a continuous flow reactor at 260°C and 4.0 MPa using as the catalyst A. H-FER-PAR. B. H-FER-REC.

Methyl oleate isomerization reactions were also carried out at 260°C and 4.0 MPa on H-FER-PAR and H-FER-REC (Figure 4-7). In concordance with the behavior previously observed at 2.0 MPa, the major products were again the straight double bond positional/geometrical isomers of methyl oleate. In the case of H-FER-PAR, the yield of straight C18 isomers increased with time-on-stream and reached an even higher value than the value obtained at 2.0 MPa (ca. 80% vs. ca. 70%), which is probably due to an increase in the diffusion of methyl oleate inside ferrierite particles with the higher pressure. It can also explain the higher maximum yield in branched products (22.0%) obtained at 4.0 MPa compared to the maximum value at 2.0 MPa (8.2%). However, this yield decreased quickly

after one hour of time-on-stream, concomitantly to the increase of straight C18 isomers, probably showing a fast deactivation of the stronger acidic sites present in the catalyst.

In the case of H-FER-REC, the yield of straight C18 isomers reached a maximum of 40% at 3h of time-on-stream, and then decreased from 40.0% to 28.9%. It can be related to a higher diffusion of the coke precursors from the microporous channels, delaying the blocking of the channels, which is responsible for the predominant mechanism being then the pore mouth catalysis [71]. At longer time-on-stream, the partial blocking of the channels reduces the catalyst performance. Concerning the yields of branched products, the maximum yield obtained with the recrystallized ferrierite is still higher than in the case of the parent sample, as it reached almost 30% after one hour. Then the yields in branched products decreased quickly with time-on-stream in both cases, with a higher residual yield (10%) in the case of H-FER-REC. As it was mentioned before, it could be related to the presence of the mesopore system. In the presence of mesopores, the precursors of coke can spread outside of the micropore system of the ferrierite framework, delaying the deactivation of acidic sites. At this pressure (2.0 MPa) and temperature (260°C), the new mesopores network played an essential role in improving the behavior of recrystallized ferrierite.

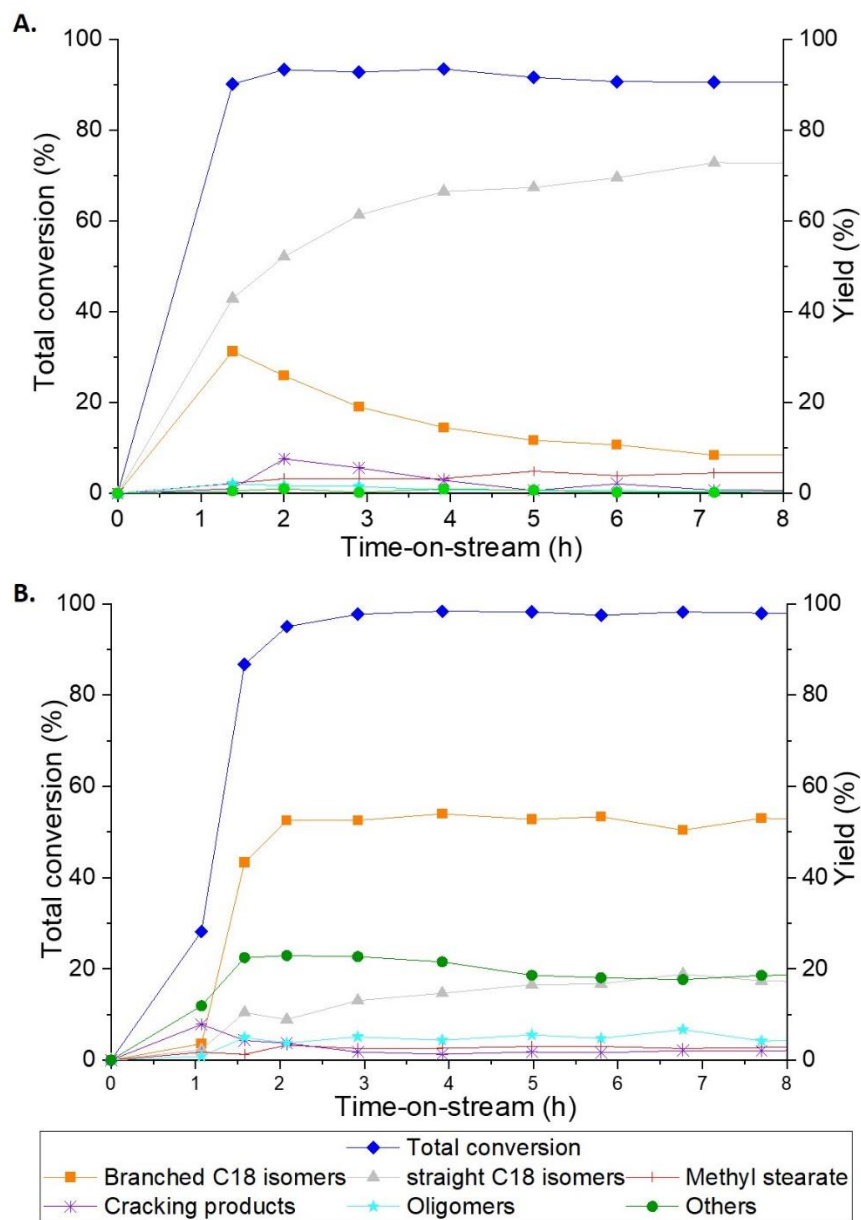


Figure 4-8 Methyl oleate isomerization in a continuous flow reactor at 285°C and 2.0 MPa using as the catalyst A. H-FER-PAR. B. H-FER-REC in the first 8h.

Finally, methyl oleate isomerization was carried out in a downstream fixed-bed continuous flow at 285°C, and a pressure of 2.0 MPa (Figure 4-8) and it showed a different behavior than at 260°C, whatever the pressure used. Reactions using both H-FER-PAR and H-FER-REC as catalysts showed higher conversion values and higher yields in branched products at these conditions. In continuous flow conditions, the temperature increase from 260°C to 285°C has a significant effect. The fast deactivation of strong Brönsted acidic sites and/or fast blocking of the micropores can, however, still be noticed in the case of H-FER-PAR, as the yield of branched product rapidly decreased from 30% to 10%, while it remained stable at a 50% level in the case of H-FER-REC. Yields in lactones, oligomers, and cracking



products showed a similar behavior, with a maximum yield at 10% and a decrease with time-on-stream in the case of H-FER-PAR. These results show that the increase of temperature to 285°C did not significantly improve the catalyst stability as a function of time-on-stream on H-FER-PAR because it has a more constrained microporous structure in which the coke precursors accumulated faster. In contrast, the positive influence of the mesoporous network in H-FER-REC is here clear in allowing a better access to the acidic sites located on the 10-MR channels, leading to the stable branched products yields observed for the first 8 hours of time-on-stream. However, at this temperature, the production of oligomers increased significantly with the use of H-FER-REC, increasing from 0.8% to 6.7% with time-on-stream. The presence of the mesoporous network could lead to a delay in spreading the coke precursors, which could consequently explain the longer time-on-stream needed to reach the maximum yield value for branched products, compared to the experiments at 260°C. Compounds described previously in the literature as coke precursors, like dodecyl benzene [76], which could correspond to what we obtain here (See CP MAS  $^{13}\text{C}$  NMR analysis), have boiling points close to 285°C. This could increase their diffusion, thus delaying the initial coke formation, which leads to pore mouth catalysis. Additionally, it can explain why the catalytic activity was kept with time-on-stream, and why the difference in behavior is so important between 260°C and 285°C. It could retard the total catalyst deactivation at these conditions.

Although a higher temperature improved the yields in branched products in batch conditions, the improvement was more significant at continuous flow conditions. This is probably due to the fact that time contact in the batch reactor is higher (especially since the optimal reaction time is not known in batch conditions) thus allowing side reactions, as well as coke formation.

In order to check if the H-FER-REC kept this activity during longer time-on-stream and with various temperatures, the raw material flow was decreased during the nights to reach a W.H.S.V. of  $1.2\text{ h}^{-1}$ , and increased back to its working value of  $3.5\text{ h}^{-1}$  during the day while also changing the temperature. Two higher temperatures were tested, 310°C and 325°C, and finally the initial temperature, 285°C, was tested again to check the state and robustness of the catalyst after 78h of work (see Figure 4-9).

After changing the temperature to 310°C and collecting samples again, the products obtained did not exhibit the same composition than at 285°C. With the increase of temperature, a significant increase of oligomers, cracking products, and other by-products were observed using both H-FER-PAR and H-FER-REC as catalysts, even if the increase is limited in the case of H-FER-PAR. In the case of methyl oleate isomerization using H-FER-PAR (Figure 4-9-A), the yield in branched products slightly increased with the increase of temperature along with the yields of lactones and oligomers. The yield of cracking products was significantly decreased. This increase in heavier products yields can be explained by the increase of the activity of Brönsted acid sites, which are not blocked yet, with the increase of temperature. However, the yields obtained were lower than the values reported in the initial hours of time-on-stream because the catalyst was already partially deactivated. In contrast, when the reaction was carried out with H-FER-REC as the catalyst

(Figure 4-9-B), a decrease was observed on the yield in branched-chain products, while the increase of temperature led to the increase of the yields in lactones and oligomers as well as the yield in cracking products. The higher amount of other by-products, especially oligomers and cracking products, could lead to the formation of a higher number of aromatic precursors, which can explain a lower yield in branched products as it could increase the deactivation of the strong acidic sites, necessary for the isomerization reaction. But contrarily to what was observed in previous experiments at 260°C, no decrease in the yield of branched products with time-on-stream could be noticed. After the overnight period at low WHSV, the behavior of the two catalysts were observed at the same temperature (310°C). As can be seen from figure 4-8 A and B, conversion values were similar to the day before in both cases, showing the stability of the catalyst with long time-on stream. Although the yield in branched products stays almost unchanged using H-FER-PAR as the catalyst, a decrease was observed in the case of H-FER-REC. It indicated that the deactivation of catalyst H-FER-REC went on, but very slowly.

The temperature was then increased to 325°C. In the case of methyl oleate isomerization using H-FER-PAR, the yield in branched products increased slightly again along with the yields of lactones and oligomers, but the deactivation of the catalyst went on. It indicated that the number of active Brönsted acidic sites of the catalytic material decreased, and the increase of temperature did not help in reducing it. Using H-FER-REC as catalyst, the yield in branched-chain products decreased with the increase of temperature, even if this value is still higher than when the reaction is done with H-FER-PAR as the catalyst. Considering that cracking reactions were favored at these conditions of temperature and pressure in accordance to what is published in the literature [77], this temperature increase led to an increase in cracking products from 20% at 310°C to 30% at 325°C. The main fraction of these gaseous cracking products was composed of low molecular weight hydrocarbons and dimethyl ether. Keeping it in mind, the use of higher temperatures or pressures can lead to dangerous situations with a higher production of volatile products. This working temperature could also lead to an increase in the amount of aromatic precursors for coke formation. This is in line with the significant increase in the oligomers amount observed.

The raw material flow was then decreased again for the night, and the temperature was changed back to 285°C to evaluate the residual activity of the catalysts at the initial working temperature. Although conversion values were unexpectedly high after the overnight period using as catalyst both H-FER-PAR and H-FER-REC, both catalytic materials showed a fast decay in yields in branched products as well as other by-products when the temperature was decreased back to 285°C. It could be related to a higher diffusion of coke precursors outside of the micropore framework of the zeolite at overnight conditions. However, after some time at 285°C both catalysts showed a clear loss of activity, probably related to a high deactivation, which should be studied in more details.

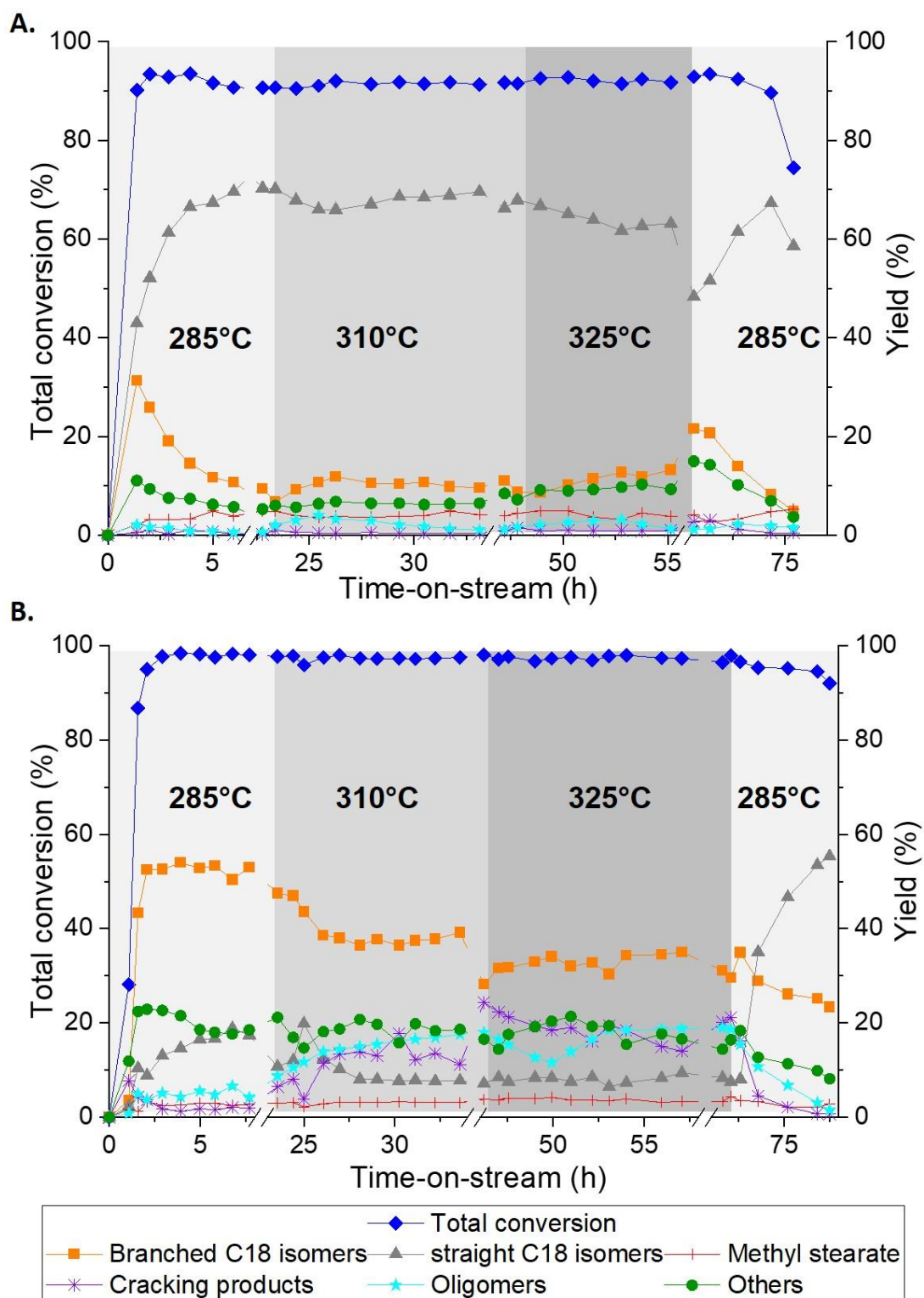


Figure 4-9 Methyl oleate isomerization in a continuous flow reactor at 285, 310, and 325°C with a return point at 285°C with a pressure of 2.0 MPa using as the catalyst A. H-FER-PAR. B. H-FER-REC carried out by 78h.

In general, the increase in temperature from 260°C to 285°C had a positive effect. It could be due to a higher diffusion of raw material molecules inside the ferrierite framework, as well as a higher diffusion of coke precursors, increasing the catalytic stability and leading to higher and stable yields in branched-chain C<sub>18</sub> methyl esters products with time-on-stream. Although higher temperatures of 310 and 325°C allowed keeping high conversions, the yields in branched products decreased. Moreover, these increases in temperature led to higher cracking products and oligomers formation.

### 4.3 Palm biodiesel isomerization in batch conditions

In order to evaluate the effect of the skeletal isomerization reaction in methyl esters from a commercial oil, this reaction was carried out using ferrierite as catalyst on biodiesel from palm oil in batch conditions. Palm oil was obtained from Sigma Aldrich, and methyl esters were obtained through basic transesterification (see section 2.3.1). This palm biodiesel is composed of 52.8% of saturated fatty acid methyl esters, mainly methyl palmitate (C16:0) and methyl stearate (C18:0) and 47.2% of unsaturated ones, mainly methyl oleate (C18:1). Considering the previous results, the reaction was done at 285°C and 2.0 MPa for 8h. The catalyst charge was of 5% wt. with respect to the total methyl ester amount. The isomerization reaction results using H-FER-PAR and H-FER-REC are shown in Figure 4-10, keeping in mind that the saturated methyl esters do not react during isomerization reaction. The unsaturated methyl esters only were taken into account to calculate the different yields.

Although similar conversion values were obtained in this reaction compared to methyl oleate isomerization, a lower yield in branched products was observed. It can be due to the diffusion of saturated fatty acids into the pore mouths of the 10-MR channels that could reduce the number of available acidic sites for isomerization reaction. Comparing the results using H-FER-PAR and H-FER-REC, it shows a slightly higher yield in branched products with H-FER-REC. Moreover, fewer oligomers were obtained using H-FER-REC but a higher amount of straight C<sub>18</sub> isomers and other byproducts. It can be explained by a faster deactivation of inner acidic sites into H-FER-PAR than in H-FER-REC. It could lead to a higher part of the reaction in acidic sites of the external surface of the crystals. This should be studied in detail in further studies.

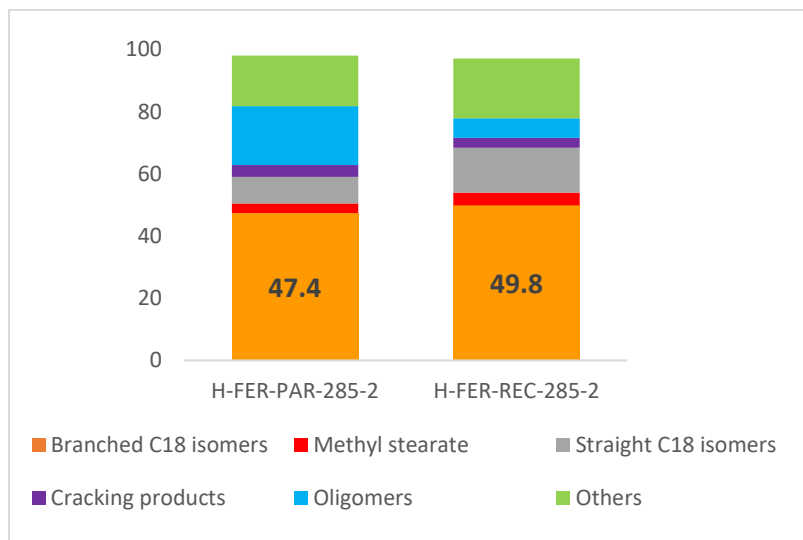


Figure 4-10 Palm biodiesel isomerization at 285°C and 2.0 MPa using ferrierite type catalytic materials

## 4.4 Conclusions

The mesopore system of parallelepiped-shaped pores of sizes from 10 to 50 nm connected to external surface of ferrierite by micropores was created by one-step recrystallization using sodium hydroxide and CTAB lead to the creation of a micro-mesoporous material. Although this led to a material with a lower total acidity than H-FER-PAR, with less Brönsted strong acidic sites (see chapter 3), the large mesopores created along 10-MR channels direction could help to improve the diffusivity of reagents and exploit inner acidic sites.

In batch conditions, the use of H-FER-REC in methyl oleate isomerization led to slight improvements in yields in branched products values from 58.4% to 59.8% at 260°C, and from 55.3% to 62.0% at 285°C. The shape selectivity losses typically associated with the loss of part of the microporosity were not observed in these experiments because the newly created mesopores are connected to the external surface of the zeolite particles through micropores, which can avoid some by-products leave until they are reconverted. The analysis of spent catalytic materials allows observing that although this mesopore system facilitates the transport of coke precursors out of the micropore ferrierite framework, part of the coke precursors stays inside the porous network blocking meso and micropores. Besides, the analysis of the liquid extract of the spent catalysts, allowed to identify one of the coke precursors as 1-dodecyl-6-methoxycyclohexa-1,3-diene.

When the methyl isomerization was carried out in a downstream fixed-bed continuous flow reactor using H-FER-REC as catalytic material, the new mesopores system played an important role in improving the catalytic behavior. Although H-FER-PAR had a higher amount of strong Brönsted acidic sites, the advantage given by the presence of mesopores

inside the zeolite framework played a decisive role in helping the diffusion of molecules, allowing a better access to the acidic sites in the 10-membered rings channels mouths. The mesopore system could also slow down pore-blocking, allowing precursors in the coke formation to spread from the micropore system to mesopores, retarding deactivation processes. From the results obtained after materials characterization (see section 3.1), these mesopores are connected only to the main microporous network through micropores. When these coke precursors grow by oligomerization reaction, they cannot leave ferrierite particles and progressively fill meso and micropores.

Additionally, in continuous flow conditions, the temperature increase from 260°C to 285°C had a significant effect. It could be due to a higher diffusion of raw material molecules inside the ferrierite framework and a better diffusion of coke precursors outside the particles, thus improving the catalytic stability. The improvements due to the use of this micro-mesopore material as the catalyst and the increase of temperature to 285°C led to a continuous flow process that keeps yields in branched products up to 50% without any sign of decrease for the first eight hours of time-on-stream.

Finally, although similar conversion values were obtained on the isomerization reaction carried out on palm biodiesel compared to methyl oleate isomerization in batch conditions, a lower yield in branched products was observed. Comparing the results using H-FER-PAR and H-FER-REC shows that the recrystallized material leads to higher yields in branched-chain products.

## **5.Performances of Zeolite Y catalytic materials in methyl oleate isomerization.**

The recrystallized zeolite Y samples and their parent materials have been evaluated as catalysts in methyl oleate isomerization in batch and continuous flow conditions. Two different Si/Al ratios have been chosen (30 and 6.5), and the main goal is to evaluate the effect of these new characteristics found in recrystallized materials, in the catalytic reaction by evaluating different parameters such as activity, conversion, selectivity and deactivation.

### **5.1 Evaluation of high silica zeolites Y (H-Y-30) as catalytic materials**

#### **5.1.1 Catalytic performance evaluation in batch conditions**

The experimental conditions chosen for the methyl oleate isomerization experiments were those determined in the last chapter that gave the best yields with the ferrierite catalysts, i.e. 260°C with 4.0 Mpa, and 285°C with 2.0 MPa. The results obtained using H-Y-30-PAR and H-Y-30-REC as catalysts are summarized in Table 5-1 and Figure 5-1.

Globally, the use of recrystallized samples led to the same levels of conversions, whatever the temperatures and pressures tested, but to higher yields and selectivities towards branched products for the two different experimental conditions tested.

The best yield value (39.1%) to C<sub>18</sub> branched-chain products was found using the H-Y-30-REC as the catalyst at 285°C and a pressure of 2.0 MPa. In contrast with the yields obtained using the ferrierite materials, this value was inferior to the 42% previously reported in the literature for the methyl oleate isomerization done at 260°C by 6h [76]. However, these results are still very interesting, considering that these materials showed an acidity about four times lower than ferrierite materials. It could be because the strong acidic sites necessary for isomerization in the zeolite Y are more accessible than in the ferrierite, allowing a better contact between the active sites and the substrate. These yields were also improved at both temperatures tested, by the presence of the hierarchical structure present in H-Y-30-REC material, which led to slightly higher yields than with H-Y-30-PAR.

Table 5-1 Methyl oleate isomerization conversion, selectivity, and yield in branched product values using high silica zeolite Y material as catalysts (Cat. amount: 5%wt.; reaction time: 8h; N<sub>2</sub> atmosphere).

Temp (°C)	Catalyst	Pressure (Mpa)	Conversion (%)	Branched products		Coke amount in spent catalyst <sup>a</sup> (% wt.)
				Selectivity (%)	Yield (%)	
260	H-Y-30-PAR	4.0	95.8	29.8	28.5	16.1
	H-Y-30-REC		93.6	30.9	28.9	14.3
285	H-Y-30-PAR	2.0	95.2	38.6	36.8	17.5
	H-Y-30-REC		95.7	40.9	39.1	11.5

<sup>a</sup> Calculated from TGA results as the sum of mass losses from 250 to 700°C.

However, as observed in Table 5-1 The experimental conditions chosen for the methyl oleate isomerization experiments were those determined in the last chapter that gave the best yields with the ferrierite catalysts, i.e. 260°C with 4.0 Mpa, and 285°C with 2.0 MPa. The results obtained using H-Y-30-PAR and H-Y-30-REC as catalysts are summarized in Table 5-1 and Figure 5-1.

Globally, the use of recrystallized samples led to the same levels of conversions, whatever the temperatures and pressures tested, but to higher yields and selectivities towards branched products for the two different experimental conditions tested.

The best yield value (39.1%) to C<sub>18</sub> branched-chain products was found using the H-Y-30-REC as the catalyst at 285°C and a pressure of 2.0 MPa. In contrast with the yields obtained using the ferrierite materials, this value was inferior to the 42% previously reported in the literature for the methyl oleate isomerization done at 260°C by 6h [76]. However, these results are still very interesting, considering that these materials showed an acidity about four times lower than ferrierite materials. It could be because the strong acidic sites necessary for isomerization in the zeolite Y are more accessible than in the ferrierite, allowing a better contact between the active sites and the substrate. These yields were also improved at both temperatures tested, by the presence of the hierarchical structure present in H-Y-30-REC material, which led to slightly higher yields than with H-Y-30-PAR.

Table 5-1, the use of the zeolite Y-based materials as catalysts led to lower values of selectivity in branched-chain products compared to the ferrierite materials. This could be caused by the lower acidity exhibited by the zeolite Y samples, and by the channels network in the faujasite-type framework, which is less constrained than the ferrierite. As previously described in the literature [76] and confirmed by our results, this constraint could be responsible for the high shape selectivity observed using ferrierite as the catalyst. Besides, as observed in Figure 5-1, the amount of oligomers was superior in the reaction products using high silica zeolite Y as catalyst (7.7 – 14.2%) than using ferrierite based materials (3.2 - 7.3%). It is a substantial disadvantage because the favoring of isomerization reaction over oligomerization is one requirement to meet to think about a future industrial application.



The presence of the mesopore system in this case did not have a clear effect on the production of oligomers. Indeed, although the mesopore system is well connected with the micropore domain in the zeolite Y, the selectivity is driven by the micropores which limit the oligomers production.

Comparing the different conditions of pressure and temperature tested here allowed us to conclude that the increase of temperature from 260°C to 285°C led to a higher yield in branched products, whatever the type of sample tested. As observed previously for ferrierite, this increase also led to a higher amount of cracking products (see Figure 5-1). Globally, the use of recrystallized H-Y-30-REC compared to the H-Y-30 led to higher yields in branched-chain products, but this effect was more pronounced at 285°C. Recrystallized material also allowed reducing the amount of cracking products generated, especially at 285°C. It could be caused by the presence of the well-connected mesopores, which facilitate the output of the branched products before they can be branched again, which could be followed by cracking processes.

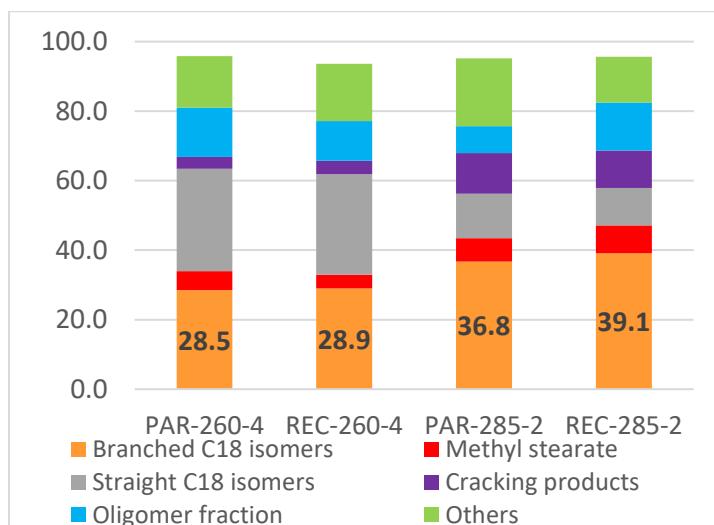


Figure 5-1 Methyl oleate isomerization products distribution using H-Y-30-PAR and H-Y-30-REC at different conditions of temperature (260, 285°C) and pressure (2.0, 4.0 MPa).

As can be observed on the coke amount present calculated from TGA results on the spent catalysts (Figure 5-3), these amounts were lower on H-Y-30-REC than on H-Y-30-PAR. As described before for ferrierite, the presence of the mesopores represents a higher diffusivity of the coke precursors. It could retard the deactivation of the acidic sites, allowing them to convert more molecules. In contrast with the observed for the ferrierite, the mesopores are well connected to the external surface of zeolite crystals. The coke precursors could escape, avoiding part of the coke formation.

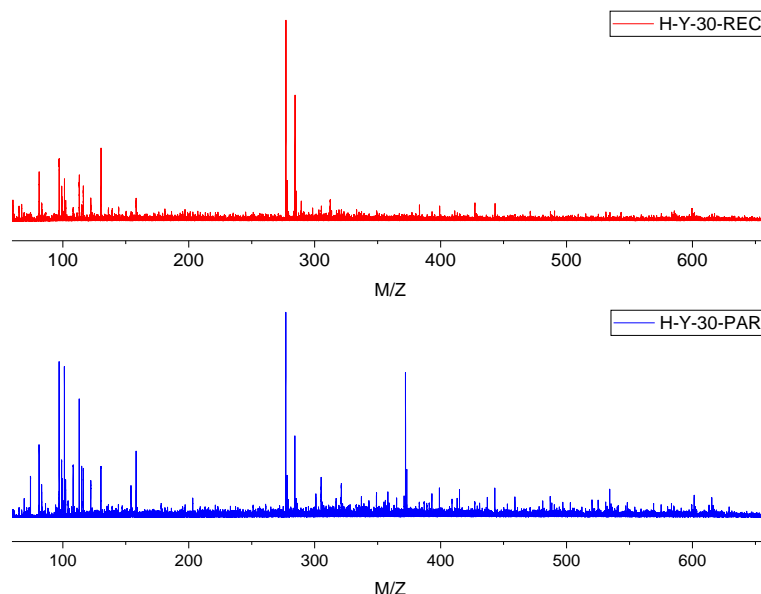


Figure 5-2 MALDI-TOF spectra of extracts of dichloromethane washing from ferrierite spent catalytic materials used in methyl oleate isomerization doped with lithium trifluoroacetate.

In order to have a description about catalyst deactivation and the nature of the coke causing deactivation, spent catalytic materials were washed and the liquid extracts were analyzed by GC-MS and MALDI-TOF as was mentioned in ferrierite experiments (see section 4.1). The solid part of the spent catalytic material was analyzed by TGA to evaluate the amount of coke remaining on the zeolite Y material, and further CP MAS  $^{13}\text{C}$  NMR analysis was carried out to give insights about the nature of the carbonaceous material present on the spent catalysts.

As the ferrierite spent materials, high silica zeolite Y spent materials were first washed with acetone, to remove remains of the products and reactants of the isomerization, according to the methodology previously described (see section 2.2.3). It was followed by Soxhlet extraction for 24 h with dichloromethane. GC-MS and MALDI-TOF analysis of the liquid phase extracted after the first step of washing by acetone showed that only traces of products of the reaction remained. Typical MALDI-TOF spectra obtained from the liquid phase extracted in the second step by dichloromethane are shown on Figure 5-2. They first showed remains of products of methyl oleate isomerization detected as lithium adducts like oleic acid ( $[\text{C}_{18}\text{H}_{34}\text{O}_2]\text{Li}^{++}=289$ ), methyl oleate ( $[\text{C}_{18}\text{H}_{36}\text{O}_2]\text{Li}^{++}=303$ ), and dimers of methyl oleate ( $[\text{C}_{38}\text{H}_{72}\text{O}_4]\text{Li}^{++}=600$ ). In the mass spectrum, the peak lower than  $m/z=130$  as the peak at  $m/z=121$  corresponds to the formula  $[\text{C}_8\text{H}_9\text{O}]^+$ , the peak at  $m/z=108$  corresponds to methoxyphenyl  $[\text{C}_7\text{H}_8\text{O}]^+$  and the fragment at  $m/z=77$  is the radical phenyl  $[\text{C}_6\text{H}_5]^+$ . They correspond to fragments that could be related to cracking products. Finally, the principal peak obtained in all the MALDI-TOF spectra is related to intermediates of alkylbenzene production ( $[\text{C}_{19}\text{H}_{33}\text{O}]^+=277$ ) previously observed in the performance tests of ferrierite-based materials. It was identified as 1-dodecyl-6-methoxycyclohexa-1,3-diene, one coke precursors [11,76].

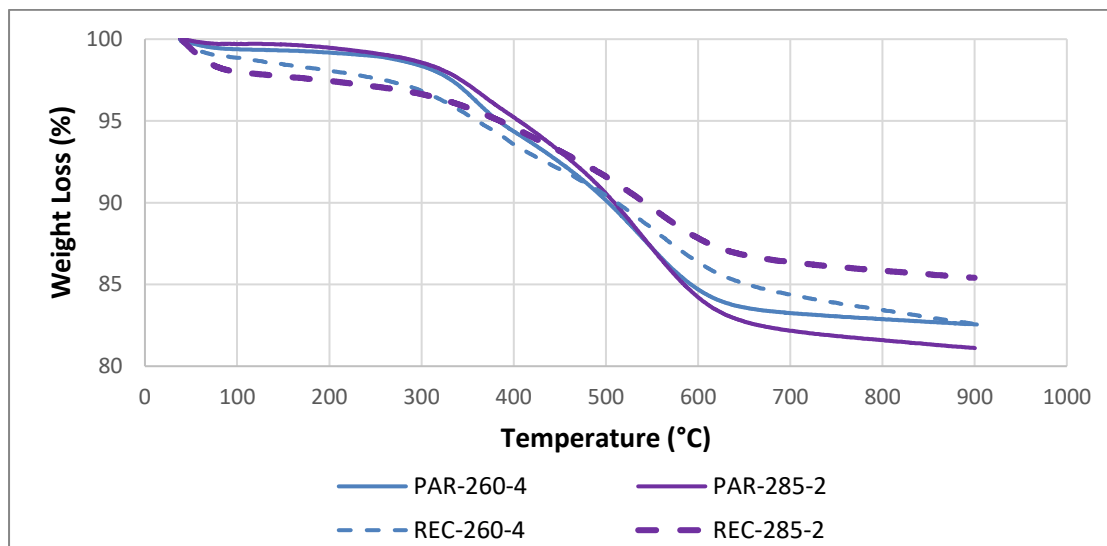


Figure 5-3 TGA analysis of parent H-Y-30 PAR (PAR) and Recrystallized H-Y-30-REC (REC) spent high silica zeolite Y-based catalytic materials.

As can be observed on the coke amount calculated from TGA results on the spent catalysts (Figure 5-3), these amounts were lower on H-Y-30-REC than on H-Y-30-PAR. As described before for ferrierite, the presence of the mesopores leads to a higher diffusivity of the coke precursors. It could retard the deactivation of the acidic sites, allowing them to convert more molecules. In contrast with what was observed for the ferrierite samples, the mesopores are well connected to the external surface of zeolite crystals. The coke precursors could then diffuse out of the zeolite particle, avoiding partly the formation of coke.

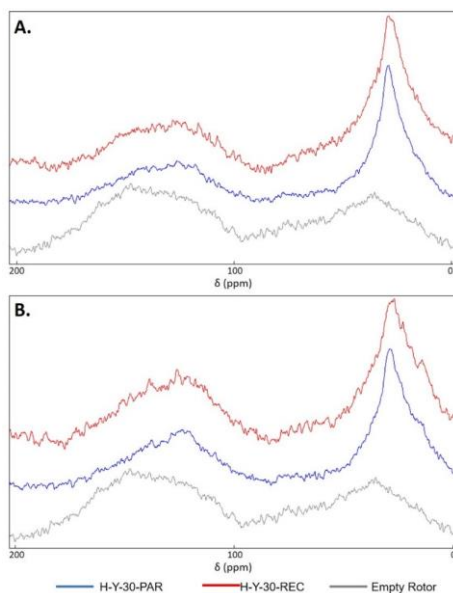


Figure 5-4 Figure 5-5 CP MAS  $^{13}\text{C}$  NMR spectra of spent catalysts based on high silica zeolite Y materials H-Y-30-PAR (blue) and H-Y-30-REC (red) after methyl oleate isomerization A. At 260°C and 4.0 MPa, and B. At 285°C and 2.0 MPa.

As done with spent catalyst based on ferrierite zeolite, to go further in the coke analysis on spent catalyst based on high silica zeolite Y, CP MAS  $^{13}\text{C}$  NMR spectrum of the spent catalyst has been carried out to give insights about the nature of the carbonaceous material (Figure 5-4). The description of the assignation of the different peaks was done in section 4.1. In general, the spent catalyst materials present the major peak centered at 28 ppm, assigned previously to methylene groups ( $-\text{CH}_2-$ ) in aliphatic chains[238], as well one broad and less intense peak centered around 130 ppm, assigned previously to aromatic carbons [238–240]. In contrast with the spectra observed in spent ferrierite-based catalysts, no peak indicated here the presence of heteroatoms. In this case, the peak were well centered around 28 ppm, indicating the presence of groups that can change the chemical environments of these carbons. From these observations, it is possible to see that in these spent catalysts the coke are mainly aliphatic, composed by long alkyl chains of hydrocarbons. No significative changes were observed in the nature of the coke from the high silica zeolite Y spent catalysts from process carried out at 260 and 285°C. Little changes in the nature of the coke were observed between H-Y-30-PAR and H-Y-30-REC in the amount of aromatics and the distribution of aliphatic carbons. However, they are not significative enough to conclude about these changes. It should be studied more in detail.

### **5.1.2 Catalytic performance evaluation in continuous flow conditions**

In order to know more about the catalytic performance of these materials in the face of future industrial applications, and to complete the results already obtained in batch reactor, the methyl oleate isomerization reaction was done in a downstream fixed-bed continuous flow reactor. It is the first time, to the best of our knowledge, that this type of reaction is carried out in a continuous flow reactor. These experiments will allow assessing the behavior and robustness of such catalytic systems and can be compared to the performances of ferrierite materials. The reaction was carried out using H-Y-30-PAR and H-Y-30-REC, both with a weight hourly space velocity (W.H.S.V.) of  $3.5\text{ h}^{-1}$  at 260 and 4.0 MPa, as well as at 285°C and 2.0 MPa.

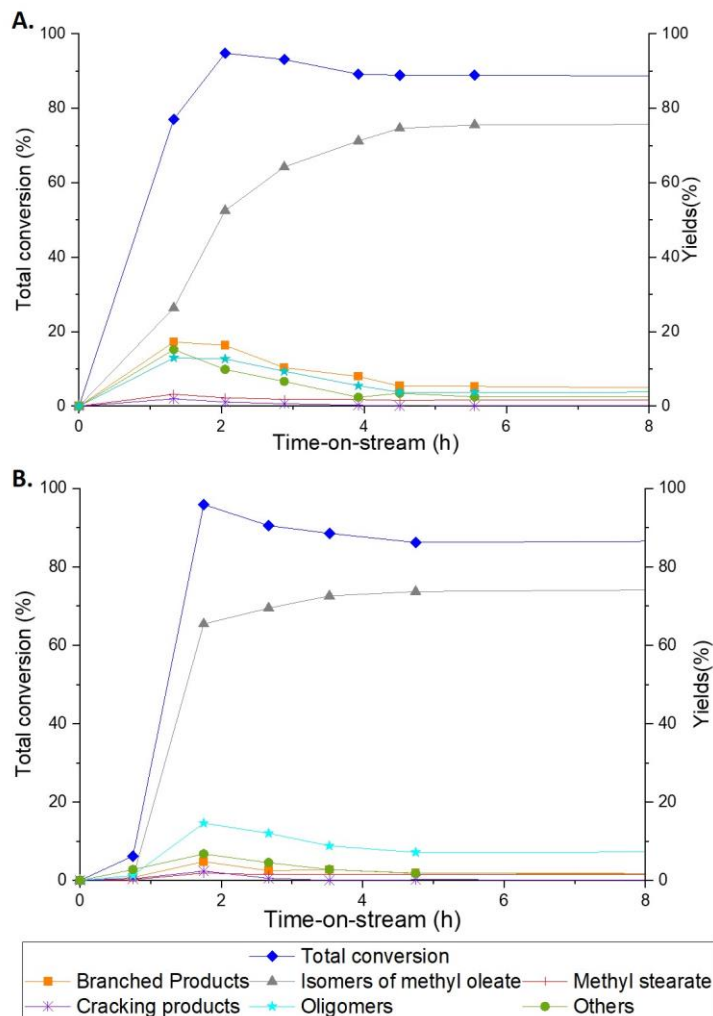


Figure 5-6 Methyl oleate isomerization carried out in continuous flow conditions with a temperature of 260°C and a pressure of 4.0 MPa. A. Using as catalyst H-Y-30-PAR. B. Using as catalyst H-Y-30-REC.

As was observed before using zeolite Y as a catalyst in methyl oleate isomerization in batch conditions, at 260°C and a pressure of 4.0 MPa (Figure 5-6), H-Y-30-PAR and H-Y-30-REC catalytic materials led to a high and stable conversion but also to a very high yield in straight C<sub>18</sub> double bond positional/geometrical (cis/trans) isomers of methyl oleate, which are the major products. At these conditions of pressure and temperature, the yield in C<sub>18</sub> branched-chain products (Y<sub>bc</sub>) was lower in continuous flow conditions (H-FER-PAR Y<sub>bc</sub>: 17.2%; H-FER-REC Y<sub>bc</sub>: 4.8%) than in batch conditions (H-Y-30-PAR Y<sub>bc</sub>: 28.5%; H-Y-30-REC Y<sub>bc</sub>: 28.9%). The composition of the products obtained during the first hours of time-on-stream (TOS) using H-Y-30-PAR did not show a higher selectivity to branched products, as it was the case with ferrierite samples. The yields in branched-chain products (17.2%), oligomers (15.2%) and others by-products (13.0%) were similar, indicating that under these conditions, the faujasite-type framework of the zeolite Y did not lead to a special shape selectivity to branched-chain products.

The use of recrystallized material as catalyst in the isomerization reaction under these conditions led to significantly lower yields in branched-chain products. The mixture of products was characterized by a higher amounts of oligomers products. It can explain why, in contrast with the behavior observed for ferrierite materials, under these conditions, the H-Y-30-REC was less stable with time-on-stream than H-Y-30-PAR. The high amount of oligomers in the micropores could block the inner acid sites, responsible for the obtention of monomer products. A high amount of oligomers could lead to a faster production of coke, with the consequent loss of catalytic activity.

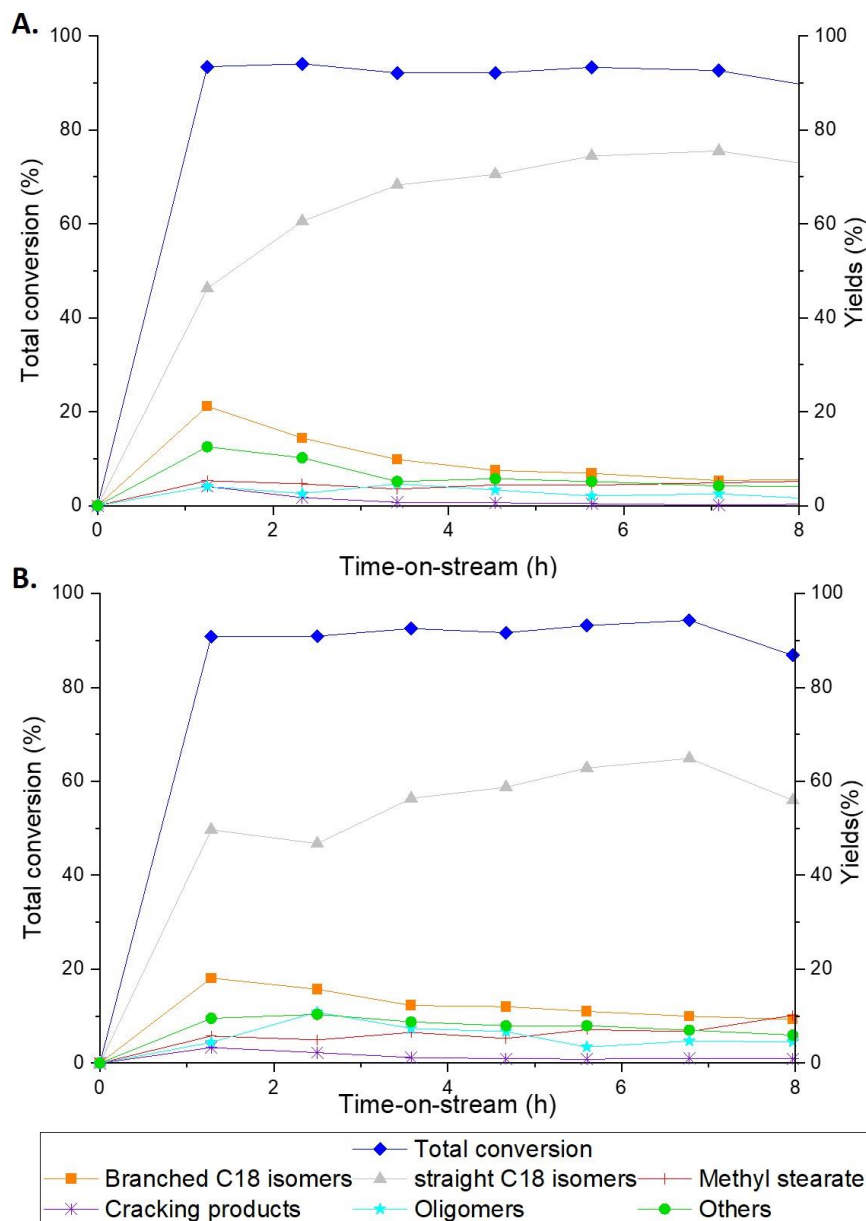


Figure 5-7 Methyl oleate isomerization carried out in continuous flow conditions with a temperature of 285°C and a pressure of 2.0 MPa. A. Using as catalyst H-Y-30-PAR. B. Using as catalyst H-Y-30-REC.

The results obtained in methyl oleate isomerization using H-Y-30-PAR and H-Y-30-REC as catalysts when the temperature was increased at 285°C as a function of time-on-stream are showed in Figure 5-7. Here, it is possible to see that both catalysts kept total conversion values over 90% during the eight hours of the experiment. However, as was mentioned before in the previous experimental conditions, they showed lower yields in branched-chain products and other by-products in comparison to ferrierite based materials. Methyl oleate is mostly converted to straight C<sub>18</sub> isomers, which represent the central part of the conversion. The use of recrystallized zeolite Y-based materials (H-Y-30-REC) as catalyst led to a slight decrease in the yield in C<sub>18</sub> branched-chain products in the first hour of the reaction in comparison with the parent zeolite (From 21% using H-Y-30-PAR to 18% using H-Y-30-REC). A higher presence of oligomers was also found when the H-Y-30-REC acted as catalyst. Comparing the stability of both catalytic materials, H-Y-30-PAR was losing faster the activity of the acidic sites allowing the formation of branched-chain products, as it showed a yield lower than 10% after four hours. In contrast, the recrystallized sample, H-Y-30-REC showed a yield in branched-chain products over 10% even after the eight hours of the experiment. The presence of the vermicular mesopore system in H-Y-30-REC might be the reason of the improvement of the catalyst stability under these conditions. As was mentioned for the experiments in batch conditions, the presence of this mesopore system could avoid or at least retard the blocking of pores by coke because it can increase the diffusion of coke precursors. A reaction temperature closer to the boiling point to coke precursors could also increase the diffusion of coke precursors.

When comparing high silica zeolite Y materials with ferrierite materials, it is possible to observe that although the use of ferrierite led to higher yields in branched-chain products, the activity per acidic site should be higher using the zeolite Y-based materials. According to the analysis of the acidity (see section 3.2.1), the acidity of the ferrierite materials are at least four times higher than the high silica zeolite Y-based materials. As one hypothesis that we propose, it could be related to the fact that there are more available acidic sites per unit in the zeolite Y materials than in the ferrierite. In the ferrierite samples, only 20% of acidic sites are available in the pore mouths of the 10-MR channels [105], and they start to be blocked quickly. On the other hand, the catalysts based on high silica zeolite Y led to a lower selectivity in branched products in comparison with the ferrierite samples, parent or recrystallized. It is probably due to the pore system in zeolite Y, which is composed of a 3D pore systems of larger micropores (0.74 nm) in which the shape selectivity obtained in well-constrained pore ferrierite system is harder to obtain. It indicates that the microporous structure plays the most preponderant role in the high selectivity obtained for Branched-chain C<sub>18</sub> products. Finally, the main effect of the presence of the mesopore system in ferrierite and zeolite Y was the improvement of the stability of the catalyst in continuous flow experiments.

## 5.2 Evaluation of low silica zeolites Y (H-Y-6) as catalytic materials

### 5.2.1 Catalytic performance evaluation in batch conditions

The methyl oleate isomerization experiment using H-Y-6 as catalyst was done under the experimental conditions giving the best yields in branched products by using the high silica zeolites Y as catalysts (285°C, 2.0 MPa). The results obtained using H-Y-6-PAR as the catalyst are summarized in Table 5-2 and Figure 5-8

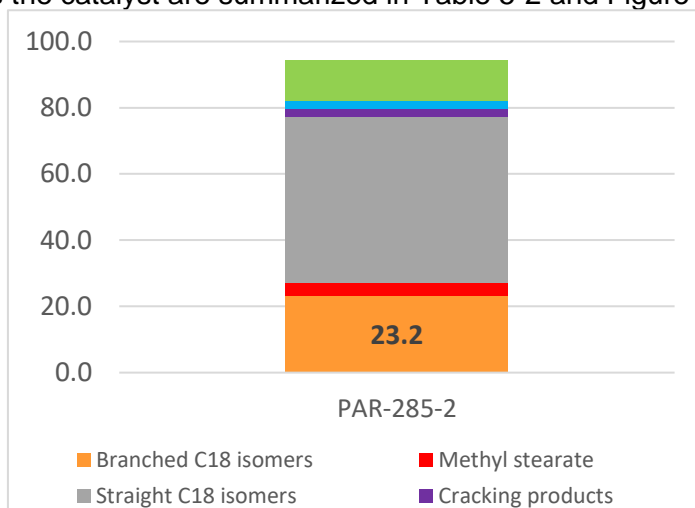


Figure 5-8. Unexpectedly, considering its higher acidity and Si/Al ratio (6.5), the yield in branched-chain products (23.2 %) was lower than using high silica zeolite Y (36.8%) at the same conditions of pressure and temperature.

Table 5-2 Methyl oleate isomerization conversion, selectivity, and yield in branched product values using low silica zeolite Y material as catalysts (Cat. amount: 5%wt.; reaction time: 8h; N<sub>2</sub> atmosphere).

Temp (°C)	Catalyst	Pressure (Mpa)	Conversion (%)	Branched products		Coke amount in spent catalyst <sup>a</sup> (% wt.)
				Selectivity (%)	Yield (%)	
285	H-Y-6-PAR	2.0	94.5	24.6	23.2	22.5

<sup>a</sup> Calculated from TGA results as the sum of mass losses from 250 to 700°C



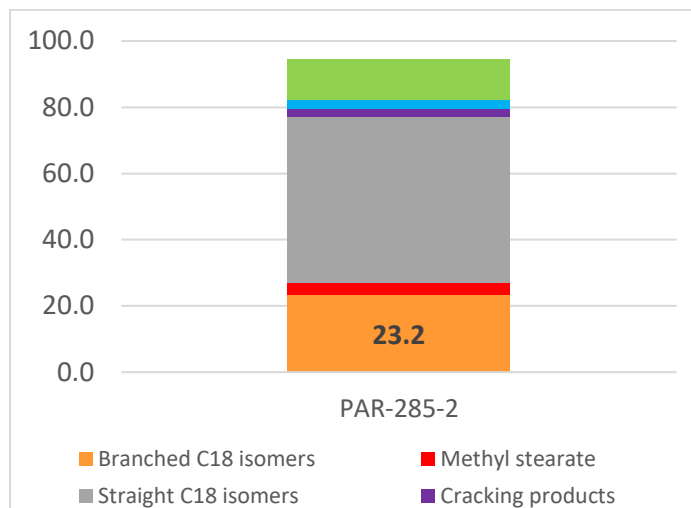


Figure 5-8 Methyl oleate isomerization products distribution using H-Y-6-PAR at 285°C and a pressure of 2.0 MPa.

A hypothesis of the possible cause of this behavior could be the presence of intercrystalline porosity connected to the external surface via micropores with a higher amount of amorphous structure. They are produced during the steaming process used to synthesize this parent material. So, although this material has more acid sites than high silica zeolite material, the acidic sites are less accessible, blocked in part by the amorphous areas present in H-Y-6. Moreover, in these conditions, these acid sites can be easily poisoned by the coke formation, allowing a fast deactivation. This hypothesis should be studied in detail to understand this unexpected lower catalytic performance.

In order to understand better the coke formation during the reaction, the coke amount present on the spent catalyst is reported in Table 5-2 (Figure 5-9). The calculated amount was higher in H-Y-6-PAR (22.5%) than on high silica zeolite Y materials (H-Y-30). Considering that high and low silica zeolite Y present the same framework as well as a similar total pore volume (H-Y-6-PAR: 0.44 cm<sup>3</sup>/g; H-Y-30-PAR: 0.45 cm<sup>3</sup>/g), this difference could be associated to the presence of the occluded large pores in H-Y-6-PAR, as observed in microscopy pictures (see section 3.2.2). As described before for ferrierite, the presence of the mesopores which connect to the surface by micropores can represent a higher diffusivity of the coke precursors but this precursors just start to accumulate, blocking the access to other acidic sites. In contrast with the results observed in the case of ferrierite, this coke formation does not lead to pore mouth catalysis. It is because the channels of the faujasite framework allow that the molecules diffuse even if some acidic sites are blocked. Therefore, the selectivity in branched-chain products does not increase.

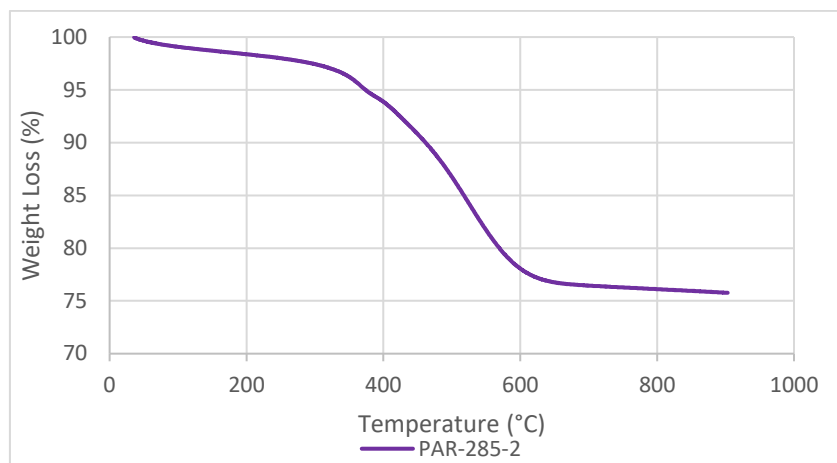


Figure 5-9 TGA analysis of parent (PAR) spent low silica zeolite Y-based catalytic material.

### 5.2.2 Catalytic performance evaluation in continuous flow conditions

In order to know more about the catalytic performance of H-Y-6-PAR and H-Y-6-REC-40h materials, the methyl oleate isomerization reaction was done in a downstream fixed-bed continuous flow reactor to evaluate for the first time, to the best of our knowledge, the behavior of these catalysts and to compare to the results obtained in batch reactor. The reaction was carried out using these catalytic materials, both with a weight hourly space velocity (W.H.S.V.) of  $3.5 \text{ h}^{-1}$  at  $285^\circ\text{C}$  and 2.0 MPa.

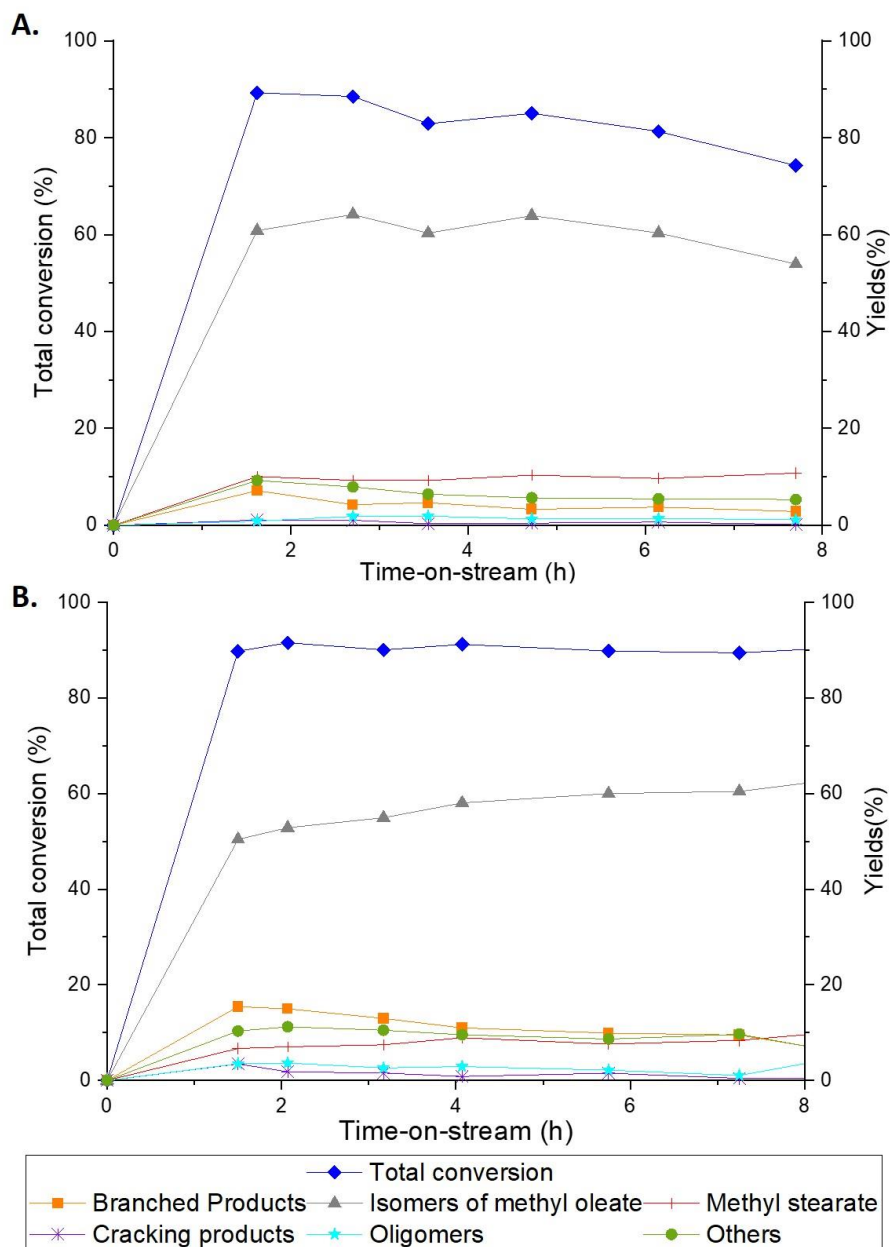


Figure 5-10 Methyl oleate isomerization carried out in continuous flow conditions with a temperature of 285°C and a pressure of 2.0 MPa. A. Using as catalyst H-Y-6-PAR. B. Using as catalyst H-Y-6-REC-40h.

The conversions and yields obtained in methyl oleate isomerization using H-Y-6-PAR and H-Y-6-REC-40h as catalysts as a function of time-on-stream (TOS) are showed in Figure 5-10. As observed using this material as catalyst in batch conditions, unexpectedly, considering its higher acidity and Si/Al ratio (6.5), the yield in branched-chain products was lower than using high silica zeolite Y under the same conditions of pressure and temperature. Comparing parent and recrystallized materials, it is possible to see that while H-Y-6-REC-40h kept the conversion value over 90% during the six hours of the experiment,

the conversion using H-Y-PAR led to a slow decrease with time-on-stream, going from 90% to 80% in 6 hours. As already mentioned concerning the batch experiments, the acid sites can be blocked by the presence of amorphous materials formed during the synthesis process of zeolite Y. Moreover, as mentioned before, they showed the lowest yields in branched-chain products and other by-products in comparison to high silica zeolite Y and ferrierite based materials. As observed with high zeolite Y material, the conversion to straight C<sub>18</sub> isomers of methyl oleate represented vast majority of the products obtained, which is probably due to the porous network arrangement. The use of recrystallized low silica zeolite Y-based materials (H-Y-6-REC-40h) as catalyst led to a significant increase in the yield in branched-chain products in the first hour of time-on-stream in comparison with the parent zeolite (From 7.2% using H-Y-6-PAR to 15.4% using H-Y-6-REC-40h). A higher presence of oligomers was also found when the H-Y-6-REC-40h acted as catalyst. Comparing the stability of both catalytic materials, H-Y-6-PAR lost its ability to form branched products faster, as it showed a yield lower than 10% after four hours of time-on-stream. In contrast, H-Y-6-REC-40h showed a slower decaying of the yield in branched-chain products. Apparently, the presence of the new intracrystalline mesoporosity helped to avoid the blocking of acidic sites by the coke, thanks to the increase of diffusion of coke precursors. It should be studied in more details to understand this unexpected lower catalytic performance.

## 5.3 Conclusions

In general, the use of zeolite Y led to lower yields in branched-chain products in comparison of the use of low silica ferrierite.

In the case of high silica zeolite Y (Si/Al: 30), the fewer number of acidic sites and the less-constrained microporous structure led to lower yields in branched-chain products. However, considering that these materials showed an acidity around four times lower than ferrierite materials, the activity per acidic site was higher using this material. It could be related to the fact that there are more available acidic sites per unit in the zeolite Y materials than in the ferrierite. It was improved by the presence of the hierarchical structure present in H-Y-30-REC material, which led to getting slightly higher yields than using H-Y-30-PAR. Comparing the different conditions of pressure and temperature allowed us to conclude that the increase of temperature from 260°C to 285°C led to a higher yield in branched products. As described before, the presence of the mesopores leads to a higher diffusivity of the coke precursors. It could retard the deactivation of the acidic sites, allowing them to convert more molecules. In contrast with for the results obtained with the ferrierite, the mesopores are well connected to the external surface of zeolite crystals. The coke precursors could escape, avoiding part of the coke formation. Then, the main effect of the presence of the mesopore system in zeolite Y was the improvement of the stability of the catalyst.

In the second case, unexpectedly, considering its higher acidity and Si/Al ratio (6.5), with a similar amount of acidic sites than low silica ferrierite, the yield in branched-chain products was lower than using high silica zeolite Y materials in batch and continuous conditions. In

this material (CVB 712®) the acid sites can be blocked by the presence of amorphous materials formed during the industrial obtainment. It should be studied in detail to understand this unexpected lower catalytic performance. Comparing the stability of both catalytic materials in continuous flow conditions, the presence of the mesopore system led to increase the yield in branched-chain products and it helped to enhance the catalyst stability at least during the first eight hours.



## **6. Determination of the cold flow properties of catalytic test products.**

Beyond the maximization of yields in branched products obtained in methyl oleate isomerization, the distribution of the different compounds in the product is crucial to know their properties and optimize their potential uses. The distribution of branched and straight geometrical and positional isomers has then to be determined in a first step.

In a second step, the behavior of these products in cold environments was evaluated through Differential Scanning Calorimetry (DSC) to know their potential to improve the cold flow properties of biodiesel with high levels of saturated fatty acids. A brief description of the evaluation of cold flow properties by DSC analysis is done in section 1.1.2.

### **6.1 Example of an analysis of methyl oleate isomerization products**

Methyl oleate isomerization reaction products are complex mixtures of gas and liquid phases. The gas phase (see Figure 6-1) is mainly composed of light hydrocarbons, methanol, dimethyl ether, water, and carbon dioxide. Dimethyl ether can be formed at these reaction conditions from methanol by acid dehydration. Light hydrocarbons of two to seven carbon atoms were observed. From the analysis of the mass spectra and retention times of the different peaks, we can conclude that there was a wide distribution of unsaturated and saturated as well as ramified hydrocarbons. It can indicate that poly-branched products were formed, which were subsequently cracked to lead to the formation of these products.

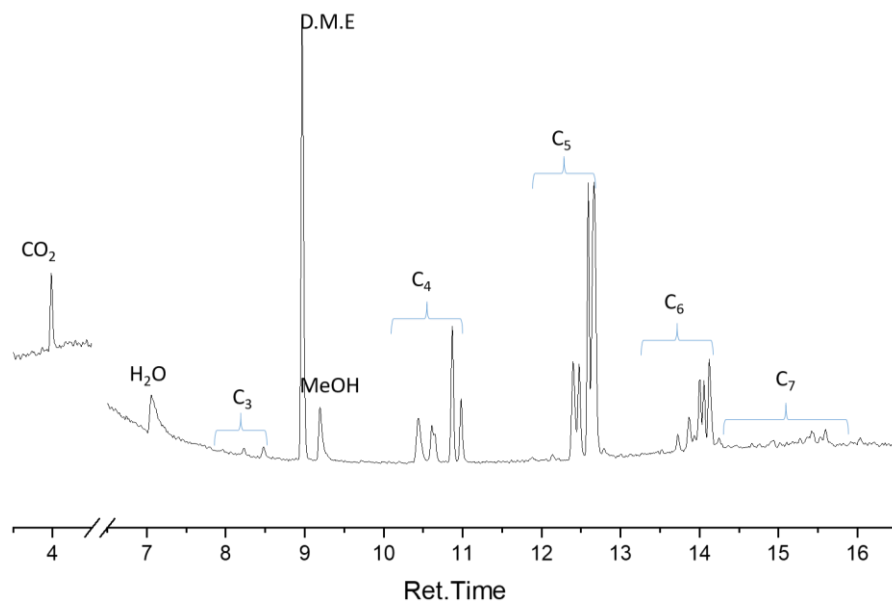


Figure 6-1 Chromatogram of the products of methyl oleate isomerization present in the gas phase.

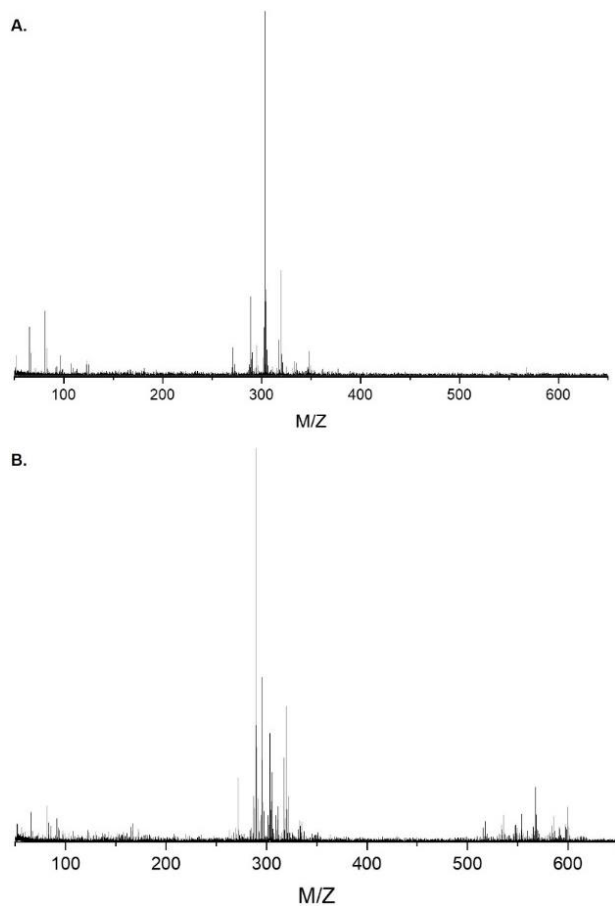


Figure 6-2 MALDI-TOF mass spectra obtained from liquid products of methyl oleate isomerization using: **A.** H-FER-PAR and **B.** H-FER-REC as the catalyst.



The products present in the liquid phase are composed of different kinds of products. In Figure 6-2, MALDI-TOF mass spectra showed the molecular weights of some cracking products ( $[M]^{+*} < 100$ ) mono-unsaturated (straight or branched)  $C_{18}$  fatty acid methyl esters ( $[M]^{+*} = 296$ ;  $[M+Li]^{+*} = 303$ ), stearolactones ( $[M+Li]^{+*} = 289$ ), hydroxy  $C_{18}$  fatty acid methyl esters ( $[M+Li]^{+*} = 319$ ), as well as oligomer products ( $[M+Li \text{ or } Na]^{+*}$  from 530 to 600). There are observable differences between the MALDI-TOF spectra of products obtained with recrystallized and parent exchanged catalysts. Although this technique is not quantitative, it is possible to see a higher amount of M/Z peaks related to oligomers in the products obtained using H-FER-REC as a catalyst.

In order to identify the different oligomers, MS-MS analysis was done on M/Z peaks of 585.5 and 599.6 (see Figure 6-3). The peak of M/Z=585.5 broke mainly into an ion fragment with M/Z of 303.3, which represented the monomer of oleic acid. It showed other minor fragments of losses of methyl (570.1), methoxy (553.5), and larger fragments. Some fragments, which represent the same losses to the monomer oleic acid, are observed too. According to this fragmentation pattern and the M/Z value, it is assigned to dimer estolides.

On the other hand, the peak of M/Z=585.5 broke to more peaks than the monomer fragment, the loss of the methoxy group being the main fragment. Here, the losses of hydrocarbon chains represent the most important breakings. This peak is assigned to dimers of oleic acid. The quantification of these products was done through high-temperature gas chromatography (see Figure 6-4). Using this technique, the discrimination between them was not possible because the resolution of the peaks was not good enough. Based on these results, the quantification was done by considering the whole oligomer fraction, without discriminating between the products identified here.

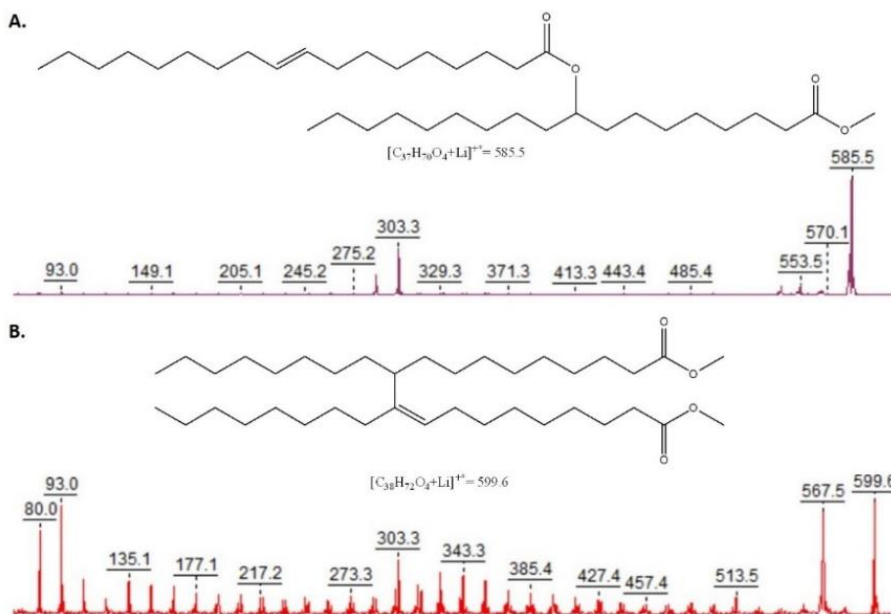


Figure 6-3 MS-MS analysis done on M/Z peaks of **A.**  $[C_{37}H_{70}O_4+Li]^{+*} = 585.5$  and **B.**  $[C_{38}H_{72}O_4+Li]^{+*} = 599.6$

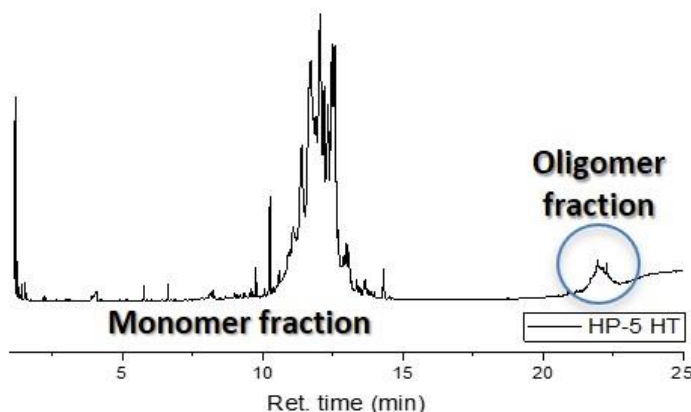


Figure 6-4 Chromatogram of the liquid phase obtained after methyl oleate isomerization (GC analysis done on HP-5ms® column).

Taking into account the low resolution among the chromatographic peaks obtained with the non-polar column, a gas chromatography coupled to mass spectrometry (GC-MS) analysis was done on the liquid phase of the products. A G48 polar column (ZB-FAMES®) was used. The monomer fraction was analyzed by GC-MS. Different kinds of products of methyl oleate isomerization were identified. In Figure 6-5 it is possible to identify cracking products, branched-chain products, and straight unsaturated fatty acid methyl esters, as well as hydroxylated products, saturated fatty acids,  $\gamma$ -stearolactones, and  $\delta$ -stearolactones. An increase in the amount of methyl stearate, already present at 1.4% in the starting methyl oleate, was observed, indicating its formation during the reaction. Cracking products in the liquid phase were easily identified because they possess a low molecular weight, and they elute in the first minutes. Some of these cracking products showed a peak of  $m/z = 74$  (Mc Lafferty rearrangement ion), which is characteristic of the carbonyl group. It indicates that some of these products were fatty acid derivatives products with lower molecular weight. Branched  $C_{18}$  fatty acid methyl esters elute before methyl stearate and have Equivalent Chain Length (ECL) values from 16.5 to 17.9. More than 30 compounds could be identified when the yields are high. The presence of geometrical Z and E isomers, positional isomers of methyl and double bond isomers could explain this wide distribution. A wide distribution of straight  $C_{18}$  mono-unsaturated isomers with ECL values from 18.1 to 18.7, which eluted after methyl stearate, was observed too. Methyl esters with the double bond position closer to carboxyl head eluted first. Adjacent peaks are typically E (trans) and Z (cis) isomers, with E isomers eluting before Z ones, when the double bond on the carbon chain is positioned similarly. In a typical GC analysis (Figure 6-5), hydroxy fatty acid methyl esters elute next with ECL values from 19.0 to 19.9 (Retention time: from 66.2 to 70.0 min), followed by  $\delta$ -lactones and  $\gamma$ -lactones in a wide range of retention times from 72.0 to 115 min.

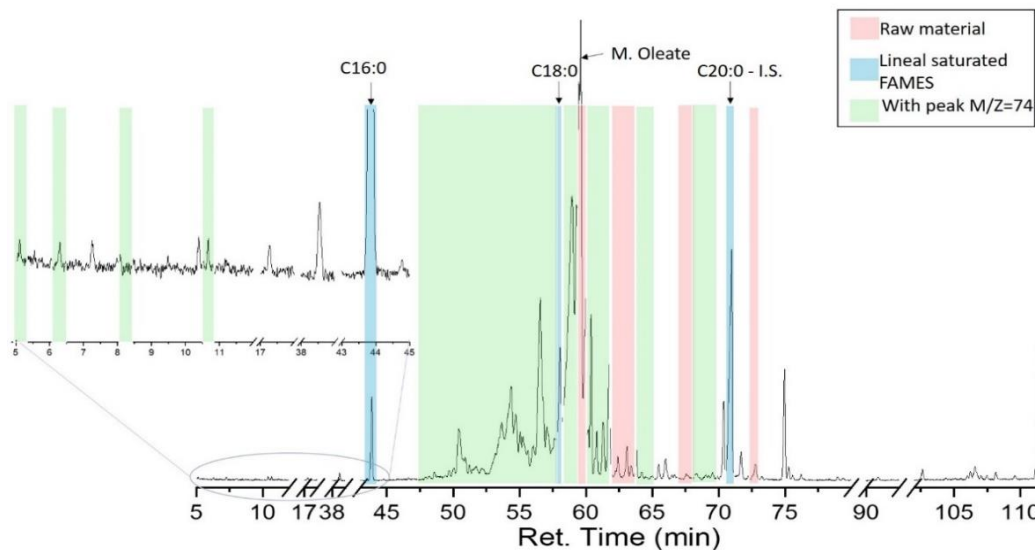


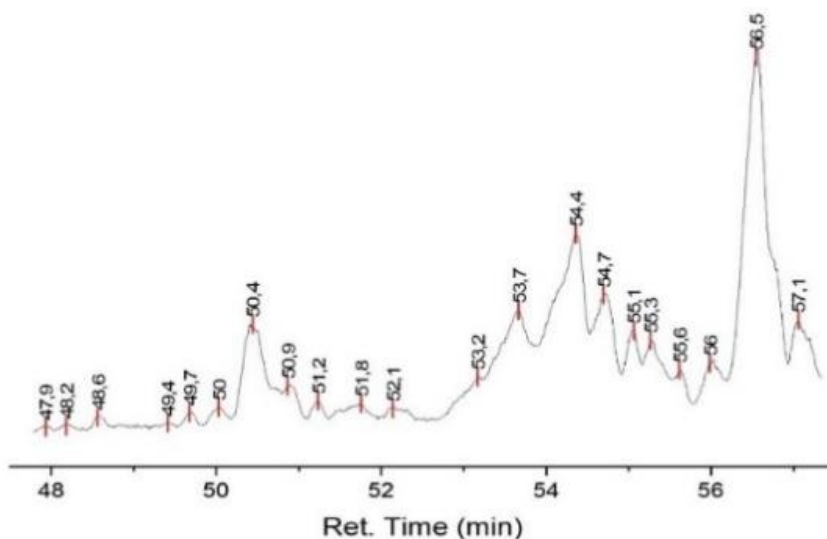
Figure 6-5 Chromatogram of the monomer fraction in the liquid product of methyl oleate isomerization (GC-MS analysis done on ZB-FAMES column).

### 6.1.1 Products of methyl oleate isomerization using ferrierite based catalytic materials

Methyl oleate isomerization using ferrierite H-form materials as catalysts produced a wide distribution of mainly mono-unsaturated branched fatty acid methyl esters. In Figure 6-6 is shown a comparison between chromatograms of branched products obtained using H-FER-PAR and H-FER-REC as the catalysts in batch (or continuous flow) reactor at 285°C and 2.0 MPa. Distribution of branched products is similar using both ferrierite materials, because the ferrierite pore structure mainly determines selectivity for products. Mass spectra analysis showed that these products are mainly mono-unsaturated ( $M/Z=296$ ). The use of these materials led to obtaining the methyl group farther from the carboxylic head (ECL closer to 18). A higher amount of branched-chain  $C_{18}$  isomers were observed using H-FER-REC as the catalyst.

The comparison of the distribution of straight  $C_{18}$  mono-unsaturated fatty acid methyl esters, which is shown in Figure 6-7, confirmed that there was a higher conversion of methyl oleate using H-FER-REC as catalyst. Therefore, there were fewer straight  $C_{18}$  compounds using this recrystallized material, indicating that they were converted to other products. Methyl esters with the double bond position closer to carboxyl head eluted first (Retention times closer to 47.0 min) Adjacent peaks are typically E (trans) isomer eluting before Z (cis) one in the same position of the double bond on the carbon chain.

A.



B.

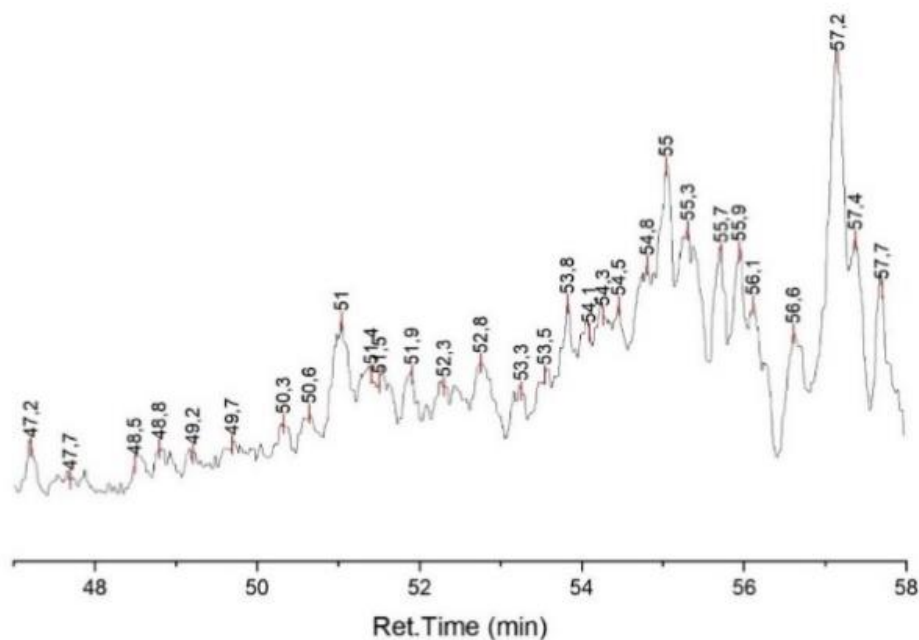


Figure 6-6 Enlargement of chromatogram of retention times from 47.0 to 56.0 min on elution of branched-chain fatty acid methyl esters of the chromatogram of initial products of methyl oleate isomerization using: A. H-FER-PAR as catalyst. B. H-FER-REC as catalyst ( GC-MS anlysis done on ZB-FAMEs® column).

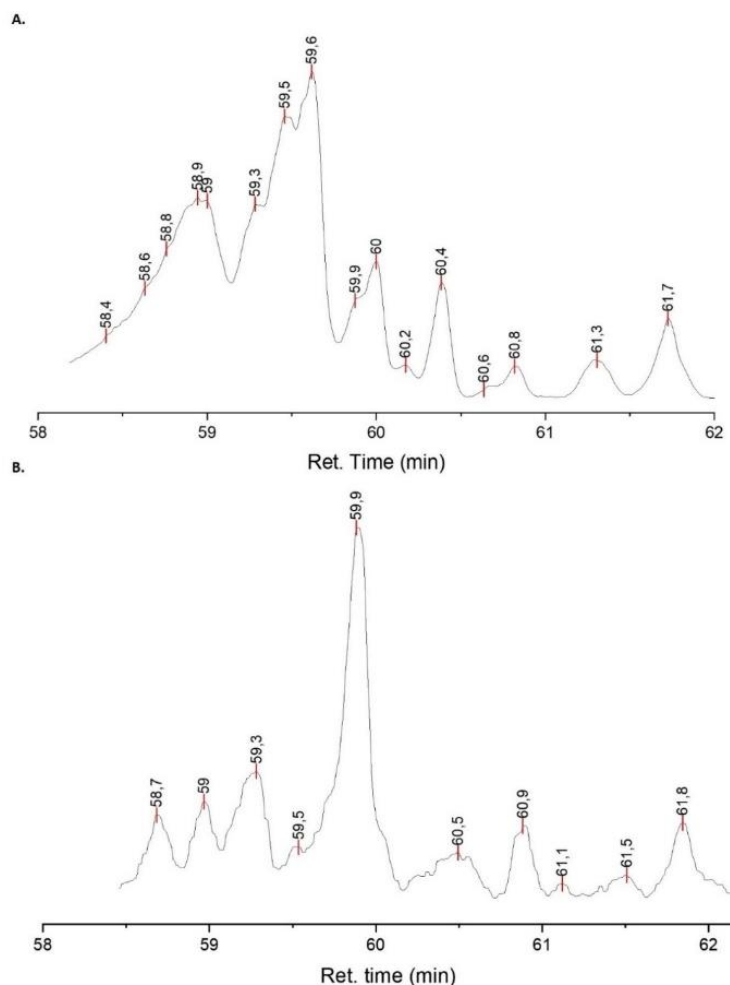


Figure 6-7 Enlargement of chromatogram of retention times from 56.0 to 62.0 min on elution of straight monounsaturated fatty acid methyl esters of the chromatogram of products of methyl oleate isomerization using: A. H-FER-PAR as catalyst. B. H-FER-REC as catalyst ( GC-MS analysis done on ZB-FAMES® column).

### 6.1.2 Products of methyl oleate isomerization using Zeolite Y based catalytic materials

In contrast, methyl oleate isomerization using zeolite Y materials as catalysts produced a mixture of saturated and mono-unsaturated branched fatty acid methyl esters. In Figure 6-8, there is a comparison between branched products obtained using H-Y-30-PAR and H-Y-30-REC as the catalysts. Mass spectra showed that these products are mixtures of mono-unsaturated ( $M/Z=296$ ) and saturated ( $M/Z=298$ ) branched fatty acid methyl esters. It is possible to see a similar distribution of compounds using these zeolite Y-based catalysts. They showed a broader distribution than in the products obtained using ferrierite materials as catalysts. These compounds are distributed in three groups depending where is located of the methyl group in the alkyl chain in the branched-chain  $C_{18}$ . The number of

positions of the methyl group branching the products is higher, thus leading to a broader signal the pore system of zeolite Y is less constrained than the ferrierite one.

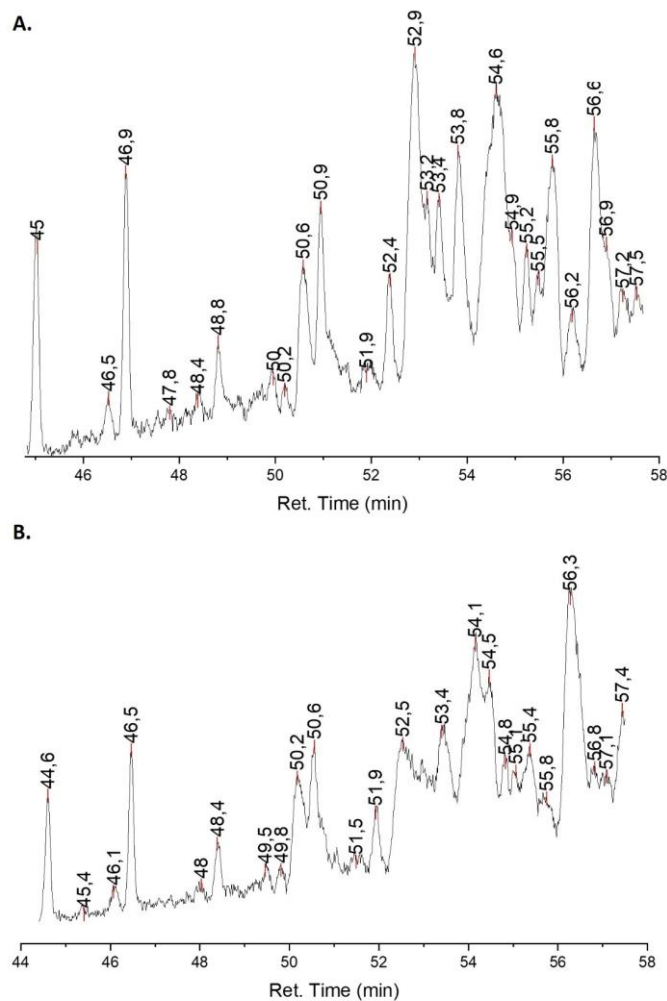


Figure 6-8 Enlargement of chromatogram of retention times from 44.0 to 58.0 min on elution of branched-chain fatty acid methyl esters of the chromatogram of initial products of methyl oleate isomerization using: A. H-Y-30-PAR as catalyst. B. H-Y-30-REC as catalyst ( GC-MS anlysis done on ZB-FAMES® column).

The use of H-Y-30-REC as the catalyst led to a slightly lower amount of C<sub>18</sub> branched-chain fatty acid methyl esters than H-Y-30-PAR in the first hour of reaction. In general, lower yields in branched products were obtained using zeolite Y than ferrierite. It can be due to a lower number of acidic sites in its structure. However, it is essential to note that although zeolite Y has from three to four times less acidic sites than the ferrierite used in this work, their yields in branched C<sub>18</sub> isomers were around 20%. It indicates that a higher proportion of the zeolite Y acidic sites are accessible to carry out the reaction. The comparison of the distribution of straight mono-unsaturated fatty acid methyl ester is shown in Figure 6-9. A similar amount of them in the products obtained using H-Y-PAR and H-Y-REC showed that at least in the initial hours of the reaction, the conversion and yield in straight mono-unsaturated isomers are similar using both catalysts.

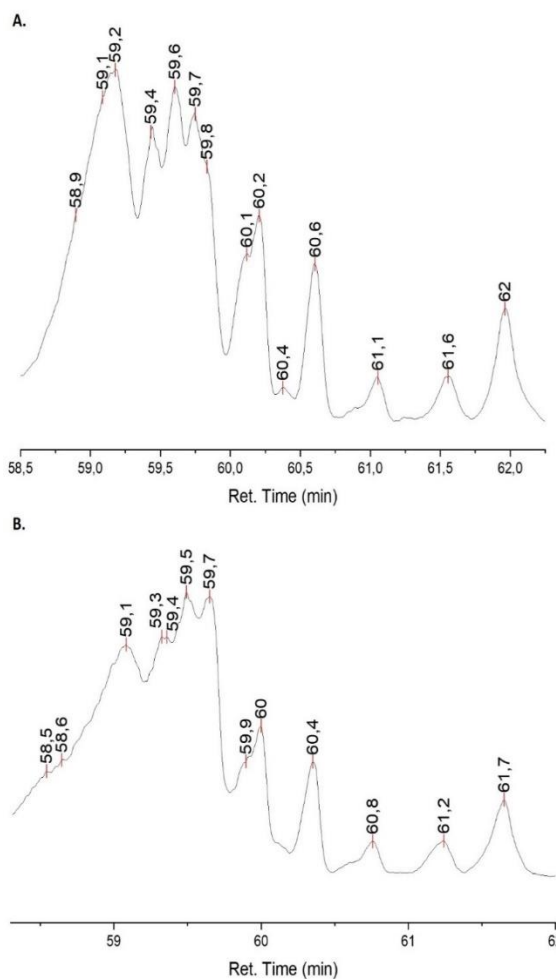


Figure 6-9 Enlargement of chromatogram of retention times from 58.0 to 62.0 min on elution of straight monounsaturated fatty acid methyl esters of the chromatogram of products of methyl oleate isomerization using: A. H-Y-30-PAR as catalyst. B. H-Y-30-REC as catalyst (GC-MS analysis done on ZB-FAMES® column).

## 6.2 Behavior in cold environments

In order to evaluate the effect of the isomerization reaction on the behavior of methyl oleate in cold environments, the cooling scans in the differential scanning calorimetry analysis were registered and the freezing behaviors of the products were compared. The temperature at which the products start to freeze was determined with the onset of the peak ( $T_{OF}$ ) observed in the scans. Methyl oleate behavior was compared to the behavior of the isomerization products using parent zeolites and recrystallized ones, in the case of ferrierite and high silica zeolite Y. In Figure 6-10 it is possible to see the effect of the reaction on the cold behavior of methyl oleate. Commercial methyl oleate has one central freezing peak



with an onset ( $T_{OF}$ ) at  $-33.6^{\circ}\text{C}$  and other peaks with  $T_{OF}$  of  $-29.5$ ,  $-14.5$ , and  $-5.9^{\circ}\text{C}$ . The main peak has been associated with the freezing point of methyl oleate. The smaller peaks are the freezing points of the other compounds present as impurities in the raw material. In contrast with methyl oleate, one of the products of the isomerization reaction with high yields in branched products (H-FER-REC 5%wt.,  $285^{\circ}\text{C}$ , 2.0 MPa  $Y_{bc}$ : 59.5%) showed one freezing peak with  $T_{OF}$  of  $-15.4^{\circ}\text{C}$ . This higher freezing peak shows that it has a worse behavior in a cold environment than the corresponding raw material.

This worsening in the product is due to the presence of E-(trans) among the branched-chain and straight isomers produced. However, the presence of the branching in the fatty acid chain has shown to improve the melting point of saturated fatty acid and their methyl ester, the change of the configuration of the double bond from the Z-isomer to E-isomer in the unsaturated fatty acids cancels this effect. The methyl as branched-chain reduced  $9$ – $11^{\circ}\text{C}$  the melting point of the  $\text{C}_{18}$  saturated fatty acid methyl esters from  $37^{\circ}\text{C}$  in the straight methyl stearate to  $26$ – $28^{\circ}\text{C}$  in branched-chain isomer [43]. However, the more significant difference of  $33^{\circ}\text{C}$  between the methyl esters of the cis- $\text{C}_{18}:1$  (methyl oleate; m.p.:  $-20^{\circ}\text{C}$ ) and the trans- $\text{C}_{18}:1$  (methyl eliadate; m.p.:  $13.5^{\circ}\text{C}$ ) led to worsening the properties of the products. So, the formation of trans-isomers is due to the fact that the catalysts used in the isomerization reaction are not selective in these diastereomers. Considering it, in the unsaturated FAMES, the effect of the branching on the freezing properties is canceled by the presence of the trans-isomers.

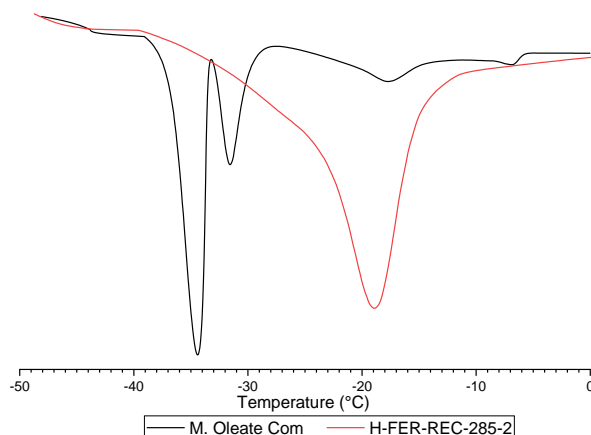


Figure 6-10 Comparison of the cooling scans in DSC analysis of the commercial methyl oleate and of the product of the isomerization reaction performed at  $285^{\circ}\text{C}$  on H-FER-REC at 2.0 MPa.

Some studies have shown that the onsets of these peaks are directly proportional to the temperatures at which the first crystal starts to appear [43,50], defined as the cloud point (CP). However, the CP of the commercial methyl oleate (Purity: 91.6% wt.) has been more related to the  $T_{OF}$  of the higher temperature peaks. The pour point (PP), defined as the lowest temperature at which movement of the test specimen is observed [61], is usually lower than the value reported for  $T_{OF}$ . The CP and PP values reported in our previous works for commercial methyl oleate were of  $-23$  and  $-25^{\circ}\text{C}$ , respectively [48]. It was closer to the value of the second peak ( $-14.5^{\circ}\text{C}$ ) observed in the DSC analysis. It is because the



appearance of the first crystals helped as nuclei to accelerate the crystallization of compounds with lower freezing temperatures. In the case of the product of methyl oleate isomerization, a lower cloud point could be expected.

In order to evaluate the effect of the different parameters of the reaction in the behavior in cold environments of the methyl oleate isomerization products, the DSC analysis of the most representative products was performed.

### 6.2.1 Products of methyl oleate isomerization using ferrierite based catalytic materials

The methyl oleate isomerization reaction done in batch conditions using ferrierite-based materials as catalysts led to the products with the highest levels of branched products. Those results and the composition of the products were described in Table 4-1 and Figure 4-1. These products were studied by DSC analysis and the results are presented here.

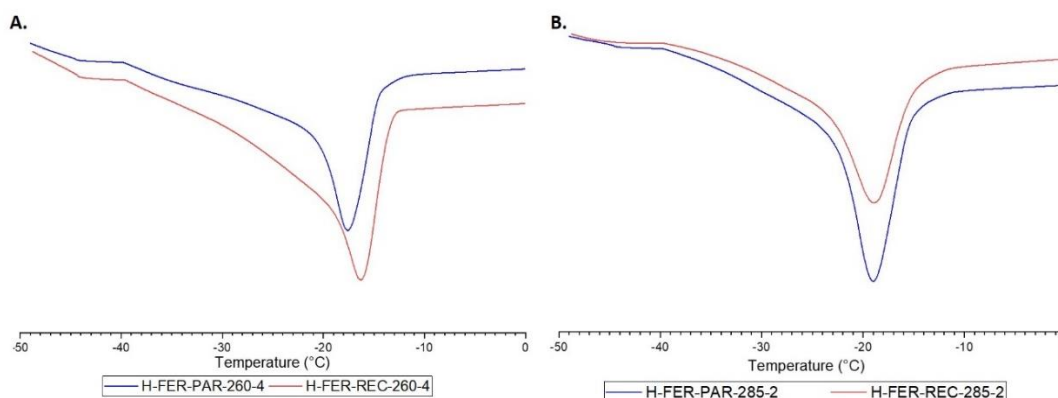


Figure 6-11 Cooling scans in DSC analysis of the methyl oleate isomerization products using ferrierite-based materials as catalysts in batch conditions. A. Reaction at 4.0 MPa and 260°C. B. Reaction at 2.0 MPa and 285°C.

In Figure 6-11 it is possible to see the behavior of the two reaction products at cold temperatures, using the parent and recrystallized materials as catalysts under the two reaction conditions mentioned here. The products of the reaction done at 260°C and 4.0 MPa (Figure 6-11-A) showed one freezing peak with  $T_{OF}$  values of -15.4°C when H-FER-PAR was used as catalyst and -13.6°C when H-FER-REC was used. Although the product using H-FER-REC had higher levels of branched-chain  $C_{18}$  FAMES ( $Y_{bc}$ : 58.2%) than the product obtained using H-FER-PAR ( $Y_{bc}$ : 55.9%), the higher levels of straight  $C_{18}:1$  isomers of methyl oleate of the first one (16.0%) compared to the second one (14.9 %) led to the increase of the  $T_{OF}$  value. In contrast, the products obtained in the isomerization reaction carried out at 285°C and 2.0 MPa showed similar freezing peaks with  $T_{OF}$  values of -15.4°C (Figure 6-11-B). Although the product obtained using H-FER-REC had higher levels of branched-chain isomers ( $Y_{bc}$ : 59.5%) than the product obtained using H-FER-PAR ( $Y_{bc}$ : 55.3%), the similar levels of the other by-products, especially the levels of straight  $C_{18}:1$  isomers (7.2% using H-FER-PAR and 7.8% using H-FER-REC) led to obtaining a

similar behavior at cold temperatures in both products. Let us note that in those both cases, the variations of  $T_{OF}$  are small.

On the other hand, the products of the methyl oleate isomerization reaction done under continuous flow conditions using ferrierite-based materials as catalysts showed a different behavior at low temperatures in the cooling scans of the DSC analysis. In Figure 6-12 is possible to see that the products of the initial hours of time-on-stream of the reaction done at 260°C with a W.H.S.V around 3.5 h<sup>-1</sup> showed different behavior. As described it is possible to see that the products of the initial hours of time-on-stream of the reaction done at 260°C with a W.H.S.V around 3.5 h<sup>-1</sup> showed different behaviors. As described previously (see section 4.2), reactions done at 260°C in continuous flow conditions were yielded lower  $Y_{bc}$  values (yield in branched-chain isomers), and the products had higher levels of straight C18:1 isomers. In Figure 6-12-A it is possible to see that the mean freezing peak of the product obtained using H-FER-PAR as the catalyst is worse than the one of the product obtained using H-FER-REC as catalyst ( $T_{OF}$ : -9.3°C). The lower yield in branched-chain isomers ( $Y_{bc}$ : 8.2%) of the first product, as well as its higher levels of straight monounsaturated isomers (71.9%), led to a higher crystallization temperature ( $T_{OF}$ : -6.4°C). The products obtained using H-FER-PAR also showed a primary freezing peak (biggest peak observed in cooling scan) with a shoulder with an onset temperature of -19.1°C. It could be due to the crystallization of a second group of molecules at lower temperatures (branched-chain isomers or other byproducts). The higher yields in branched products obtained using H-FER-REC as catalyst ( $Y_{bc}$ : 40.0%), as well as its lower levels of straight monounsaturated isomers (35.1%), led to a lower crystallization temperature ( $T_{OF}$ : -9.3°C). These reaction products also showed a smaller peak at -6.4°C and a shoulder with an onset temperature of -19.1°C. These peaks could be related to the same group of molecules present in the product obtained using H-FER-PAR. On the other hand, when the methyl oleate isomerization reaction was done at higher pressure (4.0 MPa), there was an increase in the yield in branched products formed when H-FER-PAR was used as catalyst (21.4%) while there was a decrease in the yield obtained using the H-FER-REC as catalyst (28.9%). It led to changes in the  $T_{OF}$  values of the products (see Figure 6-12-B). The increase in the yield and the decrease in the level of straight unsaturated FAMES (61.6%) lead to decrease by 1.7°C the  $T_{OF}$  value (-8.1°C) of the mean freezing peak in the isomerization product when H-FER-PAR was used as the catalyst. The presence of shoulders in the freezing peak with  $T_{OF}$  values of -14.2 and -26.0°C indicated the compounds with other regimes of crystallization. On the other hand, the  $T_{OF}$  value of the product obtained when H-FER-REC was used as catalyst increased by 1.4°C due to the lower yield in branched-chain isomers and the increase in the levels of straight isomers (42.0%). This peak also showed a shoulder in the freezing peak with a  $T_{OF}$  value of -14.2°C.

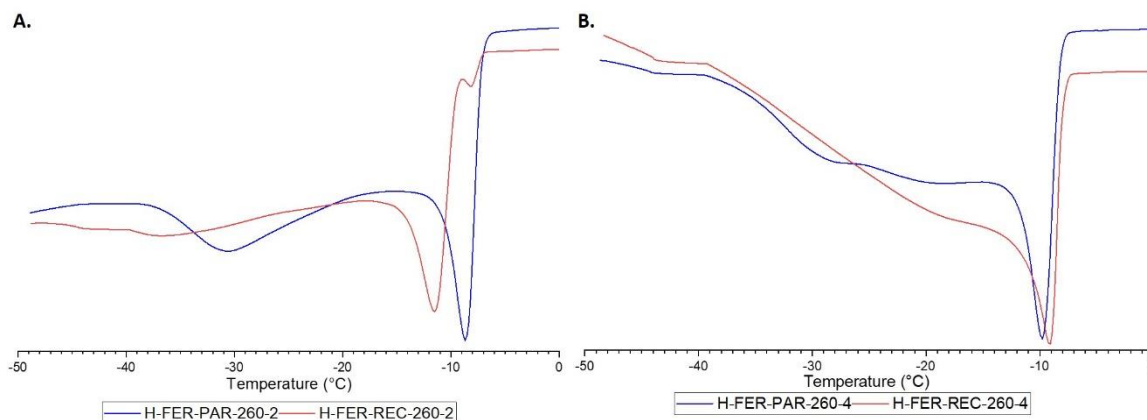


Figure 6-12 Cooling scans on DSC analysis of the methyl oleate isomerization products using ferrierite-based material as catalysts in continuous flow conditions (WHSV= 3.5 h<sup>-1</sup>).

A. Reaction at 4.0 MPa and 260°C. B. Reaction at 2.0 MPa and 285°C.

According to the results of methyl oleate isomerization in continuous flow conditions at 2.0 MPa and 285 °C it was expected that the behavior in cold environments of products using H-FER-REC ( $Y_{bc}$ : 52.5%) was better than the one obtained using H-FER-PAR ( $Y_{bc}$ : 31.3%). In Figure 6-13 it is possible to see that the  $T_{OF}$  of the product of methyl oleate isomerization using H-FER-PAR was -11.3°C while the onset  $T_{OF}$  of the product obtained using H-FER-REC was -17.4°C. The higher amount of straight C18 mono-unsaturated, which has a high proportion of E-isomers in the product obtained using H-FER-PAR led to a faster crystallization process when the temperature decreases. To get improvements in the behavior at cold temperatures of these products, high yields must be obtained. Low to medium yields in branched products lead to the presence of high amounts of E-mono-unsaturated FAMEs, which lead to worsening the behavior in cold environments.

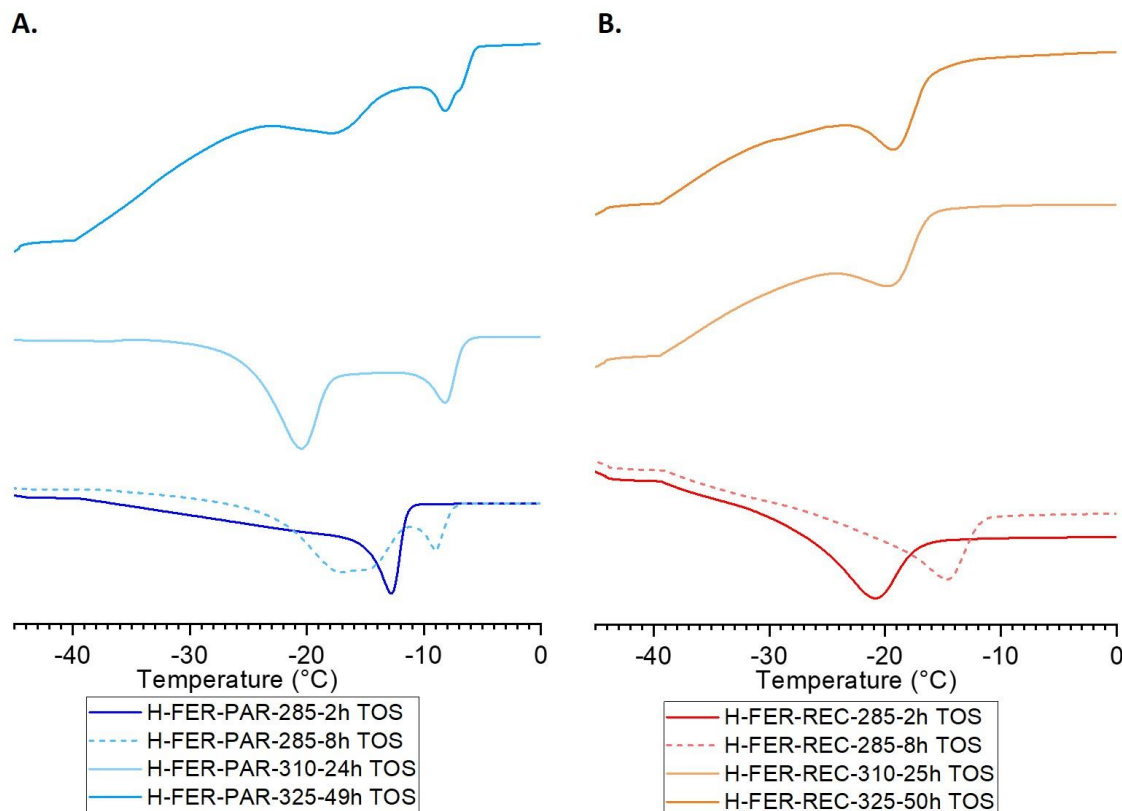


Figure 6-13 Cooling scans on DSC analysis of the methyl oleate isomerization products using ferrierite-based material as catalysts in continuous flow conditions ( $\text{WHSV}=3.5 \text{ h}^{-1}$ ) at 2.0 MPa and 285°C. A. H-FER-PAR as the catalyst. B. H-FER-REC as the catalyst.

As it is possible to see in Figure 4-9, the catalytic activity of the H-FER-PAR (Figure 4-9-A) decreased faster than the activity of the H-FER-REC (Figure 4-9-B). This leads to the fact that the difference in the behavior at low temperature of the methyl oleate isomerization products obtained after eight hours of TOS was more prominent when the parent exchanged ferrierite was used as a catalyst than when the recrystallized was used. The product obtained after eight hours of TOS when H-FER-PAR was used as catalyst (H-FER-PAR-285-8h TOS) showed two different regimes of crystallization in contrast with the only peak present in the case of the product obtained in the initial hours of TOS (H-FER-PAR-285-2h TOS). The higher temperature peak had a  $T_{\text{OF}}$  value of  $-7.3^{\circ}\text{C}$ , while the second peak kept a  $T_{\text{OF}}$  value of  $-11.6^{\circ}\text{C}$  similar to that of the sample at initial hours. This change could be due to the increase in the straight isomers observed during the time-on-stream. Unlike this behavior, the product obtained after eight hours of TOS when H-FER-REC was used as catalyst (H-FER-REC-285-8h TOS) showed just one freezing peak with a  $T_{\text{OF}}$  value of  $-11.6^{\circ}\text{C}$ . It meant an increase of  $5.8^{\circ}\text{C}$  of the  $T_{\text{OF}}$  value relatively to the product obtained in the initial hours of TOS (H-FER-REC-285-2h TOS). It was impressive that the yields in branched products were close to 50% during these first eight hours of TOS. So, the yield in branched products decreased from an initial value of 52.2 % to 50.4%. However, there was a significant increase in the level of straight unsaturated isomers of methyl oleate from an initial value of 8.9% to 17.4%. It could indicate that the levels of straight unsaturated  $\text{C}_{18}$

positional/geometrical isomers of methyl oleate has a more significant effect than the levels of branched-chain isomers in the behavior at low temperatures of the methyl oleate isomerization products.

When the temperature was increased at 310°C, the products obtained when the temperature was stabilized (H-FER-PAR-310-24h TOS and H-FER-REC-310-25h TOS) showed a behavior similar to the precedent products after eight hours of TOS at 285°C. As it was observed for the product previously mentioned, the product obtained when H-FER-PAR was used as catalyst at 310°C (H-FER-PAR-310-24h TOS) showed two different regimes of crystallization. The first peak with the  $T_{OF}$  value of -6.2°C could correspond to the crystallization of the compounds with a higher temperature of crystallization like methyl stearate or the straight C18:1 isomers of methyl oleate, while the second peak, which had a  $T_{OF}$  value of -18.1°C, could correspond to the crystallization of the compounds with a lower temperature of crystallization like the branched-chain isomers or other by-products. At the same time, the product obtained when H-FER-REC was used as catalyst at 310°C (H-FER-REC-310-24h TOS) showed one regime of crystallization as it was observed at 285°C. However, the onset of this peak was of -16.3°C, 4.7°C lower than the value obtained after eight hours of TOS at 285°C (H-FER-PAR-285-8h TOS). This decrease in the  $T_{OF}$  value was mainly related to the decreasing in the levels of straight isomers of methyl oleate. The decrease observed in the yield in branched-chain products (from 50.4 to 38.0%) should lead to an increase in the  $T_{OF}$  value. However, the decrease observed in the levels of straight isomers of methyl oleate (from 17.4 to 10.2%) improved this value.

In the same way, the products obtained when the temperature was increased to 325°C showed a similar behavior. So, the product obtained when H-FER-PAR was used as catalyst at 325°C (H-FER-PAR-325-49h TOS) showed two different regimes of crystallization with the  $T_{OF}$  value of -6.1°C and -14.0°C. The increase in the  $T_{OF}$  value of the second peak could be related to higher levels of by-products as lactones or oligomers. Furthermore, the product obtained when H-FER-REC was used as catalyst at 325°C (H-FER-REC-325-50h TOS) showed one regime of crystallization with a  $T_{OF}$  value of -15.7°C, i.e. 0.6°C higher than the value previously observed at 310°C. It could be due to the lower levels of branched-chain C<sub>18</sub> isomers or higher levels of other by-products. It is important to note that this variation is lower than previously observed, probably because the levels of straight isomers of methyl oleate were kept at similar levels.

### **6.2.2 Products of methyl oleate isomerization using Zeolite Y based catalytic materials**

As it was observed in the analysis of the results of the methyl oleate isomerization using high silica zeolite Y based materials as catalysts (see section 5.1), conversion and yield values obtained were lower than when ferrierite-based materials were used as catalysts. Similarly, the isomers composition analysis (see section 6.1.2) showed more numerous straight C<sub>18</sub> isomers of methyl oleate, and the branched-chain products could include saturated compounds. According to that, a worse behavior in cold environments is

expected. This was confirmed through the cooling scans of the DSC analysis done on different products obtained in batch and continuous flow conditions using these materials as catalysts.

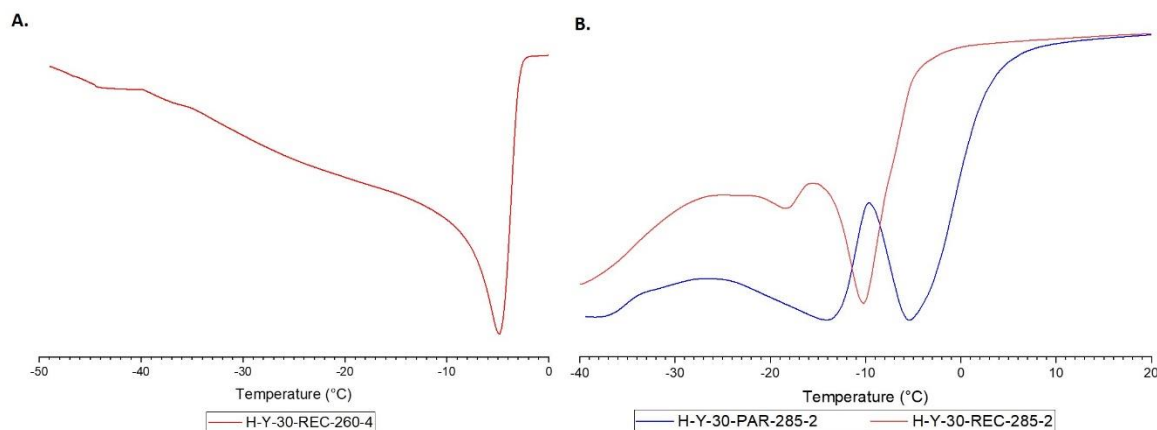


Figure 6-14 Cooling scans on DSC analysis of the methyl oleate isomerization products using Zeolite Y-based material as catalysts in batch conditions. A. Reaction at 4.0 MPa and 260°C. B. Reaction at 2.0 MPa and 285°C.

The behavior of the samples at low temperatures of the products obtained using H-Y-30 materials as catalysts in batch conditions was worse than the one obtained with H-FER materials. The DSC cooling scan of the product of the reaction done at 260°C and 4.0 MPa using H-Y-30-REC as catalyst (Figure 6-14-A) showed one freezing peak with a  $T_{OF}$  value of -3.0°C, 12.4°C higher than the  $T_{OF}$  value obtained for the product when H-FER-REC was used as catalyst. It is due mainly to the higher yields in straight isomers of methyl oleate (34.4%) using H-Y-30-PAR than when using H-FER-PAR (16.2%). The higher levels of oligomers in the product obtained with the high silica zeolite Y (H-Y-30-REC, 17.2%) than using ferrierite material (H-FER-REC, 14.5%) could lead to a worse behavior.

Similarly, the products obtained in the isomerization carried out at 285°C and 2.0 MPa using H-Y-30 materials as catalyst showed peaks at higher temperatures than ferrierite-based materials were used. The difference was of 17.7°C when H-Y-30-PAR was used as catalyst ( $T_{OF}$ : +2.3°C) and 10°C when H-Y-30-REC was used ( $T_{OF}$ : -5.4°C). The comparison of the behavior at a low temperature of the products obtained using the parent and recrystallized high silica zeolite Y materials as catalysts are shown in Figure 6-14-B. It is possible to see that the product obtained using H-Y-30-PAR as catalyst showed two freezing peaks with  $T_{OF}$  values of +2.3 and -10°C. The higher temperature peak could be produced by the higher levels of oligomer products (21.1%), which crystallize at higher temperatures and lead to the crystallization of other compounds, while the second peak could be produced by the branched-chain and other by-product crystallization. On the other hand, the cooling scan on DSC analysis of the product obtained using H-Y-30-REC as catalyst showed one freezing peak with a  $T_{OF}$  value of -5.4°C with a small shoulder with a  $T_{OF}$  value of -16.4°C. A lower amount of oligomers, straight unsaturated isomers of methyl oleate could lead to getting a lower freezing temperature.

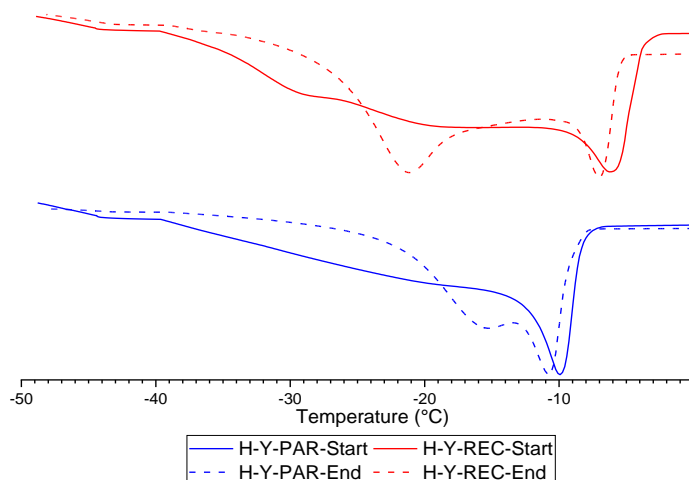


Figure 6-15 Cooling scans on DSC analysis of the methyl oleate isomerization products using zeolite Y-based material as catalysts in continuous flow conditions (WHSV=3.5 h<sup>-1</sup>), 2.0 MPa and 285°C.

According to the previous results, a similar behavior should be expected on the properties in cold environments of the products of methyl oleate isomerization using H-Y-30-PAR and H-Y-30-REC as catalysts. In Figure 6-15 it is possible to see the DSC cooling scan of the products obtained at 285°C and 2.0 MPa in continuous flow conditions. Here it is possible to see that the onset of the freezing peak ( $T_{OF}$ ) of the product of methyl oleate isomerization using H-Y-30-PAR was lower than the one obtained using H-Y-30-REC. They were of -8.2 and -3.6°C, respectively. Although these products have similar amounts of C<sub>18</sub> mono-unsaturated, a higher amount of oligomers and methyl stearate can explain this behavior. Some shoulders are observed in the freezing peak, indicating a greater variety of compounds with different freezing regimes. As it was mentioned before, low to medium yields in branched products lead to worsening the behavior in cold conditions of these products. That is one of the main reasons why, in general, the products obtained using zeolite Y materials as catalysts showed a worse behavior in cold environments than ones obtained using ferrierite materials as the catalysts.

The products after eight hours of time-on-stream showed two regimes of crystallization. In both cases, the higher temperature freezing peak showed lower  $T_{OF}$  values than the values reported at the initial hours of TOS. In the products obtained using H-Y-30-PAR as the catalyst, the  $T_{OF}$  value decreased slightly from -8.2 to -8.9°C. These experiments allowed to underline the low relevance of the change of the levels of the branched-chain products in the behavior in cold environments. The yield in branched products dropped from a value of  $Y_{bc}$  of 21.1% in the initial hours of TOS to 5.7% after eight hours. It did not affect the crystallization behavior. This underlined the higher importance of the level of straight monounsaturated isomers of methyl oleate, which kept more or less unchanged, leading this higher peak to maintain the same temperature. The appearance of the second peak could be due to the crystallization of the compounds of lower freezing points. On the other hand, in the products obtained using H-Y-30-REC as the catalyst, the  $T_{OF}$  value decreased

more, from an initial value of  $-3.6$  to  $-5.4^{\circ}\text{C}$  in the product obtained after eight hours of TOS. This decrease could be attributed to the changes in the amount of oligomers.

### 6.2.3 Palm biodiesel Isomerization

In order to evaluate the effect of the skeletal isomerization reaction in methyl esters from a commercial oil, this reaction was carried out using ferrierite as a catalyst on biodiesel from palm oil in batch conditions. This palm biodiesel is composed of 52.8% of saturated fatty acid methyl esters and 47.2% of unsaturated ones. Keeping in mind that the saturated methyl esters are not subject to isomerization, only the unsaturated ones were converted. The results of the reaction done at  $285^{\circ}\text{C}$  and 2.0 MPa during 8h were shown in section 4.3.

In Figure 6-16 are presented the cooling scans of the DSC analysis of the products of the isomerization reaction obtained from palm biodiesel using ferrierite-based materials as catalysts. Comparing the results using H-FER-PAR and H-FER-REC it is possible to see that this last one led to getting a slightly higher yield in branched-chain products. Moreover, fewer oligomers were obtained using H-FER-REC but a higher amount of straight  $\text{C}_{18}$  isomers and other by-products. It was reflected in the fact that the product obtained using H-FER-REC as catalyst just showed a freezing peak with a  $T_{\text{OF}}$  value of  $11.0^{\circ}\text{C}$  with a shoulder at  $7.4^{\circ}\text{C}$ , while the product obtained using H-FER-REC showed a freezing peak with a  $T_{\text{OF}}$  value of  $13.4^{\circ}\text{C}$  with a shoulder at  $11.4^{\circ}\text{C}$  but also other peaks with  $T_{\text{OF}}$  values of 21, 34.9 and  $39^{\circ}\text{C}$ .

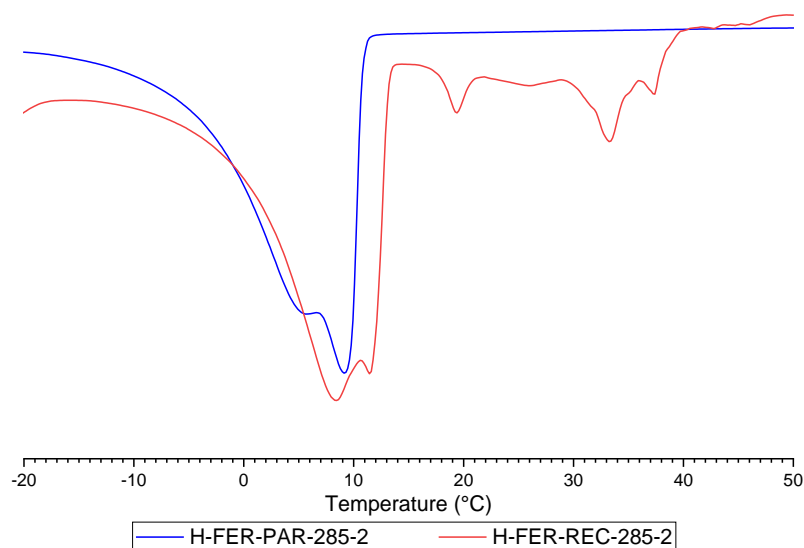


Figure 6-16 Cooling scans on DSC analysis of the palm biodiesel isomerization products using ferrierite-based material as catalysts in batch conditions at 2.0 MPa and  $285^{\circ}\text{C}$ .



## 6.3 Conclusions

Products of methyl oleate isomerization reaction are complex mixtures of gas and liquid phases. The gas-phase is mainly composed of cracking products as light hydrocarbons, methanol, water, carbon dioxide, and dimethyl ether, formed from methanol by acid dehydration. The liquid phase is composed of different kinds of oligomers and monomeric products. Among the oligomer products were seen dimers of oleic acid and estolides. The monomeric products included the desired branched-chain FAMES isomers, straight isomers of methyl oleate as well as hydroxy FAMES, delta and gamma lactones, and remains of the cracking products. The amount and the distribution of the products can affect the properties of the methyl oleate isomerization products in cold environments.

On one hand, methyl oleate isomerization using ferrierite-based materials as catalysts produced a less wide distribution of mainly mono-unsaturated branched-chain fatty acid methyl esters with methyl group farther from the carboxylic head. The well-constrained microporous system, as well as a higher number of acidic sites, led to obtaining higher yields in branched products with high selectivity. The presence of the mesoporous system into the ferrierite structure did not affect the distribution of the products. On the other hand, methyl oleate isomerization using zeolite Y based materials as catalysts produced a broader mixture of saturated and mono-unsaturated branched fatty acid methyl esters. Although high conversion values were obtained, the conversion to straight C<sub>18</sub> isomers of methyl oleate represented the central part of this conversion.

Taking into account that the methyl oleate isomerization performed using ferrierite-based materials as catalysts allowed to get the products with the highest levels of branched products and lower levels of straight mono unsaturated isomers of methyl oleate, these products showed the best freezing behavior at low temperatures. Parameters as temperature, pressure, and reaction regime (batch or continuous flow conditions) were shown to influence the freezing behavior of the product at low temperatures. The product obtained using H-FER-REC as catalyst at 285°C and 2.0 MPa in continuous flow conditions in the first hours of time-on-stream showed the lowest onset temperature of freezing point (T<sub>OF</sub>: -17.4°C). Comparing the products of the methyl oleate isomerization obtained using parent exchanged and recrystallized ferrierite-based materials as catalysts, it was possible to see that at 260°C, the use of H-FER-PAR led to getting of a better behavior at low temperatures. On the contrary, the use of the H-FER-REC led to a better behavior when the isomerization reaction was carried out at 285°C. These improved results were typically directed to obtain a product with better behavior in cold environments. It could be attributed to a lower amount of straight mono-unsaturated FAMES that are usually E-isomers and tend to worsen this behavior.

On the other hand, the lower yields in branched-chain products obtained using zeolite Y based catalyst led to the fact that these products presented a worse behavior in cold environments than the one obtained using ferrierite as catalyst. The increase in the amount of the by-products with different freezing regimes produced by the use of H-Y-30-REC led to this product showing worse behavior than the one obtained with the use of H-Y-30-REC.

The worst behavior at low temperatures was obtained using H-Y-30-PAR as the catalyst at 285°C and 2.0 MPa in batch conditions. The  $T_{OF}$  value of +2.3°C differed of 19.7°C from the lowest  $T_{OF}$  value reported in this work.

After evaluating the effect that the isomerization reaction has on the behavior at low temperatures of methyl oleate, it was possible to conclude that it led to the worsening in the product behavior, and this was due to the presence of E-(trans) among the branched-chain and straight isomers produced. In order to get improvements in the behavior at cold temperatures of these products, high yields in branched-chain products must be obtained. Low to medium yields in branched products lead to the presence of high amounts of E-mono-unsaturated FAMES, which lead to worsening the behavior in cold environments. The levels of straight unsaturated  $C_{18}$  positional/geometrical isomers of methyl oleate have a more significant effect than the levels of branched-chain isomers in the behavior at low temperatures of the methyl oleate isomerization products. The presence of high levels of oligomers products has a non-negligible effect on the behavior of these products in cold environments.

## **7. Prospective work: Hydroisomerization of methyl palmitate using recrystallized zeolites as catalytic materials**

In this chapter, a preliminary study of the methyl palmitate hydroisomerization using bifunctional metal/acid meso-microporous zeolitic materials as catalysts is described. It was proposed considering the worsening of the behavior in cold environments brought by isomerization products and more precisely the presence of straight-line saturated fatty acids (see section 6.2). The presence of straight-line saturated fatty acids is indeed more responsible for the bad behavior in cold environment than the presence of unsaturated ones. Consequently, they have to be modified to improve their behavior (see section 1.1.2).

These preliminary experiments were done using as catalysts the zeolitic materials previously synthesized, and further impregnated with platinum. The materials chosen for these tests were the ferrierite-based materials and high silica zeolite Y-based materials because they have shown the best performance in methyl oleate isomerization reaction. The effect of the recrystallization process on the distribution of platinum and the performance on hydroisomerization of methyl palmitate are discussed.

### **7.1 Results of Platinum impregnation in recrystallized materials**

In order to obtain the bifunctional catalytic materials, parent and recrystallized zeolitic materials were impregnated with hexachloroplatinic acid hexahydrate ( $\text{H}_2\text{PtCl}_6 \cdot 6\text{H}_2\text{O}$ ) to get a platinum amount of 0.5% in the catalyst (see section 2.1.3).

In the impregnated ferrierite-based zeolitic materials, a significant difference in the dispersion of the platinum on zeolite surface between parent exchanged and recrystallized materials is observed. In Figure 7-1-A, the microscopy images show that in parent exchanged material, there is a high number of metallic nanoparticles highly dispersed on the external surface of the ferrierite crystals. This result is probably due to the large size of the chloroplatinate anion, which cannot diffuse easily with its hydration sphere inside the ferrierite crystal.

In contrast, Figure 7-1-B shows that, in the recrystallized material, there is a lower number of platinum nanoparticles, dispersed mainly on the mesopores generated in the ferrierite crystals. In this case, the metallic precursor anion can diffuse in the mesopores, which is why the metallic particles were distributed inside these mesopores but not inside the microporous network. The metallic particles obtained on H-FER-REC were bigger than those obtained on H-FER-PAR. The fact that the precursor diffused inside the mesopores can cause some drops to condensate, leading to higher concentration inside the mesopores and to bigger particles. Although it negatively affected the platinum dispersion, it resulted in particles located inside the zeolite crystals.

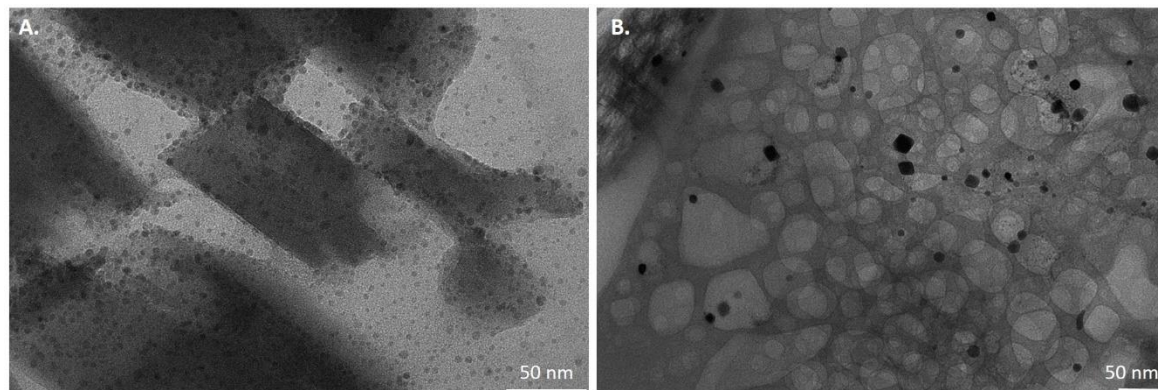


Figure 7-1 Transmission electronic microscopy (TEM) images of ferrierite materials impregnated with Platinum at 50 nm. A. Parent Ferrierite (H-FER-PAR). B. Recrystallized Ferrierite (H-FER-REC).

In the case of high silica zeolite Y, the distribution of metallic particles was also affected by the presence of the mesopores. As it was previously described in section 3.2.1, the high silica parent zeolite (H-Y-30-PAR) presents some big meso and macropores produced during the industrial synthesis due to the desilication procedure. As it can be observed in Figure 7-2-A, some platinum particles of different sizes were present randomly distributed, mainly close to this mesoporosity. Although the bigger micropore channel size allowed a larger diffusion of anion precursors inside the micropore network, the presence of this porosity could lead to drops of the solution of platinum precursor condensating inside the pores, leading to bigger particles formation around these bigger pores. It did not favor the platinum particle dispersion.

In contrast, as was previously mentioned (see section 3.2.1), the one-step recrystallization procedure of high-silica zeolite Y led to the disappearance of these big mesopores. It allowed getting a wormlike network of smaller mesopores. As shown in Figure 7-2-B, the order of obtained mesopores by recrystallization helped to get a higher dispersion of smaller platinum particles in H-Y-30-REC. These metallic particles were in average smaller than those obtained by impregnation of the parent high silica zeolite Y. The disappearance of large mesopores could cause it.

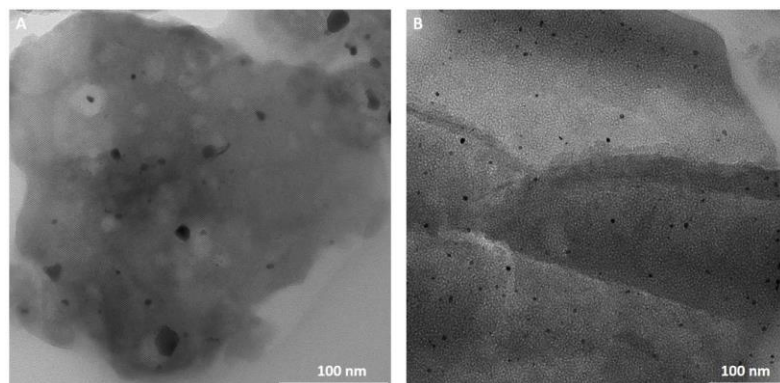


Figure 7-2 Transmission electronic microscopy (TEM) images of zeolite Y materials impregnated with Platinum (100 nm scale bar). A. Parent zeolite Y (H-Y-30-PAR). B. Recrystallized zeolite Y (H-Y-30-REC).

## 7.2 Hydroisomerization of methyl palmitate using micro-mesoporous zeolitic materials

The preliminary tests of the hydroisomerization of methyl palmitate using the materials previously described are summarized in Table 7-1. They were done at 285°C and 4.0 MPa with a mixture of hydrogen and nitrogen as atmosphere. Catalyst amounts of 1.0 and 2.5% wt. did not lead to significant conversion values. Reaction times of 6 h were not enough to get significant conversion values as well, and very low yields in branched products were obtained in all cases. With longer reaction times (18h) and higher catalyst amount (10%), conversion values up to 18.8% were obtained, similar to the results reported in the literature with another catalyst with this substrate (Cat.: NH<sub>4</sub> β-zeolite Conv.: 16% [75,241]). However, these conversions are still low compared to those reported by the same authors using palmitic acid (Cat.: NH<sub>4</sub> β-zeolite Conv.: 46% [75,241]). The highest yields obtained in branched product were only up to 2.1% using H-FER-PAR as the catalyst. Considering that low yields were obtained at long reaction time (18 h) and using a high catalyst amount (10% wt.), experimental conditions should be optimized to improve hydroisomerization reaction.

Table 7-1 Tests of methyl palmitate hydroisomerization done in a batch reactor using micro-mesoporous zeolitic materials (T: 285°C; P: 4.0 MPa).

Exp.	Catalyst Type	Catalyst Amount (%)	H <sub>2</sub> in atm. (%)	Reaction Time (h)	Conversion (%)	Yield in branched products (%)
1	H-FER-PAR	2.5	50	6	<1	0
2		10	50	18	7.6	2.1
3	H-FER-REC	2.7	37	18	<1	<1
4		10	50	18	9.3	1.5
5	H-Y-30-PAR	1.0	100	6	<1	0
6		10	50	18	14.4	1.2
7	H-Y-30-REC	1.0	100	6	<1	0
8		10	50	18	18.8	1.1

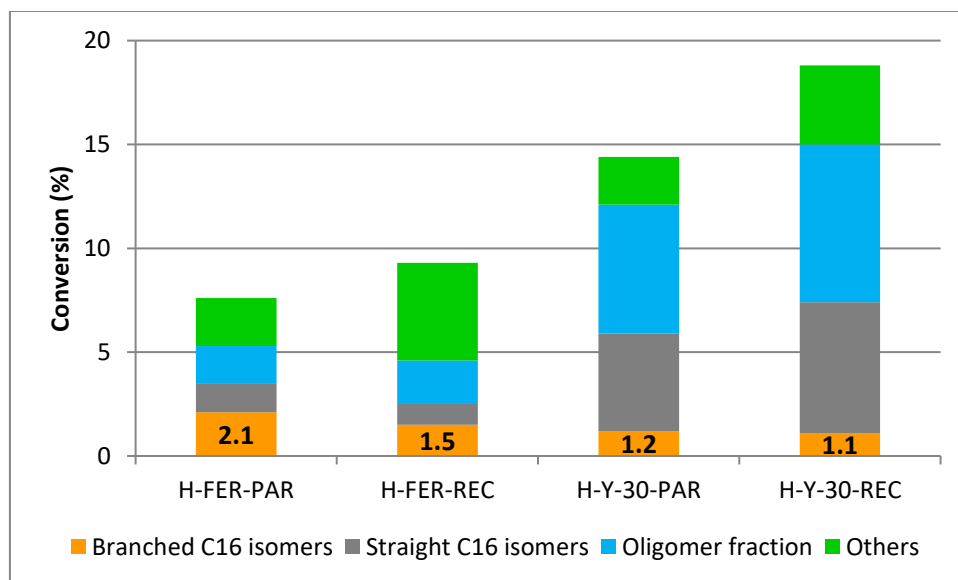


Figure 7-3 Methyl palmitate hydroisomerization products distribution using ferrierite and high silica zeolite Y materials as the catalysts (T: 285°C; P: 4.0 MPa; t: 18h Cat: 10 %wt.).

The comparison of the results obtained using the ferrierite and zeolite Y based materials are shown in Figure 7-3. The conversion values were lower using the ferrierite-based materials (H-FER-PAR: 7.6% and H-FER-REC: 9.3%) as catalyst than using high silica zeolites based-materials (H-Y-30-PAR: 14.4% and H-Y-30-REC: 18.8%). However, slightly higher yields in branched products were obtained when ferrierite-based materials were used as catalysts. It can be caused by a higher number of acidic sites and the shape selectivity produced by the highly-constrained structure of the ferrierite. So, although less unsaturated molecules obtained on metallic sites can diffuse inside the microporous network, they were converted more selectively to the desired products when they were inside the channels.

A higher selectivity to the desired products was obtained when ferrierite-based materials were used. A selectivity in branched products of 27.6% was obtained when H-FER-PAR was used as the catalyst. It allowed us to get the highest yield in branched products (2.1%) even with the lowest conversion value (7.6%). The presence of mesopores on the H-FER-REC allowed getting a slightly higher conversion value (9.3%) but a lower selectivity in branched products (23.8%). As it was observed before (see Figure 7-1-B), the mesoporous network allowed the presence of platinum particles inside these mesopores, probably shortening the path diffusion to acidic sites, leading to more unsaturated intermediate diffusion inside the zeolite particles. Two reasons can explain the decrease in the yield in branched products. The first one could be the worse Pt particle dispersion that reduces the number of acidic sites close to metallic sites. The second one could be that the metallic sites could reduce the initial coke formation significantly, necessary for the pore mouth catalysis. It could lead to the loss of the selectivity observed using H-FER-REC as catalyst. It should be studied in detail to understand how to improve catalytic performance.

On the other hand, as it was mentioned previously, the conversion values were higher using high silica zeolites based-materials (H-Y-30-PAR: 14.4% and H-Y-30-REC: 18.8%). It can be caused by a better diffusion of the unsaturated methyl esters intermediates from metallic to acidic sites inside the larger channels. However, this higher conversion led to higher yields in straight C<sub>16</sub> unsaturated FAMES and oligomers. A lower number of acidic sites can cause this. So, although more unsaturated molecules obtained on metallic sites can diffuse inside of the micropore 3D channels structure, the acidic sites were not strong enough to convert the substrate into the desired products, therefore an important part of the products consisted in straight unsaturated C<sub>16</sub> FAMES. On the other hand, a bigger micropore channel structure did not allow pore mouth catalysis because coke precursors could diffuse easier than in ferrierite-based materials. It led to a lower shape selectivity using these materials, while a higher selectivity to oligomers products was observed. Comparing the behavior of the Pt/H-Y-30-PAR and Pt/H-Y-30-REC zeolitic materials as catalysts, it is possible to conclude that the presence of the ordered mesopore system led a higher conversion value. A higher platinum dispersion was also observed on H-Y-30-REC and together with the shortening of the diffusion length, it could be responsible for this higher value. This higher conversion did also lead to a higher yield in branched products. The yield in branched products obtained using H-Y-30-REC as catalyst was within the experimental error margin when compared to the yield obtained using H-Y-30-PAR. It should be studied in detail to understand how to improve catalytic performances.

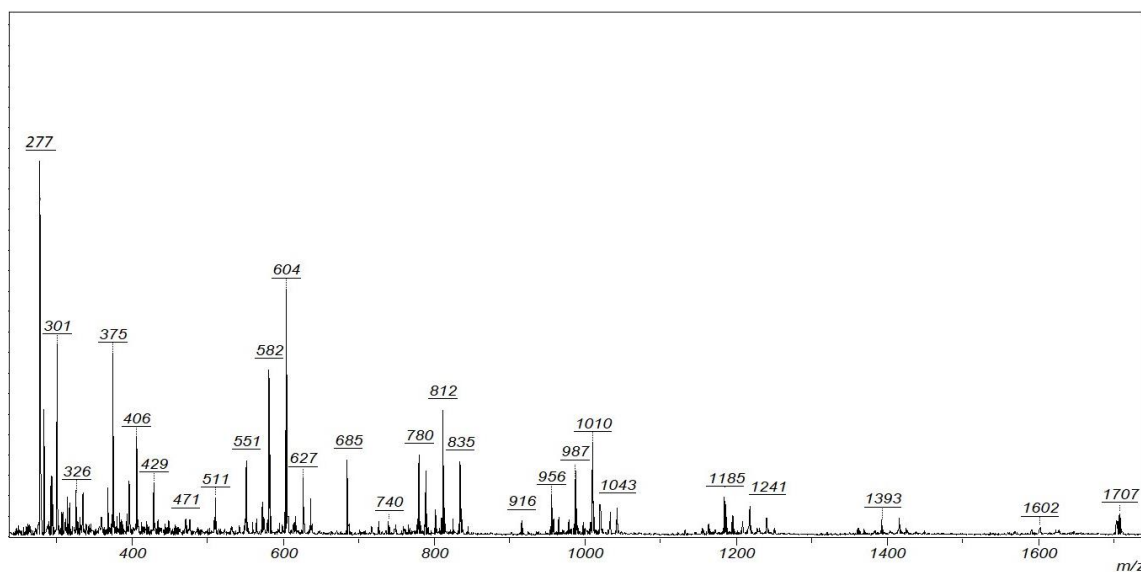


Figure 7-4 MALDI-TOF spectrum of methyl palmitate hydroisomerization products (Catalyst: H-Y-30-PAR, 4.0%wt; 285°C; 18h).

Finally, taking into account the high amount of oligomers produced in the hydroisomerization reaction, this fraction was analyzed by mass spectrometry (MALDI-TOF, see section 2.4.2). Apart from the peak characterized as methyl palmitate and its isomers ( $[M+Li]^{++} = 277$ ) and other by-products of similar molecular weight, there are peaks associated with oligomers which can be of two, three, or more palmitate or derived

monomers. It is different from the behavior observed in the isomerization of methyl oleate, where the oligomers obtained are mainly dimers of oleate monomers.

## 7.3 Conclusions

The new mesopore system in the ferrierite and high silica zeolite Y based materials showed to affect the dispersion and location of the metallic sites during the wetness impregnation process. Although the mesopore system in recrystallized ferrierite negatively affected the platinum dispersion, it allowed the location of the metallic particles inside the zeolite crystals. In contrast, the presence of the ordered mesopore system in the high silica zeolite Y led to a better dispersion of the smaller platinum particles on the zeolite crystals.

Preliminary methyl palmitate hydroisomerization experiments carried out using as catalysts the zeolitic materials, showed low conversion values and yields in branched products. To get significant results, a high amount of catalyst (10% wt.) and long reaction time (18h) was necessary. Optimal operational conditions should be determined to improve the hydroisomerization reaction. The conversion values were lower using the ferrierite-based materials as catalyst than using high silica zeolites based-materials. However, slightly higher yields in branched products were obtained when ferrierite-based materials were used as catalysts.

Comparing the performance of the parent and recrystallized zeolitic materials as catalysts, the use of the recrystallized zeolites had a substantial effect in both cases. They indeed led to higher methyl palmitate conversion, lower yields in branched products, and higher levels of high molecular weight oligomers.

Finally, unlike the behavior obtained in the methyl oleate isomerization reaction, the oligomer fraction obtained in the hydroisomerization reaction includes important amounts of oligomers composed of three or more monomer units.



## 8. Conclusions and Perspectives

### 8.1 Conclusions

The recent interest in the valorization of lipid biomass has led to considerable developments in the synthesis of porous acid materials for their use in catalytic reactions for this purpose. The use of zeolitic materials for the synthesis of alkyl-branched fatty acid methyl esters through isomerization/hydroisomerization reactions has been a breakthrough development in favoring skeletal ramification processes vs. polymerization reactions. However, the fast loss of catalytic activity is the main limitation for implementing zeolite catalysts in industrial production processes. In order to overcome the diffusion limitations which accelerate the catalyst deactivation due to the size of (micro)pores, the strategy proposed is the use of mesoporous zeolite-based materials as catalysts. We followed approaches that were previously developed in our research group for the preparation of crystalline zeolite materials possessing intra-crystalline mesopores, with the objective to improve yield and catalyst lifetime in skeletal isomerization of fatty acid methyl esters. Then, the main objective of the present work was to evaluate the catalytic performance of the prepared meso-microporous zeolitic materials and to compare their activity and selectivity to those of the parent zeolites. The performances of the zeolitic materials were evaluated through two different properties: firstly, their ability to increase the yield in branched-chain products and secondly to improve the properties of the isomerization reaction products in cold environments.

Considering these general objectives, the first goal was the synthesis of the micro-mesoporous zeolitic materials and the characterization of their structural, textural and acidic properties. The zeolite transformation was done by one-step recrystallization, consisting in a hydrothermal treatment with a base and with CTAB as the surfactant used for generating mesoporosity. Through this treatment, a secondary mesoporous system was created in two types of zeolites with different microporous frameworks: ferrierite, with a constrained 2-D pore system (8-MR: 0.35x 0.48 nm & 10-MR: 0.42 x 0.54 nm), and zeolite Y, with a less-constrained 3-D pore system with larger pores (12-MR: 0.74 x 0.74 nm).

The ferrierite-based materials obtained by recrystallization presented a micro-mesoporous ferrierite texture. An intra-crystalline mesopore system composed of occluded parallelepiped-shaped mesopores of sizes from 10 to 50 nm along the 10-MR channel direction was created, and those mesopores were connected to the external surface by

micropores. It was shown that the loss of acidity observed upon recrystallization was proportional to the loss of tetrahedral aluminum sites, which are associated with strong Brönsted acidic sites of the ferrierite framework. Additionally, a higher amount of weaker Brönsted acidic sites associated with terminal silanols in recrystallized H-FER was due to the appearance of an extra mesoporous phase grown onto the zeolite crystals.

On the other hand, the zeolite Y-based materials were obtained from high and low silica faujasites, showing different properties according to their Si/Al ratio. In the case of the recrystallization of high silica zeolite Y CBV 760® (Si/Al: 30), it was possible to prepare a hierarchically porous ordered structure of zeolite Y, in which the mesopore system is constituted of cylindrical mesopores, as in MCM-41-type materials, with mesopores of 3.8 nm diameter which are connected to the zeolite micropores.

In the case of low silica zeolite Y, the preparation of mesoporous materials from CBV 712® (Si/Al: 6.5) is proposed here for the first time, following recrystallization procedures from 40 to 330h. In this case, due to the higher stability of this material to base attack, it was necessary to perform very long recrystallization procedures for preparing materials with a significant mesoporous volume while maintaining the micropore volume quasi-constant. The obtained material was constituted of zeolitic and mesoporous domains, for which it was not obvious to confirm the presence of interconnexions between micropores and mesopores. The analysis showed that some EFAL species were removed during the recrystallization process. The appearance of a redeposited amorphous aluminosilicate phase on the low silica zeolite Y crystals did not significantly affect the low silica zeolite Y material acidic properties.

The second objective proposed in this work was to evaluate the catalytic performance of the materials previously obtained in the reaction of methyl oleate isomerization.

In the case of ferrierite-based materials used as catalysts, the presence of the large mesopores along the 10-MR channels direction in the recrystallized material improved the diffusivity of reagents and the accessibility to inner acidic sites, even with less total acidity than in the parent sample. In batch conditions, the use of recrystallized ferrierite led to slight improvements in yields in branched products going from 58.4 to 59.8% at 260°C and from 55.3% to 62.0% at 285°C, compared to the parent samples. Analysis of spent catalytic materials shows that coke is deposited on the catalyst, even if the created mesopore system allows the transport of part of coke precursors out of the microporous ferrierite framework. On the other hand, when the methyl oleate isomerization was carried out in a downstream fixed-bed continuous flow reactor, the new mesoporous network of the ferrierite played an essential role in improving catalytic behavior. The improvement in molecules diffusion indeed led to a better access to the acidic sites situated in the 10-MR channels mouths. The mesoporous network could also slow down pore-blocking, allowing precursors of coke formation to diffuse from the micropore system to mesopores, retarding deactivation processes. The created mesopores are considered as occluded, communicating with the pre-existing network only through micropores. Consequently, when these coke precursors grow by oligomerization reaction, they cannot leave ferrierite

particles and fill meso- and micropores. Additionally, in continuous flow conditions, the temperature increase from 260°C to 285°C had a very positive effect on the yield of branched products. The combination of the use of this micro-mesopore material with the increase of temperature to 285°C in the continuous flow reactor, led to develop a continuous flow process that keeps yields in branched products up to 50%, and did not show any decrease in, at least during the first eight hours of time-on-stream. To the best of our knowledge, this is the first time that such a reaction has been conducted in a continuous flow reactor for several hours / days.

When zeolite Y-based materials were used as catalysts, lower yields in branched-chain products were generally obtained compared to the use of low silica ferrierite. The effect of the mesoporous network in recrystallized materials depended on the Si/Al ratio of the parent zeolite. Although the use of high silica zeolite Y (Si/Al: 30) showed an acidity around four times lower than ferrierite materials, the acidic sites were more efficient towards branched-chain products. It could be related to the fact that there are more available acidic sites per unit in the zeolite Y materials than in the ferrierite. It was improved by the hierarchical structure present in recrystallized material, which led to getting slightly higher yields than using parent zeolite Y. In batch conditions, the increase of reaction temperature from 260°C to 285°C led to a higher yield in branched products. However, the use of this micro-mesoporous material as the catalyst in continuous flow condition led to a slight decrease in the yield in branched-chain products, even if the presence of the mesopores improved the catalyst stability with time-on-stream. In contrast with what was observed for ferrierite samples, the mesopores are well connected to the external surface of zeolite crystals. The coke precursors can then diffuse out of the catalyst, avoiding part of the coke formation. The main effect of the presence of the mesopore system in zeolite Y was the improvement of the stability of the catalyst. On the other hand, unexpectedly, considering its higher acidity (Si/Al ratio=6.5) of the low silica zeolite Y, the yield in branched-chain products was lower than when using high silica zeolite Y materials in batch and continuous conditions. In this material (CBV 712®), the acid sites can be blocked by the presence of amorphous material formed during its industrial preparation. This should be studied in detail to understand this unexpected lower catalytic performance. Comparing the stability of both recrystallized and parent low silica zeolite Y-based catalytic materials in continuous flow conditions, the mesopores presence led to an increase in the yield in branched-chain products, and it helped to enhance the catalyst stability with time-on-stream at least during the first eight hours.

Taking into account these results in which the ferrierite showed the best catalytic performance in methyl oleate isomerization, we evaluated the performances of mesoporous ferrierite based materials in the isomerization reaction from palm biodiesel. Although similar conversion values were obtained on palm biodiesel as on methyl oleate isomerization, a lower yield in branched products was observed. The comparison of the results using parent and recrystallized ferrierite-based materials showed that this last one led to a slightly higher yield in branched-chain products.

Finally, keeping in mind that methyl oleate isomerization reaction products are complex mixtures, whose properties should be determined to propose their potential uses, the last objective of this work was to give their complete composition description. Additionally, the determination of their properties in cold environments was done by differential scanning calorimetry (DSC) to evaluate their potential use as additives to improve the biodiesel cold flow properties.

The isomerization reaction products were shown to be complex mixtures of gas and liquid phases. The gas-phase is mainly composed of cracking products as light hydrocarbons, methanol, water, carbon dioxide, and dimethyl ether, formed from methanol by acid dehydration. The liquid phase is composed of different kinds of oligomers and monomeric products. Among the oligomers, dimers of oleic acid and estolides were identified by MALDI-TOF analysis. The monomeric products included the desired branched-chain FAMEs, straight isomers of methyl oleate, hydroxy FAMEs,  $\delta$ -lactones and  $\gamma$ -lactones, and the heaviest compounds of the cracking products which were in this phase. The amount and the distribution in these products can affect the cold flow properties of the methyl oleate isomerization products.

Finally, on the one hand, methyl oleate isomerization using ferrierite-based materials as catalysts produced a less wide distribution of mainly mono-unsaturated branched-chain fatty acid methyl esters with methyl group farther from the carboxylic head. On the other hand, methyl oleate isomerization using zeolite Y based materials as catalysts produced a broader mixture of saturated and mono-unsaturated branched fatty acid methyl esters. The presence of the mesoporous system in the zeolite structures did not significantly affect the isomer product distribution.

The effect of the isomerization reaction on the behavior at low temperatures of methyl oleate was evaluated and it showed that isomerization led to the worsening of the product properties at low temperatures. This was due to the presence of E-(trans) isomers among the branched-chain and straight isomers produced. In order to get improvements in the behavior at cold temperatures of these products, high yields in branched-chain products must be obtained. Low to medium yields in branched products lead to high amounts of E-mono-unsaturated FAMEs, leading to worsening the behavior in cold environments. The levels of straight unsaturated C<sub>18</sub> positional/geometrical isomers of methyl oleate have a more significant effect than the levels of branched-chain isomers in the behavior at low temperatures of methyl oleate isomerization products. The presence of high levels of oligomer products has a non-negligible effect on this product behavior in cold environments. The product obtained using H-FER-REC as catalyst at 285°C and 2.0 MPa in continuous flow conditions in the first hours of time-on-stream showed the lowest onset temperature of freezing point ( $T_{OF}$ : -17.4°C). On the other hand, the lower yields in branched-chain products obtained using zeolite Y based catalysts lead to a worse behavior in cold environments of the zeolite based materials, than the ones obtained using ferrierite as the catalyst. The worst behavior at low temperatures was obtained using H-Y-30-PAR as the catalyst at 285°C and 2.0 MPa in batch conditions. The  $T_{OF}$  value of +2.3°C differed from 19.7°C than the lowest  $T_{OF}$  value reported in this work.

As a general conclusion, it was possible to see that the presence of a secondary mesopore system in these zeolitic materials used as catalysts helped improve catalytic performances, especially these mesopores helped enhance the catalyst stability in the time-on-stream. The presence of the mesoporous system in the zeolite structures did not significantly affect the distribution of the isomer products, which are more determined by the zeolite microporous framework.

## 8.2 Perspectives

Although the potential use of the methyl oleate isomerization products as additives to improve cold flow properties is not advisable according to their properties in cold environments, the improvement of the yields in branched-chain products and of the catalyst stability in this reaction could represent a breakthrough development to the use in different applications.

In order to improve the properties of the zeolitic materials as catalysts through recrystallization, obtaining hierarchical systems of meso and micropores is certainly desired with low silica zeolitic materials. As observed in this work in the case of low silica ferrierite and in the case of low silica zeolite Y, as observed in other research works, the desilication in such materials is problematic due to the high aluminum levels. In the studied conditions, the one-step recrystallization process led to the preparation of a mesoporous system which is not homogeneously distributed in the zeolite crystals and which is mainly connected to the external surface by micropores. New conditions of temperature, pressure, hydrothermal treatment times or different reagents should be studied to improve the distribution and connectivity of these new mesopore systems in these materials.

Finally, considering that the presence of straight-line saturated fatty acids is more responsible for biodiesel lousy behavior in cold environments than the presence of unsaturated ones, a preliminary study of the methyl palmitate hydroisomerization using the bifunctional metal/acid meso-microporous zeolitic materials as catalysts was done. These preliminary results showed low conversion values and low yields in branched products. A high amount of catalyst (10% wt.) and long reaction time (18h) was necessary to get significant results. The performances of parent and recrystallized zeolitic materials impregnated with platinum as catalysts were compared, and it was shown that the use of the recrystallized zeolites had a substantial effect. Optimal operational conditions should still be determined to improve the hydroisomerization reaction. An in-depth study of the relationship between the textural and acidic properties of the zeolitic materials, which determine the isomerization step, and the metal catalytic sites, which determine the hydrogenation/dehydrogenation steps, is recommended. New investigations developing innovative ways to reduce the diffusion path of intermediates without any loss of the shape selectivity of the zeolites should improve the yields in branched-chain products in the hydroisomerization reaction.



## REFERENCES

- [1] J.A. Martens, A. Bogaerts, N. De Kimpe, P.A. Jacobs, G.B. Marin, K. Rabaey, M. Saeys, S. Verhelst, The Chemical Route to a Carbon Dioxide Neutral World, *ChemSusChem*. 10 (2017) 1039–1055. <https://doi.org/10.1002/cssc.201601051>.
- [2] D. Hales, *Renewables 2018 global status report*, 2018.
- [3] A. Callegari, S. Bolognesi, D. Cecconet, A.G. Capodaglio, Production technologies, current role, and future prospects of biofuels feedstocks: A state-of-the-art review, *Crit. Rev. Environ. Sci. Technol.* 0 (2019) 1–53. <https://doi.org/10.1080/10643389.2019.1629801>.
- [4] R.S. Singh, A. Pandey, E. Gnansounou, *Biofuels Production and future perspectives*, 2017.
- [5] C.T. Smith, B. Lattimore, G. Berndes, N.S. Bentsen, I. Dimitriou, J.W.A. (Hans) Langeveld, E. Thiffault, Opportunities to encourage mobilization of sustainable bioenergy supply chains, *Wiley Interdiscip. Rev. Energy Environ.* 6 (2017). <https://doi.org/10.1002/wene.237>.
- [6] C. Perego, A. Bosetti, Biomass to fuels: The role of zeolite and mesoporous materials, *Microporous Mesoporous Mater.* 144 (2011) 28–39. <https://doi.org/10.1016/j.micromeso.2010.11.034>.
- [7] A. Corma Canos, S. Iborra, A. Velty, Chemical routes for the transformation of biomass into chemicals, *Chem. Rev.* 107 (2007) 2411–2502. <https://doi.org/10.1021/cr050989d>.
- [8] T. Ennaert, J. Van Aelst, J. Dijkmans, R. De Clercq, W. Schutyser, M. Dusselier, D. Verboekend, B.F. Sels, Potential and challenges of zeolite chemistry in the catalytic conversion of biomass, *Chem. Soc. Rev.* (2015). <https://doi.org/10.1039/C5CS00859J>.
- [9] D. Kubička, O. Kikhtyanin, Opportunities for zeolites in biomass upgrading—Lessons from the refining and petrochemical industry, *Catal. Today*. 243 (2015) 10–22. <https://doi.org/10.1016/j.cattod.2014.07.043>.
- [10] R. Tesser, R. Vitiello, V. Russo, R. Turco, M. Di Serio, L. Lin, C. Li, *Industrial Oil Plant*, Springer Singapore, 2020. <https://doi.org/10.1007/978-981-15-4920-5>.
- [11] A. Masudi, O. Muraza, Vegetable Oil to Biolubricants: Review on Advanced Porous Catalysts, *Energy and Fuels*. 32 (2018) 10295–10310. <https://doi.org/10.1021/acs.energyfuels.8b02017>.

- [12] S.C.C. Wiedemann, P.C.A. Bruijninx, B.M. Weckhuysen, Isostearic Acid: A Unique Fatty Acid with Great Potential, *Chem. Fuels from Bio-Based Build. Blocks*. (2016) 51–78. <https://doi.org/10.1002/9783527698202.ch3>.
- [13] X. Cheng, T. Cacciaguerra, D. Minoux, J.P. Dath, F. Fajula, C. Gérardin, Generation of parallelepiped-shaped mesopores and structure transformation in highly stable ferrierite zeolite crystals by framework desilication in NaOH solution, *Microporous Mesoporous Mater.* 260 (2018) 132–145. <https://doi.org/10.1016/j.micromeso.2017.05.050>.
- [14] R. Chal, Préparation de matériaux zéolithiques à mésoporosité contrôlée à l'aide d'agents structurants recyclables dans l'eau, 2012.
- [15] L. Vaugon, Etude des performances en hydrocraquage de catalyseurs zéolithiques modèles : influence de l'architecture poreuse et de l'acidité, ENSCM, 2017.
- [16] BP p.l.c., BP Energy Outlook 2019 edition The Energy Outlook explores the forces shaping the global energy transition out to 2040 and the key uncertainties surrounding that, BP Energy Outlook 2019. (2019).
- [17] BP, Statistical Review of World Energy, 2020 | 69th Edition, Bp. (2020) 66. <https://www.bp.com/content/dam/bp/business-sites/en/global/corporate/pdfs/energy-economics/statistical-review/bp-stats-review-2020-full-report.pdf>.
- [18] BP, Energy Outlook 2020 edition, 2020.
- [19] P.G. Levi, J.M. Cullen, Mapping Global Flows of Chemicals: Supporting Information, *Environ. Sci. Technol.* (2018).
- [20] J.O. Metzger, Fats and oils as renewable feedstock for chemistry, *Eur. J. Lipid Sci. Technol.* 111 (2009) 865–876. <https://doi.org/10.1002/ejlt.200900130>.
- [21] E. Pereira, A.J.A. Meirelles, G.J. Maximo, Predictive models for physical properties of fats, oils, and biodiesel fuels, *Fluid Phase Equilib.* 508 (2020) 112440. <https://doi.org/10.1016/j.fluid.2019.112440>.
- [22] OECD/FAO, OECD-FAO Agricultural Outlook 2019-2028 - Special focus: Latin America, 2019.
- [23] USDA, Oilseeds: World Market and Trade, 2020.
- [24] K. Hill, Fats and Oils as Oleochemical Raw Materials, *Pure Appl. Chem.* 72 (2000) 1255–1264. <https://doi.org/10.5650/jos.50.433>.
- [25] U. Biermann, U. Bornscheuer, M.A.R. Meier, J.O. Metzger, H.J. Schäfer, Oils and fats as renewable raw materials in chemistry, *Angew. Chemie - Int. Ed.* 50 (2011) 3854–3871. <https://doi.org/10.1002/anie.201002767>.
- [26] Malaysian Palm Oil Board (MPOB), Pocketbook of oil palm uses, 2017. [www.mpob.gov.my](http://www.mpob.gov.my).
- [27] T.M.I. Mahlia, Z.A.H.S. Syazmi, M. Mofijur, A.E.P. Abas, M.R. Bilad, H.C. Ong, A.S. Silitonga, Patent landscape review on biodiesel production: Technology updates,



- Renew. Sustain. Energy Rev. 118 (2020) 109526. <https://doi.org/10.1016/j.rser.2019.109526>.
- [28] S.L. Douvartzides, N.D. Charisiou, K.N. Papageridis, M.A. Goula, Green diesel: Biomass feedstocks, production technologies, catalytic research, fuel properties and performance in compression ignition internal combustion engines, *Energies*. 12 (2019). <https://doi.org/10.3390/en12050809>.
- [29] I.S.A. Manaf, N.H. Embong, S.N.M. Khazaai, M.H.A. Rahim, M.M. Yusoff, K.T. Lee, G.P. Maniam, A review for key challenges of the development of biodiesel industry, *Energy Convers. Manag.* 185 (2019) 508–517. <https://doi.org/10.1016/j.enconman.2019.02.019>.
- [30] O. of the P.E. Countries, 2018 World Oil Outlook, Vienna, 2018.
- [31] J.F. Sierra-cantor, C.A. Guerrero-fajardo, Methods for improving the cold flow properties of biodiesel with high saturated fatty acids content: A review, *Renew. Sustain. Energy Rev.* 72 (2017) 774–790. <https://doi.org/10.1016/j.rser.2017.01.077>.
- [32] B. Sajjadi, A.A.A. Raman, H. Arandiyan, A comprehensive review on properties of edible and non-edible vegetable oil-based biodiesel: Composition, specifications and prediction models, *Renew. Sustain. Energy Rev.* 63 (2016) 62–92. <https://doi.org/10.1016/j.rser.2016.05.035>.
- [33] A. Anwar, A. Garforth, Challenges and opportunities of enhancing cold flow properties of biodiesel via heterogeneous catalysis, *Fuel*. 173 (2016) 189–208. <https://doi.org/10.1016/j.fuel.2016.01.050>.
- [34] U.Z.F.V.O.-U. PROTEINPFLANZEN, UFOP Report on Global Market Supply, 2019.
- [35] O. Ali, T. Yusaf, R. Mamat, N. Abdullah, A. Abdullah, Influence of Chemical Blends on Palm Oil Methyl Esters' Cold Flow Properties and Fuel Characteristics, *Energies*. 7 (2014) 4364–4380. <https://doi.org/10.3390/en7074364>.
- [36] R. El-araby, A. Amin, A.K. El Morsi, N.N. El-ibiari, G.I. El-diwani, Study on the characteristics of palm oil – biodiesel – diesel fuel blend, 27 (2018) 187–194. <https://doi.org/10.1016/j.ejpe.2017.03.002>.
- [37] Ilijian Leng, W. Li, H. Li, S. Jiang, wenguang zhou, Cold flow properties of biodiesel and the improvement methods: a review, *Energy & Fuels*. (2020). <https://doi.org/10.1021/acs.energyfuels.0c01912>.
- [38] C.B. Sia, J. Kansedo, Y.H. Tan, K.T. Lee, Evaluation on biodiesel cold flow properties, oxidative stability and enhancement strategies: A review, *Biocatal. Agric. Biotechnol.* 24 (2020) 101514. <https://doi.org/10.1016/j.bcab.2020.101514>.
- [39] B.R. Moser, Biodiesel production, properties, and feedstocks, *Vitr. Cell. Dev. Biol. - Plant.* 45 (2009) 229–266. <https://doi.org/10.1007/s11627-009-9204-z>.
- [40] S.K. Hoekman, A. Broch, C. Robbins, E. Cenicerros, M. Natarajan, Review of biodiesel composition, properties, and specifications, *Renew. Sustain. Energy Rev.* 16 (2012) 143–169. <https://doi.org/10.1016/j.rser.2011.07.143>.
- [41] G. Dwivedi, M. Sharma, Cold Flow Behavior of Biodiesel-A Review, ... *J. Renew.*

- Energy Res. 3 (2013). <http://www.ijrer.org/index.php/ijrer/article/view/860> (accessed October 13, 2014).
- [42] E.G. Giakoumis, A statistical investigation of biodiesel physical and chemical properties, and their correlation with the degree of unsaturation, *Renew. Energy*. 50 (2013) 858–878. <https://doi.org/10.1016/j.renene.2012.07.040>.
- [43] G. Knothe, R.O. Dunn, A Comprehensive Evaluation of the Melting Points of Fatty Acids and Esters Determined by Differential Scanning Calorimetry, *J. Am. Oil Chem. Soc.* 86 (2009) 843–856. <https://doi.org/10.1007/s11746-009-1423-2>.
- [44] G. Liu, Development of low-temperature properties on biodiesel fuel: a review, *Int. J. Energy Res.* 31 (2015) 135–147. <https://doi.org/10.1002/er>.
- [45] P. Benjumea, J. Agudelo, A. Agudelo, Basic properties of palm oil biodiesel–diesel blends, *Fuel*. 87 (2008) 2069–2075. <https://doi.org/10.1016/j.fuel.2007.11.004>.
- [46] P. Benjumea, J.R. Agudelo, A.F. Agudelo, Effect of the Degree of Unsaturation of Biodiesel Fuels on Engine Performance, Combustion Characteristics, and Emissions, *Energy & Fuels*. 25 (2011) 77–85. <https://doi.org/10.1021/ef101096x>.
- [47] a. Kleinová, J. Paligová, M. Vrbová, J. Mikulec, J. Cvengroš, Cold Flow Properties of Fatty Esters, *Process Saf. Environ. Prot.* 85 (2007) 390–395. <https://doi.org/10.1205/psep07009>.
- [48] J.F. Sierra-Cantor, Ésteres Alquílicos de Ácidos Grasos Isomerizados como Aditivos para el Mejoramiento de las Propiedades de Flujo en Frio del Biodiesel, 2016.
- [49] B.R. Moser, Impact of fatty ester composition on low temperature properties of biodiesel–petroleum diesel blends, *Fuel*. 115 (2014) 500–506. <https://doi.org/10.1016/j.fuel.2013.07.075>.
- [50] R.O. Dunn, Cold flow properties of biodiesel: a guide to getting an accurate analysis, *Biofuels*. 6 (2015) 115–128. <https://doi.org/10.1080/17597269.2015.1057791>.
- [51] R. Chiriac, F. Toche, C. Brylinsky, Biodiesel: Characterization by DSC and P-DSC, in: *Calorim. Therm. Methods Catal.*, 2013: pp. 455–479. <https://doi.org/10.1007/978-3-642-11954-5>.
- [52] R.O. Dunn, Cold flow properties of biodiesel : a guide to getting an accurate analysis, *Biofuels*. (2015). <https://doi.org/10.1080/17597269.2015.1057791>.
- [53] G. Ajithkumar, N.H. Jayadas, M. Bashi, Analysis of the pour point of coconut oil as a lubricant base stock using differential scanning calorimetry, *Lubr. Sci.* 21 (2009) 13–26. <https://doi.org/10.1002/lis>.
- [54] R.O. Dunn, Thermal analysis of alternative diesel fuels from vegetable oils, *JAOCS*, *J. Am. Oil Chem. Soc.* 76 (1999) 109–115. <https://doi.org/10.1007/s11746-999-0056-9>.
- [55] G. Ajithkumar, THE COLD FLOW PROPERTIES OF VEGETABLE OILS, COCHIN UNIVERSITY OF SCIENCE AND TECHNOLOGY, 2009.
- [56] I.M. Monirul, H.H. Masjuki, M.A. Kalam, N.W.M. Zulkifli, H.K. Rashedul, M.M.

- Rashed, H.K. Imdadul, M.H. Mosarof, A comprehensive review on biodiesel cold flow properties and oxidation stability along with their improvement processes, *RSC Adv.* 5 (2015) 86631–86655. <https://doi.org/10.1039/C5RA09555G>.
- [57] K.A. Sorate, P. V. Bhale, Biodiesel properties and automotive system compatibility issues, *Renew. Sustain. Energy Rev.* 41 (2014) 777–798. <https://doi.org/10.1016/j.rser.2014.08.079>.
- [58] O. Edith, R.B. Janius, R. Yunus, Factors Affecting the Cold Flow Behaviour of Biodiesel and Methods for Improvement – A Review, 20 (2012) 1–14.
- [59] T. Lei, Z. Wang, X. Chang, L. Lin, X. Yan, Y. Sun, X. Shi, X. He, J. Zhu, Performance and emission characteristics of a diesel engine running on optimized ethyl levulinate–biodiesel–diesel blends, *Energy.* 95 (2016) 29–40. <https://doi.org/10.1016/j.energy.2015.11.059>.
- [60] ASTM, Standard Test Method for Cloud Point of Petroleum Products 1, 2014. <https://doi.org/10.1520/D2500-11.2>.
- [61] ASTM, Standard test method for pour point of petroleum products, 2018. <https://doi.org/10.1520/D0097-17B.In>.
- [62] ASTM, Standard Test Method for Cold Filter Plugging Point of Diesel and Heating Fuels, 2010. <https://doi.org/10.1520/D6371-05R10.2>.
- [63] R.O. Dunn, H.L. Ngo, M.J. Haas, Branched-Chain Fatty Acid Methyl Esters as Cold Flow Improvers for Biodiesel, *J. Am. Oil Chem. Soc.* 92 (2015) 853–869. <https://doi.org/10.1007/s11746-015-2643-2>.
- [64] S.J. Reaume, Cold flow Improvements to Biodiesel through the use of Heterogeneous Catalytic Skeletal Isomerization, Elsevier Ltd, 2013. <https://doi.org/10.1016/j.biombioe.2012.12.008>.
- [65] U. Biermann, J.O. Metzger, Synthesis of alkyl-branched fatty acids, *Eur. J. Lipid Sci. Technol.* 110 (2008) 805–811. <https://doi.org/10.1002/ejlt.200800033>.
- [66] J. Habelberg, A. Behr, Saturated branched fatty compounds: Proven industrial processes and new alternatives, *Eur. J. Lipid Sci. Technol.* 118 (2016) 36–46. <https://doi.org/10.1002/ejlt.201500461>.
- [67] G. Biresaw, H.L. Ngo, R.O. Dunn, Investigation of the Physical and Tribological Properties of Iso -Oleic Acid, *JAOCS, J. Am. Oil Chem. Soc.* 96 (2019) 189–199. <https://doi.org/10.1002/aocs.12177>.
- [68] H.L. Ngo, A. Nuñez, W. Lin, T. a. Foglia, A. Nunez, W. Lin, T. a. Foglia, Zeolite-catalyzed isomerization of oleic acid to branched-chain isomers, *Eur. J. Lipid Sci. Technol.* 109 (2007) 214–224. <https://doi.org/10.1002/ejlt.200600246>.
- [69] S.J. Reaume, N. Ellis, Optimizing Reaction Conditions for the Isomerization of Fatty Acids and Fatty Acid Methyl Esters to Their Branch Chain Products, *J. Am. Oil Chem. Soc.* 88 (2011) 661–671. <https://doi.org/10.1007/s11746-010-1718-3>.
- [70] M.I. Sarker, R.J. Latona, R.A. Moreau, D. Micheroni, K.C. Jones, H.L. Ngo, Convenient and Environmentally Friendly Production of Isostearic Acid with Protonic

- Forms of Ammonium Cationic Zeolites, *Eur. J. Lipid Sci. Technol.* 119 (2017) 1700262. <https://doi.org/10.1002/ejlt.201700262>.
- [71] A.F. Elsasser, L.A. McCargar, METHOD OF PREPARING DIMERIC FATTY ACIDS AND/OR ESTERS THEREOF CONTAINING LOW RESIDUAL INTERESTERS AND THE RESULTING DIMERIC FATTY ACIDS AND/OR DIMERIC FATTY ESTERS, 2001.
- [72] M.I. Sarker, R.A. Moreau, H.L. Ngo, Comparison of Various Phosphine Additives in Zeolite Based Catalytic Isomerization of Oleic Acid, *Eur. J. Lipid Sci. Technol.* (2018). <https://doi.org/10.1002/ejlt.201800070>.
- [73] A. Dhar, R.L. Vekariya, P. Bhadja, n-Alkane isomerization by catalysis-a method of industrial importance: An overview, *Cogent Chem.* 4 (2018). <https://doi.org/10.1080/23312009.2018.1514686>.
- [74] C. Renee, A novel bifunctional catalyst for alkene isomerization : development, scope and limitations, and applications in organic transformations, University of California, 2012.
- [75] S.J. Reaume, Cold Flow Improvements to Biodiesel through the use of Heterogeneous Catalytic Skeletal Isomerization, 2013. <https://doi.org/10.1016/j.biombioe.2012.12.008>.
- [76] S.C.C. Wiedemann, J.A. Stewart, F. Soulimani, T. Van Bergen-Brenkman, S. Langelaar, B. Wels, P. De Peinder, P.C.A. Bruijninx, B.M. Weckhuysen, Skeletal isomerisation of oleic acid over ferrierite in the presence and absence of triphenylphosphine: Pore mouth catalysis and related deactivation mechanisms, *J. Catal.* 316 (2014) 24–35. <https://doi.org/10.1016/j.jcat.2014.04.018>.
- [77] J. Weitkamp, Catalytic Hydrocracking-Mechanisms and Versatility of the Process, *ChemCatChem.* 4 (2012) 292–306. <https://doi.org/10.1002/cctc.201100315>.
- [78] H.L. Ngo, E. Hoh, T. a. Foglia, Improved synthesis and characterization of saturated branched-chain fatty acid isomers, *Eur. J. Lipid Sci. Technol.* 114 (2012) 213–221. <https://doi.org/10.1002/ejlt.201000471>.
- [79] S.C.C. Wiedemann, A. Muñoz-Murillo, R. Oord, T. Van Bergen-Brenkman, B. Wels, P.C. a. Bruijninx, B.M. Weckhuysen, Skeletal isomerisation of oleic acid over ferrierite: Influence of acid site number, accessibility and strength on activity and selectivity, *J. Catal.* 329 (2015) 195–205. <https://doi.org/10.1016/j.jcat.2015.05.013>.
- [80] S.C.C. Wiedemann, Z. Ristanović, G.T. Whiting, V.R. Reddy Marthala, J. Kärger, J. Weitkamp, B. Wels, P.C.A. Bruijninx, B.M. Weckhuysen, Large Ferrierite Crystals as Models for Catalyst Deactivation during Skeletal Isomerisation of Oleic Acid: Evidence for Pore Mouth Catalysis, *Chemistry.* 22 (2016) 199–210. <https://doi.org/10.1002/chem.201503551>.
- [81] M. Guisnet, “ideal” bifunctional catalysis over Pt-acid zeolites, *Catal. Today.* 218–219 (2013) 123–134. <https://doi.org/10.1016/j.cattod.2013.04.028>.
- [82] P. Mäki-arvela, T.A. Kaka, M. Azkaar, S. Engblom, D.Y. Murzin, Catalytic Hydroisomerization of Long-Chain Hydrocarbons for the Production of Fuels,

- Catalysts. 8 (2018) 1–27. <https://doi.org/10.3390/catal8110534>.
- [83] C. Adlhart, E. Uggerud, Mechanisms for the dehydrogenation of alkanes on platinum: Insights gained from the reactivity of gaseous cluster cations, *Ptn+ n=1-21*, Chem. - A Eur. J. 13 (2007) 6883–6890. <https://doi.org/10.1002/chem.200700501>.
- [84] J.A. Martens, G. Vanbutsele, P.A. Jacobs, J. Denayer, R. Ocakoglu, G. Baron, J.A.M. Arroyo, J. Thybaut, G.B. Marin, Evidences for pore mouth and key–lock catalysis in hydroisomerization of long n-alkanes over 10-ring tubular pore bifunctional zeolites, *Catal. Today*. 65 (2001) 111–116.
- [85] J. Zecevic, G. Vanbutsele, K.P. de Jong, J.A. Martens, Nanoscale intimacy in bifunctional catalysts for selective conversion of hydrocarbons, *Nature*. 528 (2015) 245–248. <https://doi.org/10.1038/nature16173>.
- [86] J. Weitkamp, The Influence of Chain Length in Hydrocracking and Hydroisomerization of n-Alkanes, in: *Hydricracking and Hydrotreating*, 1975: p. 27.
- [87] J.A. Martens, D. Verboekend, K. Thomas, G. Vanbutsele, J. Pérez-Ramírez, J.P. Gilson, Hydroisomerization and hydrocracking of linear and multibranched long model alkanes on hierarchical Pt/ZSM-22 zeolite, *Catal. Today*. 218–219 (2013) 135–142. <https://doi.org/10.1016/j.cattod.2013.03.041>.
- [88] L. Hermida, A.Z. Abdullah, A.R. Mohamed, Deoxygenation of fatty acid to produce diesel-like hydrocarbons: A review of process conditions, reaction kinetics and mechanism, *Renew. Sustain. Energy Rev.* 42 (2015) 1223–1233. <https://doi.org/10.1016/j.rser.2014.10.099>.
- [89] S. Khan, A.N. Kay Lup, K.M. Qureshi, F. Abnisa, W.M.A. Wan Daud, M.F.A. Patah, A review on deoxygenation of triglycerides for jet fuel range hydrocarbons, *J. Anal. Appl. Pyrolysis*. 140 (2019) 1–24. <https://doi.org/10.1016/j.jaap.2019.03.005>.
- [90] A. Amin, Review of diesel production from renewable resources: Catalysis, process kinetics and technologies, *Ain Shams Eng. J.* 10 (2019) 821–839. <https://doi.org/10.1016/j.asej.2019.08.001>.
- [91] B.P. Pattanaik, R.D. Misra, Effect of reaction pathway and operating parameters on the deoxygenation of vegetable oils to produce diesel range hydrocarbon fuels: A review, *Renew. Sustain. Energy Rev.* 73 (2017) 545–557. <https://doi.org/10.1016/j.rser.2017.01.018>.
- [92] A. Kiméné, R. Wojcieszak, S. Paul, F. Dumeignil, Catalytic decarboxylation of fatty acids to hydrocarbons over non-noble metal catalysts: the state of the art, *J. Chem. Technol. Biotechnol.* 94 (2019) 658–669. <https://doi.org/10.1002/jctb.5776>.
- [93] R. Chal, C. Gerardin, M. Bulut, S. VanDonk, Overview and Industrial Assessment of Synthesis Strategies towards Zeolites with Mesopores, *ChemCatChem*. 3 (2011) 67–81. <https://doi.org/10.1002/cctc.201000158>.
- [94] W. Vermeiren, J.P. Gilson, Impact of zeolites on the petroleum and petrochemical industry, *Top. Catal.* 52 (2009) 1131–1161. <https://doi.org/10.1007/s11244-009-9271-8>.

- [95] L. Ha, J. Mao, J. Zhou, Z.C. Zhang, S. Zhang, Skeletal isomerization of unsaturated fatty acids on Beta zeolites: Effects of calcination temperature and additives, *Appl. Catal. A Gen.* 356 (2009) 52–56. <https://doi.org/10.1016/j.apcata.2008.12.018>.
- [96] S. Zhang, Z. Zhang, D. Steichen, Skeletal Isomerization of Fatty Acids, 2004.
- [97] W.R. Hodgson, W. Tijmen, C. Lok, G. Roberts, Fatty acid isomerization, US005856439A, 1999.
- [98] M.I. Sarker, H.N. Lew, R. a. Moreau, SATURATED BRANCHED CHAIN FATTY ACID PRODUCTION METHOD, US 10 , 087 , 132 B2, 2018.
- [99] H.L. Ngo, T. a. Foglia, PROCESS FOR PREPARING SATURATED BRANCHED BRANCHED CHAIN FATTY ACIDS, 2015. <https://doi.org/10.1038/incomms1464>.
- [100] H.L. Ngo, Improved zeolite regeneration processes for preparing saturated branched-chain fatty acids, *Eur. J. Lipid Sci. Technol.* 116 (2014) 645–652. <https://doi.org/10.1002/ejlt.201300315>.
- [101] H.L. Ngo, Lewis base additives improve the zeolite Ferrierite-catalyzed synthesis of isostearic acids synthesis of isostearic acids, *JAOCS, J. Am. Oil Chem. Soc.* 92 (2015) 613–619. <https://doi.org/10.1007/s11746-015-2608-5>.
- [102] M. Fan, T. Si, P. Zhang, Effect of Surface Modification of H<sup>+</sup>-Mordenite on the Isomerization of Oleic Acid into Branched-Chain Isomers, *JAOCS, J. Am. Oil Chem. Soc.* 95 (2018) 1357–1365. <https://doi.org/10.1002/aocs.12142>.
- [103] J. Zhang, J. Uknalis, L. Chen, R.A. Moreau, H.L. Ngo, Development of Magnesium Oxide–Zeolite Catalysts for Isomerization of Fatty Acids, *Catal. Letters.* 149 (2019) 303–312. <https://doi.org/10.1007/s10562-018-2601-3>.
- [104] A. Bolshakov, R. van de Poll, T. van Bergen-Brenkman, S.C.C. Wiedemann, N. Kosinov, E.J.M. Hensen, Hierarchically porous FER zeolite obtained via FAU transformation for fatty acid isomerization, *Appl. Catal. B Environ.* 263 (2019) 118356. <https://doi.org/10.1016/j.apcatb.2019.118356>.
- [105] S.C.C. Wiedemann, Ferrierite-Catalysed Branching of Unsaturated Fatty Acids, Utrecht University, 2015.
- [106] V.L. Zholobenko, D.B. Lukyanov, J. Dwyer, W.J. Smith, Ferrierite and SUZ-4 zeolite: Characterization of acid sites, *J. Phys. Chem. B.* 102 (1998) 2715–2721. <https://doi.org/10.1021/jp973340o>.
- [107] D. Verboekend, New Hierarchical Zeolite Catalysts by Post-Synthetic Design, ETH Zurich, 2012. <https://doi.org/10.3929/ethz-a-007595445>.
- [108] S. Van Donk, Adsorption, Diffusion and Reaction Studies of Hydrocarbons on Zeolite Catalysts, Utrecht university, 2002.
- [109] A. Dhar, R.L. Vekariya, P. Bhadja, n-Alkane isomerization by catalysis—a method of industrial importance: An overview, *Cogent Chem.* 4 (2018) 1–19. <https://doi.org/10.1080/23312009.2018.1514686>.
- [110] S. Kulprathipanja, Zeolites in Industrial Separation and Catalysis, 2010.

- <https://doi.org/10.1002/9783527629565>.
- [111] J. García-Martínez, K. Li, *Mesoporous Zeolites: Preparation, Characterization, and Applications*, 2015. <https://doi.org/10.1002/9783527673957>.
- [112] J. Cejka, A. Corma, S. Zones, *Zeolites and Catalysis: Synthesis, Reactions and Applications*, WILEY-VCH Verlag GmbH & Co. KGaA, Weinheim, 2010. <https://doi.org/10.1002/9783527630295>.
- [113] R. Hull, C. Jagadish, R.M. Osgood Jr, J. Parisi, Z. Wang, H. Warlimont, *Characterization and Design of Zeolite Catalysts*, 2010.
- [114] L.B. McCusker, F. Liebau, G. Engelhardt, Nomenclature of structural and compositional characteristics of ordered microporous and mesoporous materials with inorganic hosts: (IUPAC recommendations 2001), *Pure Appl. Chem.* 73 (2001) 381–394. <https://doi.org/10.1351/pac200173020381>.
- [115] R.W. Broach, *Zeolite Types and Structures*, in: *Zeolites Ind. Sep. Catal.*, 2010: pp. 27–59. <https://doi.org/10.1002/9783527629565.ch2>.
- [116] C. Demone, *Partial Atomic Charge Methods for Simulating Porous Frameworks with a Net Charge and their Application to Gas Separations in Zeolites*., University of Ottawa, 2018.
- [117] K. Li, M. Beaver, B. Speronello, J. García-Martínez, Surfactant-Templated Mesosstructuring of Zeolites: From Discovery to Commercialization, in: *Mesoporous Zeolites Prep. Charact. Appl.*, 2015: pp. 321–348. <https://doi.org/10.1002/9783527673957.ch10>.
- [118] A. Deneyer, Q. Ke, J. Devos, M. Dusselier, Zeolite Synthesis under Nonconventional Conditions: Reagents, Reactors, and Modi Operandi, *Chem. Mater.* 32 (2020) 4884–4919. <https://doi.org/10.1021/acs.chemmater.9b04741>.
- [119] K. Li, J. Valla, J. García-Martínez, Realizing the commercial potential of hierarchical zeolites: New opportunities in catalytic cracking, *ChemCatChem.* 6 (2014) 46–66. <https://doi.org/10.1002/cctc.201300345>.
- [120] Y. Tao, H. Kanoh, L. Abrams, K. Kaneko, Mesopore-modified zeolites: Preparation, characterization, and applications, *Chem. Rev.* 106 (2006) 896–910. <https://doi.org/10.1021/cr040204o>.
- [121] M. Hartmann, G. Machoke, W. Schwieger, M. Hartmann, Catalytic Test Reactions for the Evaluation of Hierarchical Zeolites, *Chem. Soc. Rev.* 45 (2016) 3313–3330. <https://doi.org/10.1039/C5CS00935A>.
- [122] J. van den Bergh, J. Gascon, F. Kapteijn, Diffusion in zeolites - impact on catalysis, in: *Zeolites Catal. Synth. React. Appl.*, 2010: pp. 361–387. <https://doi.org/10.1002/9783527630295.ch13>.
- [123] D. Schneider, D. Mehlhorn, P. Zeigermann, J. Kärger, R. Valiullin, Transport Properties of Hierarchical Micro-Mesoporous Materials, *Chem. Soc. Rev.* 45 (2016) 3439–3467. <https://doi.org/10.1039/C5CS00715A>.
- [124] E. Ruckenstein, M.C. Tsai, Optimum pore size for the catalytic conversion of large

- molecules, *AIChE J.* 27 (1981) 697–699. <https://doi.org/10.1017/CBO9781107415324.004>.
- [125] A. Galarneau, A. Sachse, B. Said, C.H. Pelisson, P. Boscaro, N. Brun, L. Courtheoux, N. Olivi-Tran, B. Coasne, F. Fajula, Les monolithes siliciques à porosité hiérarchique: une nouvelle classe de microréacteurs pour l'intensification des procédés en catalyse et en adsorption, *Comptes Rendus Chim.* 19 (2016) 231–247. <https://doi.org/10.1016/j.crci.2015.05.017>.
- [126] C. Sievers, S.L. Scott, Y. Noda, L. Qi, E.M. Albuquerque, R.M. Rioux, Phenomena affecting catalytic reactions at solid–Liquid interfaces, *ACS Catal.* 6 (2016). <https://doi.org/10.1021/acscatal.6b02532>.
- [127] V. V. Ranade, S.S. Joshi, *Catalysis and Catalytic Processes*, in: *Ind. Catal. Process. Fine Spec. Chem.*, Elsevier Inc., 2016: pp. 1–14. <https://doi.org/10.1016/B978-0-12-801457-8.00001-X>.
- [128] J.-F. Joly, F. Giroudière, F. Bertoncini, Innovation in process development: From catalyst to industrial process, *Catal. Today.* 218–219 (2013) 153–161. <https://doi.org/10.1016/j.cattod.2013.09.010>.
- [129] S. Li, J. Li, M. Dong, S. Fan, T. Zhao, J. Wang, W. Fan, Strategies to control zeolite particle morphology, *Chem. Soc. Rev.* 48 (2019) 885–907. <https://doi.org/10.1039/c8cs00774h>.
- [130] E. Koohsaryan, M. Anbia, Nanosized and hierarchical zeolites: A short review, *Cuihua Xuebao/Chinese J. Catal.* 37 (2016) 447–467. [https://doi.org/10.1016/S1872-2067\(15\)61038-5](https://doi.org/10.1016/S1872-2067(15)61038-5).
- [131] W. Schwieger, A.G. Machoke, T. Weissenberger, A. Inayat, T. Selvam, M. Klumpp, A. Inayat, Hierarchy concepts: classification and preparation strategies for zeolite containing materials with hierarchical porosity, *Chem. Soc. Rev.* 45 (2015) 3353–3376. <https://doi.org/10.1039/C5CS00599J>.
- [132] D. Verboekend, N. Nuttens, R. Locus, J. Van Aelst, P. Verolme, J.C. Groen, J. Pérez-Ramírez, B.F. Sels, Synthesis, characterisation, and catalytic evaluation of hierarchical faujasite zeolites: Milestones, challenges, and future directions, *Chem. Soc. Rev.* 45 (2016) 3331–3352. <https://doi.org/10.1039/c5cs00520e>.
- [133] K. Möller, T. Bein, *Mesoporous Zeolitic Materials*, in: *Compr. Inorg. Chem. II* (Second Ed. From Elem. to Appl., 2013: pp. 247–285. <https://doi.org/10.1016/B978-0-08-097774-4.00716-6>.
- [134] P. Dugkhuntod, C. Wattanakit, A comprehensive review of the applications of hierarchical zeolite nanosheets and nanoparticle assemblies in light olefin production, *Catalysts.* 10 (2020). <https://doi.org/10.3390/catal10020245>.
- [135] T. Pan, Z. Wu, A.C.K. Yip, Advances in the green synthesis of microporous and hierarchical zeolites: A short review, *Catalysts.* 9 (2019) 1–18. <https://doi.org/10.3390/catal9030274>.
- [136] B. Su, C. Sanchez, X.-Y. Yang, *Hierarchically Structured Porous Materials*, 2012.



- [137] M.-H. Sun, S.-Z. Huang, L.-H. Chen, Y. Li, X.-Y. Yang, Z.-Y. Yuan, B.-L. Su, Applications of hierarchically structured porous materials from energy storage and conversion, catalysis, photocatalysis, adsorption, separation, and sensing to biomedicine, *Chem. Soc. Rev.* 45 (2016) 3479–3563. <https://doi.org/10.1039/C6CS00135A>.
- [138] J. Jiang, J. Yu, A. Corma, Extra-large-pore zeolites: bridging the gap between micro and mesoporous structures, *Angew. Chemie - Int. Ed.* 49 (2010) 3120–3145. <https://doi.org/10.1002/anie.200904016>.
- [139] E. Koohsaryan, M. Anbia, Nanosized and hierarchical zeolites: A short review, *Cuihua Xuebao/Chinese J. Catal.* 37 (2016) 447–467. [https://doi.org/10.1016/S1872-2067\(15\)61038-5](https://doi.org/10.1016/S1872-2067(15)61038-5).
- [140] K. Na, M. Choi, R. Ryoo, Recent advances in the synthesis of hierarchically nanoporous zeolites, *Microporous Mesoporous Mater.* 166 (2013) 3–19. <https://doi.org/10.1016/j.micromeso.2012.03.054>.
- [141] Á. Ibarra, A. Veloso, J. Bilbao, J.M. Arandes, P. Castaño, Dual coke deactivation pathways during the catalytic cracking of raw bio-oil and vacuum gasoil in FCC conditions, *Appl. Catal. B Environ.* 182 (2016) 336–346. <https://doi.org/10.1016/j.apcatb.2015.09.044>.
- [142] M. Guisnet, P. Magnoux, Deactivation by coking of zeolite catalysts. Prevention of deactivation. Optimal conditions for regeneration, *Catal. Today.* 36 (1997) 477–483. [https://doi.org/10.1016/S0920-5861\(96\)00238-6](https://doi.org/10.1016/S0920-5861(96)00238-6).
- [143] I.I. Ivanova, E.E. Knyazeva, Micro-mesoporous materials obtained by zeolite recrystallization: Synthesis, characterization and catalytic applications, *Chem. Soc. Rev.* 42 (2013) 3671–3688. <https://doi.org/10.1039/c2cs35341e>.
- [144] M.S. Holm, E. Taarning, K. Egeblad, C.H. Christensen, Catalysis with hierarchical zeolites, *Catal. Today.* 168 (2011) 3–16. <https://doi.org/10.1016/j.cattod.2011.01.007>.
- [145] A. Sachse, J. García-Martínez, Surfactant-Templating of Zeolites: From Design to Application, *Chem. Mater.* 29 (2017) 3827–3853. <https://doi.org/10.1021/acs.chemmater.7b00599>.
- [146] M. Hartmann, W. Schwieger, Hierarchically-structured porous materials: from basic understanding to applications, *Chem. Soc. Rev.* 45 (2016) 3311–3312. <https://doi.org/10.1039/C6CS90043G>.
- [147] S. Lopez-Orozco, A. Inayat, A. Schwab, T. Selvam, W. Schwieger, Zeolitic materials with hierarchical porous structures, *Adv. Mater.* 23 (2011) 2602–2615. <https://doi.org/10.1002/adma.201100462>.
- [148] F. Rouquerol, J. Rouquerol, K.S.W. Sing, P. Llewellyn, G. Maurin, *Adsorption by Powders and Porous Solids*, 2014. <https://doi.org/10.1016/c2010-0-66232-8>.
- [149] R. Srivastava, Synthesis and applications of ordered and disordered mesoporous zeolites: Present and future prospective, *Catal. Today.* 309 (2018) 172–188. <https://doi.org/10.1016/j.cattod.2017.08.017>.

- [150] K. Zhang, M.L. Ostraat, Innovations in hierarchical zeolite synthesis, *Catal. Today*. 264 (2016) 3–15. <https://doi.org/10.1016/j.cattod.2015.08.012>.
- [151] D.P. Serrano, J.M. Escola, P. Pizarro, Synthesis strategies in the search for hierarchical zeolites, *Chem. Soc. Rev.* 42 (2013) 4004–4035. <https://doi.org/10.1039/c2cs35330j>.
- [152] M.C. Silaghi, C. Chizallet, P. Raybaud, Challenges on molecular aspects of dealumination and desilication of zeolites, *Microporous Mesoporous Mater.* 191 (2014) 82–96. <https://doi.org/10.1016/j.micromeso.2014.02.040> Review.
- [153] M. Garcia-Perez, T.T. Adams, J.W. Goodrum, K.C. Das, D.P. Geller, DSC studies to evaluate the impact of bio-oil on cold flow properties and oxidation stability of bio-diesel., *Bioresour. Technol.* 101 (2010) 6219–24. <https://doi.org/10.1016/j.biortech.2010.03.002>.
- [154] D. Verboekend, N. Nuttens, R. Locus, J. Van Aelst, P. Verolme, J.C. Groen, J. Pérez-Ramírez, B.F. Sels, Synthesis, characterisation, and catalytic evaluation of hierarchical faujasite zeolites: Milestones, challenges, and future directions, *Chem. Soc. Rev.* 45 (2016) 3331–3352. <https://doi.org/10.1039/c5cs00520e>.
- [155] M. Manko, R. Chal, P. Trens, D. Minoux, C. Gerardin, W.W. Makowski, M. Mańko, R. Chal, P. Trens, D. Minoux, C. Gérardin, W.W. Makowski, Porosity of micro-mesoporous zeolites prepared via pseudomorphic transformation of zeolite y crystals: A combined isothermal sorption and thermodesorption investigation, *Microporous Mesoporous Mater.* 170 (2013) 243–250. <https://doi.org/10.1016/j.micromeso.2012.12.016>.
- [156] I.I. Ivanova, E.E. Knyazeva, A.A. Maerle, Design and Catalytic Implementation of Hierarchical Micro-Mesoporous Materials Obtained by Surfactant-Mediated Zeolite Recrystallization, in: *Mesoporous Zeolites Prep. Charact. Appl.*, 2015: pp. 295–320. <https://doi.org/10.1002/9783527673957.ch9>.
- [157] W. Lutz, Zeolite Y: Synthesis, modification, and properties - A case revisited, *Adv. Mater. Sci. Eng.* (2014). <https://doi.org/10.1155/2014/724248>.
- [158] E. Catizzzone, M. Migliori, A. Aloise, R. Lamberti, G. Giordano, Hierarchical low si/al ratio ferrierite zeolite by sequential postsynthesis treatment: Catalytic assessment in dehydration reaction of methanol, *J. Chem.* 2019 (2019). <https://doi.org/10.1155/2019/3084356>.
- [159] Y. Wei, T.E. Parmentier, K.P. De Jong, J. Zečević, Tailoring and visualizing the pore architecture of hierarchical zeolites, *Chem. Soc. Rev.* 44 (2015) 7234–7261. <https://doi.org/10.1039/c5cs00155b>.
- [160] W.J. Roth, B. Gil, W. Makowski, B. Marszalek, P. Eliasova, Layer like porous materials with hierarchical structure, *Chem. Soc. Rev.* (2015) 3400–3438. <https://doi.org/10.1039/C5CS00508F>.
- [161] O.A. Ponomareva, I.A. Kasyanov, E.E. Knyazeva, S. V. Konnov, I.I. Ivanova, Effect of the degree of zeolite recrystallization into micro–mesoporous materials on their catalytic properties in petroleum refining and petroleum chemistry processes, *Pet. Chem.* 56 (2016) 819–826. <https://doi.org/10.1134/S0965544116090188>.

- [162] I.I. Ivanova, I.A. Kasyanov, A.A. Maerle, V.I. Zaikovskii, Mechanistic study of zeolites recrystallization into micro-mesoporous materials, *Microporous Mesoporous Mater.* 189 (2014) 163–172. <https://doi.org/10.1016/j.micromeso.2013.11.001>.
- [163] I.A. Kasyanov, A.A. Maerle, I.I. Ivanova, V.I. Zaikovskii, Towards understanding of the mechanism of stepwise zeolite recrystallization into micro/mesoporous materials, *J. Mater. Chem. A* 2 (2014) 16978–16988. <https://doi.org/10.1039/c4ta03681f>.
- [164] K.A. Cychosz, R. Guillet-Nicolas, J. García-Martínez, M. Thommes, Recent advances in the textural characterization of hierarchically structured nanoporous materials, *Chem. Soc. Rev.* (2017). <https://doi.org/10.1039/C6CS00391E>.
- [165] R. Chal, T. Cacciaguerra, S. Van Donk, C. Gérardin, Pseudomorphic synthesis of mesoporous zeolite Y crystals., *Chem. Commun. (Camb)* 46 (2010) 7840–2. <https://doi.org/10.1039/c0cc02073g>.
- [166] H. Xu, J. Zhu, L. Zhu, E. Zhou, C. Shen, Advances in the Synthesis of Ferrierite Zeolite, *Molecules* 25 (2020) 3722.
- [167] W.N.P. Van Der Graaff, E.A. Pidko, E.J.M. Hensen, Zeolites in Sustainable Chemistry, 2016. <https://doi.org/10.1007/978-3-662-47395-5>.
- [168] P.A. Vaughan, The crystal structure of the zeolite ferrierite, *Acta Crystallogr.* (1966). <https://doi.org/10.1107/S0365110X66004298>.
- [169] T. Xue, H. Liu, Y.M. Wang, Synthesis of Hierarchical Ferrierite Using Piperidine and Tetramethylammonium Hydroxide as Cooperative Structure-Directing Agents, *RSC Adv.* (2020).
- [170] M. Moliner, C. Mart??nez, A. Corma, Multipore zeolites: Synthesis and catalytic applications, *Angew. Chemie - Int. Ed.* 54 (2015) 3560–3579. <https://doi.org/10.1002/anie.201406344>.
- [171] A.B. Pinar, L. G??mez-Hortig??ela, L.B. McCusker, J. P??rez-Pariente, Controlling the aluminum distribution in the zeolite ferrierite via the organic structure directing agent, *Chem. Mater.* 25 (2013) 3654–3661. <https://doi.org/10.1021/cm4018024>.
- [172] A. Bonilla, D. Baudouin, J. Pérez-Ramírez, Desilication of ferrierite zeolite for porosity generation and improved effectiveness in polyethylene pyrolysis, *J. Catal.* 265 (2009) 170–180. <https://doi.org/10.1016/j.jcat.2009.04.022>.
- [173] J. Houžvička, V. Ponec, Skeletal isomerization of n-butene, *Catal. Rev. - Sci. Eng.* 39 (1997) 319–344. <https://doi.org/10.1080/01614949708007099>.
- [174] J.G. Goodwin, S. Natesakhawat, A.A. Nikolopoulos, S. Kim, Etherification on Zeolites : MTBE synthesis, *Catal. Rev. - Sci. Eng.* 44 (2002) 287–320.
- [175] Y.P. Khitev, I.I. Ivanova, Y.G. Kolyagin, O.A. Ponomareva, Skeletal isomerization of 1-butene over micro/mesoporous materials based on FER zeolite, *Appl. Catal. A Gen.* 441–442 (2012) 124–135. <https://doi.org/10.1016/j.apcata.2012.07.010>.
- [176] W. Liu, H. Hu, Y. Liu, L. Zhang, C. Xia, Q. Wang, M. Ke, Distribution of Effective Ferrierite Active Sites for Skeletal Isomerization of n-Butene to Isobutene, *ChemistrySelect* 4 (2019) 7851–7857. <https://doi.org/10.1002/slct.201901495>.

- [177] H. Hu, M. Ke, K. Zhang, Q. Liu, P. Yu, Y. Liu, C. Li, W. Liu, Designing ferrierite-based catalysts with improved properties for skeletal isomerization of n -butene to isobutene, *RSC Adv.* 7 (2017) 31535–31543. <https://doi.org/10.1039/c7ra04777k>.
- [178] T. Ikeda, S. Kayamori, Y. Oumi, F. Mizukami, Structure analysis of si-atom pillared lamellar silicates having micropore structure by powder x-ray diffraction, *J. Phys. Chem. C.* 114 (2010) 3466–3476. <https://doi.org/10.1021/jp912026n>.
- [179] H. Xu, Y.X. Yu, L.F. Zhu, C.Q. Bian, H.L. Zhai, J.Y. Tong, H.Z. Wu, C. Shen, Preparation of aluminosilicate ferrierite zeolite nanosheets with controllable thickness in the presence of a sole organic structure directing agent, *Molecules.* 25 (2020). <https://doi.org/10.3390/molecules25040771>.
- [180] V.J. Margarit, M.R. Díaz-Rey, M.T. Navarro, C. Martínez, A. Corma, Direct Synthesis of Nano-Ferrierite along the 10-Ring-Channel Direction Boosts Their Catalytic Behavior, *Angew. Chemie - Int. Ed.* 57 (2018) 3459–3463. <https://doi.org/10.1002/anie.201711418>.
- [181] Y. Wang, Y. Gao, W. Chu, D. Zhao, F. Chen, X. Zhu, X. Li, S. Liu, S. Xie, L. Xu, Synthesis and catalytic application of FER zeolites with controllable size, *J. Mater. Chem. A.* 7 (2019) 7573–7580. <https://doi.org/10.1039/C8TA09420A>.
- [182] H. Xu, W. Chen, G. Zhang, P. Wei, Q. Wu, L. Zhu, X. Meng, X. Li, J. Fei, S. Han, Q. Zhu, A. Zheng, Y. Ma, F.S. Xiao, Ultrathin nanosheets of aluminosilicate FER zeolites synthesized in the presence of a sole small organic ammonium, *J. Mater. Chem. A.* 7 (2019) 16671–16676. <https://doi.org/10.1039/c9ta04833b>.
- [183] Y. Lee, M.B. Park, P.S. Kim, A. Vicente, C. Fernandez, I.S. Nam, S.B. Hong, Synthesis and catalytic behavior of ferrierite zeolite nanoneedles, *ACS Catal.* 3 (2013) 617–621. <https://doi.org/10.1021/cs400025s>.
- [184] E. Catizzzone, S. Van Daele, M. Bianco, A. Di Michele, A. Aloise, M. Migliori, V. Valtchev, G. Giordano, Catalytic application of ferrierite nanocrystals in vapour-phase dehydration of methanol to dimethyl ether, *Appl. Catal. B Environ.* 243 (2019) 273–282. <https://doi.org/10.1016/j.apcatb.2018.10.060>.
- [185] M.C. Silaghi, C. Chizallet, J. Sauer, P. Raybaud, Dealumination mechanisms of zeolites and extra-framework aluminum confinement, *J. Catal.* 339 (2016) 242–255. <https://doi.org/10.1016/j.jcat.2016.04.021>.
- [186] D.P.B. Peixoto, S.M. Cabral de Menezes, M.I. Pais da Silva, Influence of different processes of dealumination on acid properties of an H-ferrierite zeolite, *Mater. Lett.* 57 (2003) 3933–3942. [https://doi.org/10.1016/S0167-577X\(03\)00243-X](https://doi.org/10.1016/S0167-577X(03)00243-X).
- [187] Q. Xu, W. Yang, Z. Chen, Y. Ye, Y. Luo, J. Street, H. Zhou, C. Xu, Formation and Regeneration of Shape-Selective ZSM-35 Catalysts for n-Butene Skeletal Isomerization to Isobutene, *ACS Omega.* 3 (2018) 8202–8211. <https://doi.org/10.1021/acsomega.8b00333>.
- [188] P. Cañizares, A. Carrero, Dealumination of ferrierite by ammonium hexafluorosilicate treatment: Characterization and testing in the skeletal isomerization of n-butene, *Appl. Catal. A Gen.* 248 (2003) 227–237. [https://doi.org/10.1016/S0926-860X\(03\)00159-5](https://doi.org/10.1016/S0926-860X(03)00159-5).

- [189] P. Cañizares, A. Carrero, P. Sánchez, Isomerization of n-butene over ferrierite zeolite modified by silicon tetrachloride treatment, *Appl. Catal. A Gen.* 190 (2000) 93–105. [https://doi.org/10.1016/S0926-860X\(99\)00265-3](https://doi.org/10.1016/S0926-860X(99)00265-3).
- [190] R. Rachwalik, Z. Olejniczak, J. Jiao, J. Huang, M. Hunger, B. Sulikowski, Isomerization of  $\alpha$ -pinene over dealuminated ferrierite-type zeolites, *J. Catal.* 252 (2007) 161–170. <https://doi.org/10.1016/j.jcat.2007.10.001>.
- [191] R. Rachwalik, Z. Olejniczak, B. Sulikowski, Catalytic properties of dealuminated ferrierite type zeolite studied in transformations of m-xylene. Part 2, *Catal. Today.* 114 (2006) 211–216. <https://doi.org/10.1016/j.cattod.2006.01.021>.
- [192] R. Rachwalik, Z. Olejniczak, B. Sulikowski, Dealumination of ferrierite type zeolite: Physicochemical and catalytic properties, *Catal. Today.* 101 (2005) 147–154. <https://doi.org/10.1016/j.cattod.2005.01.012>.
- [193] M.M. Pereira, A. Vieira, E.B. Pereira, L.R.M. dos Santos, Y.L. Lam, Propylene conversion in Ferrierite: Effect of mesoporous formation, *Appl. Catal. A Gen.* 548 (2017) 89–95. <https://doi.org/10.1016/j.apcata.2017.07.013>.
- [194] K. Brylewska, K.A. Tarach, W. Mozgawa, Z. Olejniczak, U. Filek, K. Góra-Marek, Modification of ferrierite through post-synthesis treatments. Acidic and catalytic properties, *J. Mol. Struct.* 1126 (2015) 147–153. <https://doi.org/10.1016/j.molstruc.2015.12.046>.
- [195] D. Verboekend, R. Caicedo-Realpe, A. Bonilla, M. Santiago, J. Pérez-Ramírez, Properties and functions of hierarchical ferrierite zeolites obtained by sequential post-synthesis treatments, *Chem. Mater.* 22 (2010) 4679–4689. <https://doi.org/10.1021/cm100886y>.
- [196] T. Xu, H. Liu, Q. Zhao, S. Cen, L. Du, Q. Tang, Conversion of chloromethane to propylene over fluoride-treated H-ZSM-35 zeolite catalysts, *Catal. Commun.* 119 (2019) 96–100. <https://doi.org/10.1016/j.catcom.2018.10.029>.
- [197] E.G. Fuentes-Ordóñez, J.A. Salbidegoitia, J.L. Ayastuy, M.A. Gutiérrez-Ortiz, M.P. González-Marcos, J.R. González-Velasco, High external surface Pt/zeolite catalysts for improving polystyrene hydrocracking, *Catal. Today.* 227 (2014) 163–170. <https://doi.org/10.1016/j.cattod.2013.09.004>.
- [198] W.J. Roth, B. Gil, A. Mayoral, J. Grzybek, A. Korzeniowska, M. Kubu, W. Makowski, J. Čejka, Z. Olejniczak, M. Mazur, Pillaring of layered zeolite precursors with ferrierite topology leading to unusual molecular sieves on the micro/mesoporous border, *Dalt. Trans.* 47 (2018) 3029–3037. <https://doi.org/10.1039/c7dt03718j>.
- [199] X. Niu, Y. Song, S. Xie, S. Liu, Q. Wang, L. Xu, Synthesis and catalytic reactivity of MCM-22/ZSM-35 composites for olefin aromatization, *Catal. Letters.* 103 (2005) 211–218. <https://doi.org/10.1007/s10562-005-7156-4>.
- [200] S. Xie, S. Liu, Y. Liu, X. Li, W. Zhang, L. Xu, Synthesis and characterization of MCM-49/ZSM-35 composite zeolites in the hexamethyleneimine and cyclohexamine system, *Microporous Mesoporous Mater.* 121 (2009) 166–172. <https://doi.org/10.1016/j.micromeso.2009.01.027>.

- [201] Y.P. Khitev, Y.G. Kolyagin, I.I. Ivanova, O.A. Ponomareva, F. Thibault-Starzyk, J.P. Gilson, C. Fernandez, F. Fajula, Synthesis and catalytic properties of hierarchical micro/mesoporous materials based on FER zeolite, *Microporous Mesoporous Mater.* 146 (2011) 201–207. <https://doi.org/10.1016/j.micromeso.2011.05.003>.
- [202] A. Corma, A. Martínez, V. Martínez-Soria, Catalytic performance of the new delaminated ITQ-2 zeolite for mild hydrocracking and aromatic hydrogenation processes, *J. Catal.* 200 (2001) 259–269. <https://doi.org/10.1006/jcat.2001.3219>.
- [203] T. Xue, H. Liu, Y.M. Wang, Synthesis of Hierarchical Ferrierite Using Piperidine and Tetramethylammonium Hydroxide as Cooperative Structure-Directing Agents, (2015).
- [204] P. Wuamprakhon, C. Wattanakit, C. Warakulwit, T. Yutthalekha, W. Wannapakdee, S. Ittisanronnachai, J. Limtrakul, Direct synthesis of hierarchical ferrierite nanosheet assemblies via an organosilane template approach and determination of their catalytic activity, *Microporous Mesoporous Mater.* 219 (2016) 1–9. <https://doi.org/10.1016/j.micromeso.2015.07.022>.
- [205] W. Chu, X. Li, X. Zhu, S. Xie, C. Guo, S. Liu, F. Chen, L. Xu, Size-controlled synthesis of hierarchical ferrierite zeolite and its catalytic application in 1-butene skeletal isomerization, *Microporous Mesoporous Mater.* 240 (2017) 189–196. <https://doi.org/10.1016/j.micromeso.2016.11.015>.
- [206] X. Feng, P. Zhang, Y. Fang, W. Charusiri, J. Yao, X. Gao, Q. Wei, P. Reubroycharoen, T. Vitidsant, Y. Yoneyama, G. Yang, N. Tsubaki, Designing a hierarchical nanosheet ZSM-35 zeolite to realize more efficient ethanol synthesis from dimethyl ether and syngas, *Catal. Today.* 343 (2020) 206–214. <https://doi.org/10.1016/j.cattod.2019.02.054>.
- [207] S. Jeong, H. Kim, J.H. Bae, D.H. Kim, C.H.F. Peden, Y.K. Park, J.K. Jeon, Synthesis of butenes through 2-butanol dehydration over mesoporous materials produced from ferrierite, *Catal. Today.* 185 (2012) 191–197. <https://doi.org/10.1016/j.cattod.2011.09.017>.
- [208] X. Cheng, C. Gerardin, F. Fajula, L. Vaugon, D. Minoux, J.P. Dath, MESOPOROUS ZEOLITIC MATERIAL, METHOD FOR MAKING THE SAME AND USE, US 20180185827A1, 2018.
- [209] D. Ginter, FAU Linde Type Y Si(71), Al(29), in: *Verif. Synth. Zeolitic Mater.*, 2001: pp. 156–158. <https://doi.org/10.1016/b978-044450703-7/50144-7>.
- [210] K. Nishi, R.W. Thompson, Synthesis of Classical Zeolites, in: F. Schüth, K. Sing, J. Weitkamp (Eds.), *Handb. Porous Solids*, 2002.
- [211] R. Millini, G. Bellussi, Zeolite Science and perspectives, in: *Zeolites Catal. Prop. Appl.*, 2017: pp. 1–1170.
- [212] C.H. Rüschler, N. Salman, J.C. Buhl, W. Lutz, Relation between growth-size and chemical composition of X and Y type zeolites, *Microporous Mesoporous Mater.* 92 (2006) 309–311. <https://doi.org/10.1016/j.micromeso.2006.01.016>.
- [213] A. Sachse, A. Grau-Atienza, E.O. Jardim, N. Linares, M. Thommes, J. García-

- Martínez, Development of Intracrystalline Mesoporosity in Zeolites through Surfactant-Templating, *Cryst. Growth Des.* 17 (2017) 4289–4305. <https://doi.org/10.1021/acs.cgd.7b00619>.
- [214] D. Verboekend, G. Vilé, J. Pérez-Ramírez, Hierarchical y and USY zeolites designed by post-synthetic strategies, *Adv. Funct. Mater.* 22 (2012) 916–928. <https://doi.org/10.1002/adfm.201102411>.
- [215] K. De Jong, J. Zecevic, H. Friedrich, P. De Jongh, M. Bulut, S. Van Donk, R. Kenmogne, A. Finiels, V. Hulea, F. Fajula, Zeolite Y crystals with trimodal porosity as ideal hydrocracking catalysts, *ACS Natl. Meet. B. Abstr.* (2010) 10272–10276. <https://doi.org/10.1002/ange.201004360>.
- [216] L. Vaugon, A. Finiels, T. Cacciaguerra, V. Hulea, A. Galarneau, C. Aquino, J.P. Dath, D. Minoux, C. Gerardin, F. Fajula, Impact of Pore Architecture on the Hydroconversion of Long Chain Alkanes over Micro and Mesoporous Catalysts, *Pet. Chem.* 60 (2020) 479–489. <https://doi.org/10.1134/S0965544120040180>.
- [217] M.L. Guzmán-Castillo, H. Armendáriz-Herrera, P. Pérez-Romo, F. Hernández-Beltrán, S. Ibarra, J.S. Valente, J.J. Fripiat, Y zeolite depolymerization-recrystallization: Simultaneous formation of hierarchical porosity and Na dislodging, *Microporous Mesoporous Mater.* 143 (2011) 375–382. <https://doi.org/10.1016/j.micromeso.2011.03.020>.
- [218] J. García-Martínez, J.Y. Ying, MESOSTRUCTURED ZEOLITIC MATERIALS, AND METHODS OF MAKING AND USING THE SAME, US007589041B2, 2009.
- [219] J. García-Martínez, M. Johnson, J. Valla, K. Li, J.Y. Ying, Mesostructured zeolite y - High hydrothermal stability and superior FCC catalytic performance, *Catal. Sci. Technol.* 2 (2012) 987–994. <https://doi.org/10.1039/c2cy00309k>.
- [220] D. Mehlhorn, J. Rodriguez, T. Cacciaguerra, R.D. Andrei, C. Cammarano, F. Guenneau, A. Gedeon, B. Coasne, M. Thommes, D. Minoux, C. Aquino, J.P. Dath, F. Fajula, A. Galarneau, Revelation on the Complex Nature of Mesoporous Hierarchical FAU-Y Zeolites, *Langmuir.* 34 (2018) 11414–11423. <https://doi.org/10.1021/acs.langmuir.8b03010>.
- [221] J. García-Martínez, M. Johnson, I. Valla, INTRODUCTION OF MESOPOROSITY IN LOW SI/AL ZEOLITES, US2010.0196263A1, 2010. <https://patentimages.storage.googleapis.com/3b/c9/82/c283c7b24afe69/US20100019677A1.pdf>.
- [222] B. Gil, S.I. Zones, S.J. Hwang, M. Bejblová, J. Čejka, Acidic properties of SSZ-33 and SSZ-35 novel zeolites: A complex infrared and MAS NMR study, *J. Phys. Chem. C.* 112 (2008) 2997–3007. <https://doi.org/10.1021/jp077687v>.
- [223] R. Kenmogne, A. Finiels, C. Cammarano, V. Hulea, F. Fajula, Hydroconversion of n-hexadecane over bifunctional microporous and mesoporous model catalysts. Influence of pore architecture on selectivity, *J. Catal.* (2015). <https://doi.org/10.1016/j.jcat.2015.05.026>.
- [224] A.G. Pelmenschikov, R.A. Van Santen, J. Jänchen, E. Meijer, CD3CN as a probe of Lewis and Bronsted acidity of zeolites, *J. Phys. Chem.* 97 (1993) 11071–11074.

- <https://doi.org/10.1021/j100144a028>.
- [225] T.M. Davis, C.Y. Chen, N. Žilková, D. Vitvarová-Procházková, J. Čejka, S.I. Zones, The importance of channel intersections in the catalytic performance of high silica stilbite, *J. Catal.* 298 (2013) 84–93. <https://doi.org/10.1016/j.jcat.2012.10.022>.
- [226] R. Rachwalik, M. Hunger, B. Sulikowski, Transformations of monoterpene hydrocarbons on ferrierite type zeolites, *Appl. Catal. A Gen.* 427–428 (2012) 98–105. <https://doi.org/10.1016/j.apcata.2012.03.037>.
- [227] K. Chakarova, K. Hadjiivanov, FTIR study of N<sub>2</sub> and CO adsorption on H-D-FER, *Microporous Mesoporous Mater.* 177 (2013) 59–65. <https://doi.org/10.1016/j.micromeso.2013.04.022>.
- [228] S. Bordiga, C. Lamberti, F. Bonino, A. Travert, F. Thibault-Starzyk, Probing zeolites by vibrational spectroscopies, *Chem. Soc. Rev.* 44 (2015) 7262–7341. <https://doi.org/10.1039/c5cs00396b>.
- [229] C. Pazé, A. Zecchina, S. Spera, G. Spano, F. Rivetti, Acetonitrile as probe molecule for an integrated 1H NMR and FTIR study of zeolitic Brønsted acidity: Interaction with zeolites H-ferrierite and H-beta, *Phys. Chem. Chem. Phys.* 2 (2000) 5756–5760. <https://doi.org/10.1039/B005677O>.
- [230] E. Catizzzone, M. Migliori, T. Mineva, S. van Daele, V. Valtchev, G. Giordano, New synthesis routes and catalytic applications of ferrierite crystals. Part 2: The effect of OSDA type on zeolite properties and catalysis, *Microporous Mesoporous Mater.* 296 (2020) 109988. <https://doi.org/10.1016/j.micromeso.2019.109988>.
- [231] A.A. Belhekar, R.K. Ahedi, S. Kuriyavar, S.S. Shevade, B.S. Rao, R. Anand, Z. Tvaruzkova, Effect of acid sites of Al- and Fe-Ferrierite on m-xylene isomerization, *Catal. Commun.* 4 (2003) 295–302. [https://doi.org/10.1016/S1566-7367\(03\)00056-6](https://doi.org/10.1016/S1566-7367(03)00056-6).
- [232] W. Daniell, N.Y. Topsøe, H. Knözinger, An FTIR study of the surface acidity of USY zeolites: Comparison of CO, CD<sub>3</sub>CN, and C<sub>5</sub>H<sub>5</sub>N probe molecules, *Langmuir.* 17 (2001) 6233–6239. <https://doi.org/10.1021/la010345a>.
- [233] M.A. Makarova, K.M. Al-Ghefaily, J. Dwyer, Brønsted Acid Strength in US-Y: FTIR of CO adsorption, *J Chem Soc Faraday Trans.* 90 (1994) 383–386.
- [234] C.O. Arean, M.R. Delgado, P. Nachtigall, H.V. Thang, M. Rubeš, R. Bulánek, P. Chlubná-Eliášová, Measuring the Brønsted acid strength of zeolites-does it correlate with the O-H frequency shift probed by a weak base?, *Phys. Chem. Chem. Phys.* 16 (2014) 10129–10141. <https://doi.org/10.1039/c3cp54738h>.
- [235] Y. V. Kissin, Chemical Mechanisms of Catalytic Cracking over Solid Acidic Catalysts: Alkanes and Alkenes, *Catal. Rev. - Sci. Eng.* 43 (2001) 85–146. <https://doi.org/10.1081/CR-100104387>.
- [236] S. Hamieh, Transformation des alcools sur zéolithes protoniques : “rôle paradoxal du coke” Directeur(s), Université de Poitiers, 2013.
- [237] H.S. Cerqueira, C. Sievers, G. Joly, P. Magnoux, J.A. Lercher, Multitechnique



- characterization of coke produced during commercial resid FCC operation, *Ind. Eng. Chem. Res.* 44 (2005) 2069–2077. <https://doi.org/10.1021/ie048963k>.
- [238] C.E. Snape, B.J. McGhee, S.C. Martin, J.M. Andresen, Structural characterisation of catalytic coke by solid-state  $^{13}\text{C}$ -NMR spectroscopy, *Catal. Today*. 37 (1997) 285–293. [https://doi.org/10.1016/S0920-5861\(97\)00021-7](https://doi.org/10.1016/S0920-5861(97)00021-7).
- [239] M.A. Callejas, M.T. Martínez, T. Blasco, E. Sastre, Coke characterisation in aged residue hydrotreating catalysts by solid-state  $^{13}\text{C}$ -NMR spectroscopy and temperature-programmed oxidation, *Appl. Catal. A Gen.* 218 (2001) 181–188. [https://doi.org/10.1016/S0926-860X\(01\)00640-8](https://doi.org/10.1016/S0926-860X(01)00640-8).
- [240] A. Devaraj, M. Vijayakumar, J. Bao, M.F. Guo, M.A. Derewinski, Z. Xu, M.J. Gray, S. Proding, K.K. Ramasamy, Discerning the Location and Nature of Coke Deposition from Surface to Bulk of Spent Zeolite Catalysts, *Sci. Rep.* 6 (2016) 1–11. <https://doi.org/10.1038/srep37586>.
- [241] S.J. Reaume, N. Ellis, Synergistic effects of skeletal isomerization on oleic and palmitic acid mixtures for the reduction in cloud point of their methyl esters, *Energy & Fuels*. 26 (2012) 4514–4520. <http://pubs.acs.org/doi/abs/10.1021/ef3006564> (accessed December 3, 2014).